

Magazine of Civil Engineering

ISSN 2712-8172

99(7), 2020





ПОЛИТЕХ
Санкт-Петербургский
политехнический университет
Петра Великого

Инженерно-строительный институт
Центр дополнительных профессиональных программ
195251, г. Санкт-Петербург, Политехническая ул., 29,
тел/факс: 552-94-60, www.stroikursi.spbstu.ru,
stroikursi@mail.ru

**Приглашает специалистов организаций, вступающих в СРО,
на курсы повышения квалификации (72 часа)**

| Код | Наименование программы | Виды работ* |
|---------------------------------------|--|--|
| Курсы по строительству | | |
| БС-01-04 | «Безопасность и качество выполнения общестроительных работ» | п.1,2, 3, 5, 6, 7, 9, 10, 11, 12, 13, 14 |
| БС-01 | «Безопасность и качество выполнения геодезических, подготовительных и земляных работ, устройства оснований и фундаментов» | 1,2,3,5 |
| БС-02 | «Безопасность и качество возведения бетонных и железобетонных конструкций» | 6,7 |
| БС-03 | «Безопасность и качество возведения металлических, каменных и деревянных конструкций» | 9,10,11 |
| БС-04 | «Безопасность и качество выполнения фасадных работ, устройства кровель, защиты строительных конструкций, трубопроводов и оборудования» | 12,13,14 |
| БС-05 | «Безопасность и качество устройства инженерных сетей и систем» | 15,16,17,18,19 |
| БС-06 | «Безопасность и качество устройства электрических сетей и линий связи» | 20,21 |
| БС-08 | «Безопасность и качество выполнения монтажных и пусконаладочных работ» | 23,24 |
| БС-12 | «Безопасность и качество устройства мостов, эстакад и путепроводов» | 29 |
| БС-13 | «Безопасность и качество выполнения гидротехнических, водолазных работ» | 30 |
| БС-14 | «Безопасность и качество устройства промышленных печей и дымовых труб» | 31 |
| БС-15 | «Осуществление строительного контроля» | 32 |
| БС-16 | «Организация строительства, реконструкции и капитального ремонта. Выполнение функций технического заказчика и генерального подрядчика» | 33 |
| Курсы по проектированию | | |
| БП-01 | «Разработка схемы планировочной организации земельного участка, архитектурных решений, мероприятий по обеспечению доступа маломобильных групп населения» | 1,2,11 |
| БП-02 | «Разработка конструктивных и объемно-планировочных решений зданий и сооружений» | 3 |
| БП-03 | «Проектирование внутренних сетей инженерно-технического обеспечения» | 4 |
| БП-04 | «Проектирование наружных сетей инженерно-технического обеспечения» | 5 |
| БП-05 | «Разработка технологических решений при проектировании зданий и сооружений» | 6 |
| БП-06 | «Разработка специальных разделов проектной документации» | 7 |
| БП-07 | «Разработка проектов организации строительства» | 8 |
| БП-08 | «Проектные решения по охране окружающей среды» | 9 |
| БП-09 | «Проектные решения по обеспечению пожарной безопасности» | 10 |
| БП-10 | «Обследование строительных конструкций и грунтов основания зданий и сооружений» | 12 |
| БП-11 | «Организация проектных работ. Выполнение функций генерального проектировщика» | 13 |
| Э-01 | «Проведение энергетических обследований с целью повышения энергетической эффективности и энергосбережения» | |
| Курсы по инженерным изысканиям | | |
| И-01 | «Инженерно-геодезические изыскания в строительстве» | 1 |
| И-02 | «Инженерно-геологические изыскания в строительстве» | 2,5 |
| И-03 | «Инженерно-гидрометеорологические изыскания в строительстве» | 3 |
| И-04 | «Инженерно-экологические изыскания в строительстве» | 4 |
| И-05 | «Организация работ по инженерным изысканиям» | 7 |

*(согласно приказам Минрегионразвития РФ N 624 от 30 декабря 2009 г.)

**По окончании курса слушателю выдается удостоверение о краткосрочном повышении
квалификации установленного образца (72 ак. часа)**

Для регистрации на курс необходимо выслать заявку на участие, и копию диплома об образовании по телефону/факсу: 8(812) 552-94-60, 535-79-92, , e-mail: stroikursi@mail.ru.

Magazine of Civil Engineering

SCHOLAR JOURNAL

ISSN 2712-8172

Свидетельство о государственной регистрации:
Эл № ФС77-77906 от 19.02.2020,
выдано Роскомнадзором

Специализированный научный журнал. Выходит с
09.2008.

Включен в Перечень ВАК РФ

Индексируется в БД Scopus

Периодичность: 8 раз в год

Учредитель и издатель:

Санкт-Петербургский политехнический университет
Петра Великого

Адрес редакции:

195251, СПб, ул. Политехническая, д. 29

Главный редактор:

Екатерина Александровна Линник

Научный редактор:

Виталий Владимирович Сергеев

Заместитель главного научного редактора:

Галина Леонидовна Козинец

Редакционная коллегия:

PhD, проф. Т. Аввад;
д.т.н., проф. М.И. Бальзанников
д.т.н., проф. А.И. Белостоцкий;
к.т.н., проф. А.И. Боровков;
д.т.н., проф. А. Бородинец;
PhD, проф. М. Велькович;
PhD, проф. Р.Д. Гарг;
PhD, М.Р. Гарифуллин;
Dr.-Ing, проф. Т. Грис;
д.т.н., проф. Т.А. Дацюк;
д.т.н., проф. В.В. Елистратов;
Dr.-Ing., проф. Т. Кэрки;
д.т.н., проф. Д.В. Козлов;
д.т.н., доцент С.В. Корниенко;
д.т.н., проф. Ю.Г. Лазарев;
д.т.н., проф. М.М. Мухаммадиев;
Dr.-Ing. Habil., проф. Х. Пастернак;
Dr.-Ing., проф. Ф. Рёгинер;
д.т.н., проф. Т.З. Султанов;
д.т.н., проф. М.Г. Тягунов;
акад. РАН, д.т.н., проф. М.П. Федоров;
Dr.-Ing., проф. Д. Хецк;
д.г.-м.н. А.Г. Шашкин;
д.т.н. В.Б. Штильман

Дата выхода: 27.11.2020

© ФГАОУ ВО СПбПУ, 2020
© Иллюстрация на обложке: Илья Смагин

Magazine of Civil Engineering

SCHOLAR JOURNAL

ISSN 2712-8172

Peer-reviewed scientific journal

Start date: 2008/09

8 issues per year

Publisher:

Peter the Great St. Petersburg Polytechnic University

Indexing:

Scopus, Russian Science Citation Index (WoS),
Compendex, EBSCO, Google Academia, Index
Copernicus, ProQuest, Ulrich's Serials Analysis System,
CNKI

Corresponding address:

29 Polytechnicheskaya st., Saint-Petersburg, 195251,
Russia

Editor-in-chief:

Ekaterina A. Linnik

Science editor:

Vitaly V. Sergeev

Deputy chief science editor:

Galina L. Kozinetc

Editorial board:

T. Awwad, PhD, professor
M.I. Balzannikov, D.Sc., professor
A.I. Belostotsky, D.Sc., professor
A.I. Borovkov, PhD, professor
A. Borodinets, Dr.Sc.Ing., professor
M. Veljkovic, PhD, professor
R.D. Garg, PhD, professor
M. Garifullin, PhD, postdoctorant
T. Gries, Dr.-Ing., professor
T.A. Datsyuk, D.Sc., professor
V.V. Elistratov, D.Sc., professor
T. Kärki, Dr.-Ing., professor
D.V. Kozlov, D.Sc., professor
S.V. Korniyenko, D.Sc., professor
Yu.G. Lazarev, D.Sc., professor
M.M. Muhammadiev, D.Sc., professor
H. Pasternak, Dr.-Ing.habil., professor
F. Rögener, Dr.-Ing., professor
T.Z. Sultanov, D.Sc., professor
M.G. Tyagunov, D.Sc., professor
M.P. Fedorov, D.Sc., professor
D. Heck, Dr.-Ing., professor
A.G. Shashkin, D.Sc.
V.B. Shtilman, D.Sc.

Date of issue: 27.11.2020

© Peter the Great St. Petersburg Polytechnic University.
All rights reserved.
© Coverpicture – Ilya Smagin

Contacts:

E-mail: mce@spbstu.ru

Web: <http://www.engstroy.spbstu.ru>

Contents

| | |
|---|------|
| Resatalab, S., Ahmadi, M.T., Alembagheri, M. Seismic response sensitivity analysis of intake towers interacting with dam, reservoir and foundation | 9901 |
| Rodriguez Vazquez, S., Mokrova, N. Spatial analysis methodologies using multicriteria evaluation approaches | 9902 |
| Lei, G., Weiping, S., Lixia, G., Lunyan, W. Numerical simulation of concrete dam during heavy rain | 9903 |
| Ibrahim, Y.E-H., Abdelsalam, S.S.A., Nabil, M.N.A., Elsayed, M.E. Earth pressure reduction on retaining walls using EPS geofoam | 9904 |
| Hajmohammadian Baghba, M., Hashemi, S.A.H, Kalbasi Anaraki, K, Hashemi, E.S. Influence of polypropylene-fiber on the mechanical properties of self-compacting-concrete with recycled aggregates | 9905 |
| Fedosov, S.V., Loginova, S.A. Mathematical model of concrete biological corrosion | 9906 |
| Antipov, V.V., Ofrikhter, V.G. Transition factor between elastic and deformation moduli for dispersive soils | 9907 |
| Lan, C.N., Nguyen, M.H., Thanh, B.T., Long, N.N., Tien, L.D., Ho, L.S. Bearing capacity of drilled shaft in intermediate geomaterials | 9908 |
| Rybakov, V.A., Sovetnikov, D.O., Jos, V.A. Bending torsion in Γ -shaped rigid and warping hinge joints | 9909 |
| Al-Rousan, R. Behavior of B-C connections damaged by thermal shock | 9910 |
| Aniskin, N.A., Nguyen, T.C. The effect of formworks on the temperature regime in the mass concrete | 9911 |
| Vatin, N., Gubayduln, R.G., Tingaev, A. Flange connections with high-strength bolts with technological heredity of bolts | 9912 |
| Toropov, A.S., Byzov, V.E., Melekhov, V.I. Deformations during drying of wooden corner elements of I-beams | 9913 |



DOI: 10.18720/MCE.99.1

Seismic response sensitivity analysis of intake towers interacting with dam, reservoir and foundation

S. Resatalab^a, M.T. Ahmadi^{*a}, M. Alembagheri^b

^a Department of Civil and Environmental Engineering, Tarbiat Modares University, Tehran, Iran

^b Centre for Infrastructure Engineering, Western Sydney University, Sydney, Australia.

* E-mail: Mahmadi@modares.ac.ir

Keywords: intake tower, interaction intake tower- dam- foundation, seismic response, hydrodynamic pressure

Abstract. In this paper, parameter sensitivity analysis of the dynamic response of cylindrical intake towers interacting with the concrete dam, foundation, internal and surrounding water is performed. The tower is modelled and verified using three-dimensional finite elements according to the Eulerian-Lagrangian approach in the time domain. In order to carry out a parametric study, the Taguchi optimization method is employed to distinguish the most influential parameters. Thus, the iteration algorithm and number of numerical tests are designed. The models are tested under longitudinal horizontal excitation of selected reference accelerograms for either hard soil or hard rock. The evaluation of the results indicated that the two parameters, i.e. tower's slender ratio, and the surrounding water depth are the most effective factors on both intake tower's top drift and the base shear coefficient under seismic excitations on hard soil. It is observed that the elasticity modulus of the foundation is another influential factor in the seismic response, as the tower's drift increases with the foundation's flexibility. Furthermore, the effect of dam interaction on the tower drift reduces as the distance from the dam increases and stays relatively constant for any distance higher than twice the tower's height. Interesting to note that the intake tower did not show notable sensitivity to the reference hard rock ground motion compared with that of the hard soil ground motion.

1. Introduction

Intake towers are of most importance among hydraulic structures in a dam-reservoir system. These are rather lean structures with either cylindrical or rectangular cross-sections at the vicinity of large dams, and surrounded by their reservoir water and usually containing internal water as well. However, in highly seismic areas, they are so much prone to damages due to both direct ground motion and the induced hydrodynamic pressure. In this paper, we study the sensitivity of free-standing intake towers to several geometric and material parameters.

In previous works, researchers first analytically evaluated the effects of water compressibility, surface waves and the popular "added mass" method on seismic response of the cylindrical intake tower with the fixed cross-section due to rigid ground harmonic motion. They have found that in the lower-frequencies of excitation, the effects of surface waves and water compressibility on slender towers are ignorable [1]. The latter has been found when the dam is not present in the vicinity of the tower. Liaw and Chopra used Finite-element method for the hydrodynamic solution of Laplace equation and developed an incompressible fluid formulation with reasonable boundary conditions [2]. Other works presented simplified added mass approach for calculating the hydrodynamic pressure on intake towers, while accounting for dynamic tower-water-foundation [3]. However, in their researches, the considered added mass for creating hydrodynamic pressure only included the effect of the tower vibration, and the effect of the large dam near the tower ignored. Moreover, the linear responses of the intake towers under the harmonic ground motion for different parameters, including geometry, internal and surrounding water and foundation system were idealized. Previous research on intake towers has analyzed towers that are anchored to the supporting foundation. Their results used in *engineering manuals* [4–11]. Milan et al. studied the dam body effect on the seismic response of a cylindrical intake tower on a rigid

Resatalab, S., Ahmadi, M.T., Alembagheri, M. Seismic response sensitivity analysis of intake towers interacting with dam, reservoir and foundation. Magazine of Civil Engineering. 2020. 99(7). Article No. 9901
DOI: 10.18720/MCE.99.1



This work is licensed under a CC BY-NC 4.0

foundation in the reservoir-tower system. They observed an unpredicted resonance created on the tower response due to a modified added mass, caused by the tower-dam-reservoir interaction. This event was interpreted as the results of the added mass induced by reflective waves from the dam. Additionally, the phenomenon could alter the natural frequencies of the tower and thus, the seismic response of the tower [12, 13]. Alembagheri studied the seismic response of a sample intake tower with a cone frustum, including the dam and its foundation under different conditions of the reservoir water compressibility, distance from the dam, and foundation material. Furthermore, in the absence of the dam, vertical excitation did not affect the tower response, and for slender towers, foundation interaction was intensified when the dam was absent [14, 15]. However, in his research, the effects of the tower geometry, as well as the different internal and surrounding water depths, were not evaluated. Indeed, simultaneous consideration of influential factors including the geometry of the tower has been less studied. In a recent research, an analytical solution for hydrodynamic pressure on the cylindrical tower with elliptical cross-section on a rigid foundation has been derived but without the presence of the dam [16].

The goal of the current research is to examine the effects of different parameters on the seismic response of intake towers, the consistency of the idealized model of the system of the intake tower is first verified under the Taft earthquake. After that, using Taguchi optimization method, the required test cases for a cylindrical intake tower with variable conditions including geometry, internal and surrounding water depth, foundation material and dam body distance are established in order to distinguish the most crucial parameters on the seismic response of the complete system.

2. Methods

2.1. Governing equations and boundary conditions

This section outlines the governing equations of the coupled fluid-solid interaction and its boundary conditions. The governing differential equation of the solid domain in the displacement-based Lagrangian formulation, assuming no static gravity load, is:

$$\nabla \cdot \sigma - \rho_s \ddot{u} = 0 \quad (1)$$

where σ is the Cauchy stress tensor, u is the displacement vector, ρ_s is the solid mass density, ∇ represents the Del operator, and (\ddot{u}) represents the second derivative with respect to time [17]. Using the pressure-based Eulerian formulation, assuming that the fluid as inviscid, linearly compressible, with small amplitude irrotational motion, the governing equation of the fluid domain can be represented as:

$$\nabla^2 p - \frac{1}{c^2} \ddot{p} = 0 \quad (2)$$

where p is the hydrodynamic pressure in excess of hydrostatic pressure, c the acoustic wave velocity in the water, and ∇^2 the Laplacian operator. In practice, the effects of surface gravity waves can be neglected in the analysis of high and slender intake tower, so the zero-pressure boundary, $p = 0$ [1]. The boundary condition on the fluid-structure interface, considering no flow through the fluid-solid interface, can be written as:

$$\frac{\partial p}{\partial n} = -\rho_w \ddot{u}_n \quad (3)$$

where ρ_w water mass density, and n is the boundary surface outward normal vector. In the finite element formulation, the upstream infinite fluid domain should be truncated at a sufficient distance from the fluid-solid interface, where Non-reflective Sommerfeld boundary condition is employed [18]:

$$\frac{\partial p}{\partial n} = -\frac{1}{c} \dot{p} \quad (4)$$

The wave reflection at the bottom of the reservoir in the absence of the vertical and transversal direction acceleration can be written as [20]:

$$\frac{\partial p}{\partial n} = -\frac{1}{\beta \cdot c} \dot{p} \quad (5)$$

β is acoustic impedance ratio of bottom to water acoustic impedance:

$$\beta = \frac{\rho_b \cdot c_b}{\rho \cdot c} \quad (6)$$

where c is the water wave velocity, is represented in a simplified way using an absorption coefficient α .

$$\frac{1}{\beta} = \frac{1 - \alpha}{1 + \alpha} \quad (7)$$

That $\alpha = 0$ implies a non-reflective boundary and implies a fully reflective boundary. c_b is the P-wave velocity in the bottom of reservoir.

The tower is decidedly smaller than the foundation, so the foundation is modelled massless with eight nodes elements as a rectangular shape with a depth more than two times of the tower's height for observing the interaction behaviour.

2.2. System Model Verification

The initial validity of the model is verified against Chopra and Goyal, for the case of the intake tower of the Briones dam response time history under Taft's earthquake [4]. Although they employed a novel added mass concept, instead of our rigorous hydrodynamic model, the considerable agreement is achieved between the two analyses as depicted in Figs. 3.

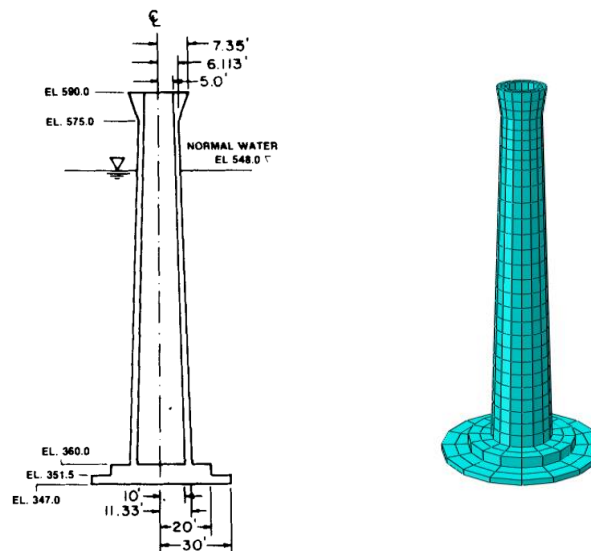


Figure 1. Geometry and the Finite element model of Briones Dam Intake Tower.

In this research, concrete Young's modulus of elasticity E_s is 31 GN/m^2 , unit weight is 24.3 kN/m^3 and Poisson's ratio 0.17. The material properties of the foundation material include; shear wave velocity $C_f = 305 \text{ m/s}$, unit weight = 25.9 kN/m^3 , Poisson's ratio = 0.33 and a constant hysteretic damping factor of $\eta_f = 0.10$.

Table 1. Different cases of analysis of Briones Dam Intake Tower to Taft ground motion.

| Case | Surrounding Water Level | Inside Water Level | Foundation |
|------|-------------------------|--------------------|------------|
| 1 | none | none | Rigid |
| 2 | normal | none | Rigid |
| 3 | none | normal | Rigid |
| 4 | normal | normal | Rigid |
| 5 | none | none | flexible |
| 6 | normal | normal | flexible |

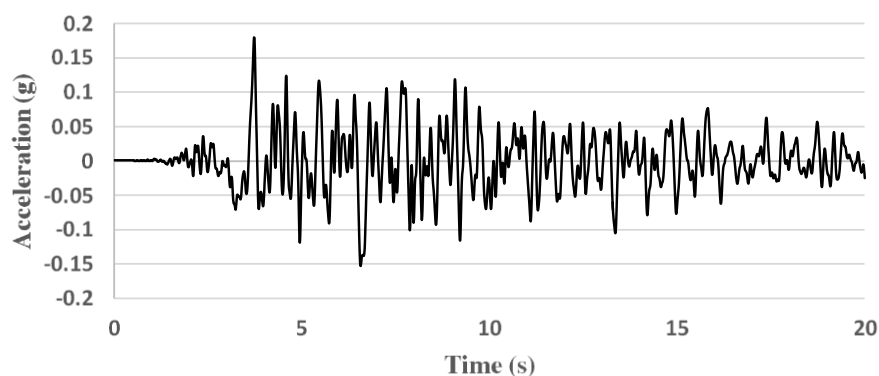


Figure 2. Ground motion recorded at Taft, California, on hard soil, Earthquake July 21, 1952 [20].

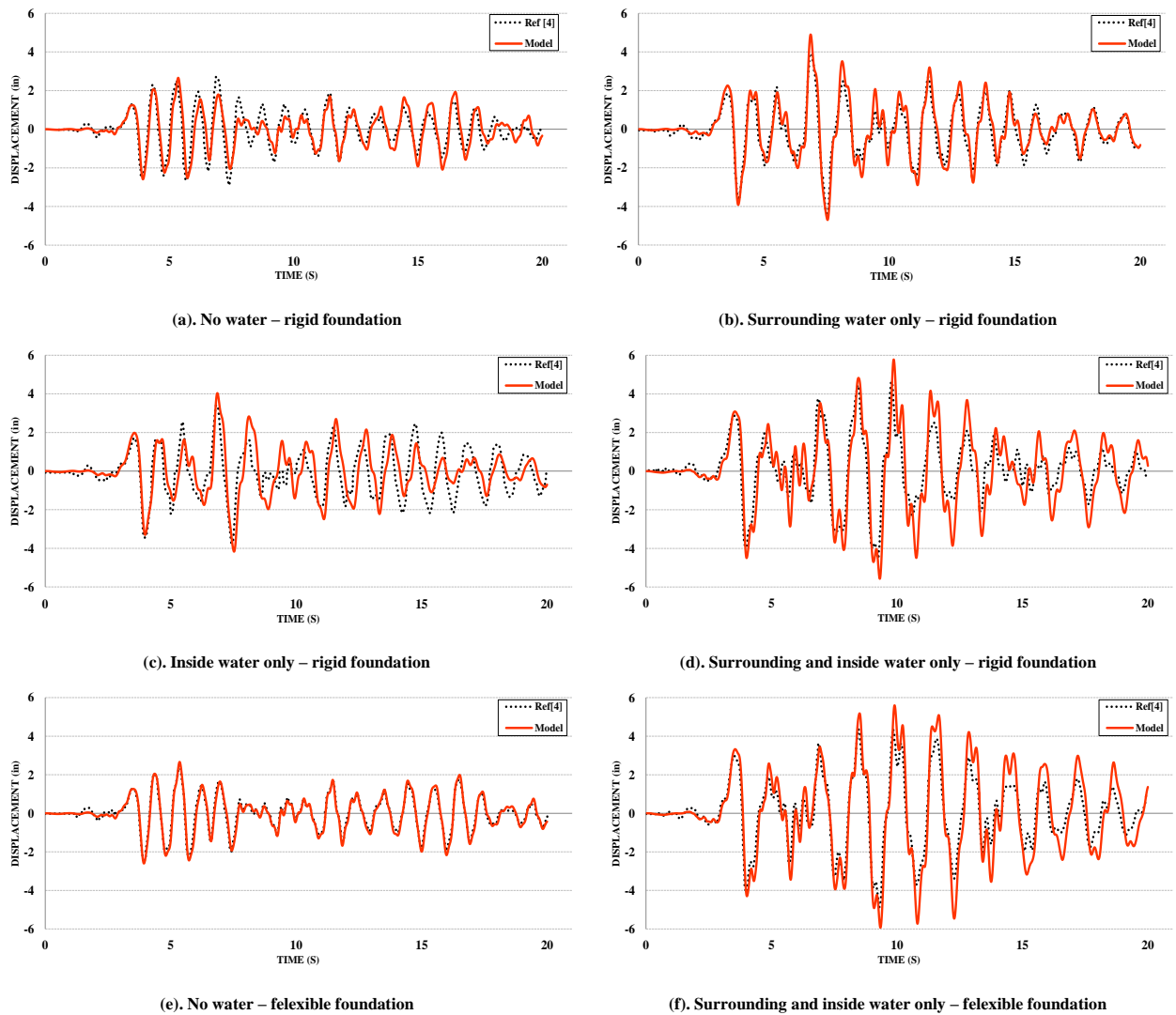


Figure 3. Horizontal displacement at the Briones Tower top due to Taft (1952) excitation in model and reference [4].

2.3. Numerical Values and Analysis Cases

2.3.1. Model and Parameters

Different parameters effects on the seismic response of the cylindrical intake tower with hydrodynamic, structural, and foundation interactions under horizontal longitudinal components of the Taft ground motion (a hard soil record) and the Loma Prieta ground motion (a hard Rock record) are studied [21]. The dam geometry is assumed as a triangular one with a vertical upstream face and a 0.8:1 slope at the downstream face. The dam and the tower heights are always the same, but variable in different cases. Reservoir transverse dimension is assumed to equal to $B = 300$ meters.

Effects of eight different parameters are studied according to Table 1-1 and Figs. 4, 5 [22]. Tower height H , along with some dimensionless parameters r/H and t/r corresponding the tower section internal radius r , and wall thickness t are considered. Moreover, for evaluating the transverse location of the tower in the reservoir, b/B parameter is used where b is the shortest distance of the tower from the reservoir vertical side banks. The effects of internal and surrounding water depths, d_i and D respectively, are also studied, using d_i/H and D/H quantities. Reservoir end boundary is always three times the tower height far from it, and foundation model extension is two times the tower's height. Foundation material parameter is considered by the E_c/E_f ratio where E_c and E_f are the concrete and the foundation elasticity moduli, respectively. Tower distance from the dam L , is also considered by the L/H ratio. For all the 8 latter parameters three different values belonging to appropriate ranges of variation are considered, as depicted in Table 2.

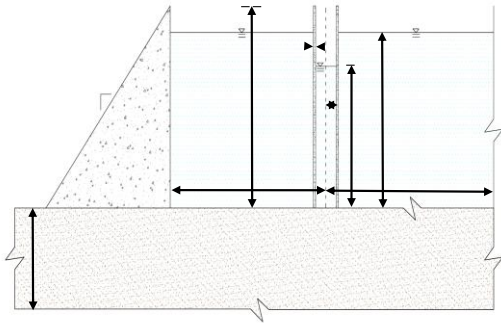


Figure 4. The geometry of the intake tower, dam, water and foundation system.

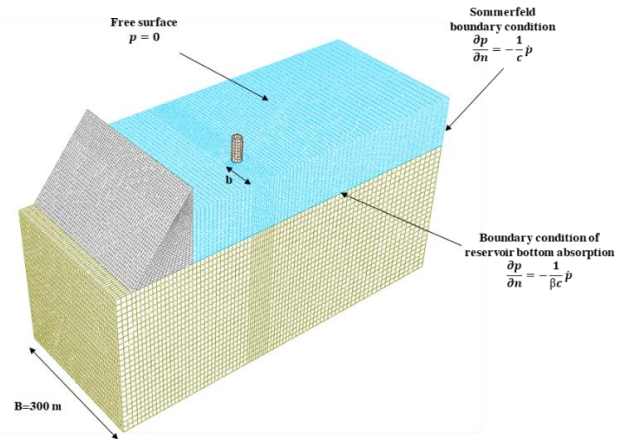


Figure 5. Three-dimensional finite element model of the whole system.

Table 2. System parameters and their selected values.

| level | 1 | 2 | 3 |
|-----------|------|-------|------|
| b/B | 0.25 | 0.5 | – |
| H (m) | 50 | 100 | 150 |
| r/H | 0.03 | 0.05 | 0.07 |
| t/r | 0.15 | 0.175 | 0.2 |
| D/H | 0.4 | 0.7 | 1 |
| di/H | 0 | 0.4 | 1 |
| E_c/E_f | 0 | 1 | 3 |
| L/H | 1 | 2 | 3 |

The assumed material properties for the dam and the intake tower are constant, including concrete modulus of elasticity $E_c = 3.45 \times 10^{10}$ N/m², Poisson ratio $\nu = 0.17$, mass density $\rho = 2480$ kg/m³, and damping ratio $\zeta = 0.05$. Water acoustic velocity C , and the mass density ρ_w , are equal to 1440 m/s and 1000 kg/m³, respectively. The wave reflection coefficient at the bottom and the lateral boundaries of the reservoir α , is assumed equal to 0.9.

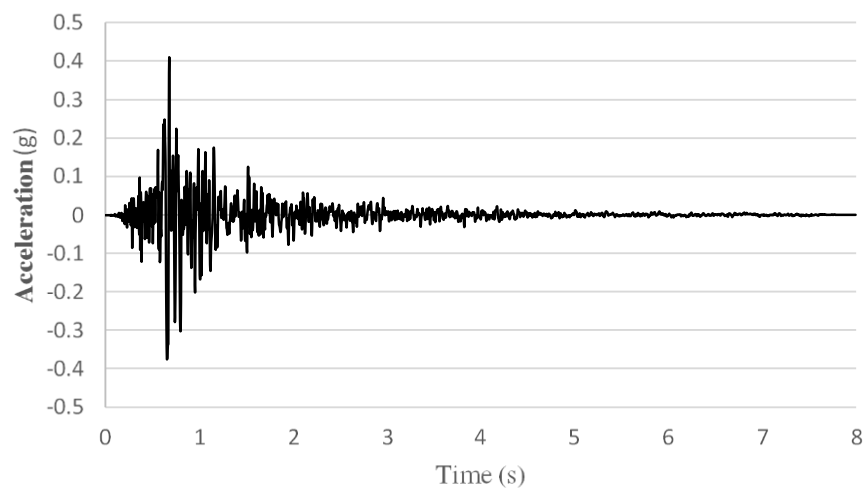


Figure 6. Ground motion recorded at Loma-Prieta, California, on hard rock, Earthquake October 18, 1989 [20].

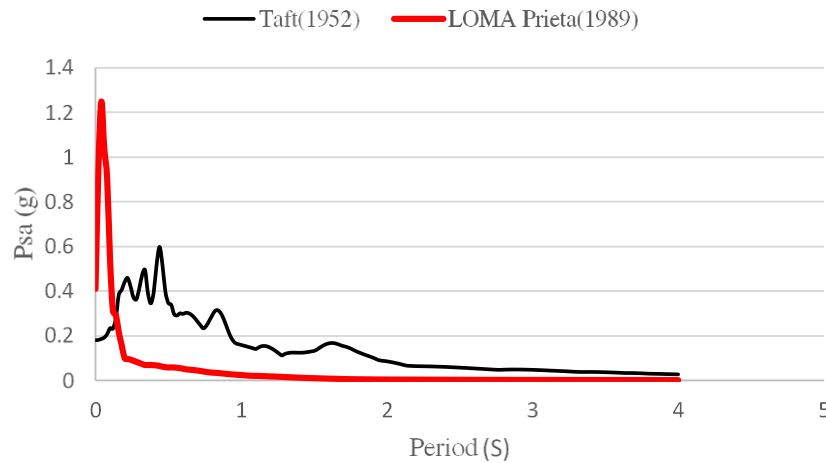


Figure 7. Response Spectra for Taft (1952) and Loma-Prieta (1989) Ground motions [20].

2.3.2. Optimizing the number of numerical experiments

There are a variety of methods for designing experiments. The first is the full factorial method. However, this method requires quite a large number of cases far from and is expensive. Therefore, optimization of the number of the experiments should be considered. One of the practical techniques for optimum design of experiments is the Taguchi method, in which a selected group of orthogonal arrays of parameters values is presented [23].

The standard orthogonal arrays would prepare instruction for partial factorial experiments that includes several combined experiments. While the combinations of levels for all factors are in discussion, the standard orthogonal arrays would satisfy most of the experimental design requirements. Based on the selected eight parameters and their levels in the Taguchi method, the orthogonal arrays $L_{18}(2^1 \times 3^7)$ are selected corresponding to seven parameters with three levels and a single parameter with two levels as seen in Table 3.

Table 3. Test cases investigated according to the Taguchi method.

| case | b/B | H (m) | r/H | t/r | D/H | di/H | E_c/E_f | L/H |
|------|-------|---------|-------|-------|-------|--------|-----------|-------|
| 1 | 0.25 | 50 | 0.03 | 0.15 | 0.4 | 0 | 0 | 1 |
| 2 | 0.25 | 50 | 0.05 | 0.175 | 0.7 | 0.4 | 1 | 2 |
| 3 | 0.25 | 50 | 0.07 | 0.2 | 1 | 1 | 3 | 3 |
| 4 | 0.25 | 100 | 0.03 | 0.15 | 0.7 | 0.4 | 3 | 3 |
| 5 | 0.25 | 100 | 0.05 | 0.175 | 1 | 1 | 0 | 1 |
| 6 | 0.25 | 100 | 0.07 | 0.2 | 0.4 | 0 | 1 | 2 |
| 7 | 0.25 | 150 | 0.03 | 0.175 | 0.4 | 1 | 1 | 3 |
| 8 | 0.25 | 150 | 0.05 | 0.2 | 0.7 | 0 | 3 | 1 |
| 9 | 0.25 | 150 | 0.07 | 0.15 | 1 | 0.4 | 0 | 2 |
| 10 | 0.5 | 50 | 0.03 | 0.2 | 1 | 0.4 | 1 | 1 |
| 11 | 0.5 | 50 | 0.05 | 0.15 | 0.4 | 1 | 3 | 2 |
| 12 | 0.5 | 50 | 0.07 | 0.175 | 0.7 | 0 | 0 | 3 |
| 13 | 0.5 | 100 | 0.03 | 0.175 | 1 | 0 | 3 | 2 |
| 14 | 0.5 | 100 | 0.05 | 0.2 | 0.4 | 0.4 | 0 | 3 |
| 15 | 0.5 | 100 | 0.07 | 0.15 | 0.7 | 1 | 1 | 1 |
| 16 | 0.5 | 150 | 0.03 | 0.2 | 0.7 | 1 | 0 | 2 |
| 17 | 0.5 | 150 | 0.05 | 0.15 | 1 | 0 | 1 | 3 |
| 18 | 0.5 | 150 | 0.07 | 0.175 | 0.4 | 0.4 | 3 | 1 |

In the following, different parameters are investigated in two groups of dynamic time history analysis, first 18 tests for hard soil under Taft acceleration record, and then 18 more tests for hard rock under Loma Prieta acceleration record.

3. Results and Discussion

Sensitivity analyses of the parameters are carried out in terms of the normalized maximum displacement of the tower top node (tower drift), and also in terms of the maximum dynamic base shear force of the intake tower normalized by the tower weight (tower base shear coefficient). Also, the first frequency

mode of each model are been dimensionless according to the first frequency mode of the single intake tower with the rigid foundation. The latter two quantities are believed as the most decisive responses for the seismic design of the tower structure.

3.1. Main effects of parameters on the tower drift

a) Cases of hard soil

According to Fig. 8, tower drift increases considerably when the tower position is more distant from the reservoir bank. This might be due to the effect of the reservoir bank partial absorption of the hydrodynamic energy. Interesting to notice that the higher the intake tower, the less its drift gets.

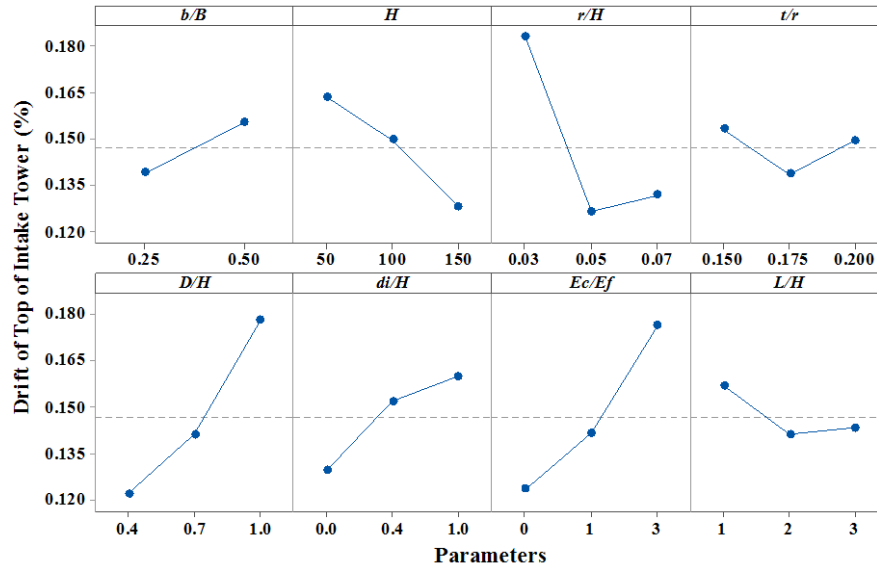


Figure 8. Main effects of different parameters on the tower drift based on hard soil (Taft 1952 record).

Table 4. Contribution of parameters due to variance analysis.

| Parameters | Contribution (%) |
|------------|------------------|
| b/B | 5.75 |
| H (m) | 9.43 |
| r/H | 28.78 |
| t/r | 1.70 |
| D/H | 23.79 |
| di/H | 7.21 |
| E_c/E_f | 21.18 |
| L/H | 2.15 |
| Total | 100% |

According to the statistical analysis on test results of the hard soil cases, the r/H ratio is the most critical parameter for the tower drift, with a share value of 28.78 %. The response of slender intake tower with $r/H = 0.03$ has more than to the other as with past research. The other important note is that the reducing trend from $r/H = 0.05$ stays nearly constant. Of course, it requires other ratios to evaluate carefully. The tower wall thickness parameter, t/r ratio has the least effect on the seismic response of the intake tower with only a 1.7 % share. However, the tower's thickness has a minimum amount, that is mean the optimized thickness of the tower for minimum drift is $t/r = 0.175$ for any similar situation to this experiment. According to the results, the second most effective parameter in the seismic response of the intake tower is the D/H ratio with 23.79 %, pertaining increased drift with increased reservoir depth, or hydrodynamic significance. Generally, the most critical drifts of the towers happen when the reservoir of the concrete dam is at its highest level.

Moreover, the tower internal water level parameter, i.e., the di/H ratio is also directly increasing the tower drift but with a lower rate than that of the surrounding reservoir. The foundation flexibility parameter, E_c/E_f ratio, is the third most effective parameter with a 21.18 % share by a direct proportion, similar to previous researches results [4].

According to Fig. 8 when the distance from the concrete gravity dam increases, the drift reduces, but remains approximately constant for distances more than twice the height of the tower. Of course, this result corresponds to horizontal actuation, as described in the past researches, while the vertical or combined excitation requires additional studies [14].

b) Cases of hard rock

According to Fig. 9, Intake tower response does not show much parametric sensitivity when a hard rock ground motion record is applied. Generally, this might be attributed to the issue of the high-frequency content of the ground motion in respect to the natural frequencies of the system. The only effective parameter in the case of the rock motion Loma Prieta record excitation is the tower height, by which the tower drift reduces for higher towers, a trend similar to the cases of hard soil, i.e., due to the Taft record.

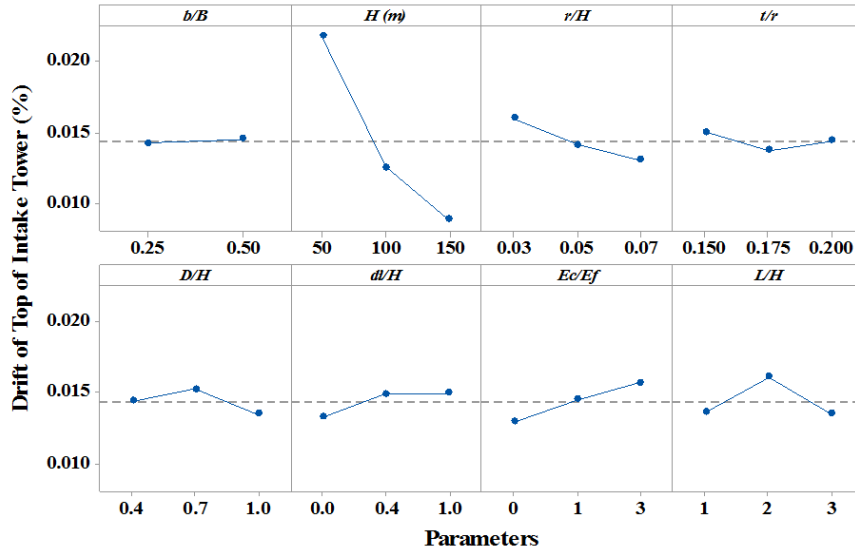


Figure 9. Main effects of different parameters on the tower drift based on the hard rock (Loma Prieta 1989 record).

3.2. Main effects of parameters on the tower base shear coefficient

a) Cases of hard soil

As shown in Fig. 10, the position of the tower in the reservoir width has the minimum effect on the shear coefficient, and thus could be neglected. As the height of the tower increases, the shear coefficient reduces, which can be explained with the tower's more pronounced weight. Moreover, it can be seen that effect of the height remains approximately constant for any height above 100 meters. Similar to the cases of tower drift, the shear force applied to the base of the tower increases for higher ratios of r/H in other words, for fatter towers, higher seismic shear force coefficient is expected. The radius ratio is the most influential parameter.

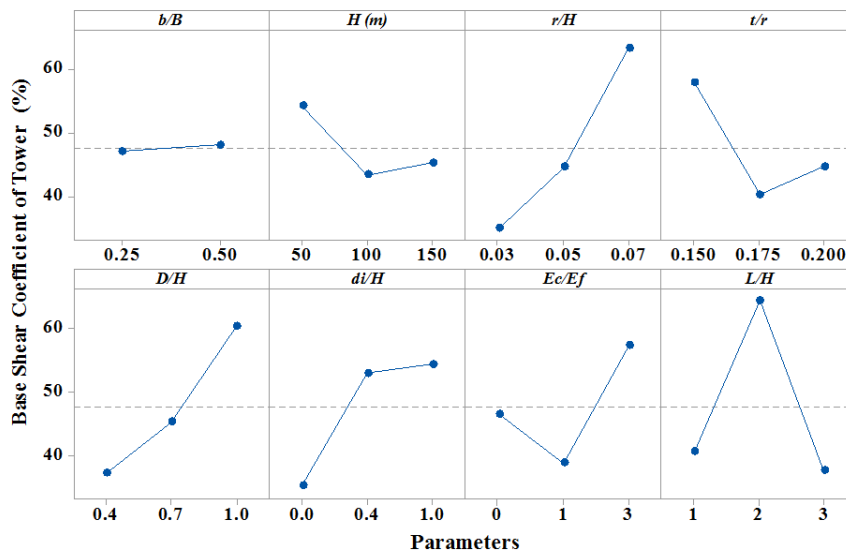


Figure 10. Main effects of different parameters on the tower base shear force coefficient based on hard soil (Taft 1952 record).

Moreover, the effect of the t/r ratio is minimum for the experiment domains, in other hands, for the lowest base shear force for similar conditions, the optimized tower thickness could be considered $t/r = 0.175$. The second effective parameter on the shear coefficient is the D/H ratio of the tower corresponding to the reservoir depth and is similar to the drift cases.

As shown in Fig. 10, the internal water parameter, di/H is again directly affecting the base shear coefficient. The effects of E_c/E_f ratio in shear coefficient is different from the drift case. When the elasticity module of the foundation and the tower were the same, the applied shear force to the tower's base is minimum, and as the foundation became flexible in comparison with the tower, the shear increased.

As for the dam distance ratio, the base shear coefficient maximizes for $L/H = 2$. This is an interesting observation that should be studied further as the hydrodynamic action could more intensively affect the tower when it is at an intermediate distance from the dam body.

b) Cases of hard rock

As shown in the Fig. 11, the reservoir water depth parameter is not effective on the shear coefficient of the intake tower. However, the most critical parameter on the base shear coefficient is the height of the tower as similar to the drift results.

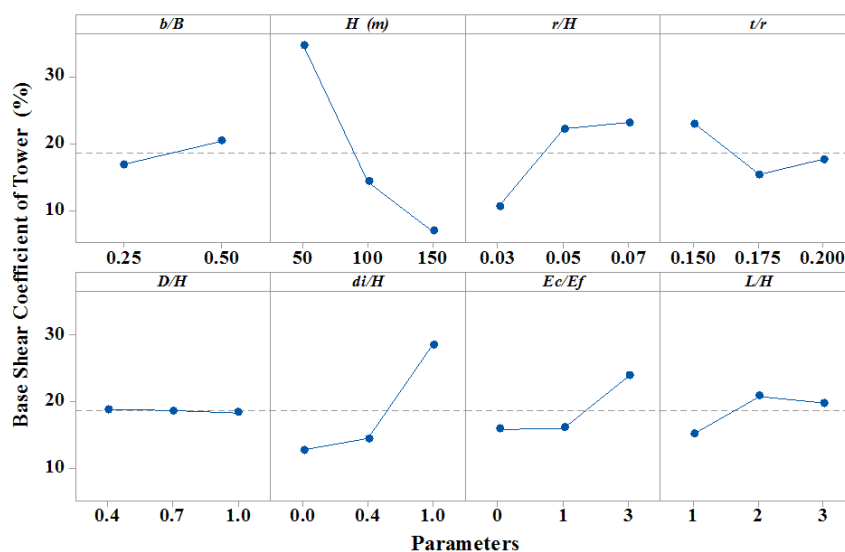


Figure 12. Main effects of different parameters on the tower base shear force coefficient based on hard rock (Loma Prieta 1989 record).

4. Conclusions

In this article, different parameter sensitivities on the dynamic response of cylindrical intake tower interacting with its internal and surrounding water, foundation, and the nearby concrete dam, is studied. For this purpose, the effect of different geometrical, material and loading parameters on the tower top drift, and tower base shear coefficient are studied after verification of the model employed through 3D-dimensional finite elements using Eulerian-Lagrangian approach in the time domain. The parameters in the current research include the height, the section radius and the wall thickness of the tower, as well as its internal and external water depth, foundation material flexibility, and the transverse and longitudinal positioning of the structure in the reservoir for a range of possible variations. Taguchi optimization method for the design of experiments is employed to reduce the number of the experiments drastically, and distinguish the most influential parameters in terms of the two major decisive response components. The study corresponds to longitudinal horizontal excitations records of both hard soil and hard rock conditions. The following conclusions are drawn based on the findings of this study:

1. The investigation of the results indicated that the two parameters of the slender tower ratio and the surrounding water depth were the most effective factors on both intake tower top drift, and the base shear coefficient, respectively under Taft record on hard soil.
2. According to the experimental results, $t/r = 0.175$ is selected as the optimized thickness for designing the tower wall thickness
3. For horizontal excitation, the effect of the tower placement in the reservoir width could be neglected.
4. The presence of the internal water is influential but weaker than the effect of the surrounding water.

5. It is observed that the foundation material, is another influential factor on the seismic response, and the tower drift increases with its flexibility.

6. The dam body interaction effect on the tower drift reduces as the distance from the dam increases and stays relatively constant for any distance higher than twice the height of the intake tower.

7. Interesting to note that the intake tower did not show notable sensitivity to the reference hard rock ground motion compared with that of the hard soil ground motion. The most critical parameter is the height of the tower when studying both the top drift and the base shear coefficient results.

References

1. Liaw, C.Y., Chopra, A.K. Dynamics of towers surrounded by water. *Earthquake Engineering & Structural Dynamics*. 1974. 3(1). Pp. 33–49.
2. Liaw, C.Y., Chopra AK. Earthquake analysis of axisymmetric towers partially submerged in water. *Earthquake Engineering & Structural Dynamics*. 1974. 3(3). Pp. 233–248.
3. Goyal, A., Chopra, A.K. Earthquake analysis of intake-outlet towers including tower-water-foundation-soil interaction. *Earthquake engineering & structural dynamics*. 1989. 18(3). Pp. 325–344.
4. Goyal, A., Chopra, A.K. Hydrodynamic and foundation interaction effects in dynamics of intake towers: earthquake responses. *Journal of Structural Engineering*. 1989. 115(6). Pp. 1386–1395.
5. Goyal, A., Chopra, A.K. Hydrodynamic and foundation interaction effects in dynamics of intake towers: frequency response functions. *Journal of Structural Engineering*. 1989 Jun. 115(6). Pp. 1371–1385.
6. Goyal, A., Chopra, A.K. Simplified evaluation of added hydrodynamic mass for intake towers. *Journal of Engineering Mechanics*. 1989 Jul. 115(7). Pp. 1393–1412.
7. ICOLD. Design and evaluation of appurtenant structures to seismic shaking. *Bulletin* 123. 1999.
8. U.S. Army Corps of Engineers. *Seismic Analysis of Intake Towers Considering Multiple-Support Excitation and Soil-Structure Interaction Effects*. 2004. ERDC/GSL TR-04-16.
9. U.S. Army Corps of Engineers *Structural Design and Evaluation of Outlet Works*. 2003. EM 1110-2-2400.
10. Keightley, W.O., Housner, G.W., Hudson, D.E. *Vibration tests of the Encino dam intake tower*. Report of earthquake Engineering Research laboratory in California institute of technology. 1961.
11. Daniell, W.E., Taylor, C.A. Full-scale dynamic testing and analysis of a reservoir intake tower. *Earthquake Engineering & Structural Dynamics*. 1994. 23(11). Pp. 1219–1237.
12. Millan, M.A., Young, Y.L., Prevost, J.H. The effects of reservoir geometry on the seismic response of gravity dams. *Earthquake engineering & structural dynamics*. 2007. 36(11). Pp. 1441–1459.
13. Millan, M.A., Young, Y.L., Prevost, J.H. Seismic response of intake towers including dam–tower interaction. *Earthquake Engineering & Structural Dynamics*. 2009. 38(3). Pp. 307–329.
14. Alembagheri, M. Dynamics of submerged intake towers including interaction with dam and foundation. *Soil Dynamics and Earthquake Engineering*. 2016. 84. Pp.108–119.
15. Alembagheri, M. Earthquake response of solitary slender freestanding intake towers. *Soil Dynamics and Earthquake Engineering*. 2016. 90. Pp. 1–4.
16. Wang, P., Zhao, M., Du, X. Analytical solution and simplified formula for earthquake induced hydrodynamic pressure on elliptical hollow cylinders in water. *Ocean Engineering*. 2018 Jan 15. 148. Pp 149–160.
17. Sommerfeld, A. *Lectures on theoretical physics*, Vol. I. Academic Press, New York. 1964.
18. Sommerfeld, A. *Partial differential equations in physics*. Vol. 1. Academic press. 1949.
19. Fenves, G., Chopra, A.K. Effects of reservoir bottom absorption on earthquake response of concrete gravity dams. *Earthquake engineering & structural dynamics*. 1983 Nov. 11(6). Pp. 809–829.
20. URL: <http://ngawest2.berkeley.edu>.
21. Hibbit, K. *Abaqus Theory Manual*. Version 6.8. ABAQUS, Inc.: Providence, RI, USA. 2008.
22. U.S. Army Corps of Engineers, *Structural Parameter Analysis of Existing Intake Tower Inventory*. Technical Report. 1996. SL-96-1.
23. Roy, R.K. *A primer on the Taguchi method*. Society of Manufacturing Engineers. 2010.

Contacts:

Soroush Resatalab, s.resatalab@modares.ac.ir

Mohammad Taghi Ahmadi, Mahmadi@modares.ac.ir

Mohammad Alembagheri, Alembagheri@modares.ac.ir



DOI: 10.18720/MCE.99.2

Spatial analysis methodologies using multicriteria evaluation approaches

S. Rodriguez Vazquez*, **N. Mokrova**

National Research Moscow State Civil Engineering University, Moscow, Russia

* E-mail: solrusita85@gmail.com

Keywords: rainwater harvesting, AHP-technique, WLC-technique, multi-criteria evaluation, GIS, dams

Abstract. Water needs for human and agricultural consumption have increased due to an increase in population and human activities. Identifying potential rainwater harvesting sites (RWHS) is an important step towards maximizing water availability for agriculture and other uses. The selection of suitable sites using computational techniques presents a great challenge, so the present study aimed to examine from a critical approach the different approaches reported, as well as the theoretical references of the topic addressed. Computational spatial analysis methodologies were analyzed using multicriteria evaluation (MCDA) approaches as well as computational technologies such as AHP and WLC supported by GIS). As a result of the study carried out, it was concluded that the identification of areas suitable for certain RWH techniques using improved geomatics techniques remains one of the important purposes of development and research. In addition, the MCDA -GIS combination has the potential to provide a rational, objective and non-biased approach to decision-making in locating potential sites for dam construction.

1. Introduction

Over time the identification of hydrological uses has been carried out through procedures that involve a large amount of time and resources. These procedures are focused on the search for geographical areas which allow the development of a jump, either through projects with derivation or projects with dam, and that, in turn, these sites have significant water availability, and available and favorable infrastructural conditions. This search should seek to find efficient projects, with short conduits or narrow canyons [1]. Once a possible site with attractive characteristics is identified, takes place a prefeasibility level analysis, whose main purpose is to make preliminary calculations regarding energy production, the identification of the main technical, environmental and social restrictions, as well as the prior quantification of the investment costs of the evaluated alternative. A good search process guarantees that the obtained benefits justify the future environmental and social impacts to which the area of influence would be subject.

Mwenge et al. [2], Durga et al. [3], Baban et al. [4] agree that, when analyzing the land's suitability or its capacity for the feasibility study and for the selection of potential areas. For the construction of dams it is important to take into account within the selection criteria:

- weather (rain);
- hydrology (rain-runoff relationship and intermittent water courses);
- topography (pending);
- agronomy (crop characteristics);
- soils (texture, structure and depth);
- socioeconomic criteria (population density, workforce, priority of people, experience);
- land tenure;
- water laws;
- accessibility;



- related costs.

Arango [1], Petheram et al. [5], Peng et al. [6] do not consider environmental and social factors within the development of their research, despite this, they recognize their importance in their final recommendations. Failure to consider such factors at the time of the development of decision-making support systems in the selection of potential sites for water collection would result in harmful damages not only at the economic level but also at the social level.

Although criteria have been established for the design of dams, general guidelines and recommended considerations, as well as technical knowledge and experience, there is no certainty that the resulting design criteria can be applied to other reservoir sites with similar conditions [7]. These requirements and pressures have made it necessary to develop a clear criterion to locate the reservoir sites in addition to a more effective system in decision-making, that is, one that can handle a large number of data sets and provide assistance to the decision makers [8].

From the beginning the engineers have carried out the studies of definition of the hydrological potential by analyzing the cartographic, topographic information, among others available in the area of interest. Through the traditional approach, this available information is processed and analyzed independently, thus drawing isolated conclusions that are then contrasted and allow, in some way, to define the potential of the area. The research process of a potential dam site usually involves an iterative process of increasingly detailed studies, which sometimes occurs in just 2 or 3 years, but often in 10 or more years [5], this considering the volume of information that needs to be analyzed manually, which makes it an inefficient and complex process. On the other hand, the fact that the analyzes are carried out independently makes the results obtained rigid and often do not allow analyzing all the possibilities and getting the most out of the processed information.

Authors such as [9], [10], [11], address the need to examine both the location of the reservoir and the site of the dam, because it is important to know the capabilities of the foundations to support the weight of both the volume of water in the reservoir as of the materials for the construction of the dam. Therefore, choosing a suitable site is a crucial phase in the construction of the site. A well-selected site will not only provide the best benefits, but will also allow the acquisition of aesthetic values that contribute to the creation of a recreational area around the reservoir. On the contrary, a poorly selected site or an incorrect decision at the time of building dams in unsuitable areas can cause flooding and therefore damage to industrial, crop or populated areas. In 1963, for example, more than 300 million meters of rock slipped into the reservoir site of the San Vaiont dam in Italy. This generated flood waves, which exceeded the dam crest by 100 m causing the death of 3,000 people downstream [12]. An investigation, at a later date, established that the rocky material on the lateral slope of the reservoir became saturated due to the water deposit and, as a result, the slope became unstable and began to slide towards the reservoir [13]. This example shows the importance of preliminary investigations and recognition in the selection and location of reservoir sites. Before the United Nations Conference on Environment and Development in 1972, the economic importance of a reservoir project preceded all other considerations [4]. Since then, environmental awareness and concern have steadily increased, therefore, decision makers have had to take into account not only technical design and economic factors, but also local and regional environmental and social impacts of a proposed reservoir.

This paper aims to carry out a study of current trends in the use of spatial analysis methodologies for the selection of potential sites for the construction of dams, as well as evaluate the criteria to identify suitable reservoir sites in order to meet future demands of water. In addition, some approaches to multiple criteria analysis techniques and their integration in a GIS context are analyzed and described, with the aim of developing in future research a specialized instrument to accelerate decision-making and planning in hydrological use.

2. Methods

Remote sensing and GIS have the ability to manage, analyze and manipulate all relevant layers of information involved, such as topography, economic and environmental data, in relation to the selection of the reservoir site. In addition, remote sensing data can allow decision makers to investigate a wider area of potential sites in a shorter period of time and at a lower cost [14]. It can also delineate areas of structural weakness by mapping the scope of the main geological lines related to failures and strikes [15], [16]. Since site selection of the site involves large data sets, GIS can be used to maintain and manipulate data in order to extract the necessary information and use the information in the decision-making process [17]. Another important advantage of using GIS in site selection is its ability to display [18].

The digital elevation models (DEM) Fig. 1, allow to obtain much of the information necessary for the definition of the potential and are fundamental at the time of generating the hydrological information, since it is from this information that the morphology of the basins of the territory, which obviously represents primary information for the estimation of the water supply.

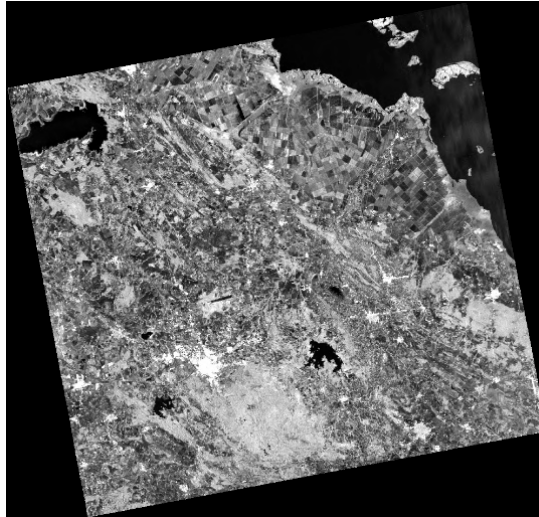


Figure 1. Example of a Digital Elevation Model (DEM).

Various methodologies have been developed for the selection of sites and techniques suitable for water collection. Mbilinyi et al. [19] applied the multi-criteria techniques (MCDA) approach to identify areas for water collection technologies within a GIS context. The approach had been used in some studies in other countries. However, in Tanzania, the approach was new in the field of rainwater harvesting (RWH), because it had not been used to identify suitable areas for such technologies. The combination was useful for evaluating multiple criteria and expert opinion consistently in order to obtain suitability maps and tabular data. He demonstrated that the MCDA-GIS combination has the potential to provide a rational, objective and unbiased approach to making decisions in the identification of potential sites for RWH technologies. Although effective, its methodology could be improved with, for example, the consideration of other factors such as social economy.

Isioye et al. [20] in another study they used Remote Sensing, a limited field survey to identify potential sites for RWH technologies. The entrance to the Decision Support System (DSS) included maps of rainfall, slope, soil texture, soil depth, drainage and land use / coverage, and the exits are maps showing potential sites of water storage systems, stone terraces, bench terraces and borders and Model Builder in ArcView was used as a platform for the DSS. Munyai [21] used GIS and Remote Sensing with primary rainfall data sets, runoff coefficient, soil, slope, land use / coverage and socio-economic aspects of the area under consideration to access the potential for water collection using the software GIS ILWIS and ArcGIS to obtain all the key spatial layers that were used for various analyzes and weighted overlays were made to produce maps showing potential sites for water collection. Weerasinghe et al. [22] focused on the use of a GIS and remote sensing. They developed an integrated methodology to evaluate water management. Consequently, the model specifies the possible water collection and storage sites for water storage and soil moisture conservation on farms [22].

Şen & Al-Suba'i [23] identified and evaluated the factors that could affect the location of the dam in the basins and, therefore, the planning of the water resources of the proposed reservoirs. These authors studied the effects of sedimentation and flooding on the location and construction of dams in Saudi Arabia. Forzieri et al. [24] presented a methodology to assess the suitability of sites for dams. The selection criteria were defined both qualitatively and quantitatively and were based on a territorial analysis using satellite data in combination with hydrological and climatological information. The methodology is particularly useful in areas where there is very little territorial information available, such as most developing countries, and it has been applied in the Kidal region of Mali, where 66 sites were evaluated, of which only 17 complied with the proposed selection criteria. The authors selected suitable construction sites from the predominant technical and engineering perspectives and neglected others, such as socio-political perspectives [24].

Ammar et al. [25] reviewed the methodologies and main criteria that have been applied in arid and semi-arid regions (ASARs) during the past three decades. They classified and compared four main site selection methodologies, identified three main sets of criteria for selecting RWH locations and identified the main characteristics of the most common water collection techniques used in ASARs. The methods were diverse, from those based only on biophysical criteria to more integrated approaches, including the use of socio-economic criteria, especially after 2000. Most studies now select water collection sites using GIS in combination with hydrological models and/or multiple criteria analysis.

In the scientific literature, several studies detail methods for the identification at regional level of promising areas for the collection and storage of water in micro and small farms or to optimize the location and size of storage units in urban drainage environments (by example, Behera et al. [26]; Zoppou [27]; Travis et al. [28], Marques et al. [29]).

In [20], a methodology is proposed in which the first stage consists in identifying and deciding which RWH technologies would be mapped. For this, a field study must be carried out in which the technologies must be defined, examples of which are:

- Collection of surface runoff from open areas and storage in terrestrial structures (ponds).
- RWH in situ and storage in soil profile for crop production.
- Other methods of groundwater recharge, such as sand dams (dam walls and dam reservoirs).
- Rock basin.

Then the criteria to be evaluated are selected and the criteria maps are created, which will be reclassified into five comparable units, that is, suitability classes: 5 (very high suitability), 4 (high suitability), 3 (medium suitability), 2 (low suitability) and 1 (very low suitability). Subsequently, it proposes the suitability model (S), through which suitability maps for water collection are generated by integrating different factor criteria maps using the Weighted Overlay Process (WOP) for the MCDA.

The MCDA was achieved through a weighted linear combination (WLC) in which the continuous criteria (factors) are standardized in a common numerical range and then combined by a weighted average. With a weighted linear combination, the criteria are combined by applying a weight to each, followed by a sum of the results to obtain a suitability map using the following equation:

$$S = (RIWS \times SS_i) + (RIWD \times SD_i) + (RIWL \times SL_i) + W \quad (1)$$

where:

$RIWS$ is relative importance weight for slope layer;

$RIWD$ is relative importance weight for drainage layer;

$RIWL$ is relative importance weight for land cover/use layer;

SS_i is suitability level of cell i in the slope layer;

SD_i is suitability level of cell i in the drainage layer;

SL_i is suitability level of cell i in the land cover/use layer;

W is buffer union of roads settlement and drainage;

i represents the type of water collection technology to use;

The higher the suitability number of a given site criterion, the more suitable it will be for water collection technologies. The weighting assigned to each of the site selection criteria represents the importance of that criterion for the decision-making process for site selection in this project. The importance was thought in terms of "Would the identification of one aspect of these criteria alter the decision to build river basins?". A weighting of 1 was assigned to the criteria with little importance, a weighting of 2 to those criteria with little significance, 3 to a moderate significance and a weighting of 4 and 5 to the criteria with a significant impact on the site selection decision.

Although the proposal is good, it is only aimed at finding the place for water collection and does not include the possibility of finding the location of potential sites for the location of dams, as well as for the prevention of natural hazards. In addition, it does not take into account factors such as the social economy, the runoff coefficient of the soil map and the rain map.

The investigation [30] proposes, as in the previous investigation, a methodology of 4 basic steps: selection of RWH technologies, selection of criteria to evaluate, classification of the criteria according to the determined suitability and subsequently the construction of the suitability map integrated by combining criteria layers using a raster calculator. The GIS database required to identify potential sites for RWH was developed using ArcGIS with vector and raster databases. A suitability model was developed using ModelBuilder in ArcGIS 10.2 to implement all processes to identify sites suitable for RWH. Areas suitable for dams were identified by reclassifying layers of biophysical criteria and combining them using the raster calculation tool in the ArcGIS 10.2 space analyst module. Each criterion was cut in the study area, reclassified to numerical values and suitability classifications for dams were assigned. Finally, the most suitable sites for dams were identified by visual interpretation of satellite images and large-scale mapping analysis.

The proposal offers a map of suitability that will be useful for hydrologists, decision makers and planners to quickly determine areas that have RWH potential. Despite these, the work is carried out using components that will only provide a map that is as appropriate as possible so that experts can identify the sites visually and

not automatically providing the proposal of said potential sites. In addition, social and environmental factors are not taken into account.

As in the previous cases [4], it makes a selection of the criteria to be taken into account and then makes a reclassification of the criteria creating a suitability map for later evaluation. To make use of GIS, create layers of information corresponding to each restriction. The relevant information obtained was converted into the required restriction layers using IDRISI, a raster-based GIS. The restriction layers needed for the study area were derived from several sources, including a land use/coverage map produced from satellite data and field data [31]. This map was used to extract information and build layers of information for defined restrictions, that is, to identify urban areas, to protect agricultural and forestry areas, respectively. The topography was derived from a DEM digitized from a topographic map at a scale of 1:50 000 [4]. Similarly, geology was also derived from the digitization of a geological map at a scale of 1: 200,000 [4]. This process is usually followed by assigning weights to each restriction layer, multiplying each layer by its weight and then successively multiplying the result by each of the restrictions to combine all layers. For them, the authors of this research considered two MCDA approaches to combine the information layers of the Boolean and WLC methods.

Using the Boolean method, all criteria are reduced to restrict Boolean images of areas, which are adequate and not adequate. In addition, all layers are considered equally important and given the same weight [18]. This procedure was applied to all layers of information using the MCDA function in IDRISI to produce the necessary restriction images. For example, Fig. 2 marks the reserved forest areas, which are clearly defined (in black) as not suitable for consideration based on the criteria developed. To obtain the locations of the potential sites, the functions OVERPLAY, GROUP, AREA and RECLASS of the IDRISI tool are used.

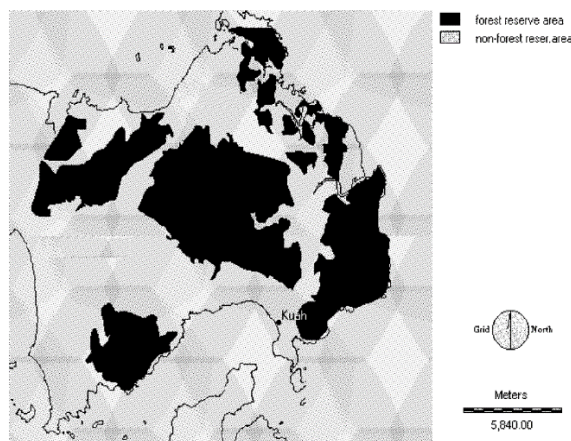


Figure 2. Forest Reserve Areas [4].

The method using the weighted linear combination requires that the main own vector of the pairwise comparison matrix be calculated to produce the best set of weights. Subsequently, the best acceptable adjustment of the respective weights is used in the MCDA function to calculate the WLC using the constraints in the criteria. The main eigenvector was calculated by taking the square reciprocal matrix of pairwise comparisons between the criteria and these weights would add 1. This result could be achieved by calculating the weights with each column and then averaging all the columns [4]. The WEIGHT function in IDRISI, which operates according to this principle, was used to determine the best fit of the weight factors. The consistency index (*CI*) was also determined. The *CI* indicates the probability that the matrix classifications are generated randomly and the value should be less than 0.10; otherwise, the classification of the matrix must be reevaluated [32]. Subsequently, the best acceptable adjustment of the respective weights was used in the MCDA function to calculate the weighted linear combination using the defined factors and constraints. To select only those areas (groups) that can meet the specified surface areas, the IDRISI GROUP, AREA and RECLASS functions were used.

At the conclusion of the investigation, the authors define that both methods provide satisfactory results, it would only depend on the expert to define which of the sites provided by both methods are the most suitable according to the needs and expectations. Although the GIS methodology makes the decision-making process more objective, there is still an element of subjectivity associated with the assignment of weights and map scales. This also allows planners flexibility to incorporate varying degrees of importance to each criterion based on their experience. Through experience, a good judgment in the evaluation of environmental, social and political limitations could produce the best alternative decisions.

The progress of the analytical hierarchy (AHP) is a model that can express a complex problem as an ordered hierarchical structure, and can order the schemes by decision of the people. This method can handle qualitative and quantitative factors in decision making, and has the advantages of systematization, simplicity, practicability and effectiveness. This method was used in article [6] to build dams in the middle and upper

sections, middle sections and lower sections. They list a table according to the criteria and sub-criteria that restrict the location of the series of dams. Then, they build the AHP site selection evaluation system consisting of the subsequent objective, the criteria layer, the sub-criteria layer and the scheme layer and as shown in Fig. 3.

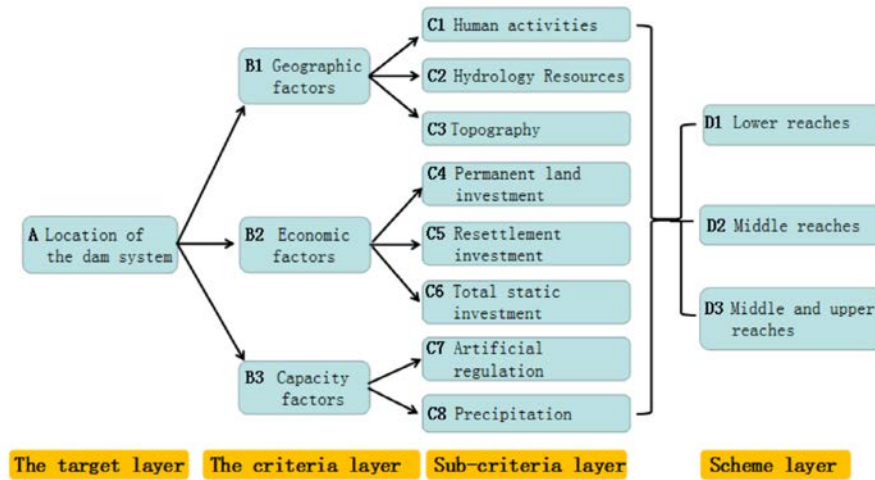


Figure 3. Structure Diagram [6].

Although the criterion in this model is not independent, it is not related to all the elements. In the Table 1 it is clearly described the connection between the factors.

Table 1. The relationship among the criteria and sub-criteria [6].

| Sequence | Factors | Relationship between the factors |
|----------|---------|----------------------------------|
| 1 | A | determined by B1, B2, B3 |
| | B1 | determined by C1, C2, C3 |
| | B2 | determined by C4, C5, C6 |
| 2 | B3 | determined by C7, C8 |
| | C1~C8 | All determined by D1, D2, D3 |

From Table 1 it is necessary to classify the degree of importance of each element that is determined by comparing it with the other elements Table 2.

($X1 > X2$) means that factor $X1$ is more important than factor $X2$; $X1 = X2$ means that factor $X1$ is as important as factor $X2$.

Depending on the degree of importance, the judgment matrix of each layer is constructed as follows, Fig. 4.

| A | B1 | B2 | B3 | B1 | C1 | C2 | C3 | B2 | C4 | C5 | C6 | B3 | C7 | C8 | |
|----|-----|-----|----|----|-----|-----|-----|----|-----|-----|-----|----|-----|-----|-----|
| B1 | 1 | 1/5 | 3 | C1 | 1 | 1/7 | 1/3 | C4 | 1 | 7 | 7 | C7 | 1 | 7 | |
| B2 | 5 | 1 | 7 | C2 | 7 | 1 | 5 | C5 | 1/7 | 1 | 1 | C8 | 1/7 | 1 | |
| B3 | 1/3 | 1/7 | 1 | C3 | 3 | 1/5 | 1 | C6 | 1/7 | 1 | 1 | | | | |
| C1 | D1 | D2 | D3 | C2 | D1 | D2 | D3 | C3 | D1 | D2 | D3 | C4 | D1 | D2 | D3 |
| D1 | 1 | 3 | 5 | D1 | 1 | 1 | 1 | D1 | 1 | 3 | 5 | D1 | 1 | 1/3 | 1/5 |
| D2 | 1/3 | 1 | 3 | D2 | 1 | 1 | 1 | D2 | 1/3 | 1 | 3 | D2 | 3 | 1 | 1/3 |
| D3 | 1/5 | 1/3 | 1 | D3 | 1 | 1 | 1 | D3 | 1/5 | 1/3 | 1 | D3 | 5 | 3 | 1 |
| C5 | D1 | D2 | D3 | C6 | D1 | D2 | D3 | C7 | D1 | D2 | D3 | C8 | D1 | D2 | D3 |
| D1 | 1 | 3 | 5 | D1 | 1 | 1/3 | 3 | D1 | 1 | 1/3 | 1/5 | D1 | 1 | 3 | 5 |
| D2 | 1/3 | 1 | 3 | D2 | 3 | 1 | 5 | D2 | 3 | 1 | 1/3 | D2 | 1/3 | 1 | 3 |
| D3 | 1/5 | 1/3 | 1 | D3 | 1/3 | 1/5 | 1 | D3 | 5 | 3 | 1 | D3 | 1/5 | 1/3 | 1 |

Figure 4. The judgment matrix of each layer [6].

Table 2. The importance degree among the criteria and sub-criteria [6].

| Sequence | Factors | Importance degree |
|----------|---------|-------------------|
| 1 | A1 | B2 > B1 > B3 |
| | B1 | C2 > C3 > C1 |
| 2 | B2 | C4 > C5 = C6 |
| | B3 | C7 > C8 |
| | C1 | D1 > D2 > D3 |
| | C2 | D1 = D2 > D3 |
| | C3 | D1 > D2 > D3 |
| | C4 | D2 > D1 > D3 |
| | C5 | D1 > D2 > D3 |
| | C6 | D2 > D1 > D3 |
| 3 | C7 | D3 > D2 > D1 |
| | C8 | D1 > D2 > D3 |

Based on the judgment matrix, the proportion of each factor was calculated using the MATLAB programming language. Subsequently, the relative parameters were calculated to test the consistency of each layer to judge the consistency of the judgment matrix.

There are some formulas to calculate CI and CR .

$$CI = \frac{\lambda_{\max} - n}{n - 1} \quad (2)$$

where:

λ_{\max} is the largest eigenvalue of every factor;

$n=3$ is the number of the factors in the criteria layer;

CI is the consistency indicators of each layer.

$$CR = \frac{CI}{RI} \quad (3)$$

where:

$RI = 0.58$ is the random consistency index of each layer;

CR is the consistency ratio of each layer;

When proposing the criteria and sub-criteria, it should be taken into account that these should be as complete as possible and refined to obtain the best results in the end, this will greatly improve the objectivity of decision making.

Although the article shows good results, it mentions the criteria to be taken into account for the evaluation and subsequent location of potential sites in the rivers or basins on a map.

That study and others like [1], [6], [9], [33], [34], that examined small and large scale water storage on farms, used techniques that involve the spatial overlap of relevant GIS data to produce a summed classified layer. These approaches, instead of identifying specific locations for dam walls, indicate the most appropriate general areas for the construction of water tanks. These techniques work well for criteria that are easily represented in space, such as large-scale geology, runoff generation, social and environmental effects, and proximity to current and future water demands. In the case of [5] it is proposed that, although composite index techniques are useful for capturing large-scale considerations in the location of dams, they do not explicitly model processes and factors relevant to the performance of large individual dams (for example, performance or construction cost), which depend on the complex game between the following factors:

- topography, p. through the dimensions of the dam wall, the volume of the reservoir and the relationship of the surface area with the volume.
- hydroclimatology, p. through the quantity and the inter and intra annual variability of the entrances to the deposit and the net evaporation of the deposit.

- reliability with which a particular performance can be achieved.

Composite index methods have a limited capacity to assess the relative promise of specific sites, mainly because they do not calculate the potential dimensions of the dam and the reservoir and, therefore, the yield, which is generally the key measure of the yield of the dam. To do this [5] describes DamSite, a series of algorithms that provide a flexible means to identify and classify the possible locations of the dam walls in a landscape from the majority to the least promising, by calculating the potential dimensions of the dam and reservoir, and performance calculation at a given reliability for each potential dam within a basin or region.

According to the stages of the proposed methodology, first, it proposes the realization of a spatial analysis to calculate the dimensions of dams and reservoirs and for this it developed a method to automatically calculate the dimensions of dams and reservoirs from a DEM. The geometric parameters are derived from a DEM and its one-way flow network. Plans and depressions should be treated so that there are no interruptions in the flow network. Once the flow paths have been defined, the model rounds the DEM elevations to whole numbers so that the storage and dam dimensions can be calculated efficiently at discrete heights.

The volume and area of a reservoir contained by a dam along the catchment limit is represented by a table of heights and corresponding areas (represented by a DEM cell count). One table is calculated for each cell in the DEM starting at the cells without entrances (hill tops and ridges), and building tables for each cell downstream by combining the tables of the cells that flow into it. Fig. 5 shows a scheme of several cells, the flow paths between them and the resulting tables of heights and cell counts for each cell.

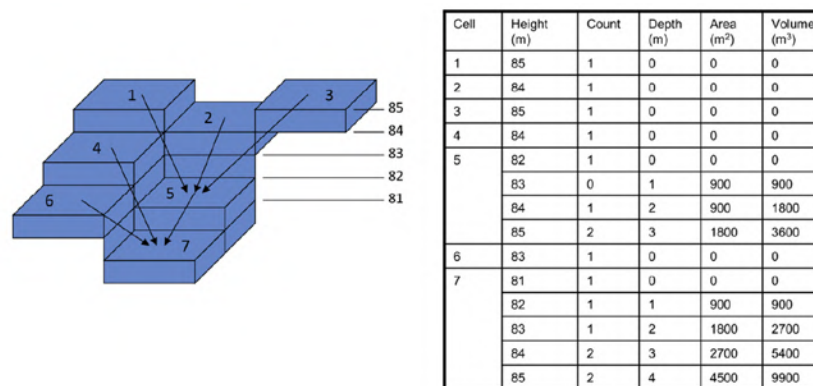


Figure 5. The construction of the height count table for a small set of cells connected by flow paths. The table for each cell is constructed by combining the tables of each contributing cell. The surface areas and volumes are computed from the counts at each depth using a cell area of 900 m² [5].

Given the height count table for a cell, the reservoir area (in m²) for a given water surface elevation is simply the sum of cell counts with heights less than the water surface elevation, multiplied by The area of the cell. The volume (in m³) is the sum of areas for heights less than or equal to the height of the water surface (using a 1m elevation increase). The table captures the depth-area-storage relationship in each DEM cell.

Subsequently, the quantification of topographic constrictions and classification of possible sites of dams was carried out in order to penalize walls of higher and longer dams and, therefore, identify economically efficient locations. Performance calculation involved a two-stage approach:

- A quick preliminary performance estimate for each dam height increase m in each pixel along each channel in the study area. The key inputs for this analysis were the annual average runoff raster's and the standard deviation in the annual runoff.
- For a selection of the 'best' potential storage locations identified during the first stage, more robust performance estimates were calculated using the most computational behavior analysis model. For this analysis, the model used squared time series of daily runoff, rain and evaporation.

Alternatively, the method does not use criteria such as minimization of the flooded area (a source of environmental impact), minimum displacement of resident populations, maximization of hydroelectric potential or flood mitigation. All these criteria require an analysis of the basin and the reservoir as an entry in the site selection.

3. Result and Discussion

One of the main inhibitors identified for the progress and economic development of most urban settlements is the lack of access to adequate water supplies for human consumption and domestic use, irrigation and industrialization [35]. The approaches previously investigated mostly are not based on the

identification of potential sites for the construction of dam walls, but rather indicate the general area to locate water deposits.

They propose the use of proprietary tools such as ArcGIS, GISILWIS, ArcView, ArcMap, among others, in which all the work is done manually using a set of functions and components present in them. In some of the cases, the tools developed or the work carried out on the tools are for certain types of dams with specific objectives, as well as environmental or social factors, nor flood prevention.

As he puts it [36] one of the most damaging factors that must be taken into account is flood prevention due to the dangers of unpredictability. Possible causal factors for flash floods include excessive rain, sudden release of water due to a break in the dam or lake bursting. This factor is important because it affects the other factors, say social, environmental, industrial, economic, etc.

These ideas further highlight the importance of applying computational techniques, as well as creating a specialized tool that allows to speed up the process in decision-making and planning in hydrological use. In this way, the potential sites that affect the most important factors in a very low probability can be obtained, which in turn will make it possible to achieve better results in the construction of the dams in their subsequent use. In addition, your employment can provide some of the following advantages:

- The need for micro dams aimed at specific objectives and that, without damaging the environment, allow the possibility of bringing crops or different branches of production towards them would eliminate the cost of taking water to farther places. This allows the dams, made for the population supply, that are the most exploited, to go directly to it without having more purposes or objectives.
- The creation of small dams aimed at specific objectives not only supports the livestock or crop industry, but also supports flood regulation and the collection of these waters.
- The efficiency (in time and/or space) of multicriteria evaluation methods depends on the number of used criteria. Therefore, by selecting the most important set of criteria, the algorithm would work faster, and would provide the potential sites for the construction of dams.
- Have a multicriteria analysis method that allows hydraulic specialists to know through a feasibility study previously carried out and a simulation and representation of the affected areas, which area of the selected river is best suited for the construction of a dam or micro dams.
- Prevention in making incorrect decisions at the time of the construction of dams in unsuitable areas that may cause flooding and therefore damage in industrial, crop or populated areas.

Finally, it can be affirmed that, although the consulted bibliography reports different approaches in order to obtain better locations of potential sites, the existing approaches still have certain limitations and are still inefficient for their application in decision making. This has led the scientific community, recently, to seek new alternatives to improve the selection results [5], [30], such as increasing the degree of abstraction of the base criteria, new methods of coding them [20], [37] or focus on multicriteria evaluation techniques [38], [39].

4. Conclusion

The large number and topicality of proposals for techniques for selecting potential areas, available in the literature, shows that this topic constitutes a very active field of research. The study confirms that:

1. Local selections are characterized by their effectiveness and efficiency in the results that they offer. However, this type of selection has certain limitations - especially related to the loss of context information - that limit its discriminatory power. Therefore, it is necessary to create and update models for selecting potential sites for the construction of dams with a view to improving the results obtained up to now.
2. The integration of mathematical models in GIS facilitates simulation, as it speeds up the spatial analysis of variables and parameters, allowing the combination of aggregated and distributed data.
3. By analyzing the GIS operations of image processing from spatial remote sensing, it's possible to draw conclusions about flood damage and conditions, and prioritize the corrective measures to be applied; and even estimate the probable maximum avenue in a watershed or the meteorological parameters of hydrological interest.
4. Finally, the creation of multicriteria evaluation methods that take into account the improvement of the initial stages of a prefeasibility analysis and that manage to select the sites with the highest discriminatory power, constitutes a current challenge for the scientific community in this field of research. In this sense, the incorporation of techniques for selecting all potential dam sites within a region is vital to guarantee their discriminatory power and, at the same time, to reduce the dimensionality of the data. Its application is possible in order to increase the effectiveness and efficiency in the prevention of decision-making and in the planning of the construction of hydraulic structures.

References

1. Arango, R.H. Metodología y Herramienta computacional para la identificación y evaluación automatizada de proyectos hidroeléctricos con Derivación y a Pie de Presa. Universidad Nacional de Colombia, 2016.
2. Mwenge Kahinda, J. marc, Lillie, E.S.B., Taigbenu, A.E., Taute, M., Boroto, R.J. Developing suitability maps for rainwater harvesting in South Africa. *Physics and Chemistry of the Earth*. 2008. 33(8–13). Pp. 788–799. DOI: 10.1016/j.pce.2008.06.047
3. Durga Rao, K.H.V., Bhaumik, M.K. Spatial Expert Support System in Selecting Suitable Sites for Water Harvesting Structures – A Case Study of Song Watershed, Uttaranchal, India. *Geocarto International*. 2003. 18(4). Pp. 43–50. DOI: 10.1080/1010604030-8542288
4. Baban, S.M.J., Wan-Yusof, K. Modelling optimum sites for locating reservoirs in tropical environments. *Water Resources Management*. 2003. 17(1). Pp. 1–17. DOI: 10.1023/A:1023066705226
5. Petheram, C., Gallant, J., Read, A. An automated and rapid method for identifying dam wall locations and estimating reservoir yield over large areas. *Environmental Modelling and Software*. 2017. 92. Pp. 189–201. DOI: 10.1016/j.envsoft.2017.02.016
6. Peng, Z. Location of dam using Analytic Hierarchy Progress. *Proceedings of the Advances in Materials, Machinery, Electrical Engineering (AMMEE 2017)*. 114(Ammee). Atlantis Press. Paris, France, 2017. Pp. 441–444. DOI: 10.2991/ammee-17.2017.82
7. S, W., R, M. Introduction. *Current Trends in Design and Construction of Embankment Dams*. Prepared f. ASCE. New York, USA, 1979. Pp. 107. ISBN: 978-0-87262-197-8.
8. Baban, S.M.J., Flannagan, J. Developing and Implementing GIS-assisted Constraints Criteria for Planning Landfill Sites in the UK. *Planning Practice & Research*. 1998. 13(2). Pp. 139–151. DOI: 10.1080/02697459816157
9. Saleh Alatawi, E.A. Dam Site Selection Using Remote Sensing Techniques and Geographical Information System to Control Flood Events in Tabuk City. *Journal of Waste Water Treatment & Analysis*. 2015. 06(01). DOI: 10.4172/2157-7587.1000189
10. Rezaei, P., Rezaie, K., Nazari-shirkouhi, S., Reza, M., Tajabadi, J. Application of Fuzzy Multi-Criteria Decision Making Analysis for evaluating and selecting the Best Location for Construction of Underground Dam. *Acta Polytechnica Hungarica*. 2013. 10(7). DOI: 10.12700/aph.10.07.2013.7.13
11. Chezgi, J., Pourghasemi, H.R., Naghibi, S.A., Moradi, H.R., Kheirkhah Zarkesh, M. Assessment of a spatial multi-criteria evaluation to site selection underground dams in the Alborz Province, Iran. *Geocarto International*. 2016. 31(6). Pp. 628–646. DOI: 10.1080/10106049.2015.1073366
12. Henderson-Sellers, B. *The History of Water Supply. Reservoirs*. Macmillan Education UK. London, 1979. Pp. 11–19. DOI: 10.1007/978-1-349-04133-6_2
13. Nelson, K.D. *Investigating and Planning. Design and Construction of Small Earth Dams* Melbourne, Australia, 1991. Pp. 7–20. ISBN: 0909605343.
14. Baban, S.M.J. Use of remote sensing and geographical information systems in developing lake management strategies. *Hydrobiologia*. 1999. 395/396(0). Pp. 211–226. DOI: 10.1023/A:1017057820780
15. Thomas, H. *Investigations. The engineering of large dams*. 1978. 1. Pp. Investigations. ISBN: 978-0471015284.
16. Avery, T.E., Berlin, G.L. *Engineering Applications. Fundamentals of remote sensing and airphoto interpretation*. 5th ed. Maxwell Macmillan International, 1992. Pp. 349–351. ISBN: 9780023050350.
17. Gupta, S.C. Evaluating geographic information systems technology. *Photogrammetric Engineering and Remote Sensing*. 1989. 55(11). Pp. 1583–1587. ISSN: 0099-1112.
18. Heywood, D.I., Cornelius, S., Carver, S. *An introduction to geographical information systems*. Prentice Hall, 2011. ISBN: 027372259X.
19. Mbilinyi, B.P., Tumbo, S.D., Mahoo, H.F., Mkiramwinyi, F.O. GIS-based decision support system for identifying potential sites for rainwater harvesting. *Physics and Chemistry of the Earth, Parts A/B/C*. 2007. 32(15–18). Pp. 1074–1081. DOI: 10.1016/J.PCE.2007.07.014
20. Isioye, O.A., Shebe, M.W., Momoh, U.O., Bako, C.N. A multi criteria decision support system (MDSS) for identifying rainwater harvesting site(s) in Zaria, Kaduna state, Nigeria. *IJASETR*. 2012. 1(1). Pp. 53–71. ISSN: 1839-7239.
21. Munyao, J.N. *Use of Satellite Products to Assess Water Harvesting Potential in Remote Sensing Areas of Africa: A Case Study of Unguja Island, Zanzibar*. International Institute for Geo-Information Science and Earth Observation Enschede, The Netherlands, 2010. ISSN: 1993-5153.
22. Weerasinghe, H., Schneider, U.A., Löw, A. Water harvest- and storage- location assessment model using GIS and remote sensing. *Hydrology and Earth System Sciences Discussions*. 2011. 8(2). Pp. 3353–3381. DOI: 10.5194/hessd-8-3353-2011
23. Şen, Z., Al-Suba'i, K. Hydrological considerations for dam siting in arid regions: a Saudi Arabian study. *Hydrological Sciences Journal*. 2002. 47(2). Pp. 173–186. DOI: 10.1080/02626660209492922
24. Forzieri, G., Gardenti, M., Caparrini, F., Castelli, F. A methodology for the pre-selection of suitable sites for surface and underground small dams in arid areas: A case study in the region of Kidal, Mali. *Physics and Chemistry of the Earth, Parts A/B/C*. 2008. 33(1–2). Pp. 74–85. DOI: 10.1016/J.PCE.2007.04.014
25. Ammar, A., Riksen, M., Ouessar, M., Ritsema, C. Identification of suitable sites for rainwater harvesting structures in arid and semi-arid regions: A review. *International Soil and Water Conservation Research*. 2016. 4(2). Pp. 108–120. DOI: 10.1016/J.ISWCR.2016.03.001
26. Behera, P.K., Papa, F., Adams, B.J. Optimization of Regional Storm-Water Management Systems. *Journal of Water Resources Planning and Management*. 1999. 125(2). Pp. 107–114. DOI: 10.1061/(ASCE)0733-9496(1999)125:2(107)
27. Zoppou, C. Review of urban storm water models. *Environmental Modelling & Software*. 2001. 16(3). Pp. 195–231. DOI: 10.1016/S1364-8152(00)00084-0
28. Travis, Q.B., Mays, L.W. Optimizing retention basin networks. *Journal of Water Resources Planning and Management*. 2008. 134(5). Pp. 432–439. DOI: 10.1061/(ASCE)0733-9496(2008)134:5(432)
29. Marques, J., Cunha, M., Savić, D.A. Multi-objective optimization of water distribution systems based on a real options approach. *Environmental Modelling & Software*. 2015. 63. Pp. 1–13. DOI: 10.1016/J.ENVSOFT.2014.09.014
30. Adham, A., Sayl, K.N., Abed, R., Abdeladhim, M.A., Wesseling, J.G., Riksen, M., Fleskens, L., Karim, U., Ritsema, C.J. A GIS-based approach for identifying potential sites for harvesting rainwater in the Western Desert of Iraq. *International Soil and Water Conservation Research*. 2018. 6(4). Pp. 297–304. DOI: 10.1016/j.iswcr.2018.07.003
31. Baban, S.M.J., Wan Yusof, K. Mapping land use/cover distribution on a mountainous tropical island using remote sensing and GIS. *International Journal of Remote Sensing*. 2001. 22(10). Pp. 1909–1918. DOI: 10.1080/01431160119220

32. Saaty, T.L. A scaling method for priorities in hierarchical structures. *Journal of Mathematical Psychology*. 1977. 15(3). Pp. 234–281. DOI: 10.1016/0022-2496(77)90033-5
33. Lamelas, M.T. Esquema metodológico para la toma de decisiones sobre el uso sostenible del suelo: Aplicación a la localización de suelo industrial. *GeoFocus. Revista Internacional de Ciencia y Tecnología de la Información Geográfica*. 2009. 9(1578–5157). Pp. 28–66. ISSN: 1578-5157.
34. Elhag, A.R., Eljack, I.H. DAM Site Selection Using GIS Techniques and remote sensing to Minimize Flash Floods in East Nile Locality (Soba Valley) – Khartoum State. *International Journal of Engineering Science Invention*. 2016. 5(12). Pp. 50–61. ISSN: 2319–6734.
35. Tripathi, A.K., Pandey, U.K. Study of Rainwater Harvesting Potential of Zura Village of Kutch District of Gujarat. *Journal of Human Ecology*. 2005. 18(1). Pp. 63–67. DOI: 10.1080/09709274.2005.11905809
36. Hapuarachchi, H.A.P., Wang, Q.J., Pagano, T.C. A review of advances in flash flood forecasting. *Hydrological Processes*. 2011. 25(18). Pp. 2771–2784. DOI: 10.1002/hyp.8040
37. Muhammad, S., Muneer, J., Gul, C., Javed, A., Malik, S. Identification of suitable site for DAM in Northern Pakistan using Geo-Spatial Techniques. *researchgate.net*. 2017.
38. Lu, B., Stocks, M., Blakers, A., Anderson, K. Geographic information system algorithms to locate prospective sites for pumped hydro energy storage. *Applied Energy*. 2018. 222(January). Pp. 300–312. DOI: 10.1016/j.apenergy.2018.03.177
39. Pincott-Miller, D., McGarry, D., Fairweather, H., Srivastava, S.K. Review and framework development for addressing flash flood potential using GIS assisted spatial-hydrologic modelling. *Papers and Presentations of Queensland Surveying and Spatial Conference 2012*. 2012. Pp. 1–16. URL: <http://research.usc.edu.au/vital/access/manager/Repository/usc:8848>.

Contacts:

Solangel Rodriguez Vazquez, solrusita85@gmail.com

Natalia Mokrova, natali_vm@mail.ru

© Rodriguez Vazquez, S, Mokrova, N, 2020



DOI: 10.18720/MCE.99.3

Numerical simulation of concrete dam during heavy rain

G. Lei^{a,b,c}, S. Weiping^a, G. Lixia^{a,b,c*}, W. Lunyan^{a,b,c}

^a School of Water Conservancy, North China University of Water Resources and Electric Power, Zhengzhou, China

^b Henan Water Valley Research Institute, Zhengzhou, China

^c Henan Key Laboratory of Water Environment Simulation and Treatment, Zhengzhou, China

* E-mail: guolx@126.com

Keywords: dams, finite element method, numerical simulation, temperature, water level, stress analysis

Abstract. In recent years, the frequent extreme weather has led to the rise of reservoir water level, and accordingly changed the reservoir water temperature. As for concrete dams, changes in reservoir water temperature and air temperature may generate temperature stress, and such effect and sudden rise of water level will inevitably change the dam force and endanger the dam safety. By means of numerical simulation and theoretical analysis, this paper analyzed the effect of the extreme rainstorm on the reservoir water level and water temperature, and selected a typical project to simulate the changes of temperature field and stress field of concrete dams in an extreme rainstorm under different working conditions. Results showed that: (1) After the storm flood entered the reservoir, the temperature stress changed little due to the change in the reservoir water temperature; (2) During the rainstorm, the compressive and tensile stresses of concrete dams increased with the time, but did not exceed the allowable values of the concrete used for the dam body; therefore, the dam body was safe; (3) By comparing the effects of the reservoir water level rise caused by heavy rain on the dam stress, the dam temperature stress response varied with the water level rising rate: the greater the reservoir water level rising rate was, the greater the maximum dam response stress was. After being affected by the rainstorm, the dam stresses were the same. Therefore, it was necessary to use a dispatching method to control the rise of the water level. This study can provide theoretical basis and reference for the operation and dispatching of reservoirs during extreme rainstorms.

1. Introduction

As the global climate is worsening, the extreme weather frequently occurs in various regions, which has become a new trend [1]. Under this trend, heavy rains that are characterized by high intensity and short duration may cause floods that exceed the design limit of dams, posing severe challenges to the safe operation of dams and reservoir dispatching during the heavy rains [2–4].

For large and medium-sized reservoirs, due to the large catchment area and wide convergence area, the water level in the reservoirs will rise rapidly and the water temperature will change accordingly in case of a heavy rain. Short-duration, high-intensity heavy rain may cause the sudden rise of water level in reservoirs [5–8]. Zeng Kang et al. [9] found that the inflow conditions (water temperature, inflow rate) of reservoirs during the flood season would change significantly, and the rainfall runoff would reduce the vertical water temperature difference, improve the water turbulence and speed up the natural mixing in reservoirs. The sudden rise and fall of the water level may reduce the safety of dams. In 2016, the Oroville Dam suffered a sharp rise of water level due to the drastic climate change, leading to the damage of the main spillway. Therefore, it was necessary to study the impact of stress response to the operation and management of dams during the rainstorm.

To address the said problems, foreign scholars have conducted relevant researches on the daily change of water temperature in lake-type reservoirs, and found that solar radiation and wind force may affect the daily change of water temperature in reservoirs [10–13]. Zhu Bofang [14] concluded that annual changes in air temperature and water temperature would cause tensile stress in concrete dams, and corresponding measures should be taken; Wang Liangming [15] calculated the effects of daily temperature changes on the temperature field and temperature stress of concrete dams. Jia Chao [17] analyzed the interaction between water temperature and water pressure induced force through finite elements. The above literature all analyzed

Lei, G., Weiping, S., Lixia, G., Lunyan, W. Numerical simulation of concrete dam during heavy rain. Magazine of Civil Engineering. 2020. 99(7). Article No. 9903 DOI: 10.18720/MCE.99.3



This work is licensed under a CC BY-NC 4.0

the effects of temperature on the stress of concrete dams; however, few researches involved the dynamic change of temperature/stress of concrete dams under the combined effect of water level and water temperature during the heavy rain. Yigit [16] found that the periodic displacement response and linear displacement response of dams were related to seasonal temperature changes and linear rise of reservoir water level respectively, indicating that there was a correlation between temperature, water load and dam deformation. All of the said researchers have not studied the stress of dams under the combined action of temperature and water level. Based on these, this paper simulated a complete rainstorm by coupling water load and temperature load, and studied the changes of the dam stress during the rainstorm, which would provide a reference for the dam's safe operation during the heavy rain.

2. Methods

2.1. Prediction of reservoir water temperature under the storm flood

Research on the reservoir water temperature started in the 1950s. To date, the water temperature is mainly estimated through empirical methods, including Zhang Dafa method of the Northeast Survey and Design Institute [18] and Zhu Bofang method [19, 20] of China Institute of Water Resources and Hydropower Research which has been recorded into the Design Specification for Concrete Arch Dams [21]. Zhu Bofang's reservoir water temperature prediction model is as follows:

$$T_{sur} = T_{mod} + \Delta b \quad (1)$$

$$T_{mod} = \frac{1}{12} \sum_{i=1}^{12} T_i \quad (2)$$

where Δb means the temperature increment caused mainly by sunlight, °C; T_{mod} means the revised annual average temperature, °C. The initial water temperature at the bottom of the reservoir is selected based on the on-site measured data and corresponding empirical data.

After a reservoir is completed and begins to store water, under the impact of reservoir water level deepening and climate change, the water temperature layering will occur in the reservoir along the depth of water. The water temperature prediction is as shown above. The storm flood may disturb the initial water temperature, and the degree of disturbance can be determined by the runoff-reservoir capacity ratio method (i.e. parameter α - β method) according to the researches of Tao Mei et al. [22].

Typical parameters in the runoff-reservoir capacity ratio method (i.e. parameter α - β method) include:

$$\alpha = \frac{\text{average annual runoff}}{\text{reservoir storage capacity}} \quad (3)$$

$$\beta = \frac{\text{Primary flood capacity}}{\text{reservoir storage capacity}} \quad (4)$$

Among the above parameters, when $\alpha < 10$, the reservoir water temperature is in a stable layer; when $\alpha > 20$, the reservoir water temperature is in a mixed layer; otherwise, it is in a transition layer. When the reservoir water temperature is in a stable layer, $\beta > 1$ indicates that the storm flood has an impact on the water temperature structure in the reservoir; $\beta < 0.5$ indicates that the storm flood has no effect on the water temperature structure in the reservoir; otherwise, the storm flood has a certain effect on the water temperature structure but doesn't damage the water temperature layering structure.

2.2. Calculation of rainfall-water level relationship

A heavy rain may finally turn into a flow in the reservoir area before the dam after runoff generation and concentration. With the rapid development of computers and continuous innovation of mathematical methods in recent years [23], rational formula method, empirical formula method, integrated unit hydrograph method and hydrological model method are often used to forecast the rainfall-flow relationship.

When calculating rainfall-runoff, the point rainfall is converted into the surface rainfall, and then the loss is subtracted to finally obtain the net rainfall. According to different conditions in different regions, the runoff generation is calculated using the principle of water balance, and then the rainfall is converted into runoff after the rain through the computing method of runoff concentration.

$$T_{sur} = T_{mod} + \Delta b \quad (1)$$

$$\begin{cases} Q_{mp} = 0.278 \left(\frac{S_p}{\tau^n} - \mu \right) F & \tau = 0.278 \frac{L}{m I^{1/2} Q_m^{1/4}} \quad (\tau_c \geq \tau) \\ Q_{mp} = 0.278 \left(\frac{n S_p \tau_c^{1-n}}{\tau} \right) F & \tau = 0.278 \frac{L}{m I^{1/2} Q_m^{1/4}} \quad (\tau_c < \tau) \end{cases} \quad (5)$$

where Q_{mp} is the design flood peak flow, m^3/s ; n is the rainstorm index, $0 < n < 1$; S_p is the rain force, mm/h ; τ_c is the duration of runoff generation, h ; τ is the flow concentration time, h ; F is the basin area, km^2 ; L is the flow length of the furthest point in the basin, km ; m is the flow concentration parameter; I is the average vertical slope along the furthest flow; Q_m is the flood peak flow, m^3/s .

During a heavy rain, if the water level is lower than the crest level, the water level will gradually rise. The rising rate is positively correlated with the inflow quantity and the inflow duration. Generally, the reservoir capacity increment is the product of the inflow quantity and the inflow duration. The water level can be obtained from the capacity hydrograph at the dam site.

2.3. Computing theory of temperature field

The differential equation of heat conduction for a concrete structure is:

$$\frac{\partial T}{\partial t} = \alpha \nabla^2 T + \frac{\partial \theta}{\partial t} \quad (6)$$

where $\alpha = \frac{\lambda}{c_p \rho}$, ρ is the object density, kg/m^3 . C_p is mass heat capacity at constant pressure, $J/Kg^{\circ}C$.

λ is thermal conductivity, $W/(m^{\circ}C)$. σ is the thermal diffusivity, m^2/s . $\nabla^2 = \frac{\partial^2}{\partial X^2} + \frac{\partial^2}{\partial Y^2} + \frac{\partial^2}{\partial Z^2}$, θ is the adiabatic temperature rise.

The corresponding initial conditions are:

$$T|_{t=0} = T_0(P), [P \in (v, s)] \quad (7)$$

Boundary conditions are:

$$T|_s = T_b(P, t), (P \in s_1, t > t_0) \quad (8)$$

$$q_n|_s = -\lambda \frac{\partial T}{\partial n}|_s = q_b(P, t), (P \in S_2, t > t_0) \quad (9)$$

where q represents the heat-flow density, $J/(m^2 * s)$, $P = P(x, y, z)$ represents the spatial point or spatial coordinate variable; N represents the direction of the outer normal. When $q_n = 0$ on a boundary surface, the boundary is an adiabatic boundary.

2.4. Finite element model

According to the engineering data and research needs, a typical project was selected for analysis. The dam is a C25 RCC gravity dam with the height of 61.6 m and the crest width of 6 m. Its downstream slope ratio is 1:0.75, the upstream slope ratio is 1:0.1, and the break point is 1/3 away from the dam heel. When established, the finite element model extended 40 m along the upstream, downstream and foundation respectively, and had a total of 17,400 nodes. In the calculation of the temperature field, the first boundary condition was taken on the contact surface between the dam body and the water, the second boundary condition was taken on the contact surface between the dam body and the air, and the adiabatic boundary condition was taken around the foundation; in stress calculation, normal constraints were imposed around the foundation, and full constraints were imposed at the bottom of the foundation.

2.5. Calculation parameters

Laboratory tests were performed according to the actual conditions of the project. The thermal parameters of the materials were shown in Table 1, and the mechanical parameters were shown in Table 2.

Table 1. List of thermal parameters of the materials.

| material types | thermal conductivity (KJ/(m*h*°C)) | thermal diffusivity (m ² /h) | specific heat (KJ/(kg*°C)) | linear expansion efficient (10 ⁻⁶ /°C) |
|----------------|---------------------------------------|--|-------------------------------|--|
| foundation | 9.8000 | 0.0034 | 1.0900 | 6.9200 |
| C25 concrete | 9.5800 | 0.0033 | 1.1000 | 6.8000 |

Table 2. List of mechanical parameters of the materials.

| material types | elastic modulus (Gpa) | poisson ratio | axial compressive strength (N/mm ²) | axial tensile strength (N/mm ²) |
|----------------|--------------------------|---------------|--|--|
| foundation | 22.00 | 0.20 | 10.00 | 1.27 |
| C25 concrete | 28.00 | 0.20 | 16.70 | 1.78 |

The temperature fitting formula is:

$$T_0 = \pi + R_0 t + A_0 \cos \left[\frac{\pi}{6} (t - 6.4) \right] \quad (10)$$

where T_0 is the average temperature, °C. A_0 is half of the difference between the maximum temperature and the minimum temperature; T is the time, month. $R_0 t$ is the ground temperature which can be ignored.

According to formulas (3) and (4), α was equal to 1.9 and β was equal to 1.2; therefore, the reservoir had water temperature layered. In case of a flood, the flood would make the water temperature structure mixed temporarily.

When there was no rain, the measured average annual water temperature on the surface was 13 °C and the water temperature at the bottom was 10.075 °C. The rainfall was mostly concentrated in July and August in the form of heavy rain, accounting for 54 % of the annual rainfall. The main stream of the reservoir contained 50 % sand. According to relevant researches [8, 9, 24, 25], the surface heat exchange did not directly act on the water layer below 15 m depth. During the flood season, the density currents fell to the bottom of the reservoir in the transition zone, and went ahead in the form of undercurrent until to the main reservoir area. The large inflow reduced the range of low-temperature water bodies and the depth of water temperature layer. Therefore, during calculation, it was considered that after storm water flowed into the reservoir, the water temperature before the reservoir was redistributed, and suddenly changed to 13 °C overall.

Due to the limited data, this paper was designed to quantitatively study the effect of the water level rising rate on the stress response of concrete dams when the water level rises from 58 m to 59.8 m under the same rainfall duration and the same amount of precipitation, and designed two working conditions: the first condition was the uniform rise of the reservoir water level at a rate of 0.0375 m/h, and the second condition was the S-shaped rise of the reservoir water level at a rate of 0.0425 m/h first and then at a rate of 0.0305 m/h.

3. Results and Discussion

3.1. Analysis of Calculation Results

3.1.1 Calculated result of temperature field

Through numerical simulation analysis, the results of the temperature field of the concrete dam were shown in Fig. 1.

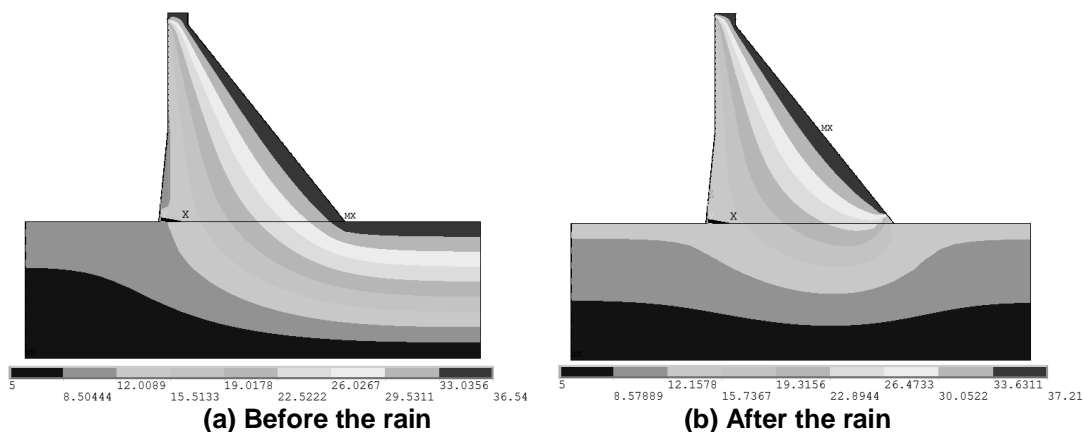


Figure 1. Distribution of dam temperature field (unit: °C).

It could be seen from the figure that under the dual effects of water temperature and air temperature, the dam body temperature changed. The dam foundation temperature was constant at 5°C. The temperature change on the surface of the dam body in contact with the air was consistent with the change of the local air temperature. Both changed in a trigonometric function and had no hysteresis.

3.1.2 Calculated result of stress field

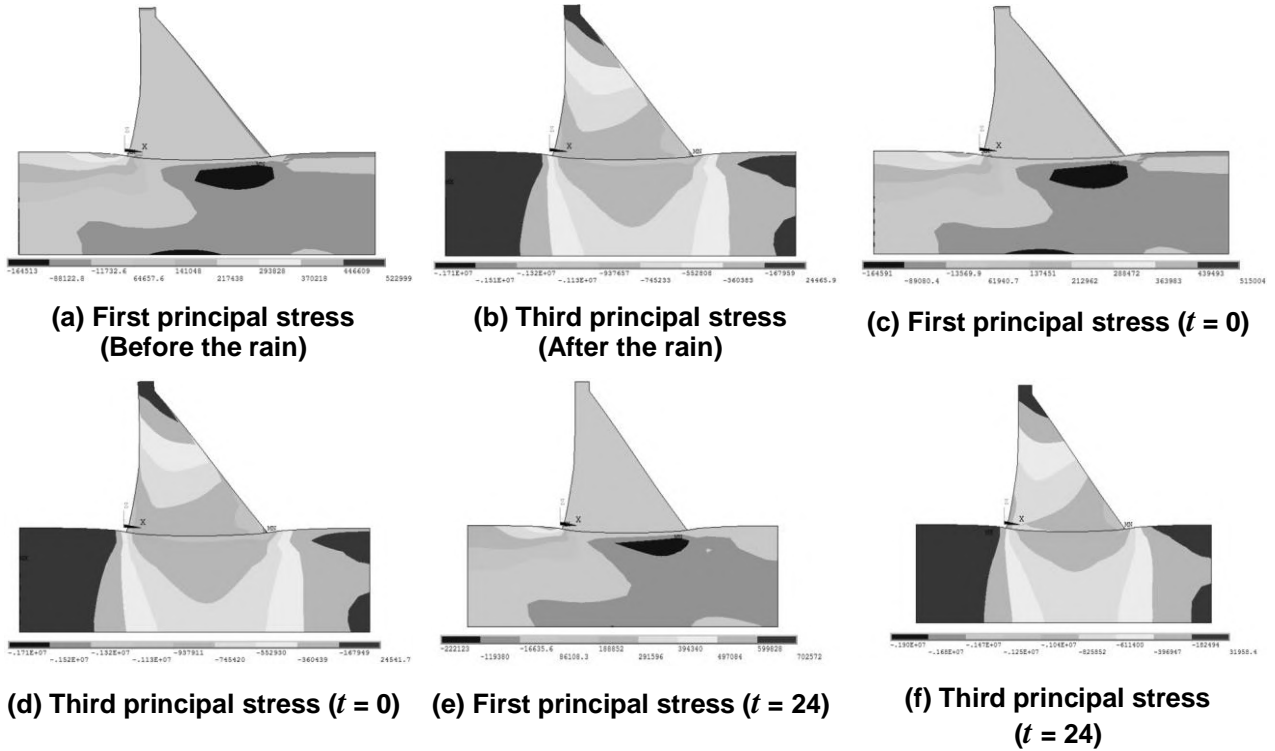


Figure 2. Distribution of stress field during uniform rise of reservoir water level (Unit: Mpa).

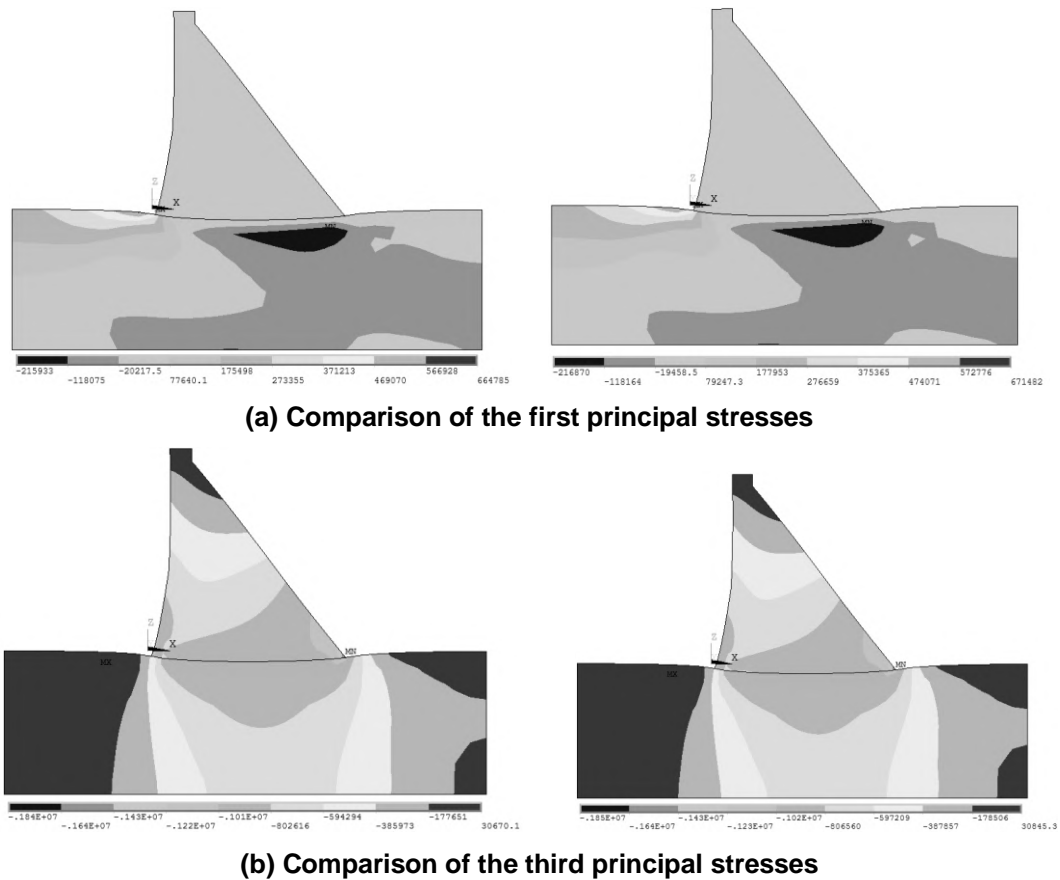
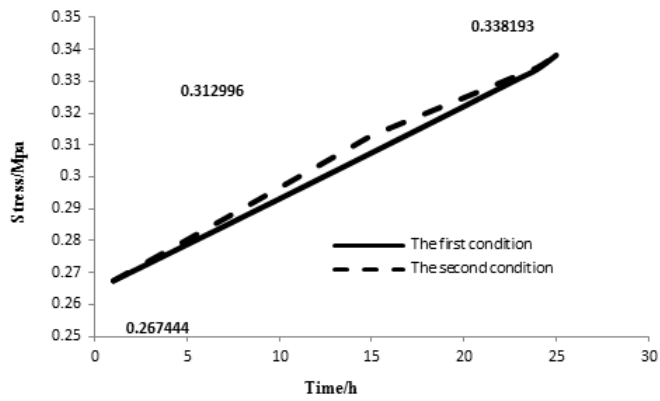
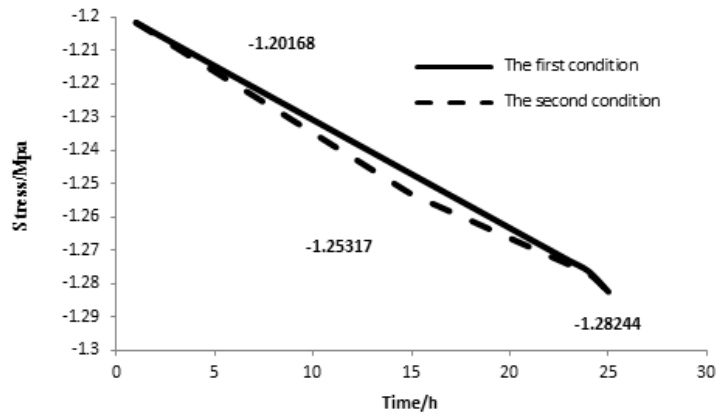


Figure 3. Comparison of stress fields under two working conditions ($t = 14h$, unit: Mpa).



(a) Duration change of the first principal stress at the dam heel



(b) Duration change of the third principal stress at the dam toe

Figure 4. Stress changes at feature points.

Table 3. Dam displacement table (unit: mm).

| Time (h) | 1 | 10 | 20 | 25 |
|----------------------|---------|---------|---------|---------|
| The first condition | 1.01123 | 1.15733 | 1.31966 | 1.40091 |
| The second condition | 1.0116 | 1.17718 | 1.33519 | 1.42382 |

From the literature [16], the periodic displacement response and linear displacement response of dams were related to seasonal temperature changes and linear rise of reservoir water level respectively. A 58 m rise in the dam water level caused a dam displacement of 10 mm. As shown in Table 3, a 1.8 m rise in the water level caused a dam displacement of 0.4 mm. The dam displacement had a linear correlation with the rise of the water level. This result was consistent with the conclusions obtained by Yigit [16] through analysis of the measured data. This model was considered reasonable.

As we all know, the temperature stress is caused by the temperature difference. As shown in Fig. 2, before the storm flood flowed into the reservoir, the temperature was high at the dam crest and after the dam, and was low before the reservoir, the temperature difference, the temperature deformation and the temperature stress were all large; after the storm flood flowed into the reservoir, the water temperature in front of the reservoir was evenly distributed, the temperature difference between the upstream and downstream reduced, the temperature deformation of the dam body was small, and the temperature stress decreased. Therefore, the stress values in Fig. 2-(c) were greater than those in Fig. 2-(a). Since the temperature difference between the said stress values decreased 2.925 °C, the first principal stresses at the dam heel differed by about 2 KPa.

The water level rise after the storm flood entered the reservoir was shown in Fig. 2. As the flood continued to flow into the reservoir, the dam deformation increased, and the tensile stress and compressive stress were positively correlated with time. The maximum compressive stress occurred at the downstream dam toe, and lasted for two days with the value of 1.9 Mpa; the maximum tensile stress occurred at the upstream dam heel, and lasted for two days with the value of 0.7 Mpa, both of which did not exceed the allowable strength of concrete (allowable compressive stress: 16.7 Mpa, allowable tensile stress: 1.78 Mpa), and met the requirements for strength specified in the Design Specification for Concrete Gravity Dams.

As shown in Fig. 3, the stress of the dam body changed accordingly through comparison of two different reservoir water level rising rates. The faster the water level rose, the greater the response stress of the dam body was. When the water level rose for 14 h, the difference between the first principal stresses under the two working conditions was 0.0067 Mpa, and the difference between the third principal stresses was 0.01 Mpa. After the rainstorm entered the reservoir for 24 h, the water level and temperature became stable, so their stresses were the same.

4. Conclusion

To analyze the response of dams during the heavy rain, this study took a typical project in summer storm as an example, and adopted numerical simulations to analyze the changes of the temperature field and stress field of the dam body before and after the storm flood entered the reservoir. The results showed that:

1. Before and after the storm flood entered the reservoir, the temperature stress changed due to the change in the reservoir water temperature. For mixed reservoirs, the stress was reduced because the temperature difference between the upstream and downstream of the reservoir got smaller;
2. As the flood continued to enter the reservoir, the dam deformation increased, the changes in water temperature and air temperature had less effect, the water load had a significant effect, and the dam stress increased with the inflow of storm floods;
3. In the case of the same rainfall duration, the same rainfall amount, and the different rainstorm intensities, the water level rising rate had a significant effect on the stress response of the concrete dam body; that was, the faster the water level rose, the greater the dam stress was, which would damage the stability of the dam body and the bank slope in the reservoir area.
4. According to the literature [26], the heavy rain had a great impact on the stability of the bank slope in reservoir area; however, it needs further research in the later period.

Such results can provide a reference for the dispatching and operation of reservoirs in the rainy season, and can also provide a theoretical basis for the safe operation of cascade hydropower stations and the control of the water level rising rate.

5. Acknowledgements

This study was funded by the national key R & D plan fund project(2018yfc0406803) and Open project of dike safety and disease prevention engineering technology research center of the Ministry of water resources:(2018008)

References

1. Guoyu, R., Yu, C., Xukai, Z., Yaqing, Z., Xiaoling, W., Ying, J., Fumin, R., Qiang, Z. Definition and trend analysis of an integrated extreme climatic index (in Chinese). *Climatic and Environmental Research*. 2010. 15(4). Pp. 354–364..
2. Asadieh, B., Krakauer, N.Y., Fekete, B.M. Historical trends in mean and extreme runoff and streamflow based on observations and climate models. *Water (Switzerland)*. 2016. 8(5). DOI: 10.3390/w8050189
3. Najibi, N., Devineni, N. Recent trends in the frequency and duration of global floods. *Earth System Dynamics*. 2018. 9(2). Pp. 757–783. DOI: 10.5194/esd-9-757-2018
4. Asadieh, B., Krakauer, N.Y. Global trends in extreme precipitation: Climate models versus observations. *Hydrology and Earth System Sciences*. 2015. 19(2). Pp. 877–891. DOI: 10.5194/hess-19-877-2015
5. Rifeng, L., Yang, L., Weixing, M., Zizhen, Z. Analysis of correlation between storm runoff and reservoir density current (in Chinese). 2017. Pp. 5–10. DOI:10.3969/j.issn.1673-9353.2017.05.006.
6. Ma, W., Huang, T., Li, X., Zhou, Z., Li, Y., Zeng, K. The effects of storm runoff on water quality and the coping strategy of a deep canyon-shaped source water reservoir in China. *International Journal of Environmental Research and Public Health*. 2015. 12(7). Pp. 7839–7855. DOI:10.3390/ijerph120707839.
7. Shiyong, H. Analysis of "99·7" storm flood and reservoir flood dispatching in Xin'an River Basin(in Chinese). *HYDROLOGY*. 2003. 23(1). Pp. 60–62.
8. Qike, X., Zhaowei, L., Yongcan, C., Xiao, C., Werk, K.T. Measurement and analysis of daily temperature changes in Xiluodu Reservoir(in Chinese). *ADVANCES IN WATER SCIENCE*. 2018. 29(4). Pp. 523–535. DOI:10.14042/j.cnki.32.1309.2018.04.008.
9. Kang, Z., Tinglin, H., Weixing, M., Zizhen, Z., Yang, L. Water-quality responses of the intrusion of high-turbidity runoff to the thermal stratified Jin-pen Reservoir during flood season (in Chinese). *China Environmental Science*. 2015. 35(9). Pp. 2778–2786.
10. van Emmerik, T.H.M., Rimmer, A., Lechinsky, Y., Wenker, K.J.R., Nussboim, S., van de Giesen, N.C. Measuring heat balance residual at lake surface using distributed temperature sensing. *Limnology and Oceanography: Methods*. 2013. 11(FEB). Pp. 79–90. DOI: 10.4319/lom.2013.11.79
11. Vercauteren, N., Huwald, H., Bou-Zeid, E., Selker, J.S., Lemmin, U., Parlange, M.B., Lunati, I. Evolution of superficial lake water temperature profile under diurnal radiative forcing. *Water Resources Research*. 2011. 47(9). Pp. 1–10. DOI: 10.1029/2011WR010529
12. Imberger, J. The diurnal mixed layer. *Limnology and Oceanography*. 1985. 30(4). Pp. 737–770. DOI: 10.4319/lo.1985.30.4.0737
13. MacIntyre, S., Romero, J.R., Kling, G.W. Spatial-temporal variability in surface layer deepening and lateral advection in an embayment of Lake Victoria, East Africa. *Limnology and Oceanography*. 2002. 47(3). Pp. 656–671. DOI: 10.4319/lo.2002.47.3.0656
14. Bofang, Z., Longshen, W., Yue, L., Guoxin, Z. Stress caused by annual temperature field changes during the gravity dam runtime (in Chinese). *Water Resources and Hydropower Engineering*. 2007. 38(9). Pp. 21–24. DOI:10.13928/j.cnki.wrahe.2007.09.002

15. He, W.S., Wang, L.M. Three-dimensional seepage field analysis of thick overburden CFRD after sealing failure. *Applied Mechanics and Materials*. 2014. 457–458. Pp. 797–800. DOI:10.4028/www.scientific.net/AMM.457-458.797.
16. Jia, C., Shao, A., Li, Y., Ren, Q. Analyses of thermal stress field of high concrete dams during the process of construction. *Asia-Pacific Power and Energy Engineering Conference, APPEEC*. 2010. (3). DOI:10.1109/APPEEC.2010.5449456.
17. Yigit, C.O., Alcay, S., Ceylan, A. Displacement response of a concrete arch dam to seasonal temperature fluctuations and reservoir level rise during the first filling period: evidence from geodetic data. *Geomatics, Natural Hazards and Risk*. 2016. 7(4). Pp. 1489–1505. DOI: 10.1080/19475705.2015.1047902
18. Dafa, Z. Analysis and estimation of reservoir water temperature(in Chinese). *Journal of China Hydrology*. 1984. 1. Pp. 19–27. DOI:10.19797/j.cnki.1000-0852.1984.01.006.
19. Bofang, Z. Prediction of water temperature in reservoirs (in Chinese). *Journal of Hydraulic Engineering*. 1985. 2. Pp. 12–21. DOI:10.13243/j.cnki.slxb.1985.02.002.
20. Ministry of Water Resources of the People's Republic of China. Design specification for concrete arch dams (in Chinese).
21. China, M. of W.R. of the P.R. of. Regulation for hydrologic computation of water resources and hydropower projects (in Chinese).
22. Mei, T., Yong, P., Hua, W., Kun, B. Effects of floods on reservoir temperature hierarchy(in Chinese). *WATER RESOURCES PROTECTION*. 2013. 29(5). Pp. 38–44.
23. Wang Fuqiang, H.F. Review on study of mid- and long-term hydrological forecasting technique(in Chinese). 2010. 27(5). Pp. 3–5. DOI: 10.3969/j.issn.1000-1379.2010.03.011
24. Wang, S., Qian, X., Wang, Q.H., Xiong, W. Modeling Turbidity Intrusion Processes in Flooding Season of a Canyon-Shaped Reservoir, South China. *Procedia Environmental Sciences*. 2012. 13(2011). Pp. 1327–1337. DOI: 10.1016/j.proenv.2012.01.125
25. Chung, S.W., Hipsey, M.R., Imberger, J. Modelling the propagation of turbid density inflows into a stratified lake: Daecheong Reservoir, Korea. *Environmental Modelling and Software*. 2009. 24(12). Pp. 1467–1482. DOI: 10.1016/j.envsoft.2009.05.016. URL: <http://dx.doi.org/10.1016/j.envsoft.2009.05.016>.
26. Siwei, W., Dezhi, J., Handong, L. Study of slope instability induced by rapid drawdown of water level (in Chinese). *The first Geotechnical hydraulic Conference*. 2005. Pp. 101–104.

Contacts:

Guo Lei, glboss@126.com

Shen Weiping, swpstudy@126.com

Guo Lixia, guolx@126.com

Wang Lunyan, 982069193@qq.com

© Lei, G.,Weiping, S.,Lixia, G.,Lunyan, W., 2020



DOI: 10.18720/MCE.99.4

Earth pressure reduction on retaining walls using EPS geofoam

Y.E-H. Ibrahim^{*a}, S.S.A. Abdelsalam^b, M.N.A. Nabil^b, M.E. Elsayed^b

^a Prince Sultan University, Rafha Street, Riyadh, Saudi Arabia

^b Zagazig University, Zagazig, Egypt

* E-mail: yibrahim@vt.edu

Keywords: EPS geofoam, finite element method, non-yielding, yielding walls, lateral earth pressure, ABAQUS

Abstract. Retaining wall structures are widely used in different civil engineering projects including building construction, highways, railways, water conservancy, harbors, and many other projects in order to resist the lateral pressure of soil and water. According to their deformation behavior, retaining walls can be classified as flexible walls and rigid walls. Deformable inclusions such as expanded polystyrene, EPS, geofoam can be used to reduce the lateral earth pressure on retaining wall structures. In this study, the effect of using EPS geofoam inclusion on the reduction of lateral earth pressure and stability behavior of non-yielding and yielding retaining walls with cohesionless backfills is examined through a finite element analysis using ABAQUS software. A parametric analysis was performed to examine the effectiveness of EPS inclusion considering different parameters including the foam thickness, short and long-term characteristics of the foam density, surcharge load on backfill and the backfill properties. According to the results obtained, the earth pressure and subsequently the sliding forces and overturning moments were reduced on non-yielding and yielding retaining walls due to the EPS inclusion. The percentage of reduction was higher in the case of non-yielding walls with zero surcharge pressure. The reduction in sliding forces and overturning moments reached 47 %. Moreover, it was found that the lateral earth pressure, sliding forces and overturning moment on retaining walls were decreased with the increases of the foam thickness. However, the lateral earth pressure was slightly increased with the increase of the foam density. Empirical equations of reduction in lateral forces and overturning moments were developed as a function of foam thickness.

1. Introduction

The stability of earth retaining wall systems represents a complex balance of external loads versus resistances' problems. Earth retaining walls are generally divided into non-yielding and yielding systems. The former system is inherently constrained against both deformation and displacement in the horizontal direction. Common examples of the non-yielding system include below-grade (e.g., basement) walls of buildings, bridge abutments, and free-standing retaining walls that are restrained against horizontal displacement due to physical restraint or structure geometry. The non-yielding earth retaining wall systems are logically designed assuming the at-rest earth-pressure state within the retained soil. The yielding system can either displace or deform or both in the horizontal direction. The yielding earth retaining wall systems can develop the active earth-pressure state within the retained soil [1].

Active earth pressures evaluation plays an important role in geotechnical engineering. Reduction in lateral earth pressure, sliding force and overturning moment on a retaining wall by providing EPS geofoam inclusions helps in reducing the project cost. The use of expanded polystyrene (EPS) geofoam as a lightweight compressible inclusion has gained extensive popularity in geotechnical engineering. Many researchers have carried out analytical, experimental work and numerical analyses on lateral earth pressure problems. These studies have shown that compressible materials between a rigid retaining wall and backfill reduced static force [2–6]. Chauhan and Dasaka [7] proved the effectiveness of EPS geofoam on reduction of lateral earth pressure. They noticed that provision of geofoam behind the retaining wall provided a thrust reduction in range of 8–42 % for surcharge pressures ranging from 10–50 kPa.



Navid and Rouzbeh [8] conducted a finite difference analysis using a 2-D FLAC computer program by considering yielding and non-yielding states for retaining walls to explore the effectiveness of geofoam panels in improving the static performance of cantilever retaining walls. They found that using EPS15 with density equal to 15 (kg/m^3), which has the lowest density among other geofoam panels, has a significant role in reduction of lateral stresses. Through their small-scale physical model tests, Dave and Dasaka [9] found that, EPS geofoam reduced the total lateral force on the retaining wall by about 23 % and 28 %, for retaining wall with and without hinge, respectively. Yadav [10] conducted a numerical analysis on static and seismic condition with inclusion of geofoam on retaining wall in using Plaxis 2D software. The thickness of geofoam was considered as 0.5 m, 1.0 m, 1.5 m and 2 m. It was found that the reduction in lateral earth pressure increases with the increase in geofoam thickness. Ertugrul and Trandafir [11] conducted experimental study to investigate the reduction of lateral earth forces on rigid retaining walls by using EPS geofoam inclusions. For rigid non-yielding retaining wall, EPS geofoam panels of three different thicknesses (characterized by the ratio of geofoam thickness to wall height, t/h , of 0.07, 0.14, and 0.28) were installed behind retaining wall. When comparing the “no buffer” case with an inclusion of $t/h = 0.14$, it was found that the reduction in the lateral pressure exceeded 50 %. Salem et al. [12] developed a small-size diaphragm wall with EPS buffer using FE program PLAXIS 3D. They concluded that, lateral pressure on diaphragm walls was significantly reduced by around 37 % using a relatively thin EPS buffer.

Veletsos and Younan [13] investigated dynamic pressures on flexible cantilever retaining walls with fixed base using an analytical approach that involved repeated application of Lagrange's equation. Results of their study emphasized the importance of wall flexibility on the lateral dynamic load and indicated that the total wall force may be reduced to about one half of the force calculated for a rigid retaining wall with a fixed base.

Bathurst et al. [14] investigated the performance of seismic geofoam buffers by carrying out physical shaking table tests on a non-yielding rigid wall with a 1.0 m height with deformable geofoam panels and granular backfill. A maximum dynamic force reduction of 31 % (compared to the control case of a rigid retaining wall with no geofoam buffer) was observed in these tests for a peak base acceleration of 0.7 g.

Fakhry et al. [15] constructed a numerical model using finite element program PLAXIS 2D. They concluded that, the lateral pressure on flexible diaphragm walls can be significantly reduced by 37 % using a relatively thin EPS buffer. Mustafa et al. [16] studied the efficiency of EPS geofoam inclusion in reducing the static earth pressure on non-yielding cantilever retaining walls with a height of 7 m, using finite element program, PLAXIS 2D. They studied the distribution and magnitude of earth pressure on retaining walls with and without geofoam when subjected to surcharge loads. A geofoam density of 10 kg/m^3 and a thickness of 0.50 m were used. The results confirmed that the earth pressure have been reduced with the geofoam inclusion by 36 %. Abdelsalam et al. [17] developed a 3-D model using PLAXIS 3D. They found that reduction in lateral earth pressure acting on flexible retaining walls ranged from 2 % to 25 % by using EPS geofoam with a foam thickness to wall height ratio ranging from 0.01 to 0.05, respectively.

Researchers considered using EPS with other geosynthetics to enhance the effect of EPS in different applications. Moghaddas Tafreshi et al. [18] conducted experimental tests to investigate the effect of inclusion EPS geofoam block and geocell to mitigate the pressure on buried flexible high-density polyethylene pipes. They found that using EPS can reduce the pressure onto the pipe, however, it may cause larger surface settlements. The effect of using EPS was enhanced by using geocell reinforcement and the resulting deformations were kept within allowable limits. Experimental tests were used to study the effect of the use of geogrid and EPS geofoam block to protect unplasticized polyvinyl chloride pipes with 160 mm diameter buried in unreinforced and reinforced trenches under cyclic loadings [19]. It was found that using geogrid with EPS block with appropriate density, thickness and width can control the behavior of these buried pipes under cyclic loading. EPS wall barrier was considered to mitigate the blast load effect on the pile foundation [20]. According to the results obtained, it was observed that the open trench and the EPS wall barrier have the best effectiveness in reducing the blast load effect on such foundations, when compared to other techniques or materials. Other researchers used fibers of polypropylene under retaining walls to enhance the stability of the soil mass [21]. It was found that retaining wall with fiber-sand backfill experience much smaller horizontal movements than that of the retaining wall with sand backfill.

The main goal of this study is to optimize the effectiveness of using geofoam inclusions as a lightweight fill material behind retaining wall structures in order to effectively reduce the lateral earth pressure and enhance the stability of the retaining walls considering the sliding forces and overturning moments on these walls. A detailed FE analysis using ABAQUS was used to model backfill soil, retaining walls and EPS geofoam. In this regard, several parameters were considered including the foam thickness, which varied from 0 to 3.0 m, foam density for short and long-term conditions, surcharge pressures on backfill surface due to foundations of adjacent structures and traffic loading and finally the backfill soil type including loose, medium and dense sand.

2. Methods

The theories proposed by Coulomb [22] and Rankine [23] remain the fundamental approaches to analyze the active earth pressures their formulation is simple, and widely accepted by practicing engineers. FE method can analyze complicated geometries and provide detailed results to the retaining wall problem. Accordingly, it is becoming an effective method of solving the earth pressure problems.

In this research, a three-dimensional FE commercial software (ABAQUS) was used in the analysis to model the retaining wall, backfill soil and soil underneath the wall. The backfill soil comprises loose sand with a height of 8.0 m, followed by dense sand extending down to a depth of 31.0 m. The wall has a height of 8.0 m, and its width varies from 3.0 m at the base to 0.80 m at the top. In the analysis, the wall was modeled as an elastic material.

Wall is modeled as elastic materials by an eight-node linear brick element with reduced integration and hourglass control (C3D8R). Soil, EPS geofoam and back fill are modeled by elastic ideal plastic constitutive model following Mohr–Coulomb yield criterion by an eight-node linear brick element with reduced integration and hourglass control (C3D8R). The Mohr–Coulomb Model considers the effect of stresses on the strength of soil. The failure criterion is defined by the friction angles and cohesion of soil. The Main parameters are summarized in Table 1. It should be noted that wall elements are relatively rigid to the surrounding soil deformations. The surface of wall elements that are in contact with the soil elements is referred to as the main surface (master). The surface of the soil elements in contact is set as the secondary surface (slave). In the ABAQUS program these surfaces are called contact pairs. The contact behavior of the two surfaces is determined by the Coulomb law of sliding friction. The Coulomb model of friction applies to the maximum allowable friction (shear), including the normal stress at the interface between the two surfaces.

A finite-sliding formulation was used at these interfaces, which allows any random motion of the surfaces including sliding, separation, and rotation of the surfaces. Hard contact model was used to define the normal contact pressure over closure relationship between the backfill and base soil and the wall. The first step of the analysis was to verify that the initial geostatic stress field is in balance with the applied loads and boundary conditions. The initial step was followed by several static analyses stages to reach an active state.

Boundary conditions of the bottom of the model were fixed. The horizontal displacement was constrained at the right and left sides of the soil block considered. The left side of retaining wall was restraint for non-yielding retaining wall and unrestrained for the case of yielding retaining wall. The vertical stress distributions behind the wall at non-yielding and yielding walls were taken as ($\Delta = 0.000H$) and ($\Delta = 0.00073H$), respectively as presented in Fig. 1 [24, 25].

Table 1. Physical and mechanical properties of soil, backfill and EPS.

| | Wall | EPS geofoam | Backfill Loose sand | Base soil |
|--|-------------------|-------------|---------------------|-----------|
| Unit weight, γ (kN/m ³) | 24 | 2.5 | 15 | 17 |
| Modulus of elasticity, E (MPa) | 2.1E ⁴ | 2.736 | 20 | 100 |
| Poisson ratio, μ | 0.20 | 0.14 | 0.3 | 0.25 |
| Internal friction angle, ϕ ° | - | 27 | 30 | 37 |
| Cohesion, C , kPa | - | 47 | 0 | 0 |

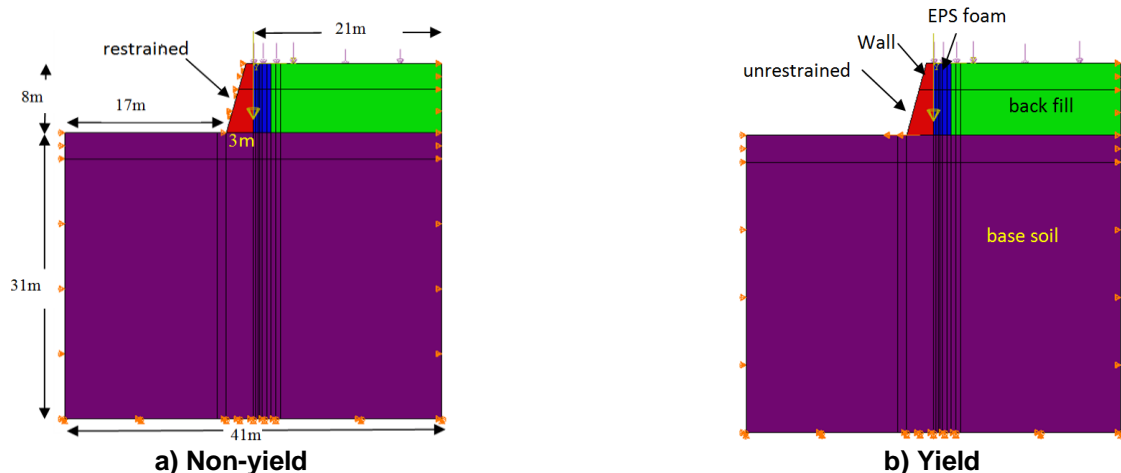


**Fig. 1: Dimensions and boundary conditions of the retaining walls
a) Non-yielding retaining wall and (b) Yielding retaining wall.**

The main purpose of the parametric study is to investigate the effect of using EPS geofoam in reducing the lateral earth pressure on yielding and non-yielding retaining walls. The following parameters were considered in this study:

- Foam thickness (case 1);
- Foam properties including short term and long-term conditions (case 2);
- Surcharge pressure on backfill surface (case 3);
- Backfill soil properties (case 4).

Table 2 through Table 5 show different parameters considered in this study in details.

Table 2. Effect of foam thickness (case 1).

| Case | a | b | c | d | e | f | g |
|--------------------|-----|-----|-----|-----|-----|-----|-----|
| Foam thickness (m) | 0.0 | 0.5 | 1.0 | 1.5 | 2.0 | 2.5 | 3.0 |

Table 3. Effect of EPS properties (case 2) [26].

| Case | | EPS properties | | | | |
|---------|------------|-------------------------------|-----------|-------|----------|-----------|
| | | γ (kN/m ³) | E (kPa) | μ | ϕ ° | C , kPa |
| a | Short term | 25 | 2736 | 0.14 | 27 | 47 |
| Foam 25 | Long term | 25 | 2072 | 0.14 | 25 | 40 |
| b | Short term | 30 | 4307 | 0.17 | 33 | 57 |
| Foam 30 | Long term | 30 | 3263 | 0.17 | 30 | 45 |
| c | Short term | 35 | 4924 | 0.2 | 36 | 84 |
| Foam 35 | Long term | 35 | 3730 | 0.2 | 33 | 67 |

Table 4. Effect of surcharge pressure (case 3).

| Case | a | b | c | d |
|----------------------------|---|----|----|----|
| Surcharge pressure, q(kPa) | 0 | 16 | 25 | 50 |

Table 5. Effect of backfill properties (case 4).

| Case | | Backfill properties | | | |
|-----------|-------------|-------------------------------|-----------|-------|----------|
| Soil type | | γ (kN/m ³) | E (MPa) | μ | ϕ ° |
| a | Loose sand | 15 | 20 | 0.3 | 27 |
| b | Medium sand | 18 | 50 | 0.3 | 35 |
| c | Dense sand | 20 | 100 | 0.25 | 37 |

3. Results and Discussion

3.1. Verification of FE Model

First, the developed FE model was verified through a comparison with the Coulomb and Rankine fundamental approaches. Lateral earth pressure distribution along wall for non-yielding retaining walls at different backfill granular soils (loose sand with Young modulus equal to 20 MPa, medium sand with Young modulus equal to 50 MPa and dense sand with Young modulus equal to 100 MPa) and at different surcharge load ($q = 0$ kPa, $q = 16$ kPa, $q = 25$ kPa and $q = 50$ kPa) are shown in Fig. 2 and Fig. 3, where they are compared with the theoretical approaches at non-yielding lateral earth pressure distribution. From these figures, it can be observed that good agreement was noted between the FE calculations and the theoretical approaches. Fig. 4 and Fig. 5 show the lateral earth pressure distribution versus the normalized height of wall for yielding retaining walls at different backfill material and at different surcharge load, where they were compared with the Coulomb active earth pressure distribution. Again, the theoretical active earth pressure agreed well with the FE results. It should be noted that the limiting active earth pressure condition occurred after the formation of a failing soil wedge adjacent to the retaining wall. The numerical simulations using ABAQUS reasonably predicted the response and the lateral earth pressure of the retaining wall. The developed model was able to predict the lateral earth pressure with a good level of accuracy. From the verification part and the comparisons for each case, it can be concluded that a reliable FE model was developed.

The plastic strain contours, shown in Fig. 6, clearly illustrate the presence of a failure plane similar to the one assumed in the Coulomb active earth pressure theory. This failure surface was inclined at an angle of $(45+\phi/2)$, according to Coulomb theory.

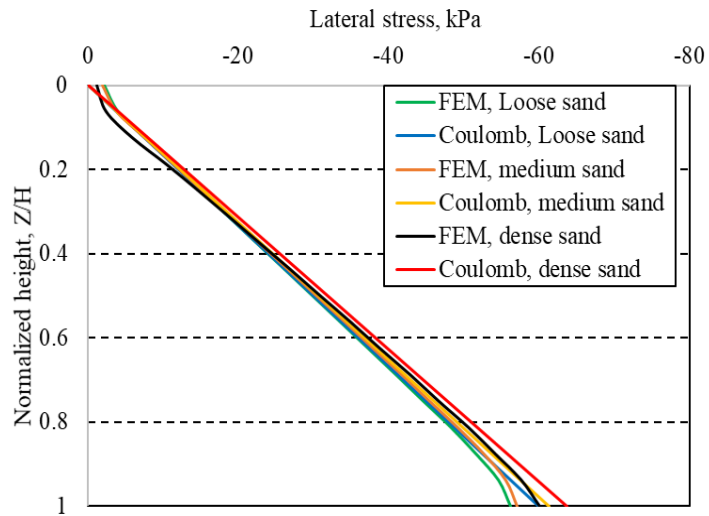


Figure 2. Lateral earth pressure against non-yielding wall model for different backfills.

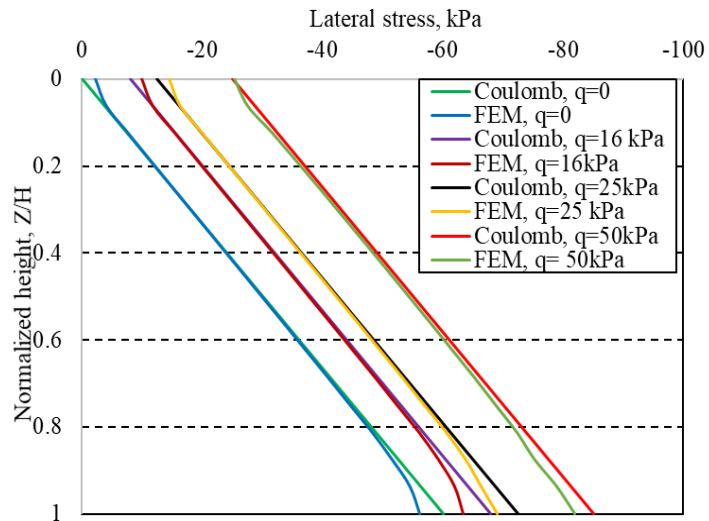


Figure 3. Lateral earth pressure against non-yielding wall model for different surcharge loads.

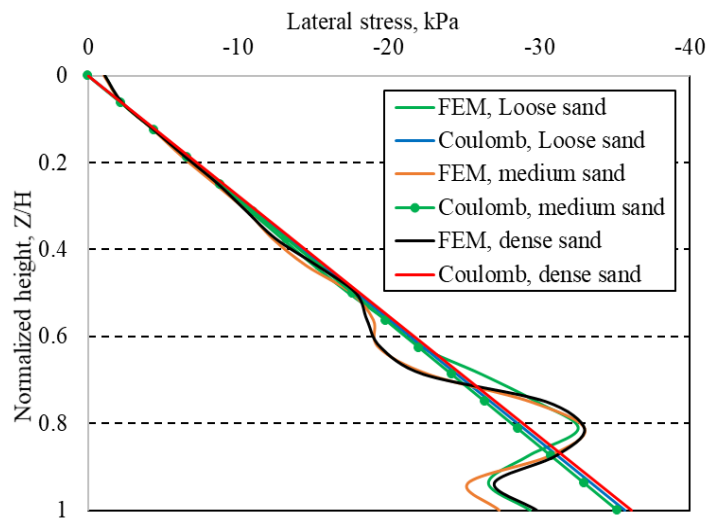


Figure 4. Lateral earth pressure against yielding wall model for different backfills.

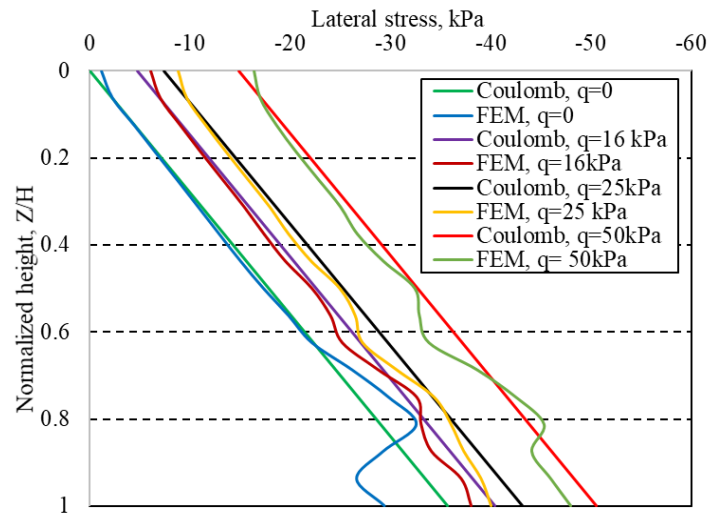


Figure 5. Lateral earth pressure against yielding wall model for different surcharge pressures, q .

The analysis was performed for a retaining wall with a height of 8 m, a surcharge load equal zero, the foam density 25 kg/m^3 , loose-sand backfill and a foam thickness varying from zero to 3.0 m as given in Table 2.

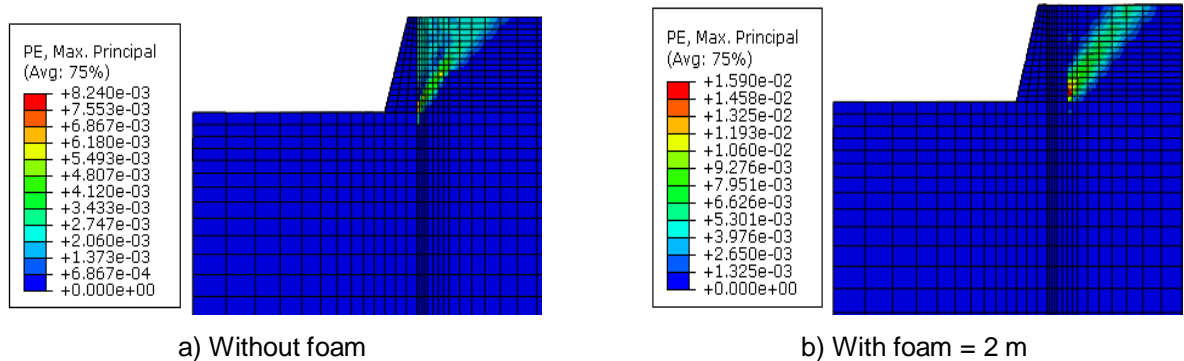


Figure 6. Distribution of plastic strain without and with foam in the backfill at active failure.

3.2. Effect of Foam Thickness

First, the effect of foam thickness on lateral earth pressure on retaining walls, and accordingly on the sliding forces and overturning moments, was investigated in case 1. In this case, foam was used with different thicknesses ranging from zero to 3.0 m. The foam density was set to 25 kg/m^3 for the whole case. No surcharge pressure was considered. The backfill soil was loose sand with unit weight of 15 kN/m^3 and modulus of elasticity of 20 MPa, Poisson ratio of 0.3 and internal friction angle of 27° with no cohesion. Both types of walls were considered; non-yielding and yielding retaining walls.

Fig. 7 shows lateral earth pressure against non-yielding wall for different foam thicknesses. The percentage of reduction in lateral force and overturning moment for non-yielding wall at different foam thicknesses is shown in Fig. 8. Fig. 9 shows factor of safety for sliding and overturning on the non-yielding wall at different foam thickness. From these figures, it can be observed that, the lateral earth pressure was significantly decreased upon using foam in front of the non-yielding retaining wall with a noticeable enhancement in the factor of safety against sliding and overturning. Figures also show that as the thickness of foam increases, the lateral earth pressure is reduced and consequently the factor of safety is increased.

The percentage of reduction in lateral earth force and overturning moment at different foam thickness can be calculated by the following equations: For the lateral force, $Y = 40.50X^{0.208}$, and for the overturning moment, $Y = 23.85X^{0.313}$, where Y is the percentage of reduction and X is the foam: thickness in meters. The factor of safety for sliding and overturning also was increased from 0.75 to 1.50 and from 1.15 to 1.75, respectively.

The effect of foam thickness on the reduction of lateral earth pressure on yielding retaining walls and the enhancement of corresponding factor of safety in terms of sliding force and overturning moment are shown in Fig. 10 to Fig. 12. Fig. 10 shows lateral earth pressure against yielding retaining wall for different foam thicknesses. Fig. 11 shows the percentage of reduction in lateral force and overturning moment for non-yielding wall at different foam thickness. Fig. 12 shows factor of safety for sliding and overturning on the

yielding wall at different foam thickness. Similar to the non-yielding retaining walls, the figures show that the lateral earth pressure was decreased as the thickness of foam was increased.

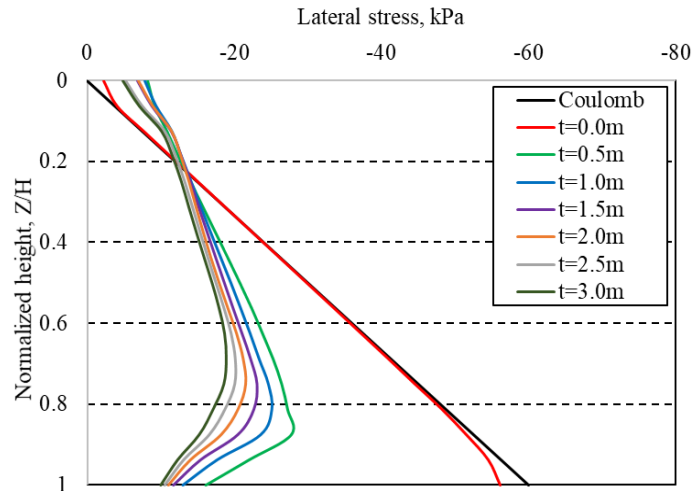


Figure 7. Lateral earth pressure against non-yielding wall for different foam thicknesses.

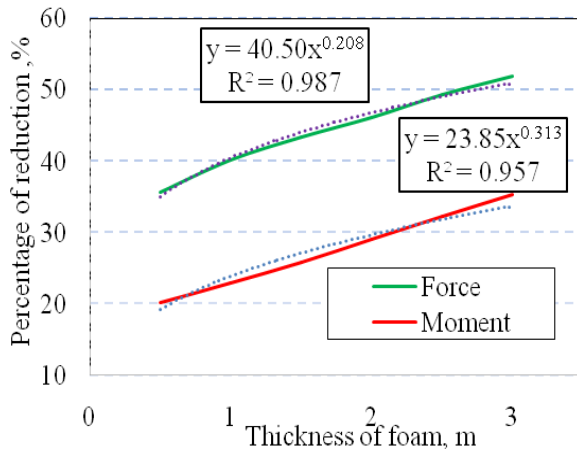


Figure 8. Percentage of reduction in lateral force and overturning moment

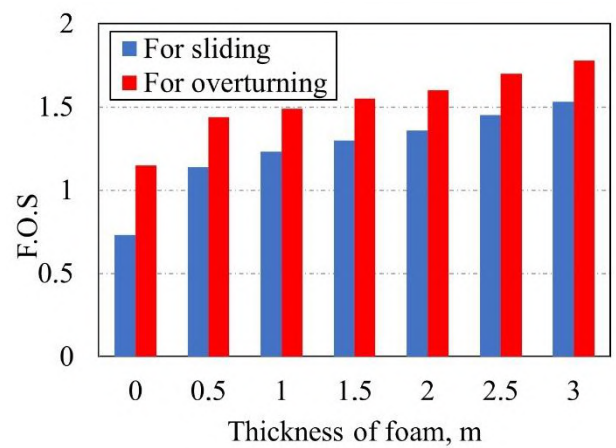


Figure 9. Factor of safety for sliding and overturning.

The percentage of reduction in lateral force and overturning moment at different foam thicknesses can be calculated by the following equations: For the force, $Y = 17.95X^{0.7502}$ and for the moment, $Y = 1.157X^2 + 3.605 X + 2.894$, as shown in Fig. 11. The factor of safety for sliding and overturning also was increased from 1.25 to 2.10 and from 1.8 to 2.60, respectively, as shown in Fig. 12.

In general, the lateral earth pressure is decreased with the increase of the foam thickness. This reduction in earth pressure reached 52 % for non-yielding walls and 41.14 % for yielding walls, when using foam with 3.0 m thickness, as shown in Fig. 7 and Fig. 10.

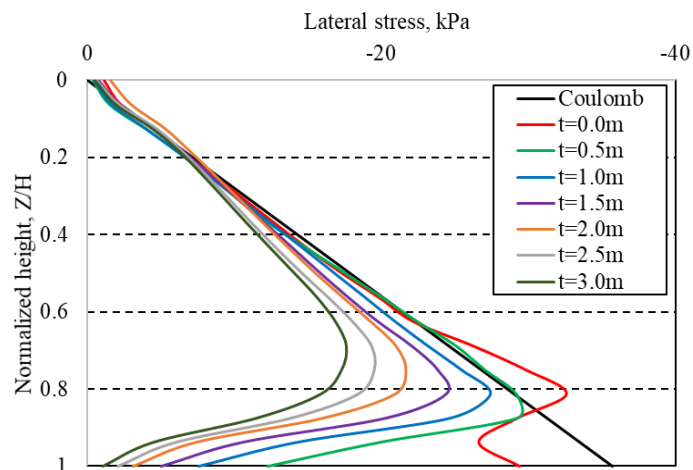


Figure 10. Lateral earth pressure against yielding wall for different foam thickness.

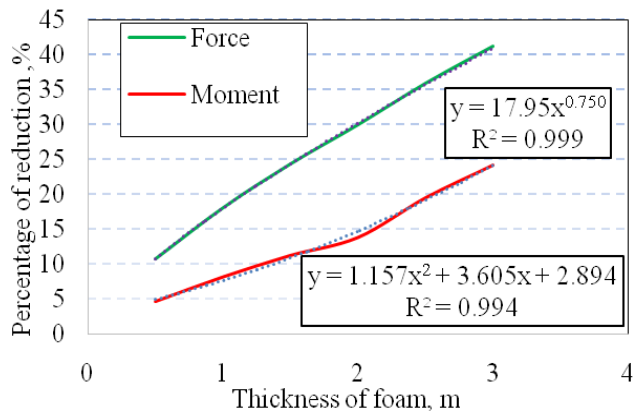


Figure 11. Percentage of reduction in lateral force and overturning moment.

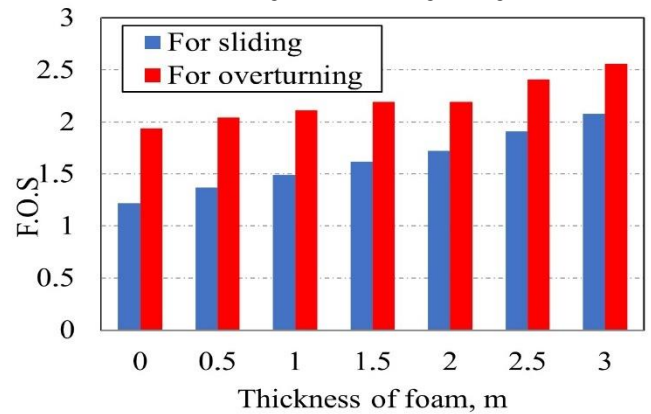


Figure 12. Factor of safety for sliding and overturning.

3.3. Effect of Foam Properties

In case 2, the effect of EPS properties on lateral earth pressure was studied considering the short term and long-term conditions of EPS. During this analysis, loose sand was considered with similar soil properties as in case 1. Also, no surcharge pressure was considered in this case. Table 3 summarizes the details of properties for the three types of EPS used: Foam 25, Foam 30 and Foam 35 in terms of unit weight, modulus of elasticity, Poisson ratio internal friction angle and cohesion. The foam thickness was 2.0 m, in this case.

Fig. 13 shows the lateral earth pressure against non-yielding wall model for different foam densities in short and long-term conditions. Fig. 14 shows the percentage of reduction in lateral force and overturning moment at different foam densities. The lateral force was decreased by 46.4 % for Foam 25, 44.5 % for Foam 30 and 43 % for Foam 35. The overturning moment was decreased by 29 % for Foam 25, 27.7 % for Foam 30 and 26.4 % for Foam 35, for short-term properties. Fig. 15 shows percentage of reduction in lateral force and overturning moment at different foam densities. The lateral force was decreased by 46.6 % for foam 25, 43.9 % for foam 30 and 43.9 % for foam 35. The overturning moment was decreased by 28.1 % for Foam 25, 26.9 % for Foam 30 and 26.9 % for Foam 35, for long-term properties.

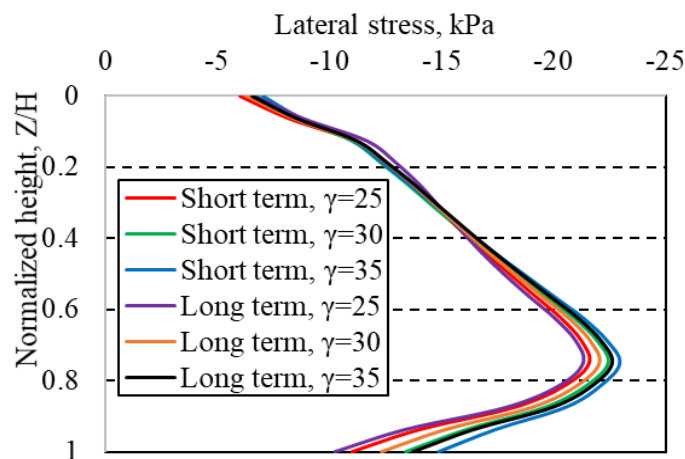


Figure 13. Lateral earth pressure against non-yielding wall model for different foam densities in the short and long-term conditions.

Fig. 16 shows Lateral earth pressure against non-yielding wall model for different foam densities in short and long-term conditions. Fig. 17 shows percentage of reduction in the lateral force and overturning moment at different foam densities. The lateral force was decreased by 29.8 % for Foam 25, 33.1 % for Foam 30 and 32.9 % for Foam 35. The overturning moment was decreased by 13.8 % for Foam 25, 21.9 % for Foam 30 and 22.8 % for Foam 35 for the short-term properties. Fig. 18 shows percentage of reduction in lateral force and overturning moment at different foam densities. The lateral force was decreased by 26.9 % for Foam 25, 30.1 % for Foam 30 and 30 % for Foam 35. The overturning moment was decreased by 7.2 % for Foam 25, 16.2 % for Foam 30 and 18 % for Foam 35 for the long-term properties.

In all studied cases, there is a general trend of having less lateral earth pressures on non-yielding retaining walls with decreasing EPS foam density. Results showed that use of Foam 25, which has the lowest density among other geofoam densities, is the most efficient in reducing the lateral pressure on non-yielding retaining walls. On the contrary, for yielding retaining walls, there is a general trend of reducing the lateral

earth pressures with the increase in EPS foam density. The results showed that use of Foam 35, which has the highest density between other geofoam densities, is the most efficient in reduction of lateral stresses on yielding retaining walls.

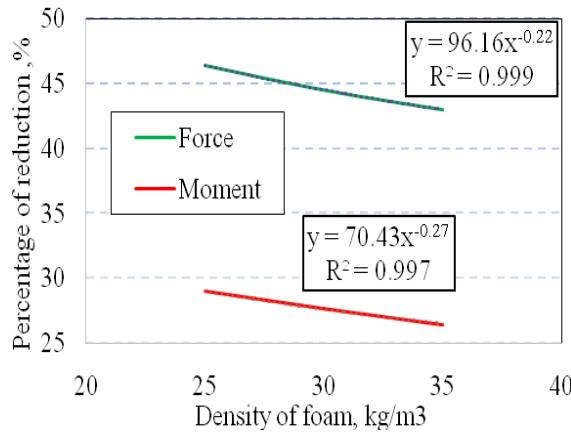


Figure 14. Percentage of reduction in lateral force and overturning moment for non-yielding wall (short-term conditions).

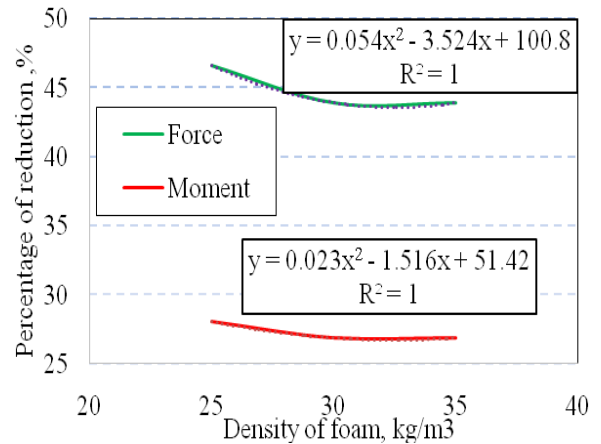


Figure 15. Reduction in lateral force and overturning moment for non-yielding wall (long-term conditions).

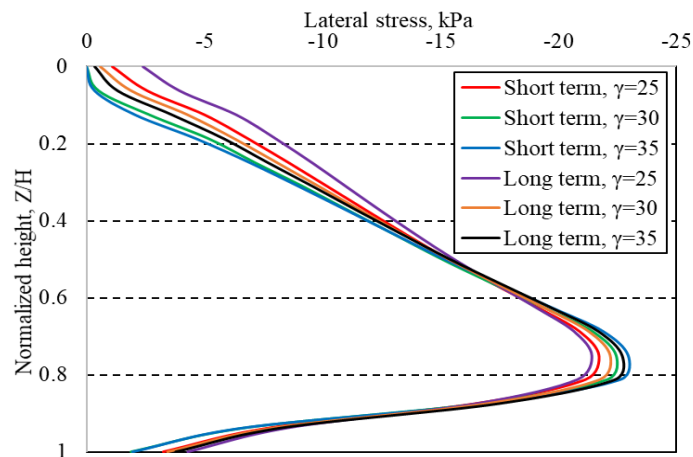


Figure 16. Lateral earth pressure against yielding wall model for different foam densities in short and long-term conditions.

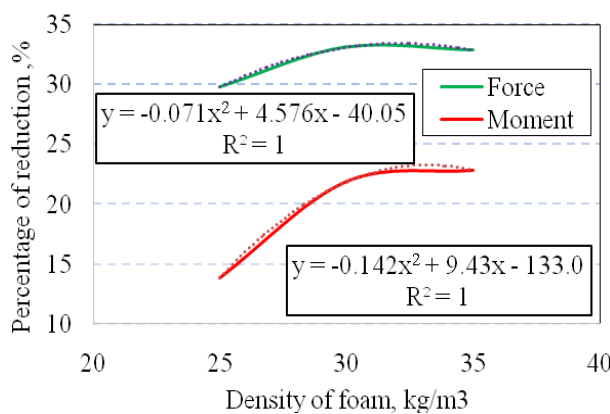


Figure 17. Reduction in lateral force and overturning moment for yielding wall (short-term condition).

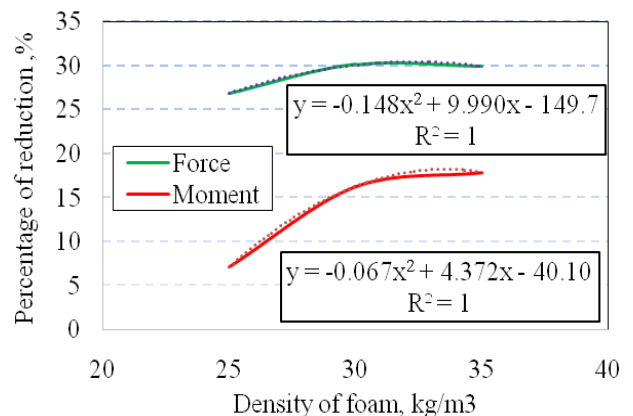


Figure 18. Reduction in lateral force and overturning moment for yielding wall (long-term condition).

3.4. Effect of Surcharge Pressure

Four different values of surcharge pressure were considered in case 3 to simulate pressure from foundations of adjacent structures and traffic loading. In this case, surcharge pressure values on backfill of

$q = 0, 16, 25$ and 50 kPa were considered. Similar soil properties were used for loose sand, as in case 1 and 2. Foam 25 with a thickness of 2.0 m in short-term conditions was considered in this case.

Fig. 19 shows the distribution of lateral earth pressure with the normalized height of non-yielding retaining wall for different values of surcharge pressures. As shown in Fig. 20, the percentage of reduction in lateral earth pressure was decreased with the increase of surcharge pressure. Considering the overturning moment, the reduction percentage was around 30% for surcharge pressure up to 20 kPa. For higher surcharge pressure, the reduction percentage was gradually decreased.

For yielding retaining wall, the distribution of lateral earth pressure on the wall is shown in Fig. 21. The percentage of reduction in lateral force was decreased from 30% in the case of zero surcharge pressure on the backfill to 21% for 50 kPa surcharge pressure. On the other hand, the maximum reduction in overturning moment was about 22% when surcharge pressure of 20 kPa was applied. Only 14% reduction was observed in the case of zero surcharge pressure on backfill surface. The percentage of reduction in lateral force and overturning moment as well as the fitting equations are shown in Fig. 22.

3.5. Effect of Backfill Soil

To investigate the effect of backfill soil properties on the effectiveness of using EPS foam on the lateral earth pressure on yielding and non-yielding retaining walls, three backfill soils were considered in case 4. These soils are loose, medium, and dense sands. The properties of each soil are presented in Table 5. The analysis was performed to investigate the lateral earth pressure and the safety of yielding and non-yielding retaining wall with a height of 8.0 m. No surcharge pressure was considered on the surface of backfill. Foam 25 in the short-term conditions with a thickness of 2.0 m was considered.

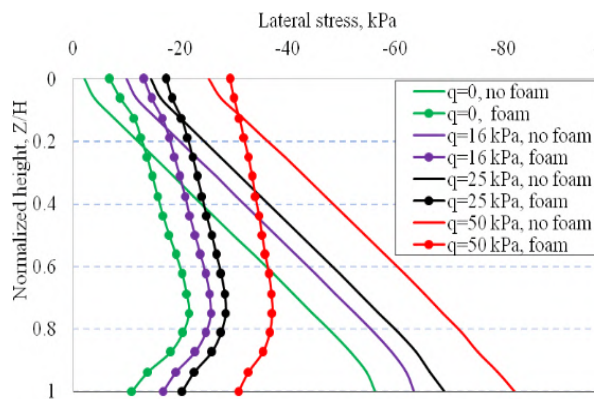


Figure 19. Lateral earth pressure against non-yielding walls for different surcharge loads.

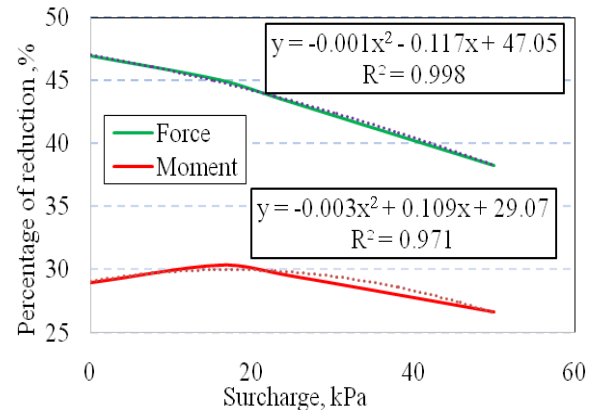


Figure 20. Reduction in lateral force and overturning moment for non-yielding walls at different surcharge loads.

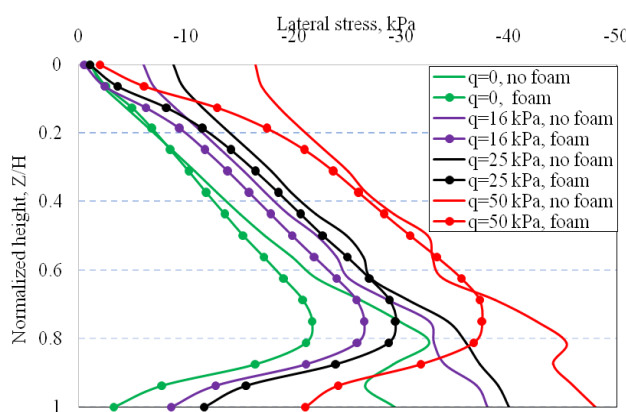


Figure 21. Lateral earth pressure against yielding wall for different surcharge loads.

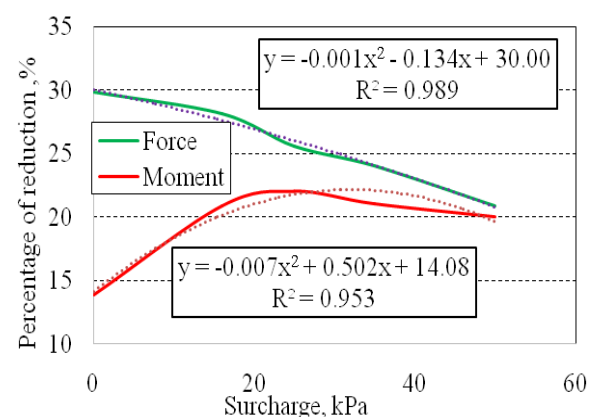


Figure 22. Reduction in lateral force and overturning moment for yielding wall at different surcharge loads.

Fig. 23 shows the distribution of lateral earth pressure on the non-yielding retaining wall for different backfill soils. According to Fig. 24, the lateral earth force and overturning moment were reduced by 49% and by 29% , respectively, for loose-sand backfill. Similar results were obtained in the case of medium-sand backfill, where the reduction was 51.3% and 33% for lateral earth force and overturning moment, respectively. For dense-sand backfill, the lateral earth pressure and overturning moment were decreased by 51.9% and by 32.1% , respectively.

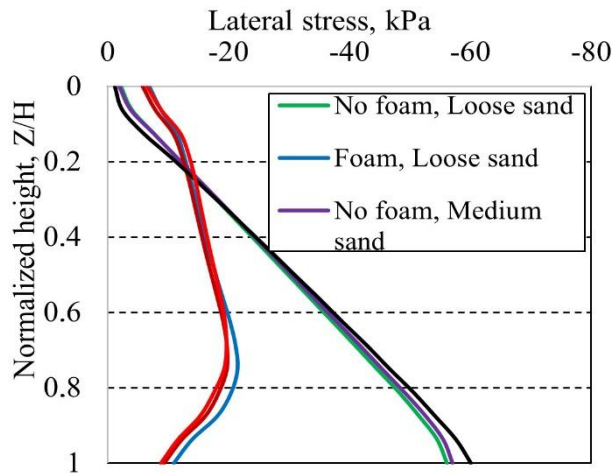


Figure 23. Lateral earth pressure against non-yielding wall for different types of backfill soil.

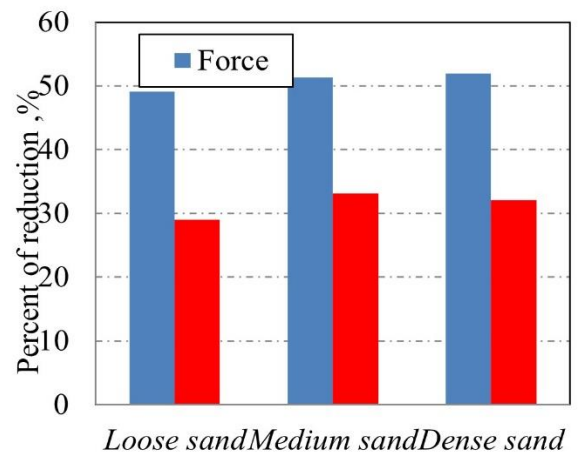


Figure 24. Percent of reduction in lateral force and overturning moment for non-yielding wall of different types of backfill soil.

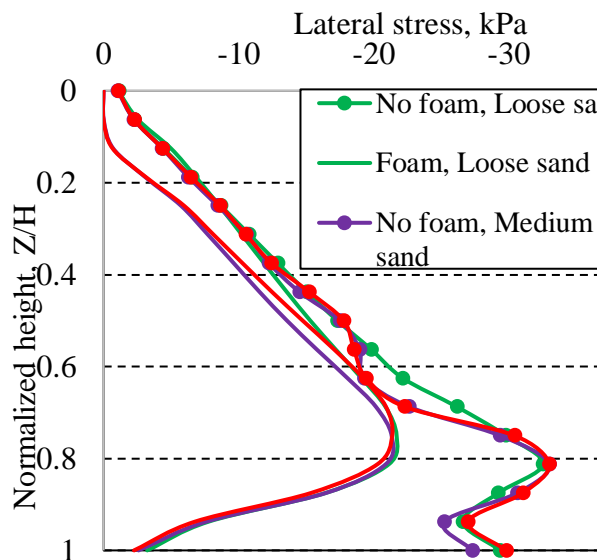


Fig. 25. Lateral earth pressure against yielding wall with different type of backfill soil

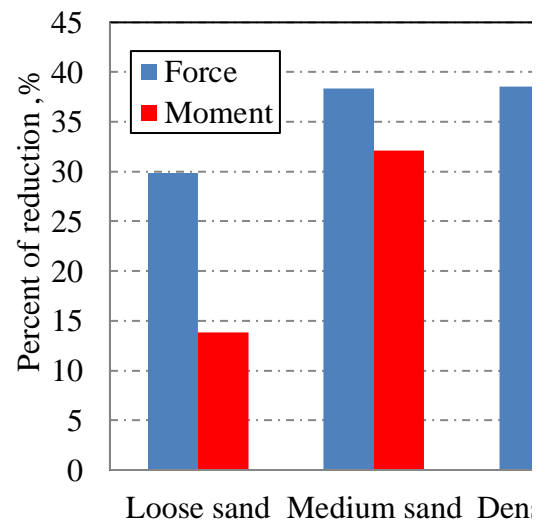


Fig. 26. Percent of reduction in lateral force and overturning moment for yielding wall with different types of backfill soil

Considering the case of yielding retaining wall, the distribution of lateral earth pressure over the wall height is shown in Fig. 25, for different types of backfill soil. The reduction in lateral earth forces and overturning moment for different backfill soils is shown in Fig. 26. The reduction in earth force was 29.8 %, 38.4 % and 38.6 % for loose, medium and dense sand backfills, respectively while the reduction in overturning moment was 13.8 %, 32.1 % and 31 %, for the considered backfill soils, respectively.

In general, using medium sand as backfill soil resulted in the best enhancement in the efficiency of EPS geofoam in reducing lateral force and overturning moment.

4. Conclusions

In this research, the inclusion of EPS geofoam was considered in order to reduce the lateral earth pressure on yielding and non-yielding retaining walls and accordingly increase the wall safety in terms of the sliding forces and overturning moments. A three-dimensional FE analysis was conducted using ABAQUS to model backfill soil, retaining wall, foam, and boundary conditions. The wall has a height of 8.0 m with a wall thickness of 0.80 m and 3.0 m at wall top and bottom, respectively. Four different parameters were considered to assess the efficiency of using EPS foam on lateral earth pressure on retaining walls and according the wall safety. These factors are:

- Foam thickness;
- Foam density and short-term and long-term properties;

- Surcharge pressure on backfill surface;
- Backfill soil properties.

According to the obtained results, the following conclusions were obtained:

1. The developed 3-D FE model using ABAQUS was able to predict the lateral earth pressure of cohesionless soil on both yielding and non-yielding retaining walls with a very satisfactory accuracy. The developed FE model can be used in similar applications to study the earth pressure on retaining walls with different deformable inclusions.

2. Increasing the EPS foam thickness results in reducing the lateral earth pressure on yielding and non-yielding retaining walls and accordingly increases the factor of safety against sliding and overturning. The reduction in lateral earth pressure was higher in the case of non-yielding retaining wall compared to the yielding retaining wall. The distribution of lateral earth pressure over wall height was considerably changed after using the EPS foam, especially in non-yielding retaining walls with maximum pressure values at a depth of 0.85 of the wall height.

3. For non-yielding retaining walls, percentage of reduction in lateral earth force and overturning moment were estimated by $40.50 X 0.208$ and $23.85 X 0.313$, respectively. For yielding retaining walls, the percentage of reduction in lateral earth force and overturning moment were estimated by $17.95 X 0.7502$ and $1.157 X 2 + 3.605 X + 2.894$, respectively, where X is the foam thickness in meters.

4. The density of EPS foam has a slight effect on the distribution and values of lateral earth pressure on yielding and non-yielding retaining walls considering the short-term and long-term conditions.

5. Inclusion of EPS foam has a considerable effect on reducing lateral earth pressure when having surcharge pressure on backfill surface against non-yielding wall while it has small effect on reducing lateral earth pressure in the case of yielding wall. For non-yielding wall, the maximum reduction in lateral earth force and turning moment was 47 % for zero surcharge pressure and 30 % for 20 kPa surcharge pressure, respectively. For yielding wall, the maximum reduction in lateral earth force and turning moment was 30 % for zero surcharge pressure and 22 % for 20 kPa surcharge pressure, respectively.

6. Similar efficiency of the inclusion of EPS foam was obtained in case of using different backfill soils in case of non-yielding retaining wall. However, the efficiency of EPS foam was higher in case of medium and dense sand backfills against yielding wall, compared to loose sand backfills.

5. Acknowledgement

Authors would like to express their thanks to Prince Sultan University for supporting the publication of this article.

References

1. Horvath, S.J. Seismic lateral earth pressure reduction on earth-retaining structures. Using Geofoams, Geotechnical Earthquake Engineering and Soil Dynamics Congress IV. 2008. Pp. 1–10.
2. Partos, A.M., Kazaniwsky, P.M. Geoboard reduces lateral earth pressures. Proceedings of Geosynthetics 87, Industrial Fabrics Association International. New Orleans, LA, USA, 1987. Pp. 628–639.
3. Karpurapu, R., Bathurst, R.J. Numerical investigation of controlled yielding of soil-retaining wall structures. Geotextiles and Geomembranes. 1992. Vol. 11. No. 2. Pp. 115–131.
4. Koerner, R. Designing with Geosynthetics, Pearson Education, London, UK, 5th edition. 2005.
5. Azzam, S.A., AbdelSalam, S.S. EPS geofoam to reduce lateral earth pressure on rigid walls. International Conference on Advances in Structural and Geotechnical Engineering, Hurgada, Egypt. 2015.
6. AbdelSalam, S.S., Azzam, S.A. Reduction of lateral pressures on retaining walls using Ggofoam inclusion. Geosynthetics International. 2016. Vol. 23. No. 6. Pp. 395–407.
7. Chauhan, V.B., Dasaka, S.M. Assessment of lateral earth pressure reduction using EPS geofoam-A numerical study. Conference on Numerical Modeling in Geomechanics. 2017.
8. Navid, H.N., Rouzbeh, D. Effects of geofoam panels on static behavior of cantilever retaining wall. Advances in Civil Engineering. 2018. Vol. 2018. Article ID 2942689. <https://doi.org/10.1155/2018/2942689>
9. Dave, T.N., Dasaka, S.M. Effect of boundary conditions on earth pressure reduction using EPS Geofoam. Japanese Geotechnical Society Special Publication. 2016. Pp. 2232–2237. DOI: 10.3208/jgssp.ind-34
10. Yadav, P.A., Singh, D.K., Dahale, P.P., Padade, A.H. Analysis of retaining wall in static and seismic condition with inclusion of geofoam using Plaxis 2D. Indian Geotechnical Conference, Indian Institute of Science Bengaluru. 2018.
11. Ertugrul, O.L., Trandafir, A.C. Reduction of lateral earth forces acting on rigid non-yielding retaining walls by EPS geofoam inclusions. Journal of Materials in Civil Engineering, ASCE. 2011. Vol. 23. No. 12. Pp. 1711–1718.
12. Salem, A.A., Beshoy, M.S., Sherif, S.A. 3D Modeling of EPS geofoam buffers behind diaphragm walls. Ground Improvement and Earth Structures, GeoMEast 2017. 2018. Pp. 46–53.
13. Veletsos, A.S., Younan, A.H. Dynamic response of cantilever retaining walls. Journal of Geotechnical and Geoenvironmental Engineering. 1997. Vol. 123. No. 2. Pp. 161–72.
14. Bathurst, R.J., Zarnani, S., Gaskin, A. Shaking table testing of geofoam seismic buffers. Soil Dynamics and Earthquake Engineering. 2007. Vol. 27. No. 4. Pp. 324–332.

15. Fakhry, B.M., Azzam, S.A., Abdelsalam, S.S. Using EPS buffers for diaphragm walls. 1st BUE Annual Conference & Exhibition-BUE ACE1 Cairo, EGYPT. 2016. Pp. 8–10.
16. Mustafa, R., Akram, W., Aman, S., Asif, M., (2017), Reduction of lateral earth pressure on rigid retaining walls using EPS geofoam inclusions. International Journal of Innovative Research in Science and Engineering. 2017. Vol. 3. No. 4.
17. AbdelSalam, S.S, Azzam, S.A., Fakhry, B. M. Reliability and 3D modeling of flexible walls with EPS inclusion. International Journal of Geomechanics. 2016. 04016153. Pp. 1–10.
18. Moghaddas Tafreshi, S.N., Joz Darabi, N., Dawson, A.R.. Combining EPS geofoam with geocell to reduce buried pipe loads and trench surface rutting, Geotextiles and Geomembranes. 2020. Vol. 48. No. 3. Pp. 400–418.
19. Azizian, M., Moghaddas Tafreshi, S.N., Joz Darabi, N. Experimental evaluation of an expanded polystyrene (EPS) block-geogrid system to protect buried pipes. Soil Dynamics and Earthquake Engineering. 2020. Vol. 129. 105965.
20. Ibrahim, Y.E-H., Nabil, M. Risk of surface blast load on pile foundations. Magazine of Civil Engineering. 2019. 90(6). Pp. 47–61. DOI: 10.18720/MCE.90.5
21. Grishina, A.S., Ponomaryov, A.B. Assessment of operation of fiber-reinforced soil located behind retaining walls. Geotechnics Fundamentals and Applications in Construction: New Materials, Structures, Technologies and Calculations – Proceedings of the International Conference on Geotechnics Fundamentals and Applications in Construction: New Materials, Structures, Technologies and Calculations, GFAC 2019. 2019. Pp. 82–85.
22. Coulomb, C.A. Essai sur une application des re`gles des maximis et minimis a` quelques proble`mes de statique relatifs a` l'architecture. In Me`moires Acade`mie Royale Pre`sente`s par Divers Savants, Paris. Vol. 7. Pp. 343–382.
23. Rankine, W. The Stability of Loose Earth. Philosophical Transactions of the Royal Society of London. Vol. 147.
24. Clough, G.W., Duncan, J.M. Earth Pressures. In Foundation Engineering Handbook. 2nd ed. Edited by H.-Y. Fang. Van Nostrand Reinhold, New York. 1991. Pp. 223–235.
25. Sadrekarimi, A., Monfared, D. Numerical investigation of the mobilization of active earth pressure on retaining walls. Proceedings of the 18th International Conference on Soil Mechanics and Geotechnical Engineering, Paris. 2013. Pp. 793–796.
26. AbdelSalam, S.S., Jama, R.A., Salah, M.A. EPS inclusion to reduce vertical stresses on shallow tunnels. Geosynthetics International. 2019. Pp. 1–40.

Contacts:

Yasser Ibrahim, yibrahim@vt.edu

Sayed Abdelsalam, s.salam@link.net

Marwa Nabil, marwa_nabil_amin@yahoo.com

Mahmoud Elsayed, eng.me5591@gmail.com

© Ibrahim, Y.E-H., Abdelsalam, S.S.A., Nabil, M.N.A., Elsayed, M.E., 2020



DOI: 10.18720/MCE.99.5

Influence of polypropylene-fiber on the mechanical properties of self-compacting-concrete with recycled aggregates

M. Hajmohammadian Baghba^a, S.A.H. Hashemi^{b*}, K. Kalbasi Anaraki^b, E.S. Hashemi^c

^a Department of Manufacturing and Civil Engineering, Norwegian University of Science and Technology (NTNU), Gjøvik, Norway

^b Department of Civil Engineering, Qazvin Branch, Islamic Azad University, Qazvin, Iran

^c Department of Civil Engineering, Faculty of Engineering, Raja University, Qazvin, Iran

* E-mail: mohammad.baghban@ntnu.no

Keywords: self-compacting concrete, compressive strength, flexural strength, impact resistance, recycled aggregates, polypropylene fiber

Abstract. In this study, the properties of self-compacting concrete (SCC) produced with different percentages of recycled aggregates (RAs) and polypropylene fibers is investigated in comparison with natural aggregates. The effect of using different percentages of 0 %, 25 %, 50 %, 75 % and 100 % RAs instead of natural aggregates (NAs) and polypropylene fibers of 0.1 %, 0.2 % and 0.3 % by volume of concrete in a fresh and hard state, consisting of a total 20 mixture composition, was investigated in SCC. SCC tests in the fresh state, including Slump Flow, J Ring, V Funnel, and L Box and hard concrete tests include compressive, tensile, and flexural and impact tests performed at the age of 28 days. Increasing the use of RAs does not significantly reduce the SCC tests in the fresh state while increasing the fibers causes a significant decrease in tests. In hardened concrete tests, with the increasing use of RAs of concrete, decreasing in compressive strength, tensile strength, flexural strength, and impact resistance were observed. While increasing the percentage of polypropylene fibers in recycled concrete, there was an increase in impact resistance and tensile strength and more energy absorption in the flexural test.

1. Introduction

One of the most important parameters for reaching proper durable concrete is the compact of the concrete. To achieve this target, usually needs to shake or vibrating to reduce the porosity of concrete air, the required strength has been obtained is increasing and prevent the formation of defective concrete. But vibrating is one of the most problems in this industry. Therefore, concrete manufacturing without vibrating was an important goal of industry experts. This issue has been discussed for several years until after major studies and experiments, were first produced by this specimen of concrete in Japan in 1980 [1]. The stability of self-compacting concrete (SCC) in the fresh state can be defined by various properties: Filling ability, passing ability and resistance to segregation. The mixture composition of concrete will be classified as a self-compacting if all the mentioned properties are present [2–4]. The Building industry is one of the largest pickup and consumers' natural materials and at the same time, it is the largest group of producers and construction wastes that damage to the environment. The appearance of numerous environmental issues caused by the increase of construction and destruction, the engineering community has pushed forward towards sustainable development. One of the suitable ways to reduce the consumption of natural materials is to recycle and reuse concrete materials. Because of the recycling, these materials can result in less environmental degradation in both disposal and dumping and in terms of harvesting less than natural primary materials [5]. In the last two decades, were extensively studied about the properties of normal concrete with recycled aggregates (RAs) [6–11]. Many Researchers from different countries study this issue: L. Solomon and H. Paulo (Brazil), and C. Poon, S. Kou and L. Lam (China) in their papers [8, 12] showed an aggregate which is got from demolished masonry and concrete structures as potentially use in new concrete. The quality of recycled aggregates (RAs) of concrete is usually lower than the quality of natural aggregates (NAs) [13]. Safiuddin et al. [14] stated that the maximum decrease in the 28-day compressive strength due to the incorporation of RAs was only 12.2 %. According to the research by Tabsh and Abdelfatah the compressive strength and tensile strength in concrete

Hajmohammadian Baghba, M., Hashemi, S.A.H, Kalbasi Anaraki, K, Hashemi, E.S. Influence of polypropylene-fiber on the mechanical properties of self-compacting-concrete with recycled aggregates. Magazine of Civil Engineering. 2020. 99(7). Article No. 9905. DOI: 10.18720/MCE.99.5



containing recycled coarse aggregates (RCAs) depends on the proportion use of the RCAs in the mixture composition and they reach to this result of overall strength of recycled concrete is about 10 to 25 percentages lower than strength the normal concrete made with NAs [15]. Etxeberria et al. [16] recorded when 100 % replacement of coarse recycled aggregate in compressive strength of concrete test at 28 days decreased to 20–25 %; when 25 % of the aggregates were replaced, there were no significant changes to the compressive strength. In the article by Farzam et al. [17] in 2014, which investigate the affection of RAs from demolished concrete on the performance of new concrete, therefore the affection of RAs 5, 25, 50, 75, 100 percent respectively on compressive strength, tensile strength and Slump Flow two types of concrete with strength 25 and 35 MPa were tested and the results showed the use of these aggregates with low percentage of participation does not have negative effect on the concrete performance and in the high rate of participating up to 26 % decrease in compressive and maximum decrease 15 % in tensile strength. These results were supported by Solyman [18] who found a decrease in tensile strength test up to 18.8 % in concrete with 70 % recycled fine aggregates (RFAs) compared with reference concrete. In comparison with NAs, recycled concrete aggregates are weaker, more porous and exhibit higher values of water absorption [19]. A piece of evidence which is important for the mix of SCC with (RCAs) is the quantity of water absorbed by the recycled aggregate (RA), which is always higher in comparison to the same type of the natural coarse aggregate (NCA). The amount of water absorption by RA was taken into account separately by some researchers [20], in addition to its wetness before mixing and the free water that formed part of the mixture. Other researchers [21–22] consider the total water content for W/C ratio because it is impossible to separate the effective water content (water absorption by RA and mixing water) from the total water content in the concrete fresh state, especially in RA. On the other hand, SCC has disadvantages in terms of it, like Low ductility and high Fragility and for compensating these disadvantages using the different methods like using various fibers that are equally spread in concrete volume and it can improve the concrete performance. The idea of this work goes back to the centuries ago the use of straw and horse hair in mud bricks. In fiber concrete, thousands of small fibers are spread on concrete and improve the concrete virtues in all directions. The fibers help to improve the ductility concrete, tensile strength of concrete, fatigue strength, impact resistance and Contraction cracks. Some researchers have been presented the Use of fibers into SCC mixes [23–25]. However, the performance of fibers as reinforcing materials in cementations' composites is needed for more research into the study [26–28]. Previous studies have clearly shown the advantages of concrete containing steel and polypropylene fibers under impact tests, and in some cases, the results of the impact test were subjected to statistical analysis [29–32]. In the United States of America in 1960 researching was about the use of steel fibers in the mixture of concrete and it was shown that the Tension concentration on the place of the cracks considerably decreased. In England in 1975 Walton and Majumdar in their research found that the addition of polymer fibers Such as nylon and polypropylene, even at the lowest proportion, it improves the impact resistance mixture of concrete [33]. Ghernouti et al in 2015 assessed the properties of self-compacting concrete containing plastic bag waste fibers (WFSCC). The Effects of length and fiber contents, Stress–strain behavior and Load–deflection behavior of the WFSCC were evaluated [34]. Hesami et al in 2016 studied the behavior of SCC pavements incorporating recycled tire rubber crumb and reinforced with polypropylene fiber. Adding this material result in increases in compressive, tensile, flexural and abrasion strength, but had no considerable effect on the modulus of elasticity of these specimens. The presence of fiber in rubberized SCC decreased water absorption based on evaluation of ultrasonic wave's velocity [35]. fathi et al in 2017 focused on the effects of fiber and glass on the mechanical properties of self-compacting concrete. The results showed that substitution of glass for aggregates in concrete reduces compressive strength. Addition of fibers to glass-containing concrete increases compressive strength and finally addition of glass to concrete reduces the tensile strength of concrete [36]. Mohseni et al in 2017 studied the fibre-reinforced self-compacting concrete containing recycled coarse aggregate. Based on the obtained results in significant improvement in tensile strength showed with increasing fiber content [37]. Aslani et al in 2018 investigated the effects of rubber granules on the fresh and hardened properties of self-compacting concrete. Based on the experiments, the optimum crumb rubber aggregate replacement percentage in SCC and optimum crumb rubber aggregate size in the SCC are provided [38]. Mahdikhani and safikhani in 2018 investigated rheological properties of self-consolidating concrete made by crushed waste tile aggregates. Based on the result of the experiments the percentage of fine aggregates have a significant impact on the properties of self-consolidating concrete [39]. Pan et al in 2019 evaluated the effects of steel slag powder on the properties of self-compacting concrete with recycled aggregates. The result showed that the 10 % replacement ratio of SSP result in superior mechanical properties and better durability [40]. Sasanipour et al in 2019 focused on the Effect of silica fume on durability of self-compacting concrete made with waste recycled concrete aggregates. Due to the results, it observed that Silica fume plays an important role to improve durability performance. Also, it made be decreased water absorption according to BS and ASTM standards [41]. Sadeghi-Nik et al in 2019 studied the effect of Recycled Concrete Aggregates and Metakaolin on the Mechanical Properties of Self-Compacting Concrete Containing Nanoparticle. They concluded that the construction of self-compacting concrete with complete replacement of recycled aggregates is possible [42]. The purpose of this study the using of recycled aggregate as fine and coarse aggregate with different percentages of replacement 0 %, 25 %, 50 %, 75 % and 100 % than to the natural aggregates, which this work, using less than natural resources as far as possible could produce the environmentally friendly concrete. Therefore, in this research, we try to improve the properties of concrete

containing RAs; the effect of polypropylene fibers with various percentages of 0.1 %, 0.2 % and 0.3 % by volume on this type of concrete is investigated. In this study investigating the fresh state tests include Slump Flow, J Ring, V Funnel, and L Box and hard concrete state includes compressive, tensile, and flexural and impact tests.

2. Methods

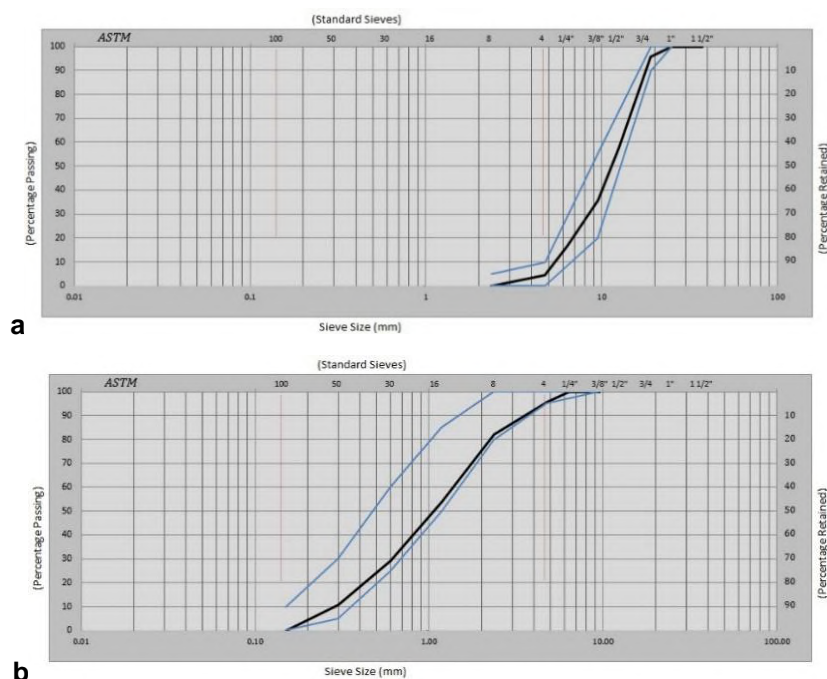
2.1. Materials

From among of variety standard cement, use the typical cement which one of that is used popularly in the normal conditions. For this reason, was used Portland cement type 2. Therefore, the chemical properties of this cement are given in Table 1.

Table 1. Chemical properties of cement.

| Composition | (%) |
|--------------------------------|-------|
| CaO | 62.28 |
| SiO ₂ | 20.79 |
| Al ₂ O ₃ | 4.76 |
| Fe ₂ O ₃ | 3.86 |
| MgO | 3.22 |
| SO ₃ | 1.89 |
| K ₂ O | 0.68 |
| Na ₂ O | 0.37 |
| CaO.f | 0.82 |

In this research, the Zhikava Company superplasticizer (SP) with that model zp-pf4 was used. This product is in harmony with various types of cement and in accordance with the ASTM C-494 standard. This material was a brown color and has a specific gravity 1.1 g/cm³. Polypropylene fibers consumed by NSG Company and at 12 mm length, which has a specific gravity 0.9–0.91 g/cm³ and tensile strength 350 Mpa. In this study, to make a concrete mixture of natural coarse aggregate (NCA), which has a uniform grain maximum; size of 19 mm and the water absorption 2.36 % were used. Natural fine aggregate (NFA) consumed from the type of river sand was washed twice without any clay and the particle size of fine aggregate was between 0–4.75 mm with softness modulus 3.28 and water absorption was used 3.38 %. RCAs were used in the 15 cm cubic specimens of a concrete company with a compressive strength less than 25 MPa. Operation crushing and separating of specimens was done by a sledgehammer and then bypassing the RAs, the related sieves of the two groups of sand and gravel were divided. RCA was used has a uniform grain and maximum size of grains 19 mm and water absorption of 8.53 percent. Recycled fine aggregate (RFA) was used in this study, 0–4.75 mm. Also, the percentage of water absorption was 9.94 %, softness modulus 3.39 and has a uniform grain. Natural and recycle coarse aggregate and Natural and recycle fine aggregate Grading used in this research are based on the ASTM C33 standard. The grain size distribution of natural and recycle coarse aggregate, natural and recycle fine aggregate is shown in Fig. 1.



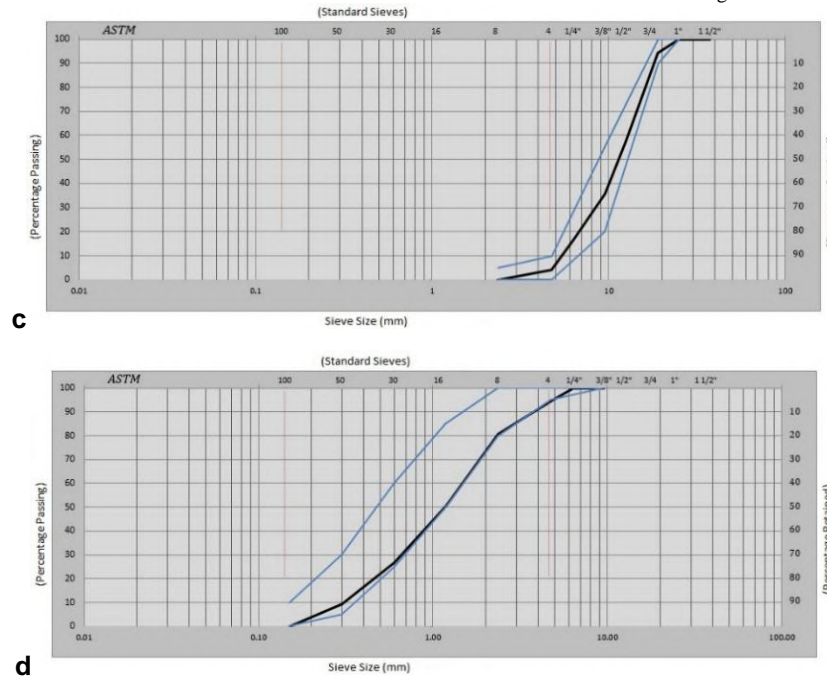


Figure 1. aggregate size distribution; a) natural coarse aggregate; b) natural fine aggregate; c) recycle coarse aggregate; d) recycle fine aggregate.

Due to the high absorption percentages of RAs compared to NAs, to compensate for the effect of reducing the concrete properties in fresh state of recycled aggregate mixes, after calculating the percentage of water absorption of natural and recycled aggregates, the difference in the water absorption percentages of these two types of aggregates is as extra water, to the final mixes contain of RA were added. The used material of natural and recycle coarse aggregate, natural and recycle fine aggregate, Cement, superplasticizer (SP) and fiber can be viewed in the Fig. 2.



Figure 2. Materials; a) natural and recycle coarse aggregate; b) natural and recycle fine aggregate; c) cement; d) superplasticizer (SP); e) fiber; f) limestone.

2.2. Mixing ratios and specimen preparation

First of all, according to the concrete properties target, a mix for starting the work is chosen. Reference concrete is completely made with natural material. The acceptance criteria of final mixture composition are firstly the compressive strength and also the proper performance by checking the slump flow. Finally, the reference concrete mixture composition was selected and then, according to this mix, the other mixes were made and tested. In the manufacture of specimens, use 0 %, 25 %, 50 %, 75 %, and 100 % RAs are replaced by NAs and also were used 0.1 %, 0.2 %, and 0.3 % by volumes of concrete of fiber. Overall 20 mixture compositions to investigate the effect of RA and polypropylene fibers were made in SCC, finally fresh and hardened concrete tests on them. Details of concrete mixes are given in Table 2.

Table 2. Proportions of mix compositions (kg.m³).

| Mix No. | Mix code | Cement | w/b | extra water | Natural aggregate | | Recycled aggregate | | Limestone | Fiber | SP |
|---------|-----------------|--------|------|-------------|-------------------|----------------|--------------------|----------------|-----------|-------|------|
| | | | | | Coarse aggregate | Fine aggregate | Coarse aggregate | Fine aggregate | | | |
| 1 | 100NA | 450 | 0.43 | - | 501.9 | 1075.5 | - | - | 215.1 | - | 4.05 |
| 2 | 100NA-0.1PP | 450 | 0.43 | - | 501.9 | 1075.5 | - | - | 215.1 | 0.91 | 4.05 |
| 3 | 100NA-0.2PP | 450 | 0.43 | - | 501.9 | 1075.5 | - | - | 215.1 | 1.82 | 4.05 |
| 4 | 100NA-0.3PP | 450 | 0.43 | - | 501.9 | 1075.5 | - | - | 215.1 | 2.73 | 4.05 |
| 5 | 75NA-0.1PP-25RA | 450 | 0.43 | 24.7 | 376.425 | 806.625 | 125.475 | 268.875 | 215.1 | 0.91 | 4.05 |
| 6 | 75NA-0.2PP-25RA | 450 | 0.43 | 24.7 | 376.425 | 806.625 | 125.475 | 268.875 | 215.1 | 1.82 | 4.05 |
| 7 | 75NA-0.3PP-25RA | 450 | 0.43 | 24.7 | 376.425 | 806.625 | 125.475 | 268.875 | 215.1 | 2.73 | 4.05 |
| 8 | 50NA-0.1PP-50RA | 450 | 0.43 | 49.4 | 250.95 | 537.75 | 250.95 | 537.75 | 215.1 | 0.91 | 4.05 |
| 9 | 50NA-0.2PP-50RA | 450 | 0.43 | 49.4 | 250.95 | 537.75 | 250.95 | 537.75 | 215.1 | 1.82 | 4.05 |
| 10 | 50NA-0.3PP-50RA | 450 | 0.43 | 49.4 | 250.95 | 537.75 | 250.95 | 537.75 | 215.1 | 2.73 | 4.05 |
| 11 | 25NA-0.1PP-75RA | 450 | 0.43 | 74.2 | 125.475 | 268.875 | 376.425 | 806.625 | 215.1 | 0.91 | 4.05 |
| 12 | 25NA-0.2PP-75RA | 450 | 0.43 | 74.2 | 125.475 | 268.875 | 376.425 | 806.625 | 215.1 | 1.82 | 4.05 |
| 13 | 25NA-0.3PP-75RA | 450 | 0.43 | 74.2 | 125.475 | 268.875 | 376.425 | 806.625 | 215.1 | 2.73 | 4.05 |
| 14 | 0.1PP-100RA | 450 | 0.43 | 98.9 | - | - | 501.9 | 1075.5 | 215.1 | 0.91 | 4.05 |
| 15 | 0.2PP-100RA | 450 | 0.43 | 98.9 | - | - | 501.9 | 1075.5 | 215.1 | 1.82 | 4.05 |
| 16 | 0.3PP-100RA | 450 | 0.43 | 98.9 | - | - | 501.9 | 1075.5 | 215.1 | 2.73 | 4.05 |
| 17 | 75NA-25RA | 450 | 0.43 | 24.7 | 376.425 | 806.625 | 125.475 | 268.875 | 215.1 | - | 4.05 |
| 18 | 50NA-50RA | 450 | 0.43 | 49.4 | 250.95 | 537.75 | 250.95 | 537.75 | 215.1 | - | 4.05 |
| 19 | 25NA-75RA | 450 | 0.43 | 74.2 | 125.475 | 268.875 | 376.425 | 806.625 | 215.1 | - | 4.05 |
| 20 | 100RA | 450 | 0.43 | 98.9 | - | - | 501.9 | 1075.5 | 215.1 | - | 4.05 |

How to name the mixes as follows:

NA: Natural aggregate, RA: Recycle aggregate, PP: Polypropylene fibers

The numbers behind each of the signs represent the percentage of each of them in the mixture composition. For example, this mix code 75NA-0.3PP-25RA means it contains 75 percent natural aggregates, 0.3 percent polypropylene fibers, and 25 percent recycled aggregate. After completion of the manufacturing of mixes, specimens are cured in the laboratory conditions for about 24 hours, after that keeps them in water with a temperature from 18 to 23 centigrade for about 28 days. In this study, the compressive strength test was performed on cubic specimens of 100×100×100 mm, Tensile strength test on cylindrical specimens with dimensions of 150×300 mm, Flexural strength test on prismatic beams specimens in the dimensions of 100×100×500 mm and for doing the impact test first concrete shape disks to diameter 152 mm and a height 63.5 mm or cylindrical specimens 150×300 mm were cut which was used the second method in this experiment. The behavior of SCC in the fresh state, including the Slump Flow test, J Ring test, V Funnel test, and L Box test was evaluated.

2.3. Setting and test methods

2.3.1. Compressive strength test

According to the structure mentioned in Table 2, each mixing design with different percentages of RAs and polypropylene fibers three cube specimens with dimensions of 100×100×100 mm were used in accordance with standard BS 1881-116 [43] for the evaluation of compressive strength and depicted in Fig. 3a. In total sixty cubic specimens were manufactured and the effect of different percentages of RA (0 %, 25 %, 50 %, 75 %, and 100 %) and polypropylene fibers (0.1 %, 0.2 %, and 0.3 %) was investigated.

2.3.2. Tensile strength test

For doing this test, an indirect method was used to do splitting tensile strength of the cylindrical specimen of 150×300 mm in accordance with the ASTM C 496 [44] standard, which is horizontally along its axis in accordance with Fig. 3b in the test device the compressive strength is placed. From each mixture composition, two specimens and a total of forty cylindrical specimens were made. Then, the load is continuous with steadily speeding within the concrete tensile stress range and between 0.66 to 1.38 MPa/min it applies until to the failure of the specimen.

2.3.3. Flexural strength test

For the analyses of the performance of SCC were made of RAs and polypropylene fibers, a number of forty prismatic beams (100×100×500 mm) were tested in accordance with ASTM C 293 [45] standard under the three point bending test. The test setup used to evaluate flexural assesses is depicted in Fig. 3c. The flexural loading on the beams was applied with a loading rate of 0.3 mm/min.

For the calculating modulus of rupture, using the below equation:

$$R = \frac{3PL}{2bd^2}, \quad (1)$$

where R is modulus of rupture, psi, or MPa;

P is maximum applied load indicated by the testing machine, lbf, or N;

L is span length, in., or mm;

b is average width of specimen, at the fracture, in., or mm;

d is average depth of specimen, at the fracture, in., or mm.

For each mixture composition, the two numbers of the specimen's prismatic beam were manufactured.

2.3.4. Impact drop weight test

The drop weight Impact test was conducted based on ACI Committee 544 [29]. This device is depicted in Fig. 3d. A steel hammer with 4.45 kg weight from 457 mm height on the steel ball with 63.5 mm diameter is fall. This steel ball is in contact with the central surface specimens. In total, sixty concrete disks with 150 mm diameter and 65 mm height from cylindrical specimens of 150×300 mm at the age of 28 days in accordance with Fig. 3d are cut.

For the calculating absorption energy, using the below equation:

$$\text{Impact energy (EN)} = N \times W \times H \quad (2)$$

While N is the number of blows, W is the weight of the steel hammer with a mass of 4.45 kg, H is the height of fall.

To evaluated disks, resistance under drop weight impact load, while for each group of mixture composition three specimens were tested.

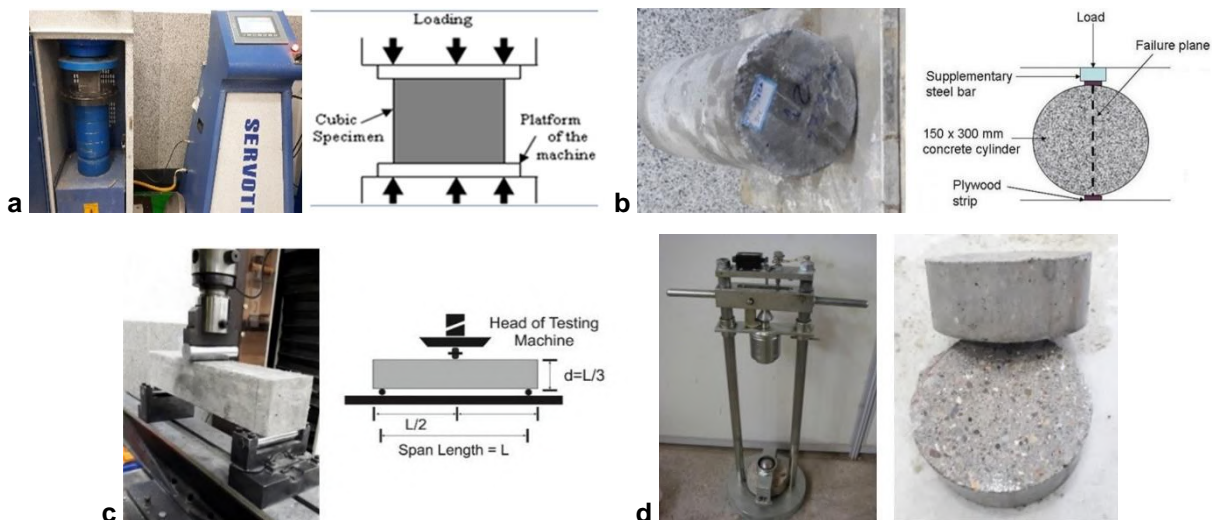


Figure 3. a) Cylindrical specimen and how to place the specimens; b) cubic specimens and apparatus of compressive test; c) Prismatic beams and test setup for the execution of three point bending test; d) Disks and apparatus of impact test.

3. Results and Discussion

3.1. Fresh mix properties

In order to measure the performance of SCC containing fiber and RAs, SCC measurement parameters have been used in accordance with European EFNARC [2] regulation. Fresh state concrete test results are depicted in Table 3.

Table 3. The test results obtained by measurement of fresh concrete.

| Mix No. | Mix code | Slump-flow test | | J-ring test | V-funnel test | | L-box test |
|---------|------------------|-----------------|-----------------------|-----------------|---------------|----------|-------------------------------|
| | | cm | T ₅₀ (sec) | Δh (mm) | T (sec) | T (5min) | H ₂ H ₁ |
| 1 | 100NA | 78 | 1.6 | 3.75 | 4.1 | 6.6 | 0.92 |
| 2 | 100NA-0.1PP | 69 | 2.2 | 6.75 | 5 | 8 | 0.82 |
| 3 | 100 NA-0.2PP | 62 | 3.1 | 7.5 | 5.7 | 9.8 | 0.72 |
| 4 | 100 NA-0.3PP | 53 | 9.8 | 9.5 | 6.5 | 11.3 | 0.6 |
| 5 | 75 NA-0.1PP-25RA | 68 | 2.4 | 6.75 | 6 | 8.2 | 0.79 |
| 6 | 75 NA-0.2PP-25RA | 62 | 4.7 | 8 | 6.7 | 10.1 | 0.68 |
| 7 | 75 NA-0.3PP-25RA | 51 | 12.4 | 13.75 | 7.5 | 12.3 | 0.59 |
| 8 | 50 NA-0.1PP-50RA | 68 | 2.5 | 7 | 6.7 | 8.3 | 0.77 |
| 9 | 50 NA-0.2PP-50RA | 61 | 5.1 | 7.5 | 7.1 | 10.6 | 0.65 |
| 10 | 50 NA-0.3PP-50RA | 51 | 15.3 | 15.5 | 7.7 | 12.5 | 0.57 |
| 11 | 25 NA-0.1PP-75RA | 65 | 2 | 7.5 | 6.8 | 8.6 | 0.73 |
| 12 | 25 NA-0.2PP-75RA | 59 | 5.1 | 9.5 | 7.1 | 11.3 | 0.64 |
| 13 | 25 NA-0.3PP-75RA | 49 | - | 16.5 | 8 | 13.1 | 0.55 |
| 14 | 0.1PP-100RA | 64 | 2.9 | 8.5 | 7.1 | 8.9 | 0.72 |
| 15 | 0.2PP-100RA | 59 | 4.1 | 9.25 | 7.6 | 11.6 | 0.64 |
| 16 | 0.3PP-100RA | 45 | - | 19.75 | 8 | 13.6 | 0.52 |
| 17 | 75 NA-25RA | 76 | 1.9 | 4 | 4 | 6.8 | 0.9 |
| 18 | 50 NA-50RA | 75 | 1.9 | 5 | 4.3 | 6.9 | 0.89 |
| 19 | 25 NA-75RA | 73 | 2 | 5.5 | 4.4 | 6.9 | 0.86 |
| 20 | 100RA | 73 | 2.2 | 7.25 | 4.6 | 7 | 0.85 |

The slump flow test is one of the widely used to measure the SCC properties to evaluate the flow ability of the SCC and resistance to segregation. This test accordance to EFNARC does and the average diameter of spread concrete in two directions perpendicular and also the time of reaching to 50 cm in diameter, is recorded based on the marking on the surface of the slump flow test. Test results are present in Fig. 4a and Fig. 4b.

As shown in the Fig. 4a it can be seen, mixes the number of 3, 6, 9, 11, 12, 14 and 15 in the category of SF1 concrete for unreinforced concrete structures or less rebar such as concrete slabs and also in small sections it does not need a long horizontal flow of concrete like piles is applicable. Mixes number 2, 5, 8, 18, 19 and 20 in the category of SF2 concrete it is suitable for many commonly use concrete applications. Number designs 1 and 17 in the category of SF3 concrete for vertical sections concreting, full rebar structures and complex structures are applicable. Finally, mixes numbers 4, 7, 10, 13 and 16 were not included in the SCC category because of a sharp drop in the slump flow. The maximum reduction in the slump flow occurred when 100 percent RA and 0.3 by volume percentages polypropylene fibers were used at the same time and resulting in a 42.31 % decrease in the slump flow. As can be seen, increasing the percentage of recycled aggregates decrease the slump flow This result agrees with the results of the reference of [39].

J Ring test based on EFNARC regulation was used, in order to determine the attribute to passing ability fresh state concrete through the rebars. The height difference between inside concrete and outside the J ring was a dimension in four points and averaging which expresses the ability to pass the concrete. Test results are depicted in Table 3 and Fig. 4c.

According to Fig. 4c, the height difference between inside and outside of the J ring with increased by consuming the amount of fiber and RA was increased. Generally, it can be said most of the mixes are included within the allowed range (Δh mm ≤ 10) and only the mixes containing 0.3 % polypropylene fibers are not included within the allowed range of this test.

According to EFNARC regulation, the L box test was designed to investigate the capability of the fresh concrete flow and blocking phenomenon due to the presence of the rebars. In this test, the first and end of the height of the L box after that passing through the fresh SCC between rebars was dimension and according to

the results of the passing ability and blockage that is estimated. Test results are present in the Table 3 and Fig. 4d.

The charts from the L box test, when an increase of fibers and RA in each mixture composition, the rate of flow concrete on the horizontal surface of L box was decreased. In other words, it is possible to mention reduce the ability of concrete to passing through from the rebars network of L box. While the mix contained 100 % RA and 0.3 % fibers, concrete was hardly reached the bottom of L box.

According to EFNARC regulation, V funnel the time of the concrete release from the funnel is measured and is used as a criterion in determining the filling ability and viscosity of concrete. Test results of the V funnel are depicted in Table 3 and Fig. 4e. It can clearly be seen, increase in the percentage of RA will increase the time of concrete releases from the V funnel, therefore, increase of fibers cause of the higher the viscosity while the amount of fiber consumed increases and this led to longer passing times of concrete from the V funnel. In the mixes contain 0.3 % fiber, the concrete release time increases sharply after 5 minutes from V funnel. But in general, most of the mixes based on the EFNARC regulation range. The notable drawback lack of water throwing of all the mixture's composition of including the fiber was in the V funnel after five minutes, this indicates shows that the fibers can prevent water thrown in concrete. In Fig. 4e, the concrete release times from the V funnel are shown on the graph after 10 seconds and 5 minutes. It is observed that in the mixed number 1, it contains 100 % NA and the lack of fiber, the difference of the concrete release times from the V funnels after 10 seconds and release time after 5 minutes is equal 2.5 seconds. While in the mixed number 16 contain 100 % of RA and 0.3 % is fibers this difference is reached in 5.6 seconds.

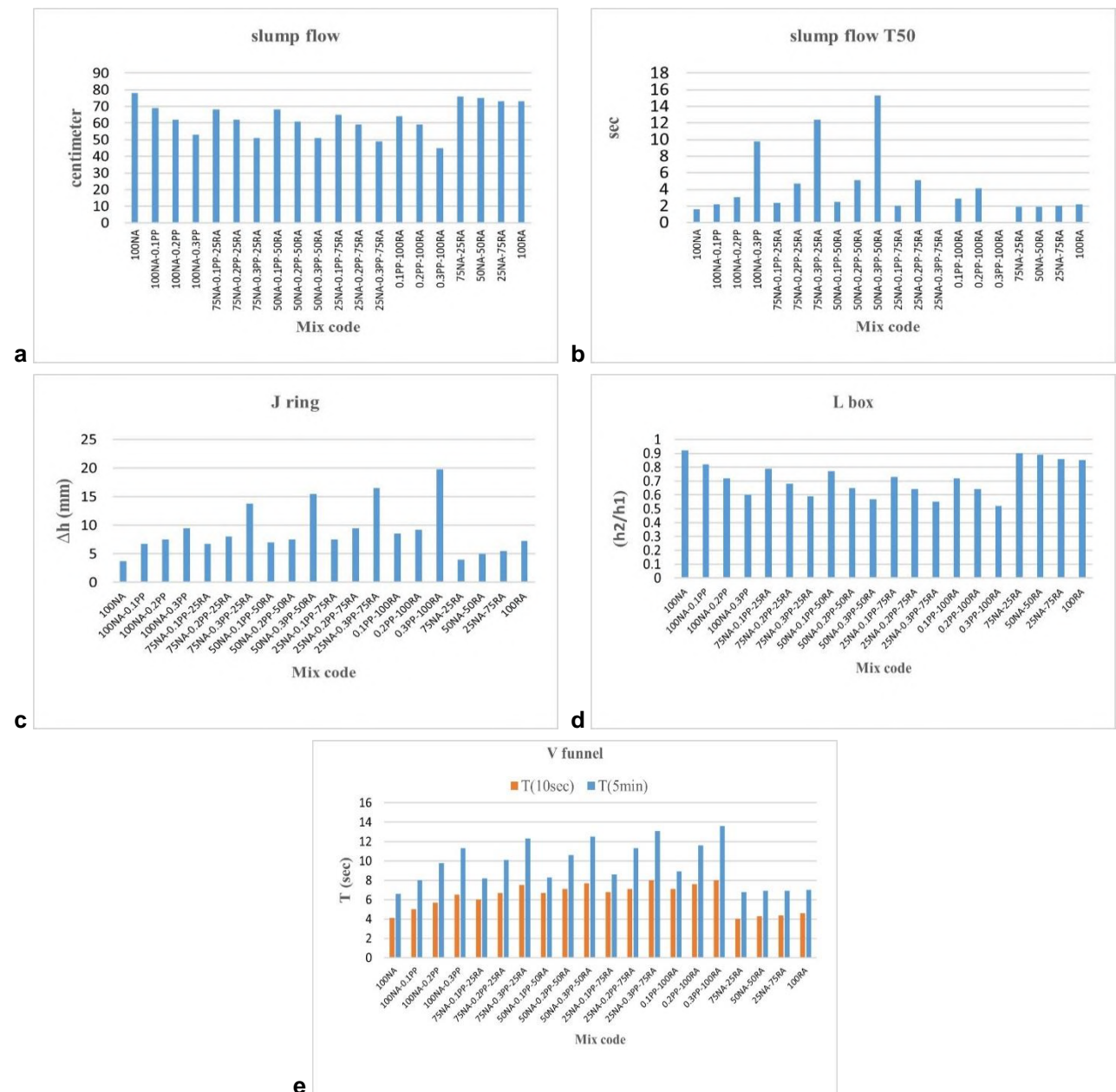


Figure 4. Effect of different fiber and recycled aggregate percentages contents on: a) slump flow; b) slump flow T50; c) J ring; d) L box; e) V funnel.

3.2. Properties of hardened concrete

All test results of hardened concrete are present in Table 4.

Table 4. Results of compressive strength, tensile and flexural strength tests.

| Mix No. | Mix code | Compressive strength (MPa) | Tensile strength (MPa) | Flexural strength | | | Blow number | | Impact energy (En) | |
|---------|-----------------|----------------------------|------------------------|-------------------|-------|-----------------------|-------------|----------------|--------------------|----------------|
| | | | | N | (MPa) | Energy absorption (J) | First crack | Ultimate crack | First crack | Ultimate crack |
| 1 | 100NA | 51.5 | 3.17 | 10126.42 | 7.59 | 2585.64 | 143 | 146 | 2910.56 | 2971.62 |
| 2 | 100NA-0.1PP | 52.3 | 3.74 | 9933.2 | 7.44 | 3733.53 | 160 | 167 | 3256.57 | 3399.04 |
| 3 | 100NA-0.2PP | 53.67 | 3.99 | 11537.89 | 8.65 | 5458.23 | 172 | 186 | 3500.81 | 3785.76 |
| 4 | 100NA-0.3PP | 48.63 | 3.94 | 8861.61 | 6.64 | 5845.8 | 187 | 198 | 3806.12 | 4030.01 |
| 5 | 75NA-0.1PP-25RA | 49 | 3.81 | 6309.02 | 4.73 | 2465.29 | 137 | 144 | 2788.44 | 2930.91 |
| 6 | 75NA-0.2PP-25RA | 50.2 | 4.02 | 5575.93 | 4.18 | 3032.77 | 148 | 159 | 3012.33 | 3236.22 |
| 7 | 75NA-0.3PP-25RA | 48.27 | 3.56 | 6476.60 | 4.85 | 4275 | 159 | 171 | 3236.22 | 3480.46 |
| 8 | 50NA-0.1PP-50RA | 40.1 | 3.66 | 5855.21 | 4.39 | 2302.31 | 122 | 128 | 2483.13 | 2605.25 |
| 9 | 50NA-0.2PP-50RA | 42.2 | 3.01 | 5735.17 | 4.30 | 2886.6 | 128 | 141 | 2605.25 | 2869.85 |
| 10 | 50NA-0.3PP-50RA | 42.73 | 3.45 | 9795.63 | 7.34 | 5223.28 | 133 | 141 | 2707.02 | 2869.85 |
| 11 | 25NA-0.1PP-75RA | 33.4 | 2.88 | 6987.29 | 5.24 | 2110.45 | 90 | 97 | 1831.82 | 1974.29 |
| 12 | 25NA-0.2PP-75RA | 35 | 2.92 | 7692.6 | 5.76 | 2876.89 | 103 | 114 | 2096.41 | 2320.30 |
| 13 | 25NA-0.3PP-75RA | 36.73 | 2.70 | 8867.92 | 6.65 | 4429.78 | 115 | 128 | 2340.66 | 2605.25 |
| 14 | 0.1PP-100RA | 22.03 | 1.98 | 6081.38 | 4.56 | 1695.68 | 75 | 81 | 1526.51 | 1648.64 |
| 15 | 0.2PP-100RA | 28.7 | 2.55 | 5636.55 | 4.22 | 1548 | 89 | 101 | 1811.46 | 2055.71 |
| 16 | 0.3PP-100RA | 35.57 | 3.19 | 6769.78 | 5.07 | 1627.65 | 108 | 122 | 2198.18 | 2483.13 |
| 17 | 75NA-25RA | 46.75 | 3.76 | 8697.55 | 6.52 | 2529.28 | 116 | 126 | 2361.01 | 2564.55 |
| 18 | 50NA-50RA | 41.33 | 3.15 | 8731.11 | 6.54 | 1975.75 | 101 | 108 | 2055.71 | 2198.18 |
| 19 | 25NA-75RA | 34.65 | 2.62 | 6977.26 | 5.23 | 1866.68 | 88 | 92 | 1791.11 | 1872.53 |
| 20 | 100RA | 26.72 | 1.84 | 5588.99 | 4.19 | 1661.01 | 52 | 55 | 1058.38 | 1119.44 |

3.2.1. Compressive strength

As previously mentioned, Compressive strength test for different ratios 0, 25, 50, 75 and 100 percent replacement of recycled coarse and fine aggregate with natural coarse and fine aggregate and polypropylene fibers with proportions 0.1, 0.2 and 0.3 by volume percent of concrete was applied to 100×100×100 mm cube specimens. This device is compressive the type of hydraulic and has a capacity of 300 tons. The results are presented in Table 4 and Fig. 5a.

Similar to the results of the reference of [36], in this study can also be said In general, increasing the percentage of RAs are causing reduce the compressive strength of concrete. Also, using the fibers in SCC to a certain amount can improve the compressive strength. The reason for this increase could be the reduction of fine-grained concrete in the concrete transfer area. Adding a lot of polypropylene fibers in SCC cause reduce the strength of specimens because were many fibers efficiencies and the flow of SCC was reduced and causing the remaining amount of air in the concrete to increase. So this reason will reduce the strength of the concrete.

According to the Table 4 and Fig. 5a, increasing the use of recycled aggregates as coarse and fine in new concrete, decreasing in the compressive strength of the specimens is observed. So that in the mixes number 17 to 20 containing 0 %, 25 %, 50 %, 75 % and 100 % RA respectively, causing reduced of the strength 9.22 %, 19.75 %, 32.72 % and 48.12 % to comparing with mix number 1 which contain 100 % NA. The reason for this reduce less resistance RAs than to NAs, first of all, is in during mixing the weakest parts of concrete into smaller pieces, to this case increases the fine aggregate (FA) in the concrete mixture, finally the concrete strength to drop. The other one, old mortars stick to RAs that have less resistance than to NAs, to this issue reduces the compressive strength of concrete containing RAs. This result indicates that if choosing reference concrete with high resistance, the possibility of manufacturing recycled concrete with a complete replacement of RA in a way resistance is a desirable level, so it is easily accessible. The results in Table 4 and Fig. 5a, are shown in mixes are contains 100 % and 75 % NA (mixes number 1 to 7) presence of fibers until 0.2 % can improve the compressive strength of concrete. While the percentage of fibers reached to 0.3 %, we are confronted to drop of the resistance which reason of this drop of the resistance can reduce efficiency and flow of SCC due to a lot of addition the polypropylene fibers can increase the remaining amount of air into the concrete and causes the drop of the resistance. In the mixes that include NAs less than 50 %

(mixes number 8 to 20) their compressive strength in mixes containing 0.1 % polypropylene fibers (mixes number 8, 11 and 14) than to mix lack of fibers with that corresponding (mixes number 18, 19 and 20) are lower. While in the mixes containing 0.2 % and 0.3 % polypropylene fibers (mixes number 9, 10, 12, 13, 15 and 16) than to the mix lack of fibers with that corresponding (mixes number 18, 19 and 20) polypropylene fibers compensate for the lost compressive strength by RAs.

3.2.2. Tensile strength

The Tensile strength results of mixtures composition, manufacturing with different percentages of recycled fine and coarse aggregate and polypropylene fiber are depicted in Table 4 and Fig. 5b.

The results are shown as totally in all mixes using fiber can cause improve the tensile strength of specimens and tensile strength of all mixes include fiber are higher than the other mixes lack of fiber. This finding is consistent with the results of the reference of [37]. Although, the increasing of the RA causes the decrease of tensile strength, which has the highest drop is relatives to the mixed number 20 it is containing 100 % RA and this drop than to mix number 1 which contains 100 % NA it is equal to 41.96 %. As can be seen, the best tensile strength was when used fiber 0.2 % by volume of concrete, but in the presence of 0.3 % fiber has little effect on the tensile strength and cause slightly reduced in tensile strength. So, in the mixed number 3, which contains 100 % NA and 0.2 % by volume of concrete is fiber it can improve the tensile strength about 21 % than to mix number 1 which has only NA. What can happen, when the increase the tensile strength is due to the use of polypropylene fibers can be explained the fiber when spread between the split sections of the concrete matrix, can withstand a greater tensile strain through the transfer of tensions from a concrete matrix to the fiber. As a result, an increase in tensile strength is observed. The appropriate spread of polypropylene fiber in the concrete matrix can be another reason for more load tolerance.

3.2.3. Flexural strength

A flexural strength test was performed to determine the rupture modulus of concrete in three point bending method on prismatic beams specimens of 100x100x500 mm. The results on the flexural strength of the mixture composition made with different percentages of replacement of the recycled fine and coarse aggregate and polypropylene fibers are shown in Table 4 and Fig. 5c.

The results of the flexural strength are shown with increasing the proportion of RAs in new concrete the flexural strength concrete up to 45 % decrease. Similar to the results of the reference of [34], when adding fiber to the concrete, it is possible to achieve the concrete with a higher flexural strength than reference concrete .Therefore, the effect of these fibers will be investigated by adding different percentages of polypropylene fibers. The presence of fibers in mixes containing 100 % NAs until to 0.2 % by volume of concrete respectively, causing increases the flexural strength up to 12.25 % compared to non-fibers. However, the presence of 0.3 % , by volume, of fiber cause the flexural strength is reduced 12.52 % than to the mix lack of fiber.

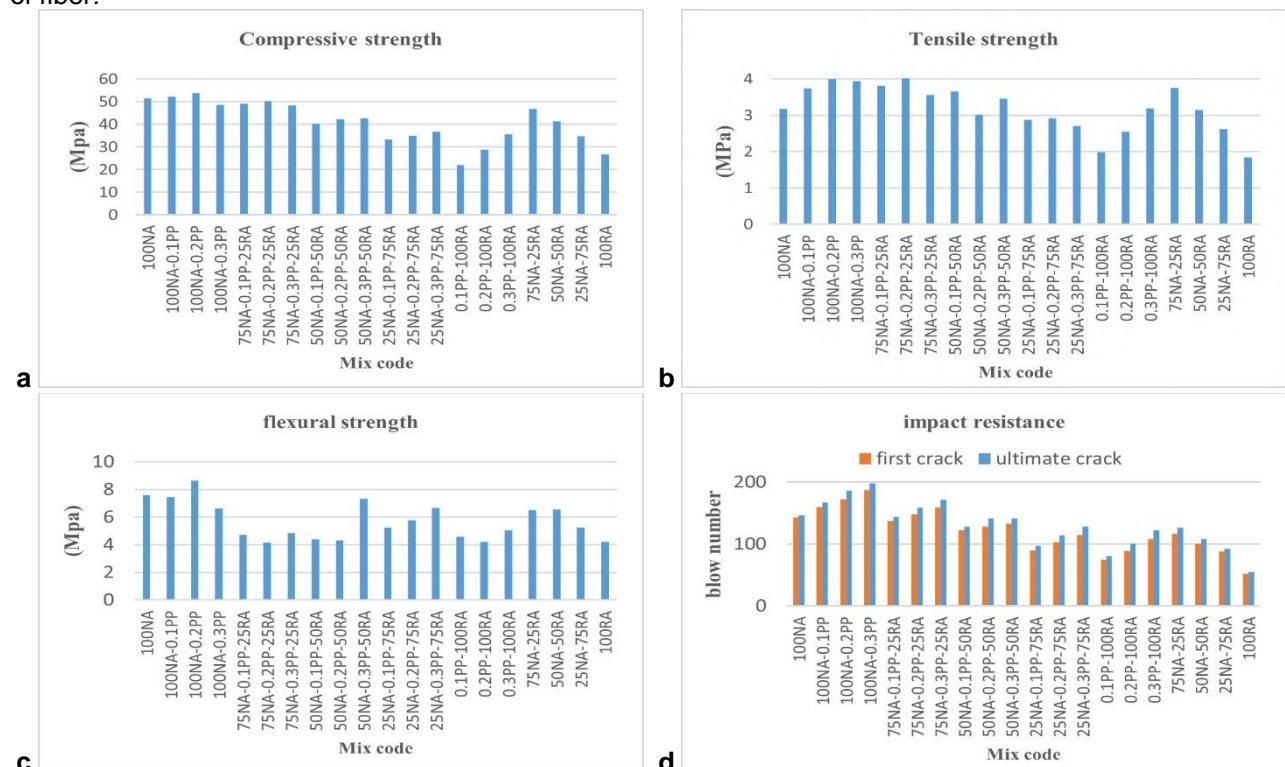


Figure 5. Effect of different fiber and recycled aggregate percentages contents on: a) Compressive strength; b) Tensile strength; c) flexural strength; d) impact resistance.

Unlike the concrete lack of fiber, concrete containing fiber is not broken immediately after the first crack and its tolerance the load of the fiber and can cause energy absorption. This point is confirmed in the results of the flexural strength test of this study. Even in cases, flexural strength was reduced than to concrete lack of fiber, the amount of specimen energy absorption was more after the first crack. The flexural durability is shown below the surface curved of load-displacement. The other hand the most important effect of the fiber in the concrete is the increase in the ductility and energy absorption, it is necessary to measure flexural durability. For this purpose, in this study concrete prismatic beams specimens with dimensions of 100×100×500 mm at the age of 28 days were tested for flexural and load–displacement chart was drawn for them. Fig. 6 Show the results of the flexural test for mixture's containing 0, 25, 50, 75 and 100 percent replacement of RAs with NAs along with 0.1 % , 0.2 % and 0.3 % by volume of polypropylene fiber.

The total stored and released energy in the element can be obtained by calculating the area under the load-displacement charts. The total energy absorption by each of the beams is presented in Table 4.

Overall, the use of fibers has increased the energy absorption of the beam. So, using 0.1 % , 0.2 % and 0.3 % polypropylene fibers in mixes containing 100 % NA (mixes number 2, 3 and 4), the energy absorption than the lack of fibers mix (mix number 1), respectively 44.4 %, 111.1 %, and 126.1 % are increasing. The percentage of energy absorption with the presence of the percentage of different fiber and RAs is variable so that the presence of RA is increasing; the percentage of energy absorption is decreasing.

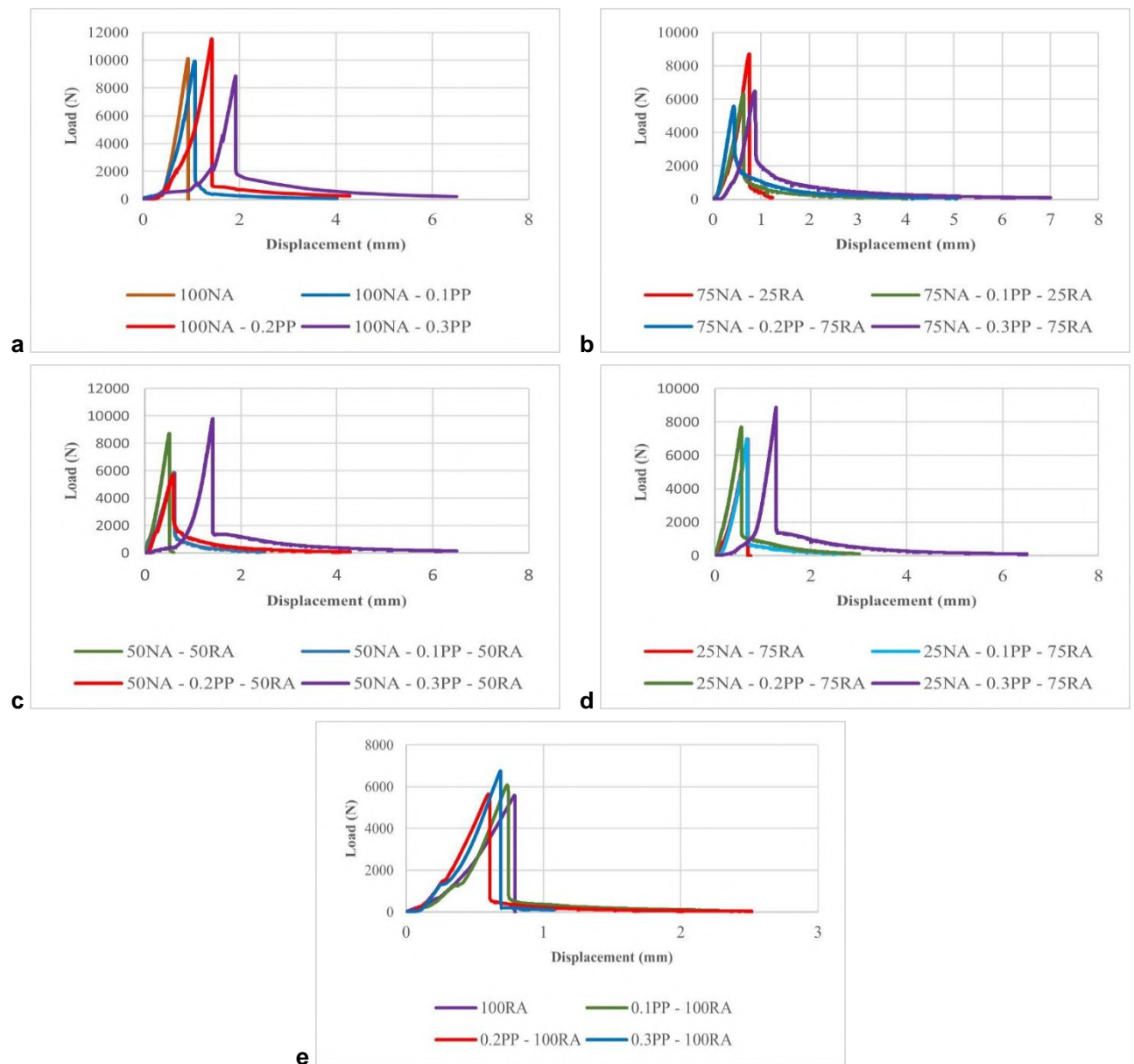


Figure 6. Load-displacement charts:

- a) SCC containing 100 % NAs and various percentages of polypropylene fibers;**
- b) SCC contains 75 % NA and 25 % RA and various percentages of polypropylene fibers;**
- c) SCC contains 50 % NA and 50 % RA and various percentages of polypropylene fibers;**
- d) SCC contains 25 % NA and 75 % RA and various percentages of polypropylene fibers;**
- e) SCC containing 100 % RA and various percentages of polypropylene fibers.**

According to the load-displacement diagrams, it is observed in all designs with increasing polypropylene fibers, surface below the curve and hence the energy absorption capacities of the specimens are increasing. Specimens lack of fiber, have more fragility behavior and effect of applied load and after reaching the final resistance specimen completely cracked and the resistance reaching to zero. But, in the specimens containing fiber, when the applied load reaches to the maximum value (load tolerance by section) the load capacity is not reached zero and the specimen will still be able to load tolerance. It should be noted that the higher presence of the percentage of fiber, the more energy absorption in specimens is observed.

3.2.4. Impact resistance

This test was done on the concrete shape disks specimens to diameter 150 and a height 65mm at the age of 28 days. The results test for the manufacturing of mixture composition with different percentages of recycled aggregate and polypropylene fiber is shown in Table 4 and Fig. 5d. As shown in Fig. 5d the effect of different percentages fiber and RA. Fiber improves the performance of concrete in this test. This is consistent with the results stated the reference of [30–33]. According to increasing 0.1 %, 0.2 % and 0.3 % polypropylene fiber in mixes include 100 % NA (mixes number 2, 3 and 4) compared to mix number 1 the lack of fiber increased by 11.88 %, 20.28 %, and 30.77 % respectively of the impact resistance against the first crack. While recycled aggregate causing reduces the concrete impact resistance against to the first crack. So that replaced by 25 %, 50 %, 75 % and 100 % RA (mixes number 17, 18, 19 and 20) instead of NA (mix number 1) in the mixes lack of fiber, respectively 18.88 %, 29.37 %, 38.46 %, and 63.63 % were decreased impact resistance against the first crack.

4. Conclusion

1. The test results of the flow slump are shown, with the increase of recycled aggregate, flow slump is decreased slightly while adding the fibers causing to the flow slump decreased rapidly.
2. The presence of the 0.3 % polypropylene fibers in mixes has to lead the steep drop of the flow slump, so it can be said that none of them not including in the categories of self-compacting concrete. Hence, the presence of polypropylene fibers until to 0.2 % in the mixes is allowed (for cement consumption: 450 kg/cm³).
3. The processing of decreasing the passing ability and filling ability self-compacting concrete in the other concrete fresh state test is slightly change confirmed.
4. By increasing the use of recycled aggregate in new concrete, it can be seen compressive strength, Tensile strength, flexural strength and impact resistance of the specimens are decreasing.
5. The using of the polypropylene fibers up to 0.2 % in the mixes containing 100 % natural aggregate causes to the slight increase of the compressive strength. While increasing 0.3 % of the fibers in the mixes, causing a decrease in the compressive strength of concrete.
6. Using 0.1 % of polypropylene fibers have not more effect on the compressive strength in different percentages of recycled aggregate. While in the mixes including 0.2 % and 0.3 % polypropylene fibers with the presence of 25, 50, 75 and 100 % recycled aggregate causes to increase the compressive strength. In other words, the fibers can to some extent compensate the drop of strength from the presence of recycled aggregates.
7. Totally, the presence of the polypropylene fibers causes the increase in the tensile strength of concrete. With the increase, the polypropylene fibers up to 0.2 % are significantly increased.
8. With the increasing by volume of percentage the polypropylene fibers in the mixes including recycled aggregates, the flexural strength of concrete were decreased. The specimens that have a lack of the fibers are fragile behavior and in the effect of applied load and after reaching the maximum resistance and the whole section are surrendered. While in the specimens containing polypropylene fibers after the applied load reaches to the maximum value load tolerance by section suddenly not surrender and the specimen will still be able to load tolerance.
9. By investigation, the load-displacement charts, it can be seen the presence of polypropylene fibers generally improves the energy absorption.
10. Using the polypropylene fibers has changed the specimen failure from Fragile to gradual failure.
11. Generally, it can be said that the presence of 25 % recycled aggregate; there was no significant drop in tests. It can easily good replacement for natural aggregate and at the same time causes less environmental degradation.
12. As the results of this study show, the presence of fibers improves the mechanical properties of concrete. This is similar to the results of other researchers.

References

1. Okamura, H. Self-Compacting High-performance Concrete. *Concrete International*. 1997. 19(7). Pp. 50–54.
2. EFNARC. Specification and Guidelines for Self-Compacting Concrete. European federation of specialist construction chemicals and concrete systems. 2002. 32 p.
3. Okamura, H., Ouchi, M. Self-compacting concrete. *Journal of Advanced Concrete Technology*. 2003. 1(1). Pp. 5–15. <https://doi.org/10.3151/jact.1.5>
4. De Larrard, F., Ferraris, C.F., Sedran, T. Fresh concrete: a Herchel–Bukley material. *Materials and Structures*. 1998. 31(7). Pp. 494–498. <https://doi.org/10.1007/BF02480474>
5. Rao, A., Jha, K.N., Misra, S. Use of aggregates from recycled construction and demolition waste in concrete. *Conservation and Recycling*. 2006. No. 50. Pp. 71–81. <https://doi.org/10.1016/j.resconrec.2006.05.010>
6. Alaejos, P. G., Sanchez, M. J. Utilization of recycled concrete aggregate for structural concrete. *International Rilem conference on the use of recycled materials in building and structures*. Amsterdam, 2004. Vol. 2. Pp. 693–702. DOI: 10.1617/2912143756.077
7. Poon, C.S., Shui, Z.H., Lam, L., Fok, H., Kou, S.C. Influence of moisture states of natural and recycled aggregates on the slump and compressive strength of concrete. *Cement and Concrete Research*. 2004. 34(1). Pp. 31–36. DOI: 10.1016/S0008-8846(03)00186-8
8. Levy, S.M., Helene, P. Durability of recycled aggregates concrete: a safe way to sustainable development. *Cement and Concrete Research*. 2004. 34(11). Pp. 1975–1980. DOI: 10.1016/j.cemconres.2004.02.009
9. Sagoe-Crentsil, K.K., Brown, T., Taylor, A.H. Performance of concrete made with commercially produced coarse recycled concrete aggregate. *Cement and Concrete Research*. 2001. 31(5). Pp. 707–712. DOI: 10.1016/S0008-8846(00)00476-2
10. Kou, S.C., Poon, C.S. Properties of self-compacting concrete, prepared with coarse and fine recycled concrete aggregates. *Cement and Concrete Composites*. 2009. 31(9). Pp. 622–627. <https://doi.org/10.1016/j.cemconcomp.2009.06.005>
11. Limbachiya, M.C., Leelawat, T., Dhir, R.K. Use of recycled concrete aggregate in high-strength concrete. *Materials and Structures*. 2000. 33(9). Pp. 574–580. <https://doi.org/10.1007/BF02480538>
12. Poon, C.S., Kou, S.C., Lam, L. Influence of recycled aggregate on slump and bleeding of fresh concrete. *Materials and Structures*. 2007. No. 40. Pp. 981–988. <https://doi.org/10.1617/s11527-006-9192-y>
13. Marinković, S., Radonjanin, V., Malešev, M., Ignjatović, I. Comparative environmental assessment of natural and recycled aggregate concrete. *Waste Management*. 2010. 30(11). Pp. 2255–2264. DOI: 10.1016/j.wasman.2010.04.012
14. Safiuddin, M., Alengaram, U.J., Salam, M.A., Jumaat, M.Z., Jaafar, F.F., Saad, H.B. Properties of high-workability concrete with recycled concrete aggregate. *Materials Research*. 2011. 14(2), Pp. 248–255. <http://eprints.um.edu.my/id/eprint/5937>
15. Sami, A.S., Tabsh, A.W. Influence of recycled concrete aggregates on strength properties of concrete. *Construction and Building Materials*. 2009. 23(2), Pp. 1163–1167. DOI: 10.1016/j.conbuildmat.2008.06.007
16. Etxeberria, M., Marí, A.R., Vázquez, E. Recycled aggregate concrete as a structural material. *Materials and Structures*. 2007. 40(5). Pp. 529–541. <https://doi.org/10.1617/s11527-006-9161-5>
17. Farzam, M. Investigating the Effect of Recycled aggregates on concrete performance. *Iranian Concrete Association – 6th Annual Iranian Concrete Conference*. Tehran, 2014.
18. Solyman, M. Classification of recycled sands and their applications as fine aggregates for concrete and bituminous mixtures. Ph.D. Dissertation. Kassel, 2005.
19. Marie, L., Quiasrawi, H. Closed-loop recycling of recycled concrete aggregates. *Journal of Cleaner Production*. 2012. No. 37. Pp. 243–248. DOI: 10.1016/j.jclepro.2012.07.020
20. Gomez Soberon, J.M.V. Porosity of Recycled Concrete with Substitution of Recycled Concrete Aggregate—An Experimental Study. *Cement and Concrete Research*. 2002. 32(8). Pp. 1301–1311. DOI: 10.1016/S0008-8846(02)00795-0
21. Zaharieva, R., Buyle-Bodin, F., Skoczylas, F., Wirquin, E. Assessment of the surface permeation properties of recycled aggregate concrete. *Cement and Concrete Composites*. 2003. 25(2). Pp. 223–232. DOI: 10.1016/S0958-9465(02)00010-0
22. Sani, D., Moriconi, G., Fava, G., Corinaldesi, V. Leaching and mechanical behavior of concrete manufactured with recycled aggregates. *Waste Management*. 2005. 25(2). Pp. 177–182. DOI: 10.1016/j.wasman.2004.12.006
23. Khayat, K.H., Roussel, Y. Testing and performance of fiber-reinforced, self-consolidating concrete. *Materials and Structures*. 2000. No. 33. Pp. 391–397. <https://doi.org/10.1007/BF02479648>
24. Groth, P. The use of steel fibres in self-compacting concrete. *Proceedings of the first international RILEM symposium on self-compacting concrete*, Sweden: Stockholm, 1999. Pp. 497–507.
25. Sahmaran, M., Yurtseven, A., Yaman, O. Workability of hybrid fiber reinforced self-compacting concrete. *Building and Environment*. 2005. 40(12). Pp. 1672–1677. DOI: 10.1016/j.buildenv.2004.12.014
26. Mohr, B.J., Nanko, H., Kurtis, K.E. Durability of kraft pulp fiber cement composites to wet dry cycling. *Cement and Concrete Composites*. 2005. 27(4). Pp. 435–438. DOI: 10.1016/j.cemconcomp.2004.07.006
27. MacVicar, R., Matuana, L.M., Balatincez, J.J. Aging mechanisms in cellulose fiber reinforced cement composites. *Cement and Concrete Composites*. 1999. No. 40. Pp. 189–196. [https://doi.org/10.1016/S0958-9465\(98\)00050-X](https://doi.org/10.1016/S0958-9465(98)00050-X)
28. A.C. 544.1R-96. State-of-the-art report on fiber reinforced concrete, approved 2002.
29. Song, P.S., Wu, J.C., Hwang, S., Sheu, B.C. Statistical analysis of impact strength and strength reliability of steel polypropylene hybrid fiber reinforced concrete. *Construction and Building Materials*. 2005. 9(1). Pp. 1–9. DOI: 10.1016/j.conbuildmat.2004.05.002
30. Song, P.S., Wu, J.C., Hwang, S., Sheu, B.C. Assessment of statistical variations in impact resistance of high strength and high strength steel fiber reinforced concrete. *Cement and Concrete Research*. 2005. 35(2). Pp. 393–399. DOI: 10.1016/j.cemconres.2004.07.021
31. Nataraja, M.C., Dhang, N., Gupta, A.P. Statistical variations in impact resistance of steel fiber reinforced concrete subjected to drop weight test. *Cement and Concrete Research*. 1999. 29(7). Pp. 989–995. [https://doi.org/10.1016/S0008-8846\(99\)00052-6](https://doi.org/10.1016/S0008-8846(99)00052-6)
32. Badr, A., Ashour, A., Andrew KPlatten, A. Statistical variations in impact resistance of polypropylene fiber reinforced concrete. *International Journal of Impact Engineering*. 2006. 32(11). Pp. 1907–1920. <http://dx.doi.org/10.1016/j.ijimpeng.2005.05.003>
33. Qian, P., Stroeven, P. Development of Hybrid Polypropylene-Steel Fiber-Reinforced Concrete. *Cement and Concrete Research*. 2000. 30(1). Pp. 63–69. DOI: 10.1016/S0008-8846(99)00202-1

34. Ghernouti, Y., Rabehi, B., Bouziani, T., Ghezraoui, H., Makhloufi, A. Mechanical behavior of self-compacting concrete pavements incorporating recycled tire rubber crumb and reinforced with polypropylene fiber. *Construction and Building Materials*. 2015. 28(1). Pp. 89–100.
35. Hesami, S., Salehi Hikouei, I., Emadi, S.A.A. Mechanical behavior of self-compacting concrete pavements incorporating recycled tire rubber crumb and reinforced with polypropylene fiber. *Journal of Cleaner Production*. 2016. 133(1). Pp. 228–234. <https://doi.org/10.1016/j.jclepro.2016.04.079>
36. Fathi, H., Lameie, T., Maleki, M., Yazdani, R. Simultaneous effects of fiber and glass on the mechanical properties of self-compacting concrete. *Construction and Building Materials*. 2017. 133(15). Pp. 443–449. DOI: 10.1016/j.conbuildmat.2016.12.097
37. Mohseni, E., Saadati, R., Kordbacheh, N., Parpinchi, Z.A., Tang, W. Engineering and microstructural assessment of fibre-reinforced self-compacting concrete containing recycled coarse aggregate. *Journal of Cleaner Production*. 2017. 168(1). Pp. 605–613. <https://doi.org/10.1016/j.jclepro.2017.09.070>.
38. Aslani, F., Ma, G., Yim Wan, D.L., Tran Le, V.X. Experimental investigation into rubber granules and their effects on the fresh and hardened properties of self-compacting concrete. *Journal of Cleaner Production*. 2018. 172(20). Pp. 1835–1847.
39. Mahdikhani, M., Safiikhani, F. Rheological properties of self-consolidating concrete made by crushed waste tile aggregates. *Journal of Structural Engineering and Geotechnics*. 2018. 8(2). Pp. 1–12.
40. Pan, Z., Zhou, J., Jiang, X., Xu, Y., Jin, R., Zhuang, y., Diao, z., Zhang, s., Si, Q., Chen, W. Investigating the effects of steel slag powder on the properties of self-compacting concrete with recycled aggregates. *Construction and Building Materials*. 2019. 200(10). Pp. 570–577. <https://doi.org/10.1016/j.conbuildmat.2018.12.150>
41. Sasanipour, H., Aslani, F., Taherinezhad, J. Effect of silica fume on durability of self-compacting concrete made with waste recycled concrete aggregates. *Construction and Building Materials*. 2019. 227(10). <https://doi.org/10.1016/j.conbuildmat.2019.07.324>
42. Sadeghi-Nik, A., Berenjian, J., Alimohammadi, S., Lotfi-Omran, O., Sadeghi-Nik, A.D., Karimaei, M. The Effect of Recycled Concrete Aggregates and Metakaolin on the Mechanical Properties of Self-Compacting Concrete Containing Nanoparticles. *Iranian Journal of Science and Technology, Transactions of Civil Engineering*. 43(1). Pp. 605–613. <https://doi.org/10.1007/s40996-018-0182-4>.
43. B. 1881–116. Determination of compressive strength of concrete cubes. British Standards Institution, London, 2003.
44. C. 496. Standard Test Method for Splitting Tensile Strength of Cylindrical Concrete Specimens. ASTM International, West Conshohocken, PA, 2004.
45. C. 293. Standard Test Method for Flexural Strength of Concrete. ASTM International, West Conshohocken, PA, 2002.

Contacts:

Mohammad Hajmohammadian Baghban, mohammad.baghban@ntnu.no

Seyed Amir Hossein Hashemi, hashemi@qiau.ac.ir

Keyvan Kalbasi Anaraki, kayvan.kalbasi@gmail.com

Elahesadat Hashemi, Hashemi@raja.ac.ir



DOI: 10.18720/MCE.99.6

Mathematical model of concrete biological corrosion

S.V. Fedosov^a, S.A. Loginova^{ab}

^a National Research Moscow State Civil Engineering University, Moscow, Russia

^b Ivanovo State Polytechnic University, Ivanovo, Ivanovo Region, Russia

* E-mail: sl79066171227@yandex.ru

Keywords: cement, concrete, bio-corrosion, mathematical model, mass transfer, calcium hydroxide, microorganisms, biofilm.

Abstract. As objects for study samples of cement concrete exposed to biological growth-around have been used. A physical and mathematical model of diffusion processes in system "cement concrete-biofilm-liquid", taking into account the kinetics of the processes of growth, reproduction and death of microorganisms, has been developed. The model of mass transfer in an unlimited two-layer plate in the form of a system of partial differential equations of parabolic type with boundary conditions of the second kind at the boundary of concrete with liquid and the fourth kind at the boundary between concrete and biofilm is considered for the first time. The mathematical model takes into account the kinetics of the change in time of the thickness of the biofilm due to the birth and death of populations of microorganisms. The results of calculations of dimensionless concentrations of "free" calcium hydroxide by the thickness of a concrete structure and biofilm are presented. The results of the numerical experiment showing the influence of mass transfer criteria (Furier, Kirpichov) on the dynamics of corrosive destruction processes have been analyzed. With an increase in the mass transfer criteria of Kirpichov and Furier, large concentration gradients appear. It has been established that carrying out work on cleaning concrete and reinforced concrete underwater structures from biofouling once every 5 years, in conjunction with other scheduled preventive measures, will increase the time between repairs between 1.5 times. Practical recommendations were developed to monitor and increase the corrosion resistance of concrete and reinforced concrete structures in biologically active environments.

1. Introduction

Microbial destruction of concrete and reinforced concrete structures has increasingly attracted scientists' attention as a major problem related to structural integrity and durability of bridge constructions and different hydro facilities. Practically all building materials are subject to microbiological corrosion. It is estimated [1] that not less than 20 % of all corrosion damages are caused by activities of microorganisms.

An analysis of literary sources [2–8] has shown that to date, a large amount of scientific data on corrosion processes in concrete has been accumulated in building materials science: the basic schemes of chemical reactions have been established and investigated; mathematical descriptions of some corrosion processes are given; created a system of regulatory documents on corrosion protection. However, the process of concrete biocorrosion remains a poorly studied problem both in Russia and abroad [2–8]. Mathematical models to predict the durability of concrete structures with biological corrosion are completely absent [3, 5].

Prediction of wear of concrete and reinforced concrete structures resulted from corrosion is a complex task whose solution requires looking for new methods and approaches. It is appropriate to evaluate the effect of different exploitation conditions of a structure on its durability through mathematical modeling and conducting on its basis numerical experiments. The efficiency of methods of mathematical modeling as an integral part of successful predictions of premature wear of structures has been proven by high practical applicability of the obtained results [1–3].

The problem of exposure of underwater concrete and reinforced concrete structures to bio-growth-around is still burning. Although a variety of methods for protection from bio-growth-around are already applied, until now no efficient methods have been found [4, 6]. Traditional methods of corrosion prevention prove to be low-efficient as far as bio-corrosion is concerned.

Fedosov, S.V., Loginova, S.A. Mathematical model of concrete biological corrosion. Magazine of Civil Engineering. 2020. 99(7). Article No. 9906. DOI: 10.18720/MCE.99.6



This work is licensed under a CC BY-NC 4.0

Studies in the field of microbial influence on concrete [5, 7, 8] showed that microorganisms participating most frequently in bio-destruction of concrete include bacteria, cyanobacteria, fungi, seaweed and lichens. Their growth and development depend on composition, porosity, water resistance of material exposed to corrosive destruction as well as on environmental conditions [9]. The danger of microbiological corrosion is related to the fact that microorganisms tend to intensively multiply, easily adapt to changing physical and chemical conditions of the environment. It was found out that most of microbial activity proceeds on the concrete surface. The researchers note a logarithmic reduction of microbial populations with the depth of concrete due to the limited entrance of hydrogen sulfide and oxygen [6].

Bio-destruction of concrete structures contributes to the increase in concrete porosity and acceleration of diffusion processes in it which boosts corrosive processes. The main component that accelerates the general corrosion process in concrete is a mixture of organic acids ($C_6H_8O_7$, $C_4H_6O_5$, etc.), which is the product of the vital activity of microorganisms [7].

The aim of the study is to develop a physical and mathematical model of the diffusion process of the target component of "free" calcium hydroxide in the solid phase of cement concrete and in a biofilm formed by microorganisms in a liquid medium, which will allow solving the boundary-value problem of mass transfer in the system of "cement concrete – biofilm – liquid", which together will make it possible to develop a calculation method with the aim of monitoring the mass transfer processes in the field of monitoring the biodegradation of cement concrete in liquid media.

An integral part of mathematical modeling is conducting a numerical experiment with the purpose to establish the influence of mass transfer criteria of similarity (Furier, Kirpichov) on the dynamics of corrosive destruction processes.

2. Methods

As objects of the study of corrosive resistance sample cubes with 0.03 m brink made from Portland cement CEM I 42.5 N with 0.3 water/ cement ratio were used. The system under study was composed of tightly fitted plates with a size of 1×3×3 cm. After 28-day preliminary consolidation (consolidation conditions: temperature 20 +/- 2 °C and relative humidity 50–70 %) the samples were contaminated with microorganisms suspensions (*Aspergillus niger* van Tieghem, *Bacillus subtilis*) and were kept for 28 days in conditions optimal for their growth. After that the samples were immersed in water with 1000 cm² volume. As reactive medium for studies of corrosive processes distilled water (pH = 6.6) was used. Five surfaces of the studied system were isolated. Only one surface remained open for interaction with an aggressive liquid. After certain time intervals, the samples were taken out of the container and the content of Ca²⁺ ions was determined in each of the plate elements, as a result, the concentration distribution curves along the coordinate were built.

In this case, mass transfer processes from the point of view of mathematical formalization are presented as occurring in an unlimited plate. From an experimental point of view, this made it possible to solve not only the problem of studying the kinetics of processes in the liquid phase (determining the time variation of the concentration of Ca²⁺ ions), but also studying the dynamics of processes in the solid phase. Based on the data obtained, the coefficients of mass conductivity and external mass transfer were calculated.

3. Results and Discussion

While conducting experiments it was established that on the 28th day of keeping the samples in water, microorganisms form a biofilm (Fig. 1). Later a gradual increase of biomass takes place.



Figure 1. Pictures of the surface of the cement stone on the 28th day of the experiment.

Forming of biofilms as a rule starts with introducing bacterial cells into the substrate. The growth of heterotrophic organisms that follows is provided in this case due to metabolites of primary organisms and organic compounds from outside [6]. Biofilms change electro-chemical conditions along the border of the division of the phases "concrete – liquid" that bring about the corrosion [7].

With the beginning of mass transfer processes between the concrete and the liquid environment, the concentration of dissolved Ca(OH)_2 in concrete pores begins to decrease causing the dissolution of "free" calcium hydroxide crystals. A decrease in the content of calcium hydroxide as a result of "washing-out" it out of concrete leads to the decomposition of hydrosilicates, hydroaluminates and calcium hydroferrites, etc.

The size of the biofilm is essentially influenced by particularities of hydrodynamics of the liquid flow in the area of reinforced concrete support [1, 3]. It was [3] established that the size of biofilm thickness depends on the opposite processes of biomass birth and death. Kinetics of those processes, in its turn, depends on hydrodynamics of liquid stream flowing around bridge supports [4].

In case of biological corrosion, the proceeds of liquid corrosion are worsened by additional effect of microorganisms-destructors.

Fig. 2 shows physical and mathematical model of mass transfer process of "free" calcium hydroxide from solid phase (concrete) to liquid phase (water) with the account of the effect caused by microorganisms [2].

The system "cement concrete – biofilm – liquid" is represented by two unlimited plates being in touch. The concrete δ_1 thick is covered with biofilm δ_2 thick on the right side (Fig. 2). The task comes down to determining the changes in concentration of "free" calcium hydroxide for time (τ) by the thickness of the structure (x).

The presented physical and mathematical model of mass transfer in half-limited two-layered plate can be presented as differential equations with boundary conditions of second kind on the border between concrete and liquid and those of the fourth kind on the border between concrete and biofilm.

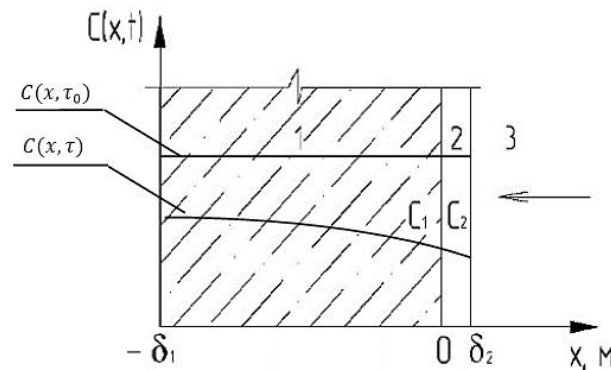


**Figure 2. Illustrates the model of concrete structure bio-growth-around:
(1) – concrete; (2) – biofilm; (3) – liquid.**

$$\frac{\partial C_1(x, \tau)}{\partial \tau} = k_1 \cdot \frac{\partial^2 C_1(x, \tau)}{\partial x^2}, \quad \tau > 0, -\delta_1 \leq x \leq 0, \quad (1)$$

$$\frac{\partial C_2(x, \tau)}{\partial \tau} = k_2 \cdot \frac{\partial^2 C_2(x, \tau)}{\partial x^2}, \quad \tau > 0, 0 \leq x \leq \delta_2. \quad (2)$$

where $C_1(x, \tau)$ is concentration of "free" calcium hydroxide in relation to CaO in concrete at the time moment at an arbitrary point with coordinate x , (kg CaO/ kg concrete); $C_2(x, \tau)$ is concentration of "free" calcium hydroxide in relation to CaO in biofilm at the time moment at an arbitrary point x , (kg CaO/ kg biomass); $k_{1,2}$ are coefficients of mass conductivity, m^2/s ; δ_1 is thickness of concrete structure, m; δ_2 thickness of biofilm, m.

Initial conditions:

$$C_1(x, \tau) \Big|_{\tau=0} = C_1(x, 0) = C_{1,0} \quad (3)$$

$$C_2(x, \tau) \Big|_{\tau=0} = C_2(x, 0) = C_{2,0} \quad (4)$$

where $C_{1,0}$ is initial concentration of "free" CaO, kg CaO/ kg concrete;

$C_{2,0}$ initial concentration of free CaO, kg CaO/ kg biomass.

Boundary conditions. Left:

$$\left. \frac{\partial C_1(x, \tau)}{\partial x} \right|_{x=-\delta_1} = 0. \quad (5)$$

At the point of contact of concrete and biofilm. The balance in the system follows the Henry law:

$$C_1(x, \tau) \Big|_{x=0} = m \cdot C_2(x, \tau) \Big|_{x=0}, \quad (6)$$

where m is Henry equilibrium constant, kg biofilm/ kg concrete.

$$-\rho_{con} \cdot k_1 \cdot \left. \frac{\partial C_1(x, \tau)}{\partial x} \right|_{x=0} = -\rho_{biom} \cdot k_2 \cdot \left. \frac{\partial C_2(x, \tau)}{\partial x} \right|_{x=0}, \quad (7)$$

where ρ_{con}, ρ_{biom} are densities of concrete and biomass, kg/m³.

On right:

$$-k_2 \cdot \left. \frac{\partial C_2(x, \tau)}{\partial x} \right|_{x=\frac{\delta_2}{\delta_1}} = q_H(\tau). \quad (8)$$

where $q_H(\tau)$ is density of mass flow leaving the biofilm for the liquid flow.

The system of equations (1) – (2) is of a linear type, coefficients of mass conductivity being variable values in common case and dependent on concentration are brought out of signs of mathematical differentiation operators. With the use of zonal method of calculation or "method of micro-processes" the whole process is divided into N elementary micro-processes, within each of which coefficients of mass conductivity are meant as constant. So the non-linear problem of mass transfer comes down to the totality of N linear problems.

Since on the left border of concrete structure there is no substance flow, the boundary condition (5) is represented as a condition of the second kind.

Boundary conditions (6) and (7) are conditions of the fourth kind and illustrate the fact that at the point of plates' contact the concentrations of "free" calcium hydroxide are equal and densities of mass flows are equal as well.

To solve the system (1) – (8) Laplas's method of integral transformations was used which got a good reputation while solving problems on heat mass transfer [10–13].

Mathematically the problem of mass transfer (1) – (8) in a dimensionless form can be presented as the following system of equations (9) – (16):

$$\frac{\partial Z_1(\bar{x}, Fo_m)}{\partial Fo_m} = \frac{\partial^2 Z_1(\bar{x}, Fo_m)}{\partial \bar{x}^2}, Fo_m > 0, -1 \leq \bar{x} \leq 0. \quad (9)$$

$$\frac{\partial Z_2(\bar{x}, Fo_m)}{\partial Fo_m} = \frac{\partial^2 Z_2(\bar{x}, Fo_m)}{\partial \bar{x}^2} \cdot K_k, Fo_m > 0, 0 \leq \bar{x} \leq K_\delta. \quad (10)$$

Initial conditions:

$$Z_1(\bar{x}, Fo_m) \Big|_{Fo_m=0} = Z_{1,0}(\bar{x}); \quad (11)$$

$$Z_2(\bar{x}, Fo_m) \Big|_{Fo_m=0} = Z_{2,0}(\bar{x}). \quad (12)$$

Boundary conditions:

$$\left. \frac{\partial Z_1(\bar{x}, Fo_m)}{\partial \bar{x}} \right|_{\bar{x}=-1} = 0, \quad (13)$$

$$Z_1(\bar{x}, Fo_m)|_{\bar{x}=0} = Z_2(\bar{x}, Fo_m)|_{\bar{x}=0}, \quad (14)$$

$$\frac{\partial Z_1(\bar{x}, Fo_m)}{\partial \bar{x}}|_{\bar{x}=0} = N \cdot \frac{\partial Z_2(\bar{x}, Fo_m)}{\partial \bar{x}}|_{\bar{x}=0}, \quad (15)$$

$$\frac{\partial Z_2(\bar{x}, Fo_m)}{\partial \bar{x}}|_{\bar{x}=K\delta} = Ki_H^*, \quad (16)$$

where $Z_1(\bar{x}, Fo_m)$ is dimensionless concentration of the transferred component by the thickness of concrete; $Z_2(\bar{x}, Fo_m)$ is dimensionless concentration of the transferred component by the thickness of biofilm; $\bar{x} = x / \delta_1$ is dimensionless coordinate; $K_k = k_2 / k_1$; $K_\delta = \delta_2 / \delta_1$; q_H are density of mass flow leaving the biofilm for liquid flow; m is Henry' s constant (kg biofilm/ kg concrete); $N = (\rho_{biom} \cdot k_2) / (\rho_{con} \cdot k_1 \cdot m)$ is coefficient considering characteristics of phases; $Fo_m = (k_1 \cdot \tau) / \delta_1^2$ is Fourier criterion;

$Ki_H^* = \frac{q_H \cdot \rho_{con} \cdot m \cdot K_\delta}{\delta_2 \cdot \rho_{biom} \cdot k_2 \cdot C_0}$ is Kirpichov's mass transfer criterion.

It is possible to take into account the complex mechanism of growth, reproduction, and death of microorganisms by introducing the coefficient N , which takes into account changes in the biomass density.

Kinetic equations describing the growth, reproduction and death of microorganisms, taking into account natural mortality, taking into account the stochastic nature of these processes, for a system of isolated cells can be represented as [13, 14]:

$$\frac{dm}{dt} = \mu(t)m = U_1(m, C), \quad (17)$$

$$\frac{dm}{dt} = \beta S(t)\psi(t) = U_2(m, C), \quad (18)$$

where $m(t)$ is the mass of an individual cell at time t (m is a determinate value); t is the cell division time; $U_{1,2}(m, C)$ is cell growth rate; C is the concentration of the substrate; β is the mass transfer coefficient; $\beta = D_M/d$, D_M is the molecular diffusion coefficient depending on the temperature of the culture fluid; d is the thickness of the "boundary film", depending on the hydrodynamic situation in the vicinity of the cell; $S(t)$ the outer surface of the cell at time t .

After system of equations (9) – (16) was transferred in the area of complex numbers where the solution of the system was obtained and then the solution was transferred in the area of the originals. The general solution of the mass conductivity problem describing the dynamics of concentration fields looks as follows:

$$Z_1(\bar{x}, Fo_m) = \frac{1}{1 + NK_k K_\delta} \left\{ 1 - NK_\delta + NKi_H^* \left[Fo_m + \frac{(1 - \bar{x})^2}{2} + \phi(K_k, N, K_\delta) \right] \right\} +$$

$$+ 2 \sum_{n=1}^{\infty} \frac{1}{\mu_n^2 \psi_1'(\mu_n)} (\mu_n \sin \mu_n \left[\cos(\mu_n \bar{x}) \cos(\mu_n \sqrt{K_k} K_\delta) - \sqrt{K_k} K_\delta \sin(\mu_n \bar{x}) \sin(\mu_n \sqrt{K_k} K_\delta) \right] -$$

$$- \frac{N}{\sqrt{K_k}} \cos(\mu_n (1 + \bar{x})) \exp(-\mu_n^2 Fo_m).$$

$$Z_2(\bar{x}, Fo_m) = \frac{1}{1 + NK_k K_\delta} (1 - NK_\delta + Ki_H^* [\bar{x} - Fo_m K_k, K_\delta] + NKi_H^* (\phi(K_k, N, K_\delta) -$$

$$- \frac{1 + K_k \bar{x}^2}{2}) - 2 \sum_{m=1}^{\infty} \frac{J}{\mu_m^2 \psi_1'(\mu_m)} (\mu_m \sin \mu_m \cos [\mu_m \sqrt{K_k} (K_\delta - \bar{x})] -$$

$$- \frac{\mu_m}{\sqrt{K_k}} \sin(\mu_m \sqrt{K_k} K_\delta) \left[N \cos \mu_m \cos(\mu_m \sqrt{K_k} \bar{x}) + \frac{J}{\sqrt{K_k}} \sin \mu_m \sin(\mu_m \sqrt{K_k} \bar{x}) \right] +$$

$$+ Ki_H^* \left[N \cos \mu_m \cos(\mu_m \sqrt{K_k} \bar{x}) + \frac{1}{\sqrt{K_k}} \sin \mu_m \sin(\mu_m \sqrt{K_k} \bar{x}) \right] \exp(-\mu_m^2 K_k Fo_m), \quad (20)$$

where μ_m is roots of characteristic equation:

$$\phi(K_k, N, K_\delta) = \frac{1 + K_k K_\delta (3K_\delta + 3N + NK_k K_\delta^2)}{6(1 + NK_k K_\delta)}, J = \int_0^1 Z_{1,0}(\xi) \cos[\mu_m(1 - \xi)] d\xi, \quad (21)$$

$$tg \mu_m = N \sqrt{K_k} tg(\mu_m \sqrt{K_k} K_\delta).$$

The expressions (19) and (20) make it possible to calculate the dynamics of mass transfer of the target component of the structure's inner layers towards the border of the division of the phases (concrete/ biofilm) [15, 16].

Table 1. The change in the values of the concentration of "free" calcium hydroxide in the solution of the pores of the sample from time to time and coordinates.

| Time | Concentration, $\text{kg}_{\text{CaO}}/\text{kg}_{\text{bet}} \cdot 10^4$ at the point with the coordinate | | | | | |
|-----------------|--|-------------------------|-------------------------|-------------------------|-------------------------|-------------------------|
| | Experimental values | | | Estimated Values | | |
| | $x_1 = 0.005 \text{ m}$ | $x_2 = 0.015 \text{ m}$ | $x_3 = 0.025 \text{ m}$ | $x_1 = 0.005 \text{ m}$ | $x_2 = 0.015 \text{ m}$ | $x_3 = 0.025 \text{ m}$ |
| 1 T_1 14 days | 2.47 | 2.23 | 1.93 | 2.52 | 2.29 | 1.99 |
| 2 T_2 28 days | 2.38 | 1.98 | 1.76 | 2.42 | 2.01 | 1.79 |
| 3 T_3 42 days | 2.16 | 1.81 | 1.48 | 2.26 | 1.97 | 1.62 |
| 4 T_4 56 days | 1.88 | 1.53 | 1.23 | 2.01 | 1.67 | 1.39 |
| 5 T_5 70 days | 1.68 | 1.45 | 1.20 | 1.81 | 1.53 | 1.25 |

For the evaluation of the influence of mass transfer parameters, a numerical experiment was conducted illustrating the influence of similarity criteria (Furier, Kirpichov) on the dynamics of corrosive destruction process [17].

Fig. 3 illustrates the dependence of dimensionless concentrations on Kirpichov's mass transfer criterion. It was established that with the increase in Kirpichov's mass transfer criterion large gradients of concentration appear. Curves (picture 4) illustrate the dynamics of dimensionless concentrations of the transferred component with different values of Furier mass transfer criterion.

The obtained dependencies make it possible to solve the reverse problem when the available experimental data allow with the help of this model to predict the numerical value of "free" calcium hydroxide by the thickness of the structure and the film [13, 16, 18].

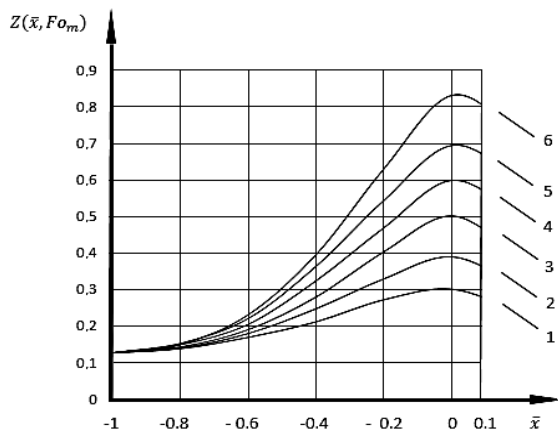


Figure 3. Profiles of dimensionless concentrations by the thickness of concrete and biofilm with

$K_k = 1; K_\delta = 0.1; N = 1; Fo_m = 1$ and different values Ki_H^* : 1 – 0.5; 2 – 1; 3 – 1.5; 4 – 2; 5 – 2.5; 6 – 3.

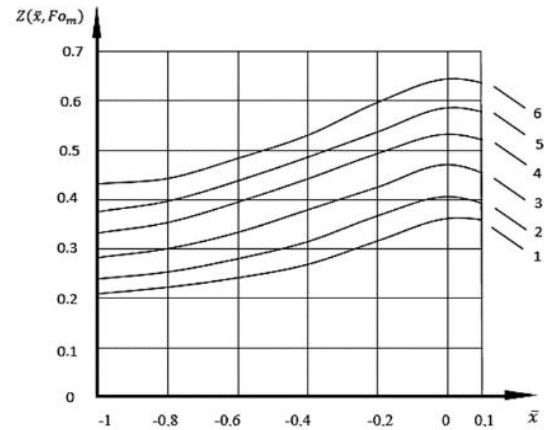


Figure 4. Profiles of dimensionless concentrations by thickness of concrete and biofilm with $K_k = 1; K_\delta = 0.1; N = 1; Ki_H^* = 0.5$ and different values Fo_m : 1 – 0.5; 2 – 1; 3 – 1.5; 4 – 2; 5 – 2.5; 6 – 3.

The results of mathematical modeling are confirmed by the results of experimental studies of concrete biocorrosion of the scientific school of Professor V.T. Erofeeva [8]. The obtained expressions allow to determine concentration values of the transferred component by thickness of both the concrete structure, and in the biofilm itself at any period of time, and also make it possible to calculate concentration of "free" calcium hydroxide in liquid phase, the kinetics of the process in solid, liquid phases and in biofilm which eventually allows with minimal error to predict durability and reliability of building structures [19–23]. However, those calculations are possible only with availability of objective information about characteristics of mass transfer – coefficients of mass conductivity and mass giving away of particular corrosive processes that can be obtained in the course of experimental studies.

Based on the results of mathematical modeling, practical recommendations were developed to monitor and increase the corrosion resistance of concrete and reinforced concrete structures in biologically active environments, which were used during the industrial examination of LLC «Basic Engineering» (Ivanovo, Russia) [24]. The economic effect amounted to 8.9 % of the estimated cost of work.

In the future, the generality of the mathematical description will make it possible to disseminate the developed mathematical model and the proposed calculation method for various types of concrete biocorrosion, taking into account experimentally determined mass transfer coefficients depending on the taxonomic composition of biofouling.

4. Conclusion

1. A physical and mathematical model of diffusion process of target component of “free” calcium hydroxide in solid phase of cement concrete and biofilm formed in liquid medium has been developed which allows to obtain a solution of the boundary problem of mass transfer in the system “cement concrete – biofilm – liquid” which in totality makes it possible to monitor the processes of mass transfer in the field of controlling bio-destruction of cement concretes.

2. A numerical experiment has been conducted to illustrate the influence of similarity criteria (Furier, Kirpichov) on the intensity of the process of corrosive mass transfer. With an increase in the mass transfer criteria of Kirpichov and Furier, large concentration gradients appear.

3. Practical recommendations were developed and implemented to monitor and increase the corrosion resistance of concrete and reinforced concrete structures in biologically active environments. It has been established that carrying out work on cleaning concrete and reinforced concrete underwater structures from biofouling once every 5 years, in conjunction with other scheduled preventive measures, will increase the time between repairs between 1.5 times. The economic effect was 8–15 % of the estimated cost of work.

4. Since abiotic environmental factors change over time, only the joint application of the obtained solutions using the zonal calculation method will allow continuous monitoring of bio-corrosion damage and manage them in the field of scheduled preventive repairs.

References

1. Tsvivilis, S., Batis, G., Chaniotakis, E., Grigoriadis, G., Theodossis, D. Properties and behavior of limestone cement concrete and mortar. *Cement and Concrete Research*. 2000. 30. Pp. 1679–1683. DOI: 10.1016/S0008-8846(00)00372-0
2. Levandovskiy, A.N., Melnikov, B.E., Shamkin, A.A. Modeling of porous material fracture. *Magazine of Civil Engineering*. 2017. 69(1). Pp. 3–22. DOI: 10.18720/MCE.69.1
3. Travush, V.I., Karpenko, N.I., Erofeev, V.T., Rodin, A.I., Smirnov, V.F., Rodina, N.G. Development of Biocidal Cements for Buildings and Structures with Biologically Active Environments. *Power Technology and Engineering*. 2017. 4(51). Pp. 377–384. DOI: 10.1007/s10749-017-0842-8
4. Newale, R., Sartape, Y., Ramane, A., Telrandhe, S., Vairal, S., Girish, J. Structural Audit, Repair and Rehabilitation of Building. *International Journal of Innovative Research in Science*. 2017. 6(3). Pp. 4679–4693. DOI: 10.15680/IJRSET.2017.0603255
5. Selyaev, V.P., Neverov, V.A., Selyaev, P. V., Sorokin, E. V., Yudina, O.A. Predicting the durability of concrete structures, including sulfate corrosion of concrete. *Magazine of Civil Engineering*. 2014. 1(45). Pp. 41–52. DOI: 10.5862/MCE.45.5
6. Pepe, O., Sannino, L., Palomba, S., Anastasio, M., Blaiotta, G., Villani, F., Moschetti, G. Heterotrophic microorganisms in deteriorated medieval wall paintings in southern Italian churches. *Microbiological Research*. 2010. 165(1). Pp. 21–32. DOI: 10.1016/j.micres.2008.03.005
7. Han, F., Zhang, Z. Hydration, mechanical properties and durability of high-strength concrete under different curing conditions. *Journal of Thermal Analysis and Calorimetry*. 2018. 132. Pp. 823–834. DOI: 10.1007/s10973-018-7007-3
8. Erofeev, V., Rodin, A., Rodina, N., Kalashnikov, V., Irina, E. Biocidal Binders for the Concretes of Unerground Constructions. *Procedia Engineering*. 2016. 165. Pp. 1448–1454. DOI: 10.1016/j.proeng.2016.11.878
9. Brenna, A., Bolzoni, F., Beretta, S., Ormellese, M. Long-term chloride-induced corrosion monitoring of reinforced concrete coated with commercial polymer-modified mortar and polymeric coatings. *Construction and Building Materials*. 2013. 48. Pp. 734–744. DOI: 10.1016/j.conbuildmat.2013.07.099
10. Patel, R.A., Perko, J., Jacques, D., De Schutter, G., Ye, G., Van Bruegel, K. Effective diffusivity of cement pastes from virtual microstructures: Role of gel porosity and capillary pore percolation. *Construction and Building Materials*. 2018. 165. Pp. 833–845. DOI: 10.1016/j.conbuildmat.2018.01.010
11. Kolchunov, V.I., Dem'yanov, A.I. The modeling method of discrete cracks in reinforced concrete under the torsion with bending. *Magazine of Civil Engineering*. 2018. 81(5). Pp. 160–173. DOI: 10.18720/MCE.81.16
12. Fedosov, S.V., Roumyantseva, V.E., Konovalova, V.S., Loginova, S.A. Mathematical modeling of diffusion processes of mass transfer of «Free calcium hydroxide» during corrosion of cement concretes. *International Journal of Computational Civil and Structural Engineering*. 2018. DOI: 10.22337/2587-9618-2018-14-3-161-168
13. Luo, J., Chen, X., Crump, J., Zhou, H., Davies, D.G., Zhou, G., Zhang, N., Jin, C. Interactions of fungi with concrete: Significant importance for bio-based self-healing concrete. *Construction and Building Materials*. 2018. 164. Pp. 275–285. DOI: 10.1016/j.conbuildmat.2017.12.233
14. Flemming, H.C., Wingender, J., Szewzyk, U., Steinberg, P., Rice, S.A., Kjelleberg, S. Biofilms: An emergent form of bacterial life. *Nature Reviews Microbiology*. 2016. 14. Pp. 563–575. DOI: 10.1038/nrmicro.2016.94
15. Lushnikova, V.Y., Tamrazyan, A.G. The effect of reinforcement corrosion on the adhesion between reinforcement and concrete. *Magazine of Civil Engineering*. 2018. 80(4). Pp. 128–137. DOI: 10.18720/MCE.80.12

16. Mullard, J.A., Stewart, M.G. Corrosion-induced cover cracking: New test data and predictive models. *ACI Structural Journal*. 2011. 108(1). Pp. 71–79. DOI: 10.14359/51664204
17. Fedosov, S.V., Rummyantseva, V.E., Krasilnikov, I.V., Konovalova, V.S., Evsyakov, A.S. Mathematical modeling of the colmatation of concrete pores during corrosion. *Magazine of Civil Engineering*. 2018. 83(7). Pp. 198–207. DOI: 10.18720/MCE.83.18
18. Vu, K., Stewart, M.G., Mullard, J. Corrosion-induced cracking: Experimental data and predictive models. *ACI Structural Journal*. 2005. 102(5). Pp. 719–726. DOI: 10.14359/14667
19. Chromková, I., Čechmánek, R. Influence of biocorrosion on concrete properties. *Key Engineering Materials*. 2018. 760. Pp. 83–90.
20. Ksiazek, M. Biological corrosion of the sandstone of the quay of the river of Odra in Wrocław. *Engineering Failure Analysis*. 2014. 44. Pp. 338–344. DOI: 10.1016/j.engfailanal.2014.05.003
21. Wei, S., Jiang, Z., Liu, H., Zhou, D., Sanchez-Silva, M. Microbiologically induced deterioration of concrete - A review. *Brazilian Journal of Microbiology*. 2013. 44. Pp. 1001–1007. DOI: 10.1590/S1517-83822014005000006
22. Loto, C.A. Microbiological corrosion: mechanism, control and impact—a review. *International Journal of Advanced Manufacturing Technology*. 2017. 92(9-12). Pp. 4241–4252. DOI: 10.1007/s00170-017-0494-8
23. Vupputuri, S., Fathepure, B.Z., Wilber, G.G., Sudoi, E., Nasrazadani, S., Ley, M.T., Ramsey, J.D. Isolation of a sulfur-oxidizing *Streptomyces* sp. from deteriorating bridge structures and its role in concrete deterioration. *International Biodeterioration and Biodegradation*. 2015. Pp. 128–134. DOI: 10.1016/j.ibiod.2014.11.002
24. Fedosov, S.V., Roumyantseva, V.E., Krasilnikov, I.V., Narmania, B.E. Formulation of mathematical problem describing physical and chemical processes at concrete corrosion. *International Journal for Computational Civil and Structural Engineering*. 2017. 13(2). Pp. 45–49. DOI: 10.22337/2587-9618-2017-13-2-45-49

Contacts:

Sergey Fedosov, FedosovSV@mgsu.ru

Svetlana Loginova, sl79066171227@yandex.ru

© Fedosov, S.V., Loginova, S.A., 2020



DOI: 10.18720/MCE.99.7

Transition factor between elastic and deformation moduli for dispersive soils

V.V. Antipov*, V.G. Ofrikhter

Perm National Research Polytechnic University, Perm, Russia

* E-mail: seekerva@mail.ru

Keywords: Multichannel Analysis of Surface Waves, MASW, elastic moduli, deformation modulus, experimental investigations, Plate Load Test, PLT, Triaxial Test, numerical models

Abstract. The paper is devoted to the perspective trend of researches on estimation of physical and mechanical characteristics of dispersive soils by means of non-destructive methods of in-situ testing by wave analysis. The paper presents the results of comparison of the values of the transition coefficient between the soil dynamic elastic modulus, which can be calculated from the results of in-situ tests by means of non-destructive technique of Multichannel Analysis of Surface Waves, and the soil deformation modulus. Application of such a transition factor makes it possible to estimate the soil deformation modulus according to the soil elastic characteristics determined using modern non-destructive express techniques of wave analysis of the low velocity zone of the upper part of the profile. Due to the application of such express methods, labor and time costs of field investigations are significantly reduced during preliminary geotechnical site assessment. Comparison of different values of the transition factor was made on the basis of the results of laboratory standard triaxial tests and numerical experiments with the values calculated on the basis of dependencies proposed by the results of in-situ tests with Plate Load Tests and Multichannel Analysis of Surface Waves in previous in-situ studies. The results of standard triaxial tests on samples of cohesive and non-cohesive soils confirm the dependence of the transition factor on the soil unit weight, obtained in the previous stage of in-situ researches. The values of the transition factor based on the results of numerical experiments do not exceed the results obtained by field research methods. The results of the research will be useful in estimating the physical and mechanical properties of the soil during preliminary geotechnical calculations of the foundations. All in-situ investigations are carried out using non-destructive technique. No permits or approvals are required to perform the work according to the proposed methodology.

1. Introduction

At present, obtaining initial data about soils strata and also physical and mechanical characteristics for geotechnical calculations can take quite a long time, and application of conventional test methods requires relatively large labor costs at the preparation and execution stages. These disadvantages are clearly apparent when conducting an express preliminary geotechnical assessment of the soil base of a future or existing building or structure. The task of reducing the labor and time required to conduct a preliminary geotechnical situation assessment at the pre-design stage is relevant. To solve this problem, modern non-destructive wave methods can be used, in particular, Multichannel Analysis of Surface Waves (MASW).

MASW is a modern non-destructive technique of wave analysis of the low velocity zone at the upper part of soil profile, which allows obtaining a velocity profile of the surface wave distribution in the upper section. MASW was first presented in the Park et al paper. [1]. Different researchers (C.B. Park, J. Xia, S. Foti, J.N. Louie, N. Ryden, K. Suto, R. Miller, M. Carnevale, Z. Lu, B. Mi, A. Levshin, C. Li et al. [2–14]) continue to improve the technique, increasing the speed of the in-situ procedure and the resolution of velocity profiles. The results of MASW are generally used for dynamic (elastic) soil calculations [15–19], but they can also be used for preliminary geotechnical assessment of soil bases. In the Russian Federation, the Regulation SP 11-105-97 "Engineering geological site investigations for construction. Part VI. Regulations for geophysical surveys" presents several empirical dependencies to determine the deformation modulus (calculated by service limit state) as well as cohesion and the internal friction angle (calculated by ultimate limit state) based



on longitudinal and/or transverse wave velocities for different types of dispersed soils. No such dependencies are given for the surface wave velocity that can be determined using MASW.

Conventional Plate Load Tests (PLT) are used in the Russian Federation to determine the deformation modulus of the soil base during engineering and geological surveys. Deformation modulus corresponds to the straight-line section of the load-settlement curve of PLT in accordance with the State Standard GOST 20276-2012 "Soils. Field methods for determining the strength and strain characteristics". The straight-line section ends at the fourth point of the load-settlement chart, counting from the point of accepted initial pressure. In previous papers of the authors [20, 21], based on comparison of the in-situ PLT and MASW tests, the dependence (1) was proposed to estimate the deformation modulus E using the initial shear modulus G_0 and transition factor k_G . Non-dimensional transition factor k_G can be calculated by means of empirical relation (2) as a function of the soil unit weight.

$$E = k_G G_0 \quad (1)$$

$$k_G = -0.005286\gamma^3 + 0.314254\gamma^2 - 6.248539\gamma + 41.723895 \quad (2)$$

where E is deformation modulus, corresponding to the PLT deformation modulus E_{PLT} for a 5000 cm² round plate, MPa; G_0 is the initial shear modulus, MPa, it can be estimated using (3) [22] via density (unit weight) and surface wave velocity based on MASW results [20, 21]; γ is the soil unit weight, kN/m³, it can be estimated using (4) [22] via surface wave velocity, proposed on the basis of known empirical relationships for shear wave velocity [23, 24].

$$G_0 = 1.096 \cdot 10^{-6} \rho V_R^2, \text{ MPa} \quad (3)$$

$$\gamma = \ln \left(\frac{V_R^{3.61}}{z^{0.7}} \right) + 0.166372, \text{ kN/m}^3 \quad (4)$$

where ρ is soil density, kg/m³, calculated via soil unit weight; V_R is surface wave velocity, m/s; z is soil base depth, m.

To increase the accuracy of dependence (2) inferred from in-situ tests it is necessary to compare it with the results of deformation modulus determination on the basis of triaxial tests, because of all laboratory tests only triaxial tests simulate the behavior of soil under load most closely to the actual behavior [25]. In addition, it is also necessary to carry out numerical experiments based on the results of triaxial tests, since the numerical modeling at preliminary geotechnical assessment of soil bases allows us to eliminate the need for costly and lengthy field tests and, at the same time, to calculate the parameters required for engineering calculations.

The purpose of the paper is to compare the values of transition factor between the elastic modulus and the deformation modulus obtained by means of field tests [20, 21], laboratory triaxial tests and numerical experiments.

2. Methods

2.1. Triaxial tests

Comparison of the values of transition factor between the elastic and deformation moduli was performed based on the results of standard drained triaxial tests of cohesive and non-cohesive soil samples with prescribed parameters at a full water-saturated state (Table 1, soils a and b). The tests were carried out with a triaxial compression unit GT 2.0.9 manufactured by NPP Geotek, LLC (Penza City, Russian Federation), and pressure control panel GT 2.0.11 with static and kinematic loading modes, maximum load of 1 ton (10 kN). Tests were performed in the triaxial compression cell GT 2.3.8 of type A (isotropic compression), the test data was processed using the ASIS automatic software.

To reduce the amount and time of triaxial tests, an analysis of the provided results of triaxial tests on the samples of cohesive soils was performed. The results were provided by NPP Geotek, LLC and the "MIKS" Center for Technological Innovation and Modernization in Construction at PNRPU (Table 1, soils c – g).

The summary list of soils studied in laboratory conditions:

- a is fine, saturated, dense sand;
- b is heavy, tough clay;
- c is medium-hard, light, silt clay;
- d is very soft sandy clay;

e is very soft sandy clay;

f is soft, silt clayey sand.

Table 1. Physical parameters of the studied soils.

| Soil | z^* (m) | W | W_L | W_P | I_P | I_L | ρ (g/cm ³) | ρ_s (g/cm ³) | ρ_d (g/cm ³) | e | S_r |
|------|--------------|------|-------|-------|-------|-------|--------------------------------|----------------------------------|----------------------------------|------|-------|
| a | 1.5 | 0.22 | – | – | – | – | 2.01 | 2.66 | 1.68 | 0.58 | 1.00 |
| b | 1.5 | 0.24 | 0.39 | 0.11 | 0.28 | 0.47 | 1.85 | 2.74 | 1.65 | 0.66 | 1.00 |
| c | 6.5 | 0.25 | 0.40 | 0.22 | 0.18 | 0.15 | 1.98 | 2.73 | 1.59 | 0.72 | 0.94 |
| d | 2.5 | 0.22 | 0.27 | 0.11 | 0.16 | 0.69 | 1.79 | 2.54 | 1.47 | 0.73 | 0.77 |
| e | 4.5 | 0.23 | 0.27 | 0.12 | 0.15 | 0.73 | 1.85 | 2.54 | 1.50 | 0.69 | 0.84 |
| f | 3.9 | 0.24 | 0.26 | 0.23 | 0.03 | 0.33 | 1.97 | 2.58 | 1.59 | 0.62 | 0.99 |

z^* is sampling depth, for soils a and b the depth is specified; W is water content; W_L is liquid limit; W_P is plastic limit; I_P is plasticity index; I_L is liquidity index; ρ is density; ρ_s is particle density; ρ_d is dry soil density; e is void ratio; S_r is degree of saturation.

The samples with prescribed parameters were formed according to State Standard GOST 30416-2012 "Soils. Laboratory testing. General". Before installation on the cell base the samples of sandy soil were previously stabilized at a negative temperature for 1 hour. The formed sample was squeezed out of the holder using a special device and installed in the triaxial cell.

To restore the assumed natural state of the studied soils, the reconsolidation of the prepared samples was carried out by the phase state restoration method (a special case of the backpressure method) in automatic mode, according to Appendix E of State Standard GOST 12248-2010 "Soils. Laboratory methods for determining the strength and strain characteristics".

Cell pressure increment and stabilization period were assigned according to Table 5.4 of State Standard GOST 12248-2010 (Table 2). Due to the fact that in-situ tests were conducted at a shallow depth in the low-velocity zone, a "sensitive" model at low cell pressures was adopted for triaxial tests.

Table 2. Parameters of triaxial tests.

| Parameters | a | b |
|---|--|-------|
| Vertical overburden pressure σ_1 (kPa) | 30 | 30 |
| Cell pressure σ_3 (kPa) | 30 | 30 |
| Cell pressure increment (kPa) | 30 | 30 |
| Stabilization period of PSR method (min) | 5 | 30 |
| Stabilization period (h) | 0.5 | 18 |
| Loading/unloading rate (mm/min) | | 0.001 |
| Unloading stages by deformation value (%) | 0.05; 0.10; 0.15; 0.20; 0.30; 0.40; 0.50; 1.00; 2.00; 3.00; 4.00; 5.00 | |
| Sample sizes, $h \times d$ (mm x mm) | 100x50 | |

The deformation curve obtained as a result of triaxial tests was used to determine the soil deformation modulus E . The deformation modulus is not a constant value. Its values depend on the loading interval [25] determined by the future load on the soil from the foundation. At a preliminary estimation of the deformation modulus, the future loads are not yet known, therefore, like the assumption about the first four points of the load-settlement curve in State Standard GOST 20276-2012, deformation modulus was determined for the initial linear section of the deformation curve directly from the charts. The first point of the deformation modulus interval corresponds to overburden pressure in accordance with State Standard GOST 20276-2012, so when defining the deformation modulus from deformation curves, the initial point was taken as zero deviatoric load $\sigma_{dev} = 0$. The end point of linear approximation by the deformation modulus is taken for relative deformation $\varepsilon_1 = 0.005$. The deformation modulus was calculated according to formula (5).

$$E = \frac{\sigma_{dev}}{\varepsilon_1} \quad (5)$$

For further calculation of the transition coefficient, the static elastic modulus $E_{0,st}$ was also determined. For this, an unloading-reloading of the samples was carried out at different relative deformations (Table 2) to determine the values of recovering strains at specific pressure, and the unloading modulus was taken equal

to the static elastic modulus, similar to [26], at a relative strain of the order 10^{-3} (restored strain being not more than 10^{-4}). Then the dynamic elastic modulus $E_{0,dyn}$ was estimated based on the value of static elastic modulus using coefficient K which is the ratio of dynamic and static moduli of elasticity according to (6) and Fig. 1 proposed in [26]. The dynamic modulus of elasticity was taken for deformations of less than 10^{-6} , which occur during the field tests by MASW method.

$$K = \frac{E_{0,dyn}}{E_{0,st}} \quad (6)$$

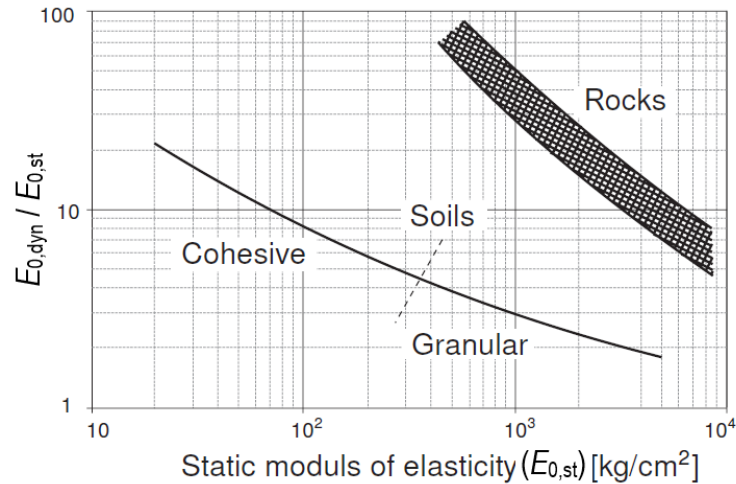


Figure 1. Empirical curve of dynamic and static elastic moduli ratio proposed in [26].

To shorten the test time, the kinematic loading mode was adopted. To create a “sensitive” model, the smallest loading rate of 0.001 mm / min possible for the device was taken (Table 2). Tests were carried out until the destruction of the sample or up to the maximum relative deformation of the sample of 0.15 according to paragraph 5.3.6.13 of State Standard GOST 12248-2010.

Provided results of triaxial tests on cohesive soils (Table 1, soils c–g) did not contain unloading stages, so it was not possible to determine the static modulus of elasticity directly, and the dynamic elastic modulus could not be estimated from Fig. 1 either. Therefore, the dynamic modulus of elasticity was estimated indirectly. First, the surface wave velocity V_R was estimated using formula (4). Further, the initial shear modulus G_0 was calculated from the theory of elasticity using a well-known formula (3). Finally, the dynamic elastic modulus $E_{0,dyn}$ was estimated via formula (7) using dynamic Poisson's ratio.

$$E_{0,dyn} = 2G_0(1 + \nu_{dyn}), \text{MPa} \quad (7)$$

where G_0 is the initial shear modulus, MPa; ν_{dyn} is the dynamic Poisson's ratio assumed by Appendix G of Regulations SP 23.13330.2018 “Foundations of hydraulic structures”.

2.2. Numerical modeling

Numerical modeling to determine transition factor values was carried out by modeling in-situ PLT tests by a plate of 5000 cm² (diameter $D \approx 80$ cm) in the conditions of natural soil occurrence at the depth of sampling. It was performed in the PLAXIS 2D software package. The geometric model is axisymmetric, 3.0×3.0 m, boundary conditions are standard. The finite element mesh is very fine. Two vertical distributed loads were applied to the geometrical model: the first was the overburden pressure; the second was a variable step load applied to the plate. Loading was made by stages accepted in accordance with State Standard GOST 20276-2012 depending on the soil type and void ratio.

Numerical experiment was carried out using the model of Hardening Soil [27] with Small Strains (HSSS) [28, 29]. The initial shear modulus G_0 was estimated using formula (7) through the dynamic elastic modulus $E_{0,dyn}$, which in turn was calculated using formula (6) through the ratio K of the dynamic and static moduli of elasticity. The ratio K was estimated using the empirical chart in Fig. 1 [26]. The unloading/loading modulus E_{ur} was assumed to be equal to the static elastic modulus $E_{0,st}$, which in turn was taken for abraded soils according to the results of triaxial tests, and for intact soils was $E_{0,st} = 6-7 E_{50}$ (E_{50} was taken from triaxial tests) according to recommendations [30]. The power coefficient m of HSSS model [29] was adopted according to recommendations [29] and [31], depending on the soil type. According to [31], the coefficient m

is usually assumed to be 0.5 for sand; 1.0 for clay; and intermediate values are assumed for sandy clay and loam.

To improve the accuracy of soil behavior modeling, the parameters of model deformation curves were calibrated in the PLAXIS software module SoilTest on the parameters of triaxial test curves according to the method proposed in [32]. The calibrated soil model parameters are presented in Table 3.

Table 3. Parameters of numerical soil models.

| Parameter | a | b | c | d | e | f |
|--|----------|----------|----------|----------|----------|----------|
| Soil model | HSSS | HSSS | HSSS | HSSS | HSSS | HSSS |
| Material type | Drained | Drained | Drained | Drained | Drained | Drained |
| γ_{unsat} (kN/m ³) | 20.075 | 20.069 | 19.404 | 17.542 | 18.130 | 19.306 |
| γ_{sat} (kN/m ³) | 20.075 | 20.069 | 19.653 | 18.534 | 18.713 | 19.342 |
| e | 0.58 | 0.66 | 0.72 | 0.73 | 0.69 | 0.62 |
| E_{50}^{ref} (kN/m ²) | 14000 | 10000 | 7100 | 4300 | 7000 | 8800 |
| $E_{\text{oed}}^{\text{ref}}$ (kN/m ²) | 14000 | 26400 | 7100 | 4300 | 4000 | 8800 |
| $E_{\text{ur}}^{\text{ref}}$ (kN/m ²) | 160000 | 60000 | 49700 | 25800 | 24000 | 61600 |
| m | 0.5 | 0.9 | 0.9 | 0.8 | 0.8 | 0.6 |
| c (kN/m ²) | 12 | 13.5 | 83 | 10 | 39 | 30 |
| φ | 41 | 7 | 22 | 19 | 21 | 23 |
| ψ | 0 | 0 | 0 | 0 | 0 | 0 |
| G_0 (kN/m ²) | 140000 | 170000 | 66400 | 45000 | 43000 | 77000 |
| $\gamma_{0.7}$ | 2.00E-04 | 1.00E-05 | 1.00E-05 | 8.84E-05 | 3.51E-04 | 1.47E-04 |
| p^{ref} (kN/m ²) | 30 | 30 | 150 | 100 | 100 | 77 |
| R_f | 0.9 | 0.9 | 0.9 | 0.9 | 0.9 | 0.9 |

γ_{unsat} is soil unit weight; γ_{sat} is saturated soil unit weight; e is void ratio; E_{50}^{ref} is the secant deformation modulus at 50 % of the maximum deviatoric stress; $E_{\text{oed}}^{\text{ref}}$ is tangent modulus for primary oedometer loading; $E_{\text{ur}}^{\text{ref}}$ is unloading/reloading modulus; m is power coefficient; c is cohesion; φ is angle of internal friction; ψ is angle of dilatancy; G_0 is initial shear modulus; $\gamma_{0.7}$ is shear strain level at which shear modulus is reduced to about 70 % of G_0 ; p^{ref} is reference pressure; R_f is failure ratio [23].

The deformation modulus E was calculated according to State Standard GOST 20276-2012 using formula (8) from load-settlement curves obtained during numerical experiments.

$$E = (1 - \nu^2) K_p K_1 D \frac{\Delta P}{\Delta S} \quad (8)$$

where ν is Poisson's ratio; K_p is the specific-conditions-of-use factor according to paragraph 5.5.2 of State Standard GOST 20276-2012; K_1 is the coefficient that depends on the plate shape, for a round plate $K_p = 0.79$; D is the plate diameter, cm; ΔP is pressure increment $P_n - P_0$, MPa, P_n is the end of the chosen load interval, P_0 is the initial point of the chosen load interval, according to State Standard GOST 20276-2012, P_0 is usually taken equal to the overburden pressure; ΔS is settlement increment that corresponds to ΔP , cm.

2.3. Transition factor k_E

After determining deformation and elasticity moduli, the transition factor was calculated. For ease of comparison, instead of the transition factor k_G , the transition factor k_E (9) between the dynamic elastic modulus $E_{0,\text{dyn}}$ and the deformation modulus E was calculated in the same way [26]. Dynamic elastic modulus can be calculated using the well-known formula (7). The relationship between transition factors k_G and k_E is represented by the formula (10).

$$E = k_E E_{0,\text{dyn}} \quad (9)$$

$$k_E = k_G \frac{1}{2(1 + \nu_{\text{dyn}})} \quad (10)$$

where ν_{dyn} is dynamic Poisson's ratio that can be evaluated by means of wave analysis or estimated using Appendix G of Regulations SP 23.13330.2018.

3. Results and Discussion

Deformation curves obtained from triaxial tests are shown in Fig. 2. Elastic parameters of soils determined and evaluated during standard drained triaxial tests are presented in Table 4. Accepted loading intervals for the calculation of deformation modulus and its values, as well as obtained values of the transition factor k_E are given in Table 5.

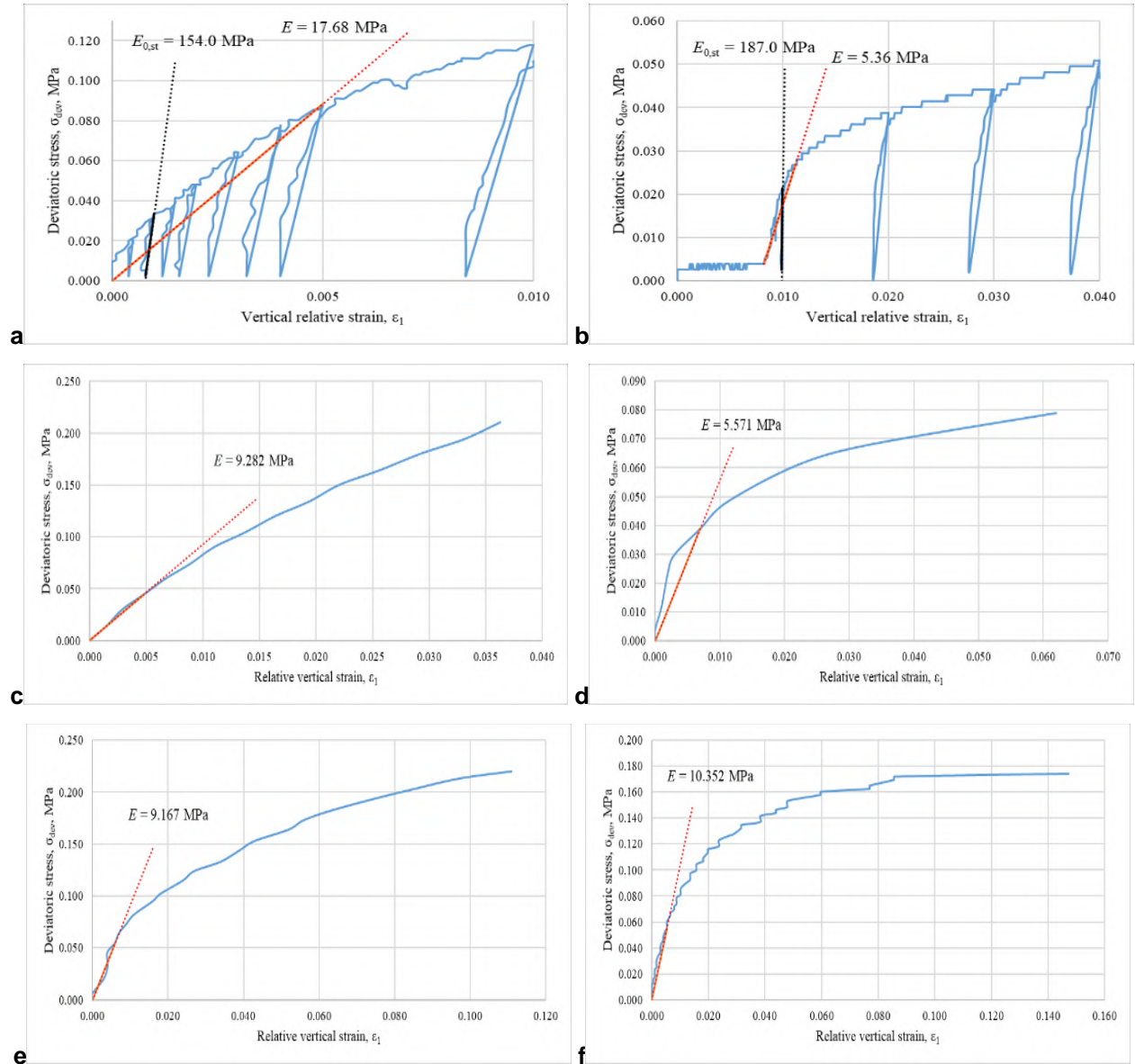


Figure 2. Deformation curves obtained by means of standard drained triaxial tests, the figure letters correspond to soil type letters.

Table 4. Estimation of elastic parameters based on triaxial tests.

| Soil | σ_{ov} (MPa) | γ (kN/m ³) | $E_{0,st}$ (MPa) | K | $E_{0,dyn}$ (MPa) | ν_{dyn} | G_0 (MPa) |
|------|------------------------|----------------------------------|---------------------|-----|----------------------|-------------|----------------|
| a | 0.030 | 20.075 | 154.000 | 2.5 | 385.000 | 0.48 | 130.068 |
| b | 0.030 | 20.069 | 187.000 | 2.5 | 467.500 | 0.45 | 161.207 |
| c | 0.150 | 19.404 | – | – | 550.915 | 0.46 | 188.669 |
| d | 0.045 | 17.542 | – | – | 121.083 | 0.44 | 42.043 |
| e | 0.082 | 18.130 | – | – | 217.542 | 0.44 | 75.535 |
| f | 0.077 | 19.306 | – | – | 423.139 | 0.45 | 145.910 |

σ_{ov} is overburden pressure; γ is soil unit weight; $E_{0,st}$ is static elastic modulus; K is ratio of dynamic and static elastic moduli according to (6) [26]; $E_{0,dyn}$ is dynamic elastic modulus; ν_{dyn} is dynamic Poisson's ratio estimated using Appendix G of Regulations SP 23.13330.2018; G_0 is initial shear modulus.

Table 5. Estimation of elastic parameters based on triaxial tests data k_E from triaxial tests.

| Soil | σ (MPa) | ε_1 | E (MPa) | $E_{0,dyn}$ (MPa) | k_E triaxial |
|------|-------------------|-----------------|--------------|----------------------|-------------------|
| a | 0.0884 | 0.0050 | 17.680 | 385.000 | 0.046 |
| b | 0.0268 | 0.0050 | 5.360 | 467.500 | 0.011 |
| c | 0.0439 | 0.0047 | 9.282 | 550.915 | 0.017 |
| d | 0.0279 | 0.0050 | 5.571 | 121.083 | 0.046 |
| e | 0.0550 | 0.0060 | 9.167 | 217.542 | 0.042 |
| f | 0.0557 | 0.0054 | 10.352 | 423.139 | 0.024 |

σ is deviatoric stress; ε_1 is axial strain, corresponding to the deviatoric stress σ .

The total calculation of the deformation modulus from numerical experiments is shown in Table 6. It was assumed that the tests were performed in the borehole, so, according to State Standard GOST 20276-2012, the K_p coefficient is assumed to be 1.0. Calculation of transition factor k_E values based on the results of numerical experiments is presented in Table 7. Final comparison of obtained transition coefficient k_E values based on the triaxial tests and numerical experiments with the values according to proposed formulas (1) and (2) on the results of PLT and MASW is presented in Table 8 and Fig. 3.

Table 6. Calculation of deformation modulus E from numerical experiments.

| Soil | h_{PLT} (m) | ν | P_1 (MPa) | P_4 (MPa) | S_1 (cm) | S_4 (cm) | E (MPa) |
|------|------------------|-------|----------------|----------------|---------------|---------------|--------------|
| a | 1.5 | 0.30 | 0.030 | 0.180 | 0.18 | 0.67 | 17.61 |
| b | 1.5 | 0.42 | 0.030 | 0.060 | 0.29 | 0.37 | 18.37 |
| c | 6.5 | 0.42 | 0.150 | 0.300 | 5.80 | 6.66 | 9.11 |
| d | 2.5 | 0.35 | 0.045 | 0.120 | 1.08 | 1.78 | 5.98 |
| e | 4.5 | 0.35 | 0.082 | 0.157 | 4.15 | 4.94 | 5.31 |
| f | 3.9 | 0.30 | 0.077 | 0.227 | 2.23 | 3.09 | 9.98 |

h_{PLT} is plate depth; ν is Poisson's ratio; K_p is specific-conditions-of-use factor; P_1 and P_4 are first and fourth points of load-settlement curves; S_1 and S_4 are settlements at P_1 and P_4 respectively; E is deformation modulus.

Table 7. Evaluation of transition factor k_E from numerical tests.

| Soil | G_0 (MPa) | ν_{dyn} | $E_{0,dyn}$ (MPa) | E (MPa) | k_E numerical |
|------|----------------|-------------|----------------------|--------------|--------------------|
| a | 140.000 | 0.48 | 414.400 | 17.606 | 0.042 |
| b | 170.000 | 0.45 | 493.000 | 18.371 | 0.037 |
| c | 66.400 | 0.46 | 193.888 | 9.111 | 0.047 |
| d | 33.000 | 0.44 | 95.040 | 5.985 | 0.063 |
| e | 36.300 | 0.44 | 104.544 | 5.305 | 0.051 |
| f | 77.000 | 0.45 | 223.300 | 9.985 | 0.045 |

Table 8. Overall comparison of different values of transition factor k_E .

| Soil | k_E PLT | k_E triaxial | Deviation of the | |
|------|--------------|-------------------|---|--|
| | | | triaxial k_E from the PLT one (%) | numerical k_E from the PLT one (%) |
| a | 0.050 | 0.046 | -8.5 | -15.3 |
| b | 0.051 | 0.011 | -77.6 | -27.3 |
| c | 0.056 | 0.017 | -69.7 | -15.6 |
| d | 0.091 | 0.046 | -49.3 | -30.7 |
| e | 0.075 | 0.042 | -43.8 | -32.4 |
| f | 0.057 | 0.024 | -57.1 | -21.6 |

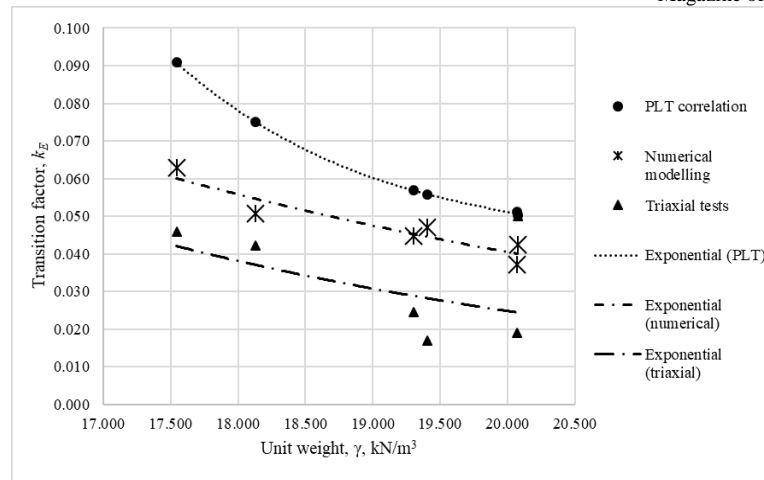


Figure 3. Overall comparison of different values of transition factor k_E .

The comparison of different values of the transition factor confirms its dependence on the soil unit weight.

The lowest values of the transition factor k_E (and, accordingly, the deformation modulus E) were obtained for the triaxial tests, and the highest values were obtained for formula (10) on the basis of the dependencies derived from in-situ tests with PLT and MASW. The deviation of the triaxial test results from the in-situ dependencies does not exceed 78 %.

The results of numerical simulation do not exceed the calculated in-situ dependencies, and the deviation of numerical values from the calculated in-situ ones does not exceed 33 % to the lesser side.

A comparison with the results of experiments performed by other researchers is not given in the article because the transition factor between the elastic modulus and the deformation modulus are determined by the results of MASW for the first time.

4. Conclusions

1. Standard drained triaxial tests allow evaluating dynamic and static modulus of elasticity during a single experiment.
2. The triaxial tests on cohesive and non-cohesive soil samples confirm the dependence of the transition factor on the soil unit weight.
3. The deviation of triaxial test results from in-situ dependencies is not more than 78 %.
4. The comparison of the transition factor k_E from the dynamic modulus of elasticity to the deformation modulus based on the results of in-situ tests and numerical experiments showed that the deviation of the numerical experiments results is not more than 33 % to the lesser side. Values of the transition factor k_E by the results of numerical experiments are less than values of this factor by the results of in-situ tests. This indicates sufficient accuracy of the proposed dependencies (1) and (2) for express assessment of the soil deformation modulus based on the wave analysis by MASW at a preliminary geotechnical site assessment.
5. Correctness of numerical modeling depends on the adequacy of adopted soil model, which requires calibration of input parameters and, accordingly, of the model deformation curve on the experimental deformation curve based on standard triaxial tests.

5. Acknowledgements

The authors thank the research support services of Perm National Research Polytechnic University for providing the equipment for field and laboratory testing. This research did not receive any specific grant funding from agencies in the public, commercial, or not-for-profit sectors.

References

1. Park, C.B., Miller, R.D., Xia, J. Multichannel analysis of surface waves. *Geophysics*. 1999. 64(3). Pp. 800–808. DOI: 10.1190/1.1444590
2. Xia, J., Miller, R., Park, C.B. Estimation of near-surface shear-wave velocity by inversion of Rayleigh waves. *Geophysics*. 1999. No. 64. Pp. 691–700. DOI: 10.1190/1.1444578
3. Foti, S. Multistation methods for geotechnical characterization using surface waves. PhD thesis. [Online]. System requirements: AdobeAcrobatReader. URL: http://www.soilmec.polito.it/content/download/117/592/file/SF_PhD_diss.pdf (date of application: 01.02.2020).
4. Louie, J.N. Faster, Better: Shear-Wave Velocity to 100 Meters Depth from Refraction Microtremor Arrays. *Bulletin of the Seismological Society of America*. 2001. 91(2). Pp. 347–364. DOI: 10.1785/0120000098

5. Ryden, N., Park, C.B. Fast simulated annealing inversion of surface waves on pavement using phase-velocity spectra. *Geophysics*. 2006. 71(4). Pp. R49–R58. DOI: 10.1190/1.2204964
6. Suto, K. Multichannel analysis of surface waves (MASW) for investigation of ground competence: an introduction. *Proceedings of the Sydney Chapter 2007 Symposium*. Australian Geomechanics Society. Sydney, 2007. Pp. 71–81.
7. Park, C.B., Miller, R.D. Roadside Passive Multichannel Analysis of Surface Waves (MASW). *Journal of Environmental and Engineering Geophysics*. 2008. 13(1). Pp. 1–11. DOI: 10.2113/JEEG13.1.1
8. Park, C.B., Carnevale, M. Optimum MASW survey – revisit after a decade of use. *Proceedings of GeoFlorida 2010, Advances in Analysis, Modeling, and Design*, Florida, Feb. 20-24, 2010. American Society of Civil Engineering. West Palm Beach, 2010. Pp. 1303–1312. DOI: 10.1061/41095(365)130
9. Lu, Z., Wilson, G.V. Imaging a soil fragipan using a high-frequency multi-channel analysis of surface wave method. *Journal of Applied Geophysics*. 2017. No. 143. Pp. 1–8. DOI: 10.1016/J.JAPPGEO.2017.05.011
10. Mi, B., Xia, J., Shen, C., Wang, L., Hu, Y., Cheng, F. Horizontal Resolution of Multichannel Analysis of Surface Waves. *Geophysics*. 2017. 82(3). Pp. EN51–EN66. DOI: 10.1190/geo2016-0202.1
11. Mi, B., Xia, J., Bradford, J., Shen, C. Estimating Near-Surface Shear-Wave-Velocity Structures Via Multichannel Analysis of Rayleigh and Love Waves: An Experiment at the Boise Hydrogeophysical Research Site. *Surveys in Geophysics*. 2020. Pp. 1–19. DOI: 10.1007/s10712-019-09582-4.
12. Jaganathan, A. Multichannel surface wave analysis of reinforced concrete pipe segments using longitudinal and circumferential waves induced by a point impact. *Journal of Applied Geophysics*. 2019. No. 163. Pp. 40–54. DOI: 10.1016/j.jappgeo.2019.02.010
13. Sastry, R.G., Chahar, S. Geoelectric versus MASW for geotechnical studies. *Journal of Earth System Science*. 2019. No. 128. Pp. 13. DOI: 10.1007/s12040-018-1061-x
14. Baglari, D., Dey, A., Taipodia, J. A state-of-the-art review of passive MASW survey for subsurface profiling. *Innovative Infrastructure Solutions*. 2018. No. 3. Pp. 1–13. DOI: 10.1007/s41062-018-0171-2
15. Levshin, A., Barmin, M.P., Ritzwoller, M.H. Tutorial review of seismic surface waves' phenomenology. *Journal of Seismology*. 2018. 22(2). Pp. 519–537. DOI: 10.1007/s10950-017-9716-7
16. Li, C., Ashlock, J.C., Lin, S., Vennapusa, P.K.R. In Situ Modulus Reduction Characteristics of Stabilized Pavement Foundations by Multichannel Analysis of Surface Waves and Falling Weight Deflectometer. *Construction and Building Materials*. 2018. 188(10). Pp. 809–819. DOI: 10.1016/j.conbuildmat.2018.08.163
17. Karray, M., Tremblay, S.-P., Hussien, M., Chekired, M. Importance of coherence between geophysical and geotechnical data in dynamic response analysis. *E3S Web of Conferences*. 2019. No. 92. 6 p. DOI: 10.1051/e3sconf/20199218007
18. Abudeif, A., Fat-Helbary, R., Mohammed, M.A., Alkhashab, H.M., Masoud, M.M. Geotechnical engineering evaluation of soil utilizing 2D multichannel analysis of surface waves (MASW) technique in New Akhmim city, Sohag, Upper Egypt. *Journal of African Earth Sciences*. 2019. No. 157. 10 p. DOI: 10.1016/j.jafrearsci.2019.05.020
19. Robertson, P.K. Interpretation of cone penetration tests – a unified approach. *Canadian Geotechnical Journal*. 2009. 46(11). Pp. 1337–1355. DOI: 10.1139/T09-065
20. Antipov, V.V., Ofrikhter, V.G. Correlation between wave analysis data and data of plate load tests in various soils. *Proceedings of the International Conference on Geotechnics Fundamentals and Applications in Construction: New Materials, Structures, Technologies and Calculations, GFAC*, Feb. 6-8, 2019. Taylor & Francis Group. London, 2019. Pp. 16–20. DOI: 10.1201/9780429058882-4
21. Antipov, V.V., Ofrikhter, V.G. Field Estimation of Deformation Modulus of the Soils by Multichannel Analysis of Surface Waves. *Data in Brief*. 2019. 24. 5 p. DOI: 10.1016/j.dib.2019.103974
22. Ofrikhter, V.G., Antipov, V.V. Sposob otŝenki modul'ia deformatsii grunta [The method of estimation of soil deformation modulus]. Patent Russia no. 2704074, 2019. (rus)
23. Mayne, P.W. Stress-strain-strength-flow parameters from enhanced in-situ tests. *Proceedings of the International Conference on In-Situ Measurement of Soil Properties*, Bali, May 21-24, 2001. Parahyangan Catholic University. Bali, 2001. Pp. 27–48.
24. Moon, S.W., Ku, T. Empirical estimation of soil unit weight and undrained shear strength from shear wave velocity measurements. *Proceedings of the 5th International Conference on Geotechnical and Geophysical Site Characterization, ISC 2016*, Gold Coast, Australia, Sep. 5-Sep. 9, 2016. Australian Geomechanics Society. Gold Coast, 2016. Pp. 1247–1252.
25. Boldyrev, G.G., Melnikov, A.V., Novichkov, G.A. Part IV. Interpretation of Laboratory Test Results to Determine Soil Deformation Characteristics. *Engineering survey*. 2014. No. 5-6. Pp. 98–105. (rus)
26. Alpan, I. The geotechnical properties of soils. *Earth Science Reviews*. 1970. 6(1). Pp. 5–49. DOI:10.1016/0012-8252(70)90001-2.
27. Duncan, J.M., Chang, C.Y. Nonlinear Analysis of Stress and Strain in Soils. *Journal of the Soil Mechanics and Foundation Division*. 1970. 96(SM5). Pp. 1629–1653.
28. Hardin, B.O., Drnevich, V.P. Shear modulus and damping in soils: Design equations and curves. *Journal of the Soil Mechanics and Foundation Division*. 1972. 98(SM7). Pp. 667–692.
29. Brinkgreve, R.B.J. (ed). *Plaxis Material Models Manual*. [Online] System requirements: AdobeAcrobatReader. URL: https://www.plaxis.com/?plaxis_download=2D-3-Material-Models.pdf (date of application: 11.12.2019).
30. Melnikov, R.V. Oedometer test data for finding Hardening Soil model. *Akademicheskij Vestnik UralNIIproekt RAASN*. 2014. No. 4. Pp. 90–94. (rus)
31. Gouw, T.L. Common mistakes on the application of Plaxis 2D in analyzing excavation problems. *International Journal of Applied Engineering Research*. 2014. 9(21). Pp. 8291–8311.
32. Melnikov, R.V., Sagitova, R.H. Calibration of Hardening Soil Model Parametres According to the Results of Laboratory Testing in Program "Soiltest". *Akademicheskij Vestnik UralNIIproekt RAASN*. 2016. No. 3. Pp. 79–83. (rus)

Contacts:

Vadim Antipov, seekerva@mail.ru

Vadim Ofrikhter, ofrikhter@mail.ru



DOI: 10.18720/MCE.99.8

Bearing capacity of drilled shaft in intermediate geomaterials

C.N. Lan^a, M.H. Nguyen^b, B.T. Thanh^a, N.N. Long^a, L.D. Tien^a, L.S. Ho^{b,c,*}

^a University of Transport and Communications, Vietnam

^b University of Transport Technology, Vietnam

^c Civil and Environmental Engineering Program, Graduate School of Advanced Science and Engineering, Hiroshima University, Higashi-Hiroshima, Hiroshima, Japan

* E-mail: lanhhs@utt.edu.vn

Keywords: drilled shaft, weathered rock, intermediate geomaterials, bearing capacity, static loading test, FEM, FB-MultiPier

Abstract. Weathered rock or IGMs (Intermediate Geomaterials) is still a controversy in designing the bearing capacity of the drilled shaft. At present, Vietnamese standards separately defined the load capacity of the pile in soils and rocks. That leads to both underestimation and overestimation in case IGMs assumed to be soil and rock, respectively. In this paper, a case study of a project in central Vietnam basing on experienced equations, finite element method (FEM), and field measurement was conducted. The static loading and pull-out tests were conducted for drilled shaft with 0.8 m in diameter installing in the weathered rock. In these tests, instruments were installed including the displacement device, strain gage, and extensometers, which were distributed along the drilled shaft to measure the side and tip bearing capacity of the piles. In addition, FEM was employed to simulate the static loading and pull-out tests of the piles. The obtained results indicated that FEM had a similar behavior at the medium loading stage compared to the field tests (static loading and pull-out tests). Thus, FEM could be a potential method that can be used for calculating and estimating the bearing capacity of the drilled shaft in the IGMs layer. An empirical equation was proposed for computing the side resistance of the pile in the IGMs layer. Finally, this study could help to choose properly the pile length in the design of the pile placed on IGMs layer so that the safety and cost-effective problems can be optimized.

1. Introduction

At present, estimation of the bearing capacity for a drilled shaft is divided into two cases. For the first case, when the pile is placed in the soil, the formulas related to the resistance of the ground are used, such as the internal friction angle of loose soil and unconfined compressive strength in the undrained condition q_u for cohesive soil, based on the field test results such as Cone Penetration Test (CPT), Standard Penetration Test (SPT). For the second case, when the pile is placed on the rock, the formula is used based on the compressive strength q_u of the rock. However, for some cases, the pile tip of the drilled shaft located in a strong weathered rock that has the strength is smaller than that of rock but much larger than that of soil. This leads to difficulties in using the equation specified in standards as well as monitoring and acceptance. In order to address these issues, several researchers have introduced the concept of Intermediate Geomaterials (IGMs) into the design [1–4]. The results of SPT-N experiment or unconfined compression test can be used to determine the bearing capacity of the pile in this case [5–8]. Several authors have proposed some methods to compute the bearing capacity of the drilled shaft that placed into the IGMs layer [4, 7, 9, 10].

It is known that load-bearing capacity and settlement of drilled shaft affected by axial compressive load and depended on many different factors such as physic-mechanical properties of soil, characteristics of piles, mechanism load distribution in piles, and interaction between pile and soil [1, 7, 11–17]. These mentioned factors cannot be completely simulated in the calculation formula, thus the best method to predict the load-settlement relationship of the drilled shaft is to use the static loading test and pull-out tests. In general, the bearing capacity of the drilled shaft is determined through the static loading and pull-out tests on site. The static loading test for measuring axial displacement along the pile has been applied since 1969 for precast reinforced concrete piles. It was then applied in many countries around the world to determine the level of

Lan, C.N., Nguyen, M.H., Thanh, B.T., Long, N.N., Tien, L.D., Ho, L.S. Bearing capacity of drilled shaft in intermediate geomaterials. Magazine of Civil Engineering, 2020, 99(7), Article No. 9908. DOI: 10.18720/MCE.99.8



This work is licensed under a CC BY-NC 4.0

friction mobilization along with the pile [1]. In the 1980s, experimental studies on the drilled shaft were also carried out in order to propose inverse analysis methods for determining the loading transfer line in the pile, thereby determining the side resistance as well as the tip resistance of the single pile [1, 11, 18, 19]. However, many case studies in the United States showed the static loading test can only determine the bearing capacity of the entire pile rather than determining the side resistance and tip resistance of the pile. It means that this test is not enough to evaluate the behavior of the pile [19, 20].

It is noted that the pile resistance in the rock is mobilized at a displacement of less than 13 mm and the shear strength will mobilize residual and strain-hardening to the maximum value of displacement exceeding 38 mm [21]. Thus, it is needed to consider the side resistance of the pile in this case. In addition, there are several studies on the bearing capacity of the drilled shaft with the measurement of pile deformation were conducted [8, 11, 13]. In Vietnam, for many central regions, drilled shaft constructed in the IGMs layer (see Appendix 1). However, there are almost no studies concerning bearing capacity of the pile that has the pile tip located in IGMs layer. In general, in Vietnam the calculation of the pile placed into the IGMs layer employed the formula used for soil or rock. This calculation method caused underestimated bearing capacity for the case of the pile located into rock layer and overestimated bearing capacity for the case of the pile placed into soil (i.e. clay or soil). As a result, the pile length will be too short and too long, which leads to both safety and cost-effective problems. A proper calculation for the pile placed into this IGMs layer must be done to have a suitable design. Thus, it is necessary to study the bearing capacity of drilled shaft constructed on the weathered rock layer (IGMs) in Vietnam with different and specific geological conditions.

Therefore, this study aims to investigate the bearing capacity of the drilled shaft on weathered rock layers through the static loading and pull-out tests for a case study in Vietnam (i.e. Quang Tri province); in which deformation devices attached at the side and tip of the pile to determine stresses and strain. From the obtained deformation values along the side of the pile during the static loading and pull-out test and some hypotheses, it is possible to determine not only the load distribution in the pile, the side friction distribution, unit friction resistance, pile tip resistance, but also the relationship curves between displacement/pile diameter and side friction/maximum side friction ($t-z$ curve). Simultaneously, this study also simulated the static loading and pull-out tests using the finite element method (*FB-MultiPier* software) for the piles those having the pile tip placed in the weathered rock layer (IGM) for comparison. Finally, a comparison between the results obtained from actual tests and modeling was done to evaluate the feasibility application of FEM model. Based on the results of this study, an empirical formula was proposed for calculating the bearing capacity of the pile in the IGMs layer in geological of Vietnam. As a result, the pile length will be determined properly so that the safety and cost-effective of projects will be well designed.

2. Materials and methods

2.1. Geological condition

The case study is conducted for the drilled shaft with a diameter of 0.8 m belonging to the construction project of a reinforced concrete bridge (bridge length is 36.2 m). The geological condition consists of three layers: layers 1 to 3 are sandy clay and layer 4 is claystone (strongly weathered rock). Their thickness and other properties can be found in Table 1 and Fig. 1.

Table 1. Geological conditions and soil parameters.

| Layer | Thickness (m) | Undrained strength S_u (kPa) | Unit weight (kN/m ³) | Unconfined compressive Strength for rock layer (kPa) |
|---|---------------|--------------------------------|----------------------------------|--|
| 1. Sandy clay | 2.2 | 24 | 18 | - |
| 2. Soft clay mixed with sand | 1.3 | 36 | 18 | - |
| 3. Sandy clay mixed gravel | 8.1 | 180 | 18 | - |
| 4. Claystone, strong weathered (RQD = 20 %) | 5.6 | - | 19 | 4800 |

2.2. Static loading test and pull-out test

To estimate the strength of the pile and bearing capacity of the weathered rock layer, static loading and pull-out tests were conducted. The deformation, as well as strain, were measured using the devices attached along the pile to assess the results.

2.2.1. Static loading test

The static loading test was conducted for a drilled shaft according to ASTM D1143 standard [22]. The diameter and length of the pile are 0.8 m and 14.5 m, respectively. The load was applied to the pile head. The design load for the drilled shaft is 153 tons calculated according to AASHTO LRFD 2010 standard [23]. The maximum load for the static loading test is 150 % of the design load. The instruments for both static loading and pull out the tests are installed along with the pile. For each pile, measuring devices including pile head displacement, loadcell, pile deformation measurement, extensometers are shown in Fig. 1.

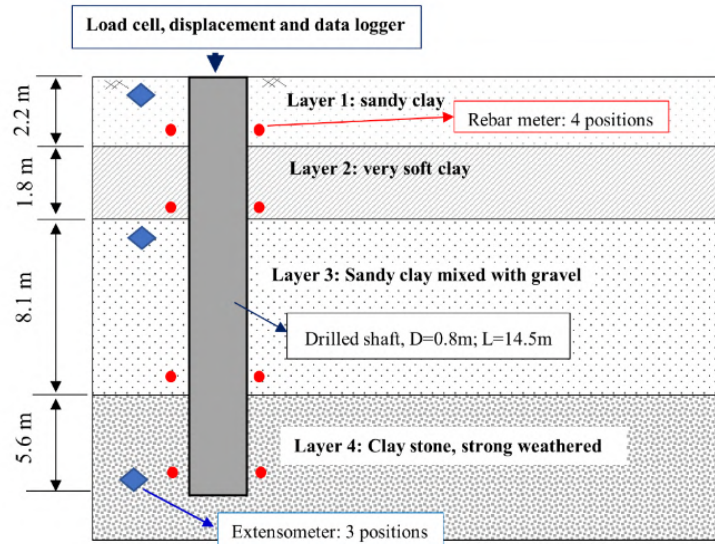


Figure 1. Soil profile and installation of instruments along with the drilled shaft.

a. Displacement

Displacement measuring device (DT-100A; KYOWA, JAPAN) with an accuracy of 0.01 mm and maximum displacement of 10 cm, is connected to the data logger system and fixed to the standard beam. There are 4 displacement measuring devices installing around the top of the pile (Fig. 2). Displacement devices were used for measuring the displacement of the pile head.



Figure 2. Pile head displacement measuring device.

b. Extensometer

In order to measure the displacement of the pile at a different depth, the extensometer was employed. Extensometers were steel bars and were installed at the top, center, and tip of the pile (Fig. 3). These instruments were used for measuring the displacement of the pile along the pile's length.



Figure 3. Extensometer equipment for measuring the displacement of pile.

c. Strain gage

In the static loading test, the displacement of concrete was measured using strain gage (GT-VG4200 GEOTECH, Taiwan). The strain gage is usually used for monitoring the change of strain in either reinforced concrete or mass concrete structure during the construction period. This strain gage is high accuracy and good precision with a measurement range up to $\pm 3000 \mu\epsilon$. For the drilled shaft, strain gages were arranged at 4 different depths and 2 strain gauges were attached to each depth. A total of 8 strain gages were used for measuring the displacement of concrete. Strain gage was attached to the main reinforced bar as shown in Fig. 4.



Figure 4. Strain gage for measuring concrete displacement.

2.2.2. Pullout test

The pull-out test was conducted according to ASTM D1143 standard to determine the bearing capacity at the pile body under tension condition [24]. This experiment will be analyzed in conjunction with the static loading test to be able to evaluate and provide the bearing capacity of the pile in accordance with the actual condition. Fig. 5 shows an overview of the pull-out test at the site condition and the schematic of the pull-out test for 0.8 m in diameter of the drilled shaft.

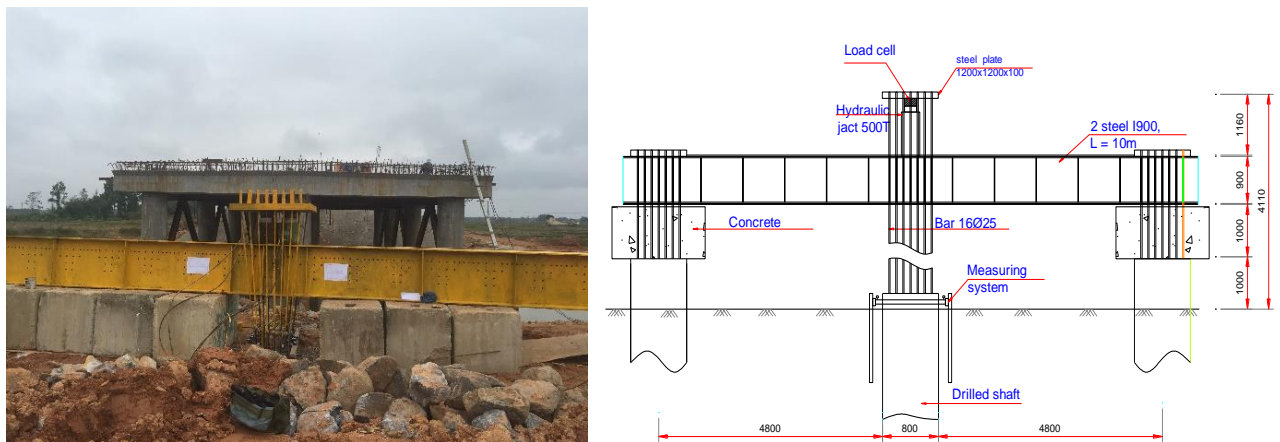


Figure 5. Overview (left) and a schematic (right) of the pull-out test.

2.2.3. Analysis data from static test and pull out test

The deformation of concrete and displacement of the pile at loading stages can be used for analyzing side resistance and tip resistance. The applied force at each depth is calculated according to the formula:

$$P = \epsilon_c E_c A_c \quad (1)$$

where, A_c is the cross-section area of the pile and the area of reinforcement, E_c is the elastic modulus of concrete, and ϵ_c is the deformation of concrete at each depth is determined by the sensor (strain gage).

Based on the correlation between E_c and the deformation of concrete at each depth (at each loading level), the stress of the pile at each loading stage is calculated. The side resistance f_i (of pile segment i) is calculated according to the following equation:

$$f_i = \frac{(P_i - P_{i-1})}{A_i} = \frac{(P_i - P_{i-1})}{\pi D_i L_i} \quad (2)$$

where, P_i and P_{i-1} are the applied forces at the depth of i^{th} and $i-1^{\text{th}}$ and are calculated by E.q (1). A_i is the surface area of pile side (m^2), D_i is the diameter of the pile (m), and L_i is the distance between two strain gage mounting positions (m).

2.3. Finite element method

FB-MultiPier is a nonlinear finite element analysis program that can analyze multiple bridge pier structures interconnected by bridge spans. The program was developed by Bridge Software Institute and the University of Florida [25]. *FB-MultiPier* are widely used to deal with analyzing of pile foundations with the case of nonlinear soil models for axial, lateral, and torsional problems [26–28]. In *FB-MultiPier*, the “*p-y*” and “*t-z*” methods were employed to calculate lateral and axial soil-pile interaction, respectively. Each method uses nonlinear springs to represent the resistance between surrounding soil and the pile. These springs are combined into the equations to model the interaction between pile and the surrounding soil [26]. The resistance to lateral displacement of the pile caused by the surrounding soil was described via the “*p-y*” curve proposed by Matlock and Reese [26, 29]. The characteristics of “*p-y*” curve are depended on the soil types including clay, sand or rock [26]. While the “*t-z*” curve is employed to describe soil resistance provided to an axially loaded pile (frictional and end bearing resistance) against corresponding vertical (axial) displacement. *FB-MultiPier* was used for modeling the static loading test and pull-out test of the drilled shaft (Fig. 6). In this study, layers 1, 2, and 3 can be modeled as clay. Thus, in this model, soil–pile interaction can be modeled as “*p-y*” curve and “*t-z*” curve. For the fourth layer, the soil is classified as strongly weathered claystone, which is modeled as a weak rock (Reese) model with the calculation method (Axial/Torsional) form of Drilled Shaft IGM and Hyperbolic in *FB-MultiPier*. The main parameters of soils (layers 1, 2, and 3) used for modeling are unit weight, undrained strength S_u (see Table 1). While the parameters of the IGM layer are the following: Unit weigh=19 kN/m^3 , RQD = 20 %, Modulus = 398 MPa and unconfined compressive strength = 4.8 MPa. In this modeling, the pile was divided into 16 embedment nodes and 5 free length nodes. The nonlinear springs (*p-y* curve) are applied to get the resistance of soil-pile for all layers.

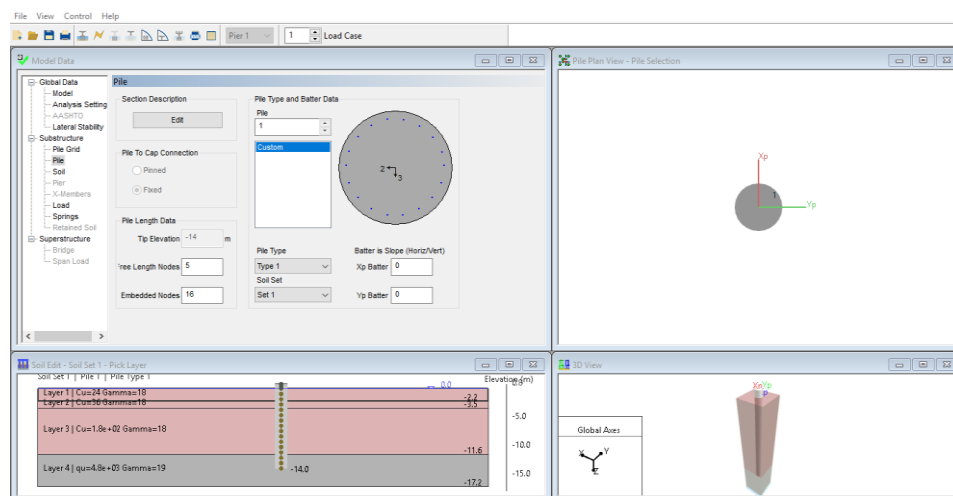


Figure 6. Model of the drilled shaft in *FB-MultiPier*.

3. Results and Discussion

3.1. Loading test and pull-out test result

Based on the measured value of strain gage and displacement, the side and tip resistance with depth as was shown in Fig. 7. Generally, it can be seen that the side resistance increased with increasing in depth. Besides, the side resistance increased with the magnitude of loading from 25 % to 150 % at different depths, particularly in the IGMs layer. The side resistance at the pile tip in the IGMs layer achieved the highest value of approximately 0.116 Mpa. The maximum value of side resistance in this study (0.116 MPa) is smaller than that recommended in previous studies [30, 31]. Tan and Chow summarized the side resistance of drilled shaft for the IGMs layer in Malaysia conducted, and they recommended that for the RQD value smaller than 25 %, the allowable side resistance is 0.3 MPa [30].

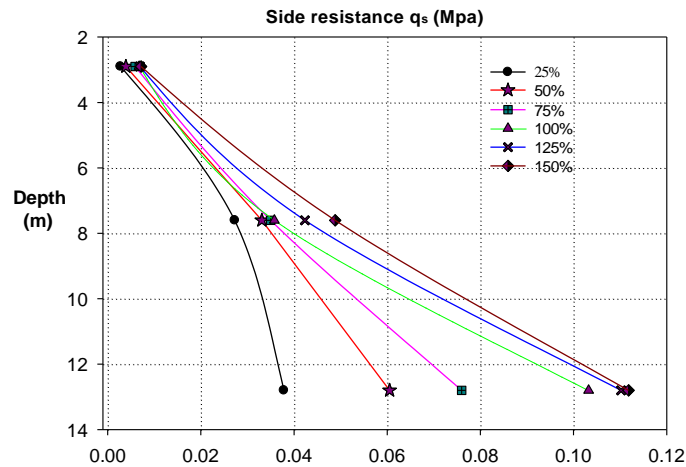


Figure 7. Side resistance versus depth for static loading test.

Similar to the case of the static loading test, the side resistance in the pull-out test is calculated based on the measured value of strain gauge and displacement, the side resistance with the depth of the pile in the pull-out test is depicted in Fig. 8. The side resistance was almost stable or slightly increased from 3 m to around 7.5 m for all loading conditions because the soil from 3 to 7.5 m is the soft clay and sandy clay. However, at the tip of the pile, the side resistance increased significantly even from 25 % of loading to 200 % of loading. Because the tip of the pile was placed in the IGMs layer. The maximum value of side resistance was approximately 0.17 MPa for the cases of 175 % and 200 % loading. From the results of Figs. 7 and 8, it is clear that for the load level from 25 % to 75 % of the design load, the side resistance at the pile tip of the pull-out test was almost the same as that of static loading test. The results of this study agreed well with previous studies [2, 32–34]. However, for the case of the load from 100 % to 150 % of design load, it can be seen that the side resistance at the pile tip of the pull-out test was higher than that of the loading test, this is different from with the case of the load level from 25 % to 75 % of design load and the previous study [33]. The difference may be explained as follows. In the previous study, the final layer is gravelly soil that has lower unconfined compressive strength as well as modulus compared to the IGMs layer in this study.

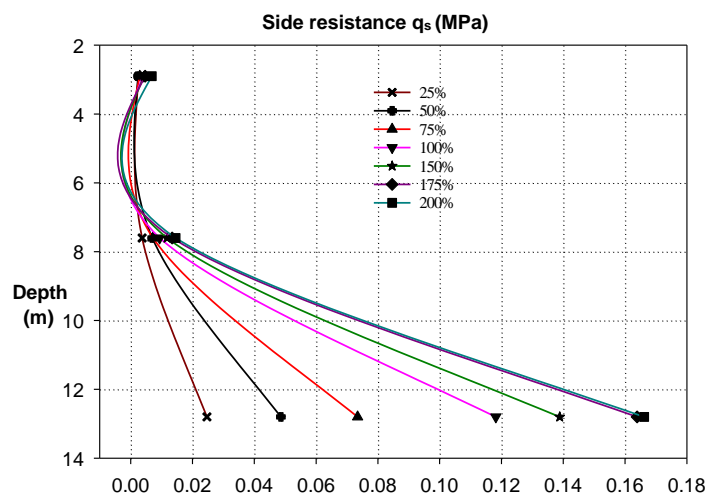


Figure 8. Side resistance versus depth for pull out test.

Fig. 9 shows the load versus settlement curve of the static loading test. It can be seen that there is no settlement at the tip of the pile. The maximum of settlement in the center of the pile was approximately 0.5 mm at the loading of 250 tons. This result of the pile head in this study agreed well with the results of the previous study of drilled shaft placed in the IGMs layer, which had the displacement of pile head was smaller than the allowable value [6, 35]. Fig. 10 presents the load versus displacement curve of the pull-out test at the pile head, center, and tip. For the maximum pull-out load of 260 tons, the displacement was approximately 2.0 mm, 5.8 mm, and 11.3 mm for the bottom, center, and head of the pile, respectively.

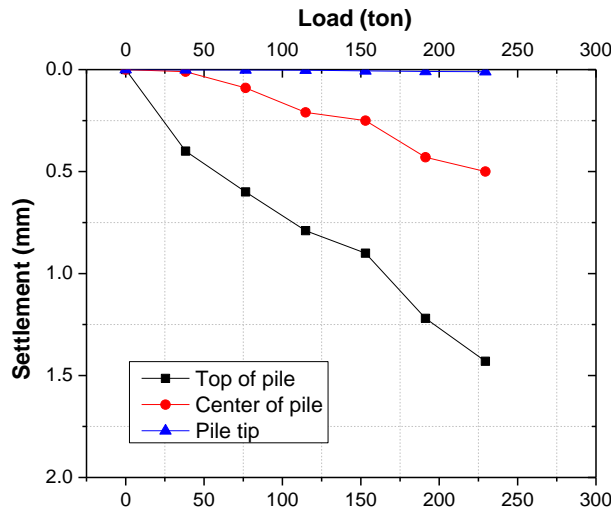


Figure 9. The load-settlement curve for static loading test.

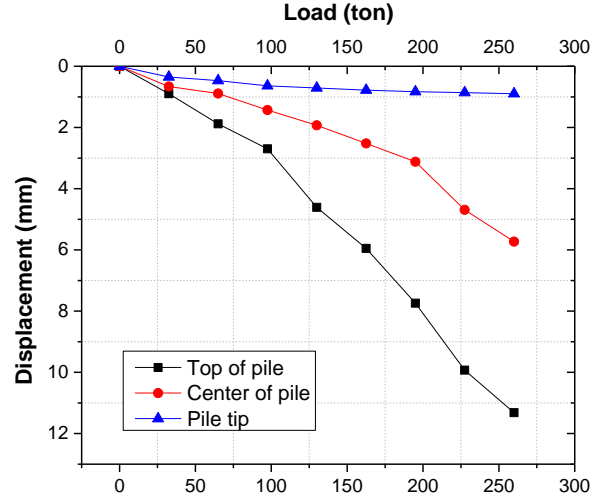


Figure 10. Load-displacement for pull-out test.

3.2. FEM method results and comparison with measured results

From FEM results, load and displacement curves for static loading and pull-out test are presented in Fig. 11 and Fig. 12, respectively. For the case of the static loading test, at the pile tip, the maximum value of the settlement was approximately 0.75 mm; and the center of the pile was around 1.25 mm, while the pile head achieved the biggest value of 2.1 mm. Compared to the results of the actual test (field test), the model results give a greater value of settlement than the actual results at the final load level (Fig. 11). The difference might be related to the degraded and reworked geomaterial on the borehole wall, which decreased the modulus of geomaterial mass, as indicated in a previous study [36]. However, these values are not much different, thus, the calculation model can be considered acceptable. Fig. 12 shows the load-displacement relationship in the pull-out test. The displacement of the pile tip was approximately 1.2 mm for the maximum load, while it was around 1.7 mm for the center of the pile. The biggest displacement was observed for the case of displacement of the pile head, the displacement value was 4.5 mm for the maximum load condition. From Fig. 12, we can observe that the settlement values of the pull-out tests in the modeling were similar to that of the actual field test for the cases of small and medium load conditions.

The results of actual and modeling show that the results of the settlement and the load of the pile are quite similar to that of small and medium loads. However, for the case of the pile head, there was a big gap between the actual value and model value, the displacement of the actual value was much bigger than that of the modeled one. In summary, we can see that both static loading and pullout tests showed that the values of the settlement and displacement of the pile into the cracking weathered rock (IGMs) were quite small, indicating that the strength of IGMs layer is quite large. Thus, when designing the load capacity of piles in many cases, if it is considered that the weathered stone layer (IGMs) as a sand layer and using the formula of the sand layer to calculate the load-bearing capacity as current will lead to underestimating the bearing capacity of the pile that prone too safety and also causing the difficulty to drill deep into the weathered rock fractured in the field.

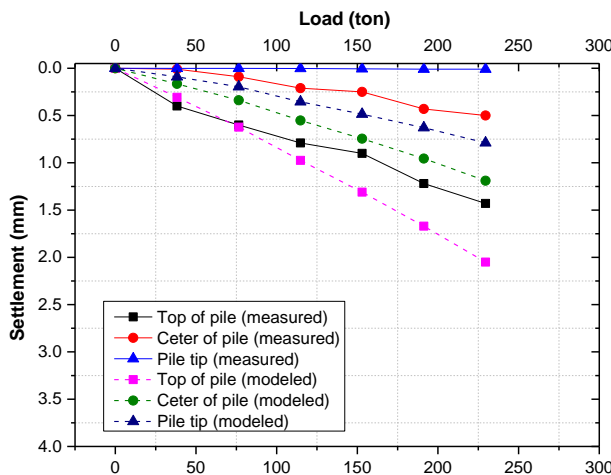


Figure 11. Comparison between the results of FB-MultiPier software and actual results for static loading experiments.

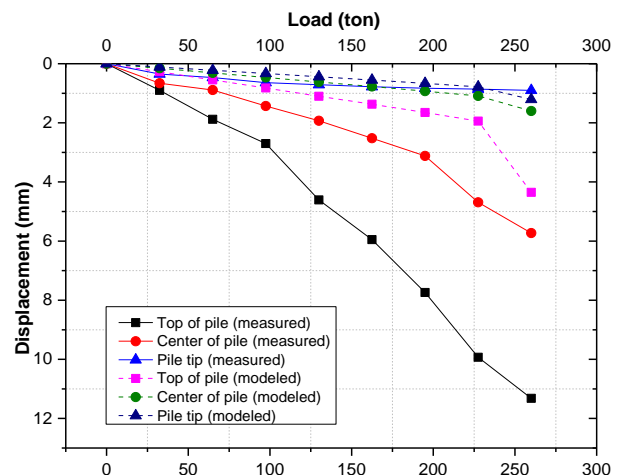


Figure 12. Comparison between the results of FB-MultiPier software and actual results for the pull-out test.

Table 2 shows the comparison between the results of the static loading test calculated by FEM (*FB-MultiPier*) and actual results measured on-site. It is obvious that for the IGM layer 4, the results of side resistance and tip resistance of the pile calculated using *FB-MultiPier* was almost similar to that measured on-site. This indicates that FEM (*FB-MultiPier*) can be used to calculate the bearing capacity of the pile in the IGM layer with high accuracy. The table also shows the comparison results of the pull-out test; it is clear that for IGM layer 4, the side resistance of the pile is consistent for 3 methods, whereas the tip resistance for the LRFD method is higher compared to other methods. From Table 2, we can also observe that the tip resistance results for the pull-out test of the LRFD method also was higher than that of the measured value and FEM method. However, static loading and pull out the tests showed that the value of the settlement and displacement of the pile into the weathered rock is quite small.

Table 2. Comparison results between modeled and for the static loading and pull-out tests.

| Resistance for layer 4 (IGM) | Static loading test | | | Pull-out test | | |
|---|---------------------|----------------|------------|---------------|----------------|------------|
| | LRFD method | Measured value | FEM result | LRFD method | Measured value | FEM result |
| Side resistance $q_s = f_s$ (MPa) | 0.1728 | 0.1096 | 0.1118 | - | - | - |
| Tip resistance q_p (MPa) | 0.7094 | 0.48 | 0.5542 | 0.1728 | 0.1662 | 0.1511 |

3.3. Side resistance correlation

According to AASHTO standard, side resistance of pile in IGM layer can be calculated as the following equation.

$$q_s = \alpha \varphi q_u \quad (3)$$

where q_u is unconfined compression strength of IGM. Several correlations have been developed by various authors for estimating unit side resistance in IGM layer and relationships to unconfined compressive strength q_u as well as SPT N blow count. The methods adopted by AASHTO using q_u as the main design parameter as shown in equation 3. Based on the testing result from static load test (Fig. 6), q_s can be corrected to q_u as equation below:

$$q_s(\text{correction}) = 0.81 \alpha \varphi q_u \quad (4)$$

4. Conclusions

Based on the obtained results of the static loading test and the piling test with the measuring devices attached along with the pile and the *FB-MultiPier* pile testing model, some main conclusions can be drawn as follows:

1. The results of the experiment and modeling showed that side resistance is similar for all methods. However, the LRFD method provided a higher value of side and tip resistance.
2. The static loading and pull-out tests with strain gauge along with the pile body could produce a more accurate calculation of the bearing capacity of the drilled shaft into the weathered rock layer.
3. FEM method using *FB-MultiPier* software can be used to estimate the load capacity, the result of FEM is quite similar to the actual static loading and pull-out tests when the load applied at small and medium levels.
4. A correction value for drilled shaft into the weathered rock layer (IGMs) in a case study in Vietnam is proposed. However, more field tests should be conducted to provide a precise result for practical design as well as validate the results of simulation using FEM software.
5. Based on the results of this study, the pile length placed into the IGMs layer in Vietnam geological condition can be designed properly so that the safety and cost-effective problems can be optimized.

This study investigated the bearing capacity of drilled shaft placed into the IGMs layer, the side and tip resistance of the pile could be obtained using the deformation devices attached to the pile. The finding of this

study indicated that FEM (*FB-MultiPier*) could be used to estimate the bearing capacity of the drilled shaft placed into the IGMs layer. In addition, this study also proposed an empirical formula to calculate the side resistance of the pile in this case. However, this study only conducted for a case study, thus, it is needed to extend this study for many projects as well as different geological conditions to validate the application of FEM method as well as the proposed equation.

Appendix 1. Distribution of the weathered rock (IGMs) in the central of Vietnam

| Province | Name of bridge | Type of soil/rock | SPT value | Rock quality Design | Thickness (m) |
|-------------|----------------------------------|-----------------------------------|---------------|---------------------|--------------------|
| Danang | CauDo (National road 1A) | Shale | – | 0 % | 24 |
| | Qua Giang (National road 1A) | Shale | – | 0–10 % | > 36.5 |
| | CoCo | Shale and limestone | 50–100 | 0 % | > 22.5 |
| | Nguyen Tri Phuong | Shale | – | 0–27 % | 29.0 |
| | Hoa Phuoc | Shale and limestone | 70–100 | 0 % | 52.5 |
| | Tran Thi Ly | Shale | – | 10–30 % | 36.7 |
| | Hoa Xuan Cau Km5 at ring road | Shale Shale | > 100 > 50 | 0–10 % 0 % | > 30 > 10 |
| Quang Binh | Sao Vang Elevated bridge | Limestone | – | 10–20 % | 2.5–7.3 |
| | | Sandstone | – | 8–15 % | 1.4–6.2 |
| QuangTri | Song Hieu | Limestone | > 50 | 15–25 % | 20.5–27.5 |
| | Khe Luoc | Limestone | > 50 | 0–10 % | 0.45–0.9 |
| | Bridge at 2 district 2, Dong Ha | Sandstone | > 50 | 0 % | 5.0–7.3 |
| | Quy Thien | Siltstone | > 50 | 0–12 % | 11.6–13. |
| | An Mo | Shale | > 50 | 5–18 % | 1.8–9.1 |
| | Thanh Co | Sandstone, Siltstone | 39–56 | < 25 % | 1.1–10.2 |
| | Nhan Bieu | Sandstone, Siltstone | > 50 | 0–15 % | 10,8–13.7 |
| | Lai Phuoc | Sandstone, Siltstone | > 36 | 8–20 % | 5.5–7.0 |
| | Ben Loi | Sandstone, Siltstone | 47–55 | 0 % | 2.2–2.4 |
| | Ai Tu Phuoc My | Claystone Sandstone, Siltstone | 20 % > 50 | 0 % 0 % | 1.8–5.6 1.1–2.0 |
| Lai Phuoc 2 | Siltstone | > 50 | 0–18 % | 2.8–3.1 | |
| Cầu Ai Tu 2 | Claystone | 33–54 | 0–20 % | 3.4–7.3 | |

Note: – means N/a

From the data collected through the geological survey results of bridge construction in the Central region. We can see the geology of the central region and Quang Tri province has a relatively thin cover layer with a thickness from 1–5 m thick, followed by fractured weathered rock (IGMs) with a relative thickness of 4–25 m.

References

1. Fellenius, B.H., Haagen, T. New pile force gauge for accurate measurements of pile behavior during and following driving: research note. Canadian Geotechnical Journal. 1969. DOI: 10.1139/t69-034
2. Federal Highway Administration (FHWA). Drilled shafts: Construction procedures and LRFD design methods. FHWA-NHI-10-106. FHWA GEC 010. Design Manual. 2010. DOI: 10.1016/0886-7798(90)90101-O
3. Herrera, R., Jones, L.E. Drilled shaft design and load testing in Florida intermediate geomaterial and weak limestone. Transportation Research Record. 2016. DOI: 10.3141/2579-04
4. Rowe, R.K., Armitage, H.H. Design method for drilled piers in soft rock. Canadian geotechnical journal. 1987. DOI: 10.1139/t87-011
5. Long, J.H. Static Pile Load Tests on Driven Piles into Intermediate-Geo Materials. 2016. (0092).
6. Gupta, R.C. Load-settlement behavior of drilled shafts in multilayered deposits of soils and intermediate geomaterials. Geotechnical Testing Journal. 2013. DOI: 10.1520/GTJ20130016

7. Gupta, R.C. Hyperbolic model for load tests on instrumented drilled shafts in intermediate geomaterials and rock. *Journal of Geotechnical and Geoenvironmental Engineering*. 2012. DOI: 10.1061/(ASCE)GT.1943-5606.0000697
8. Hayes, J., Simmonds, T. Interpreting strain measurements from load tests in bored piles. *Proc., 9th International Conference on Piling and Deep Foundations*. 2002.
9. Lianyang Zhang, Einstein, H.H. End bearing capacity of drilled shafts in rock. *Journal of Geotechnical and Geoenvironmental Engineering*. 1998. DOI: 10.1061/(ASCE)1090-0241(1998)124:7(574)
10. Carter, J.P., Kulhawy, F.H. *Analysis and Design of Foundations Socketed into Rock*. Electric Power Research Institute. 1988.
11. Fellenius, B.H. Capacity versus deformation analysis for design of footings and piled foundations. *Geotechnical Engineering*. 2011. 42(2). Pp. 70–77.
12. Brown, M.J., Hyde, A.F.L., Anderson, W.F. Analysis of a rapid load test on an instrumented bored pile in clay. *Geotechnique*. 2006. DOI: 10.1680/geot.2006.56.9.627
13. Lee, J.S., Park, Y.H. Equivalent pile load-head settlement curve using a bi-directional pile load test. *Computers and Geotechnics*. 2008. DOI: 10.1016/j.compgeo.2007.06.008
14. Kim, U.G., Zhuang, L., Kim, D., Lee, J. Evaluation of cyclic shear strength of mixtures with sand and different types of fines. *Marine Georesources and Geotechnology*. 2017. DOI: 10.1080/1064119X.2014.987891
15. Nam, M.S., Vipulanandan, C. Roughness and unit side resistances of drilled shafts socketed in clay shale and limestone. *Journal of Geotechnical and Geoenvironmental Engineering*. 2008. DOI: 10.1061/(ASCE)1090-0241(2008)134:9(1272)
16. Pipinato, A. *Innovative bridge design handbook: Construction, rehabilitation and maintenance* 2015.
17. Ma, M., Liu, J., Ke, Z., Gao, Y. Bearing Capacity Estimation of Bridge Piles Using the Impulse Transient Response Method. *hindawi.com*. 2016. DOI: 10.1155/2016/4187026
18. Bica, A. V.D., Prezzi, M., Seo, H., Salgado, R., Kim, D. Instrumentation and axial load testing of displacement piles. *Proceedings of the Institution of Civil Engineers: Geotechnical Engineering*. 2014. DOI: 10.1680/geng.12.00080
19. Fellenius, B.H., Harris, D.E., Anderson, D.G. Static loading test on a 45 m long pipe pile in Sandpoint, Idaho. *Canadian Geotechnical Journal*. 2004. DOI: 10.1139/T04-012
20. Nguyen, T., McVay, M., Song, X., Herrera, R., Wasman, S., Wang, K. Strength Envelopes of Florida Carbonate Rocks near Ground Surface. *Journal of Geotechnical and Geoenvironmental Engineering*. 2019. DOI: 10.1061/(ASCE)GT.1943-5606.0002069
21. Officials, T. *AASHTO guide specifications for LRFD seismic bridge design* 2011.
22. ASTM. *Standard Test Methods for Deep Foundations Under Static Axial Compressive Load*. Astm D1143/D1143M-07. 2013. DOI: 10.1520/D1143
23. Aashto. *AASHTO LRFD Bridge Design Specifications* 2010.
24. ASTM D3689. *Standard Test Methods for Deep Foundations Under Static Axial Tensile Load*. Annual Book of ASTM Standards. 2013. DOI: 10.1520/D3689
25. Chan, C.L., & Low, B.K. (2012). Probabilistic analysis of laterally loaded piles using response surface and neural network approaches. *Computers and Geotechnics*, 43, 101–110. doi.org/10.1016/j.compgeo.2012.03.001
26. Lin, C., Bennett, C., Han, J., Parsons, R.L. Integrated analysis of the performance of pile-supported bridges under scoured conditions. *Engineering Structures*. 2012. 36. Pp. 27–38. DOI: 10.1016/j.engstruct.2011.11.015
27. Zhang, L., McVay, M.C., Lai, P. Numerical analysis of laterally loaded 3 x 3 to 7 x 3 pile groups in sands. *Journal of Geotechnical and Geoenvironmental Engineering*. 1999. 125(11). Pp. 936–946. DOI: 10.1061/(ASCE)1090-0241(1999)125:11(936)
28. Ruesta, P.F., Townsend, F.C. Evaluation of laterally loaded pile group at Roosevelt Bridge. *Journal of Geotechnical Engineering*. 1997. 123(12). Pp. 1153–1161. DOI: 10.1061/(ASCE)1090-0241(1997)123:12(1153)
29. Matlock, H., & Reese, L.C. (1962). Generalized solutions for laterally loaded piles. *Transactions of the American Society of Civil Engineers*, 127(1), 1220–1247.
30. Tan, Y.C., Chow, C.M. *Foundation Design and Construction Practice in Limestone Area in Malaysia*. Proceedings of Seminar on Geotechnical Works in Karst in South-East Asia. 2006.
31. Li, W.W., Wong, C.T., Yim, K.P., Leung, M.K. Shaft friction between marble and concrete in rock-socketed large diameter bored pile: A review of state of art. *Procedia Engineering*. 2011. DOI: 10.1016/j.proeng.2011.07.220
32. Chen, Y.J., Kulhawy, F.H. Evaluation of drained axial capacity for drilled shafts. *Geotechnical Special Publication*. 2002. DOI: 10.1061/40601(256)86
33. Kulhawy, F.H. *Drilled Shaft Foundations*. Foundation Engineering Handbook 1991.
34. Rollins, K.M., Clayton, R.J., Mikesell, R.C., Blaise, B.C. Drilled shaft side friction in gravelly soils. *Journal of Geotechnical and Geoenvironmental Engineering*. 2005. DOI: 10.1061/(ASCE)1090-0241(2005)131:8(987)
35. Ke, T.N., Khanh, H.N.P. Determine load capacity of pressed piles using ζ method. *Procedia Engineering*. 2016. DOI: 10.1016/j.proeng.2016.02.054
36. Hassan, K.M., O'Neill, M.W., Sheikh, S.A., Ealy, C.D. Design method for drilled shafts in soft argillaceous rock. *Journal of Geotechnical Engineering*. 1997. DOI: 10.1061/(ASCE)1090-0241(1997)123:3(272)

Contacts:*Nguyen Chau Lan, nguyenchaulan@utc.edu.vn**May Huu Nguyen, maynh@utt.edu.vn**Bui Tien Thanh, btthanh@utc.edu.vn**Nguyen Ngoc Long, nguyenngoclong@utc.edu.vn**Le Duc Tien, ductiensogvtqt@gmail.com**Lanh Si Ho, lanhs@utt.edu.vn*



DOI: 10.18720/MCE.99.9

Bending torsion in Γ -shaped rigid and warping hinge joints

V.A. Rybakov^{*a}, D.O. Sovetnikov^b, V.A. Jos^a

^a Peter the Great St. Petersburg Polytechnic University, St. Petersburg, Russia

^b Bryden Wood Technology Ltd, London, United Kingdom

* E-mail: fishermanoff@mail.ru

Keywords: lightweight gauge steel structures, warping hinge, plane frame, thin-walled rods, Slivker's semi-shear theory, rigid joint, bimoment, warping

Abstract. This paper investigates the effect of bending torsion which is the cross-sectional warping of thin-walled rods at plane frame joints in the framework of the "semi-shear" theory of V.I. Slivker. Studied are the shell finite element models of rigid and "warping hinge" joints in thin-walled bar structures, designed and calculated in the software package Ansys Workbench. The correlation of the geometric characteristics of thin-walled profiles and the connecting plate is considered towards the change in the value of normal stresses and bimoments when the cross-sectional axis is rotated. The obtained ratios of the bimoment stresses before and after the rotation of the cross-sectional axis of the joints are presented. The study concentrates the distribution of the bimoments and warpings in the plane frame with rigid joints with and without the consideration of the coefficient of the cross-sectional axis rotation. The comparison of the obtained results for both cases is shown.

1. Introduction

This article is an extended version of the report presented on the International Scientific Conference on Energy, Environmental and Construction Engineering (EECE 2019) [1].

Nowadays thin-walled systems play a significant role in the civil engineering industry. This technology has a wide range of applications in the construction. The development of light gauge steel structures (LGSS) counterbalanced by the insufficiently research-supplied normative documents awakes interest in the scientific world and challenges engineers and scientists to take efforts in order to establish the most rational and universal methods of design for such structures. In recent years there have been dozens of publications concerning different types of problems.

Today, one of the most applicable and appropriate approaches in the design and analysis of thin-walled systems is the «semi-shear» theory of V.I. Slivker, which was firstly published in [2]. In the framework of this theory V. Lalin et al. developed the cycle of numerical methods, concerning the stiffness matrices of various thin-walled finite elements [3, 4].

The variational formulations and the finite element method are the fundamental issues of the analysis of the structures [5, 6]. The finite element analysis of the thin-walled cold-formed Z-purlins supported by sandwich panels using finite elements in the software package MSC Nastran were described by O. Tushina [7, 8]. The numerical examples in the framework of the problems of geometrically nonlinear dynamic analysis based on the corotational finite element formulation were presented in [9].

The study [10] proposed the methods of parametric optimization of thin-walled structures together with presenting the results of this optimization.

There were several papers dealing with the finite element models of cold-formed thin-walled steel profiles with solid and slotted webs. The papers [11, 12] presents results of numerical experiments about elastic shear buckling and ultimate shear strength. The derived equations demonstrate high accuracy results compare to the finite element simulation results. More detailed numerical parametric study concerning cold-formed thin-walled steel profiles was conducted in [13, 14], where the different geometric parameters and types of boundary conditions were varied in order to understand their influence on stress-strain state of the

Rybakov, V.A., Sovetnikov, D.O., Jos, V.A. Bending torsion in Γ -shaped rigid and warping hinge joints. Magazine of Civil Engineering. 2020. 99(7). Article No. 9909. DOI: 10.18720/MCE.99.9



This work is licensed under a CC BY-NC 4.0

constructions. The effects of boundary conditions on the elastic shear buckling load and the ultimate shear strength were investigated.

The buckling analysis of thin-walled steel frames with rigid joints based on the Generalised Beam Theory (GBT) was performed in [15, 16]. The shell finite element models were designed in the program package ANSYS to conduct analysis. One of the goals of these studies was simulating the warping transmission at frame joints connecting two or more members using a GBT-based beam finite element. Based on the same theory the post-buckling analysis of the thin-walled L-shaped frames and symmetric portal frames was studied in [17]. For validation purposes, most analytical results were compared to the numerical values obtained in the program package. The GBT-based (beam) finite elements were applied by authors of [18]. These finite elements were combined with the shell finite elements in order to propose a general and efficient approach to model thin-walled members with the sophisticated geometries and/or connected through joints. To validate the obtained results full shell finite element model solution were presented, confirming the high accuracy and excellent match.

The describing of the buckling of thin-walled structures was shown in [19]. This paper studies the buckling of the thin-walled two bar frame, loaded by a dead force at the joint. Various warping constraints at the bar ends are considered and the relevant buckling modes and loads are numerically evaluated.

The influence of the rotational stiffness of the beam to column connection on the strength and the stability of thin-walled structure was considered in [20]. The surrogate models and the basic techniques of their construction to calculate initial rotational stiffness of welded rectangular hollow section (RHS) joints were discussed in study [21]. Rectangular hollow section T-joints were vastly investigated in the context of axial and initial in-plane rotational stiffnesses, employing finite element modelling in order to test the existing calculation approaches; new equations, describing the chord stress behavior were derived and validated as well [22, 23].

There were investigated some methods of solving problems of bending torsion avoiding sophisticated calculational process [24]. The suggested formula makes it possible to calculate the bimoment using the previously known values of the bending moment and the eccentricity of the applied load. The paper [25] focused on the determination of the torsional characteristics. These parameters plays a significant role in the process of design of members subjected to the bending with respect to lateral torsional buckling.

Also, it is important to note that one of the core problems in creation of a universal algorithm for calculating random thin-walled rod systems is the determination of boundary conditions in joints.

One of the approaches aiming at the consideration of the boundary conditions on the ends of thin-walled rods neglects the warping of them [26]. The hypothesis within the framework of the A.R. Tusnin theory is that the warping is equal for each rod intersecting in a joint [27, 28].

The work of V.V. Yurchenko and M.A. Perelmuter disproves the Tusnin theory and states that the warping is different for each intersecting rod and does not have any dependencies [26].

The goal of the present work is the analysis of the stress-strain state of shell finite element models of the rigid and «warping hinge» joints designed in the software package Ansys Workbench and the search for the approach, considering the warping in terms of the stress transition from one element to the other in the rigidly connected plane frame joints within the framework of the V.I. Slivker theory.

Object of the research is thin-walled plane bar systems.

Subject of the research is the stress-strain state of thin-walled plane bar systems under the transverse bending load with an eccentricity.

2. Methods

The computational model is considered to be the Γ -shaped joint of a plane frame, made of thin-walled profiles.

The following symbol is introduced for further reference.

K_ω is the coefficient of the cross-sectional axis rotation that characterizes the ratio of bimoments in cross-sections on each side of the joint:

$$K_\omega = \frac{B_2}{B_1} \quad (1)$$

where B_1 is the value of the bimoment in the cross-section of the loaded thin-walled member; B_2 is the value of the bimoment in the cross-section of the load-free member.

The ratio of bimoments in the joint cross-section is equal to the ratio of the normal stresses:

$$\sigma_i = \frac{N}{A} + \frac{M_y}{I_y} z_i + \frac{M_z}{I_z} y_i + \frac{B}{I_\omega} \omega_i \quad (2)$$

It is known from literature review [2, 9, 28] that tangential stresses, appearing in the cross-sections of the joint elements, are considerably (more than 10 times) lower than normal stresses – the effect is negligible. Longitudinal force is not applied to the elements, therefore, for the estimation of the bimoments only normal stresses are accounted for:

$$\sigma \sim \frac{B}{I_\omega} \omega \rightarrow K_\omega = \frac{B_2}{B_1} = \frac{\sigma_2}{\sigma_1} \quad (3)$$

This paper investigates 3 different shell finite element models of joints in bar structures. One of them represents a rigid joint, and others are the so-called «warping hinge» joints (Fig. 1). Under «warping hinge» a bar fixation which does not correspond to the rotation of the support cross-section is assumed (the cross-section is fixed against rotation of the longitudinal axis), wherein the cross-section can get freely warped out of its plane (sectorial longitudinal forces (bimoment) are not present). This definition was firstly introduced in [29]. These models were designed and calculated in the software package Ansys Workbench.

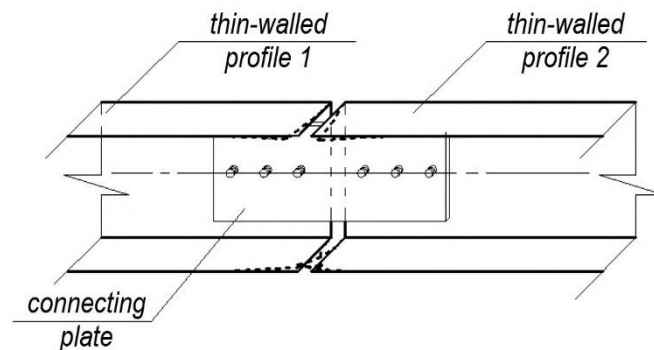


Figure 1. «Warping hinge».

2.1. Rigid joint

The Table 1 provides main geometric parameters of the rigid joint corresponding to the Standards of the Organization 83835311.001–2015 (Russia).

Table 1. Geometric parameters of the rigid joint.

| Characteristics | | Value | Unit of Measurement |
|--|--------|--------------------|---------------------|
| Basic dimensions of the profile | | 200×50×1.5 | mm |
| Length of the «beam» | | 105 | mm |
| Length of the «column» | | 450 | mm |
| Basic dimensions of the connecting plate | | 300×300×6 | mm |
| Steel density | ρ | 7858 | kg/m ³ |
| Young's modulus | E | 2·10 ¹¹ | Pa |
| Poisson's ratio | ν | 0.3 | mm |

The rigid joint is a Γ -shaped joint (Fig. 2), made of two thin-walled profiles with identical cross-sections wherein the corresponding flanges of the «beam» and «column» are extended to each other. The «beam» and «column» are rigidly assembled by non-thin connecting plate. The connection between the cross-sections of the «beam» and «column» are considered firm during the calculation. The bottom of the «column» in all of the cases is rigidly fixed.

The applied load is linearly distributed over the flanges of the cross-section simulating the action of the bimoment. The load is applied to the nodes of the finite elements (Fig. 3). The modulus of the maximum magnitude of the applied linearly distributed load is equal to 1000 N.

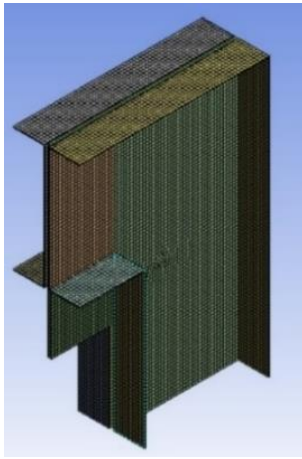


Figure 2. Finite element model of the rigid joint.

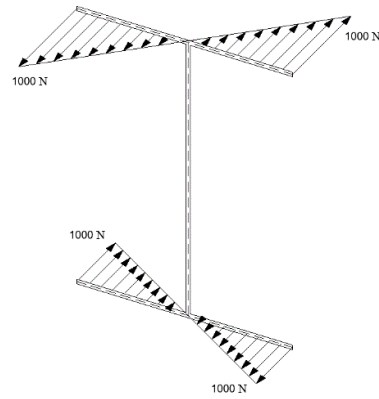


Figure 3. Applied load.

Researched are the normal stresses in the cross-sections of the “beam” and “column” one finite element (5 mm) away from the connecting plate under different parameters:

1. The thickness of the connecting plate;
2. The linear dimensions of the connecting plate;
3. The thickness of thin-walled profiles.

Table 2. Value of the coefficient of the rotation with varying connecting plane thickness for the rigid joint.

| | Normal stresses in the “beam”, MPa | | | | | | Normal stresses in the “column”, MPa | | | | | | $\frac{\bar{\sigma}_b^1}{\sigma_b^2} = \frac{B_1}{B_2}$ | $\frac{\bar{\sigma}_t^1}{\sigma_t^2} = \frac{B_1}{B_2}$ | |
|-----------------------------|------------------------------------|-----------------|-----------------|-----------------|--------------------|--------------------|--------------------------------------|-----------------|-----------------|-----------------|--------------------|--------------------|---|---|---------|
| | σ_{C1}^1 | σ_{D2}^1 | σ_{A1}^1 | σ_{B2}^1 | $\bar{\sigma}_b^1$ | $\bar{\sigma}_t^1$ | σ_{B1}^2 | σ_{D2}^2 | σ_{A1}^2 | σ_{C2}^2 | $\bar{\sigma}_b^2$ | $\bar{\sigma}_t^2$ | | | |
| Connecting plate 300x300 mm | | bottom | bottom | top | top | top (average) | top (average) | bottom | bottom | top | top | bottom (average) | top (average) | bottom/bottom | top/top |
| t = 4 mm | -28.673 | -28.673 | 28.674 | 28.674 | 28.673 | 28.674 | 6.5926 | 6.5926 | -5.3649 | -5.3649 | 6.5926 | -5.3649 | 4.349 | 5.345 | |
| t = 6 mm | -28.675 | -28.675 | 28.675 | 28.675 | 28.675 | 28.675 | 5.5515 | 5.5515 | -5.0338 | -5.0338 | 5.5515 | -5.0338 | 5.165 | 5.696 | |
| t = 8 mm | -28.679 | -28.679 | 28.676 | 28.676 | 28.679 | 28.676 | 3.9542 | 3.9542 | -3.9935 | -3.9935 | 3.9542 | -3.9935 | 6.346 | 6.665 | |

Table 2 contains the normal stresses in the «beam» and «column» in the case of the unchanging cross section of the thin-walled profile 200x50x1.5 mm and the plate with lineal dimensions 300x300 mm with varying connecting plane thickness (t = 4 mm, t = 6 mm, t = 8 mm) for the rigid joint. The numbering of cross section points is shown in the Fig. 4, Fig. 5.

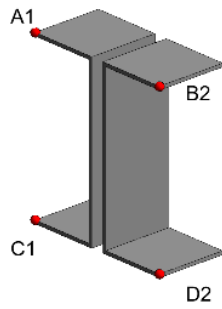


Figure 4. Calculation points in the “beam”.

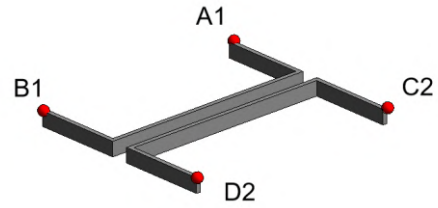


Figure 5. Calculation points in the “column”.

The obtained ratios of the bimoment stresses before and after the rotation of the cross-sectional axis of the rigid joint are reflected in the Table 3.

The graphs of the influence of the various geometric characteristics on the ratio of the normal stresses/bimoments for the rigid joint are shown in Fig. 6, Fig. 7, Fig. 8.

Table 3. Ratio of bimoment stresses in the “beam” and “column” cross-sections, depending on different geometric factors for the rigid joint.

| | Profile 200x50x1.5 mm | | | | | | Connecting plate 300x300x6 mm | | |
|------------------------|-----------------------------|----------|----------|---------------------------|------------|------------|-------------------------------|------------|----------|
| | Connecting plate 300x300 mm | | | Connecting plate t = 6 mm | | | Profile 250x50 mm | | |
| | t = 4 mm | t = 6 mm | t = 8 mm | 250x250 mm | 300x300 mm | 350x350 mm | t = 1 mm | t = 1.5 mm | t = 2 mm |
| σ bottom/bottom | 4.35 | 5.17 | 6.35 | 4.79 | 5.17 | 5.08 | 5.61 | 5.17 | 5.00 |
| σ top/top | 5.34 | 5.70 | 6.67 | 6.67 | 5.70 | 5.42 | 5.84 | 5.70 | 5.83 |

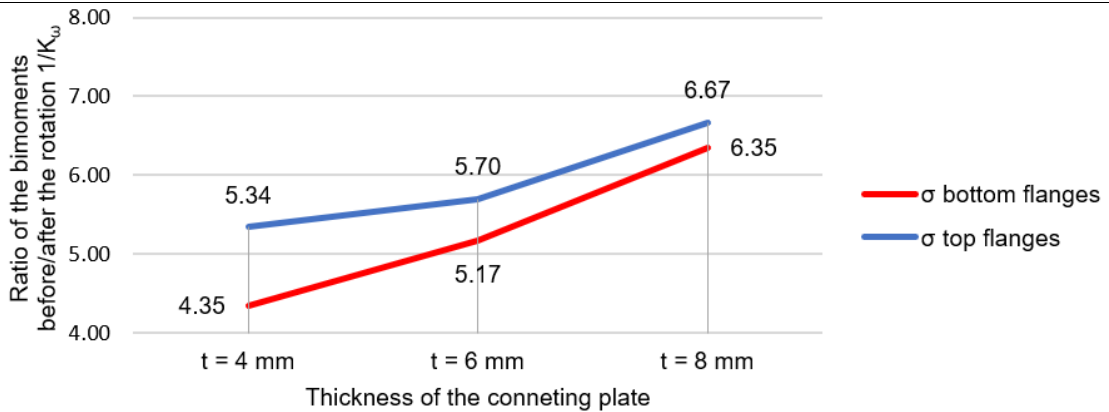


Figure 6. Dependence graphs of the bimoment change on the connecting plate thickness for the rigid joint.

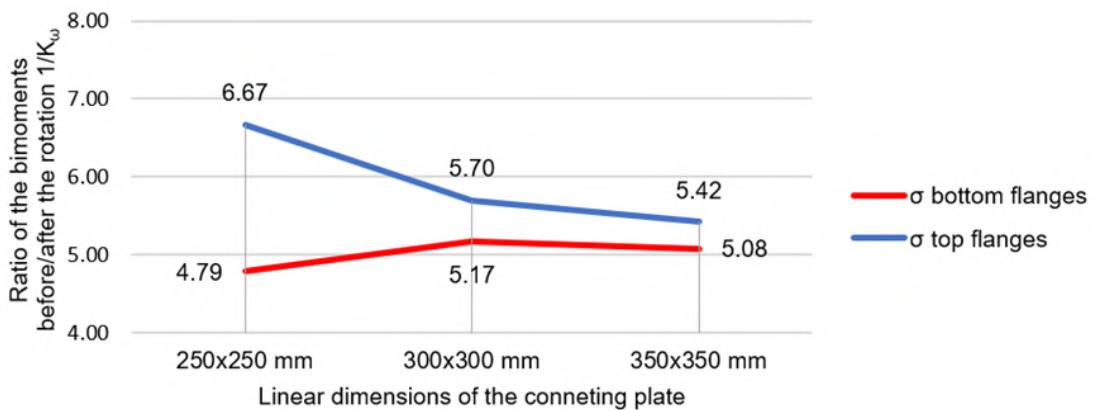


Figure 7. Dependence graphs of the bimoment change on the connecting plate linear dimensions for the rigid joint.



Figure 8. Dependence graphs of the bimoment change on the thin-walled profiles thickness for the rigid joint.

Based on the obtained results, the next conclusions were made:

1. The ratio of the normal stresses/bimoments before/after the rotation of the cross-sectional axis of the rigid joint are compatible for the top and bottom flanges;
2. The change of the normal stresses and bimoments of the rigid joint with varying connecting plane thickness has a linear dependence;
3. The change of the normal stresses and bimoments of the rigid joint with varying linear dimensions of the connecting plate has the linear dependence for the top flanges of the cross-section and has a constant value for the bottom flanges of the cross-section;
4. The change of the thickness of thin-walled profiles of the rigid joint has a negligible contribution to the value of normal stresses/bimoments before and after the rotation of the cross-sectional axis.

2.2. "Warping hinge" joints

The paper investigates two configurations of the "warping hinge" connection. The Configuration 1 represents a Γ -shaped node of two thin-walled profiles of the same cross-section firmly assembled by non-thin connecting plate (Fig. 10). The Configuration 2 is a Γ -shaped node of two thin-walled profiles of the same cross-section wherein the upper point of the "column" coincides with the level mark of the upper "beam" shelf (Fig. 11).

The connection between the flanges is not considered while the calculations – the connection represents the so-called "warping hinge" joint, which is achieved by the spacing one finite element wide (5 mm) in-between the flanges. Since the flanges of the "column" and the "beam" are not connected to each other, the connection is realized through the webs, the flanges can get freely warped out of their planes (there are no normal stresses on the ends of the flanges because the ends of the flanges are not loaded with bimoment or other axial loads). The Fig. 9 demonstrates the distribution of sectorial coordinates, which justifies the applicability of the selected models for calculation [30]. According to the graph it is clear that values along the web are equal to zero.

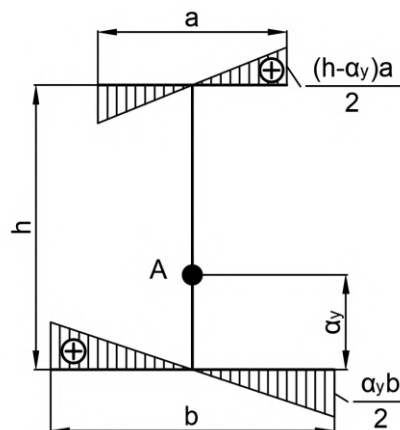


Figure 9. Distribution of sectorial coordinates.

The Table 4 demonstrates general geometric characteristics of the "warping hinge" joints corresponding to the Standards of the Organization 83835311.001–2015 (Russia).

Table 4. Geometric parameters of the “warping hinge” joint.

| Characteristics | | Value | Unit of Measurement |
|--|-----------------|--------------------|---------------------|
| Basic dimensions of the profile | | 200x50x1.5 | mm |
| Length of the “beam” | | 105 | mm |
| Length of the “column” | Configuration 1 | 250 | mm |
| | Configuration 2 | 450 | |
| Basic dimensions of the connecting plate | | 300x300x6 | mm |
| Steel density | ρ | 7858 | kg/m ³ |
| Young's modulus | E | 2·10 ¹¹ | Pa |
| Poisson's ratio | ν | 0.3 | mm |

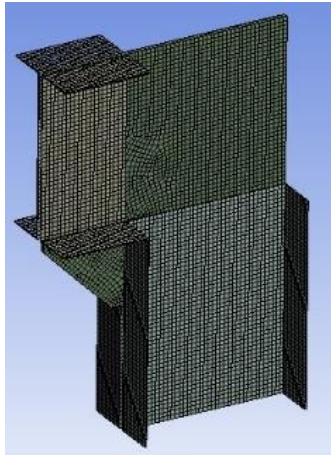


Figure 10. Finite element model of the “warping hinge” joint (Configuration 1).

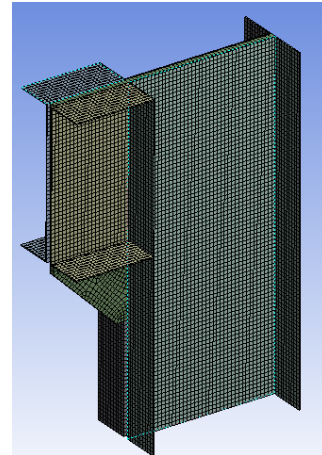


Figure 11. Finite element model of the “warping hinge” joint (Configuration 2).

The applied load has an equal value and character as it was realized with the rigid joint.

The whole algorithm of analyzing the “warping hinge” models is the same as for the rigid joint. Researched are the normal stresses in the cross-sections of the “beam” and “column” one finite element (5 mm) away from the connecting plate in the Configuration 1 and in the same points in the Configuration 2 under different parameters.

The obtained ratios of the bimoment stresses before and after the rotation of the cross-sectional axis of the “warping hinge” joints are reflected in the Table 5.

The graphs of the influence of the various geometric characteristics on the ratio of the normal stresses/bimoments for the “warping hinge” connections are shown in Fig. 12, Fig. 13, Fig. 14.

Table 5. Ratio of bimoment stresses in the “beam” and “column” cross-sections, depending on different geometric factors for the “warping hinge” joints.

| | Profile 200x50x1.5 mm | | | Connecting plate 300x300x6 mm | | | | | |
|------------------------|-----------------------------|----------|----------|-------------------------------|------------|------------|-------------------|------------|----------|
| | Connecting plate 300x300 mm | | | Connecting plate t = 6 mm | | | Profile 250x50 mm | | |
| | t = 4 mm | t = 6 mm | t = 8 mm | 250x250 mm | 300x300 mm | 350x350 mm | t = 1 mm | t = 1.5 mm | t = 2 mm |
| Configuration 1 | | | | | | | | | |
| σ bottom/bottom | 9.58 | 11.13 | 13.38 | 10.51 | 11.13 | 11.65 | 12.22 | 11.13 | 10.62 |
| σ top/top | 12.68 | 12.67 | 14.44 | 14.04 | 12.67 | 12.81 | 12.70 | 12.67 | 13.15 |
| Configuration 2 | | | | | | | | | |
| σ bottom/bottom | 5.58 | 5.93 | 7.98 | 4.75 | 5.93 | 7.10 | 6.56 | 5.93 | 6.36 |
| σ top/top | 5.52 | 6.40 | 7.93 | 4.74 | 6.37 | 7.54 | 6.51 | 6.40 | 6.30 |

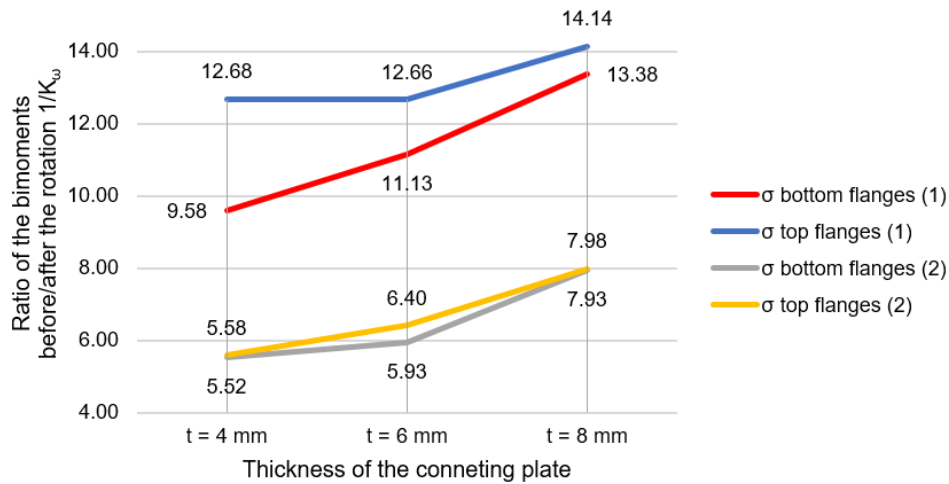


Figure 12. Dependence graphs of the bimoment change on the connecting plate thickness for the “warping hinge” joints.

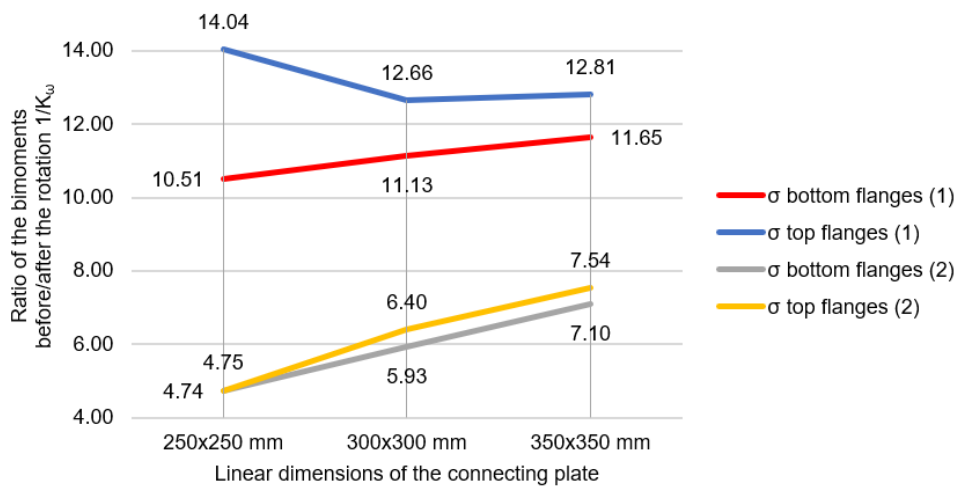


Figure 13. Dependence graphs of the bimoment change on the connecting plate linear dimensions for the “warping hinge” joints.

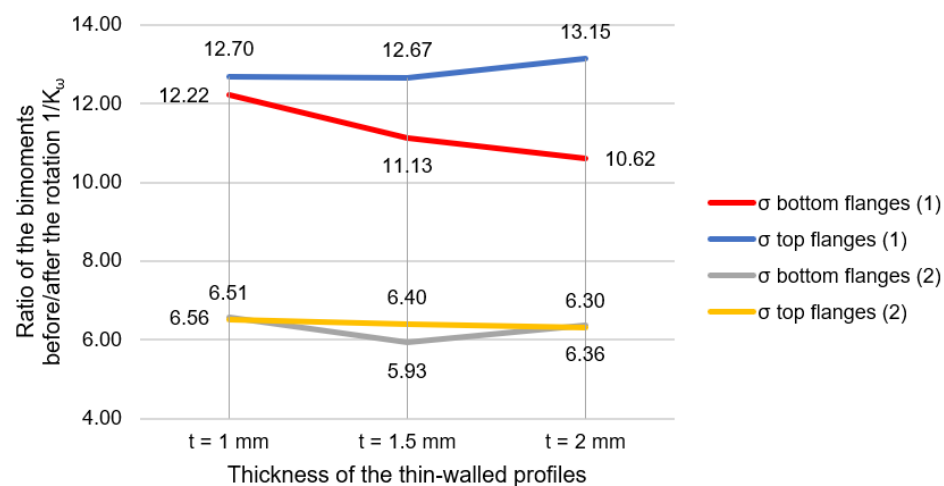


Figure 14. Dependence graphs of the bimoment change on the thin-walled profiles thickness for the “warping hinge” joints.

Based on the obtained results the following conclusions can be drawn:

1. The reduction coefficient should be regarded when the rotation of the axis of the “warping hinge” in considered;
2. The relation between the normal stresses/bimoments before/after the rotation of the cross-sectional axis in case of the Configuration 1 has a divergence for low and upper flanges of more than 15 %. For the Configuration 2 these ratios have approximately the same values;

3. The change of normal stresses and bimoments under different geometrical characteristics of the connecting plate (when measuring the thickness and linear dimensions) has a linear dependency in case of “warping hinge” connection;

4. The change in the profile thickness does not have a significant influence on the ratio between the normal stresses/bimoments before/after the rotation of the cross-section.

3. Results and Discussion

Within the framework of the Tusnín theory [26] the rotation cosine of the warping measure is equal to 1, which means that the warping does not depend on the coordinate system.

For the comparison with the Tusnín theory let us assume the bimoment to be a conditional vector, rotation angle cosine of which is define as a ratio of the bimoment after the rotation of the structure axis to the bimoment before the rotation (i.e. instead of 1 assume the value of the coefficient K_ω).

The computational model is the frame consisting of three bars (Fig. 15). The length of columns is 4 m, the length of the crossbar is 6 m. The calculation was performed in the software Maple. The parameters of the bar cross-section are taken as for the coupled out of two thin-walled profiles PN200–50–1.5 (Fig. 16).

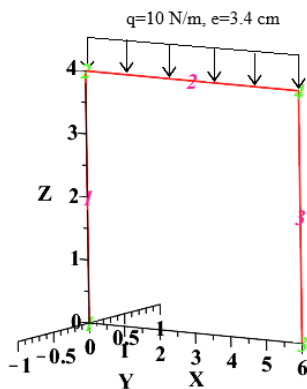


Figure 15. Computational model in Maple.

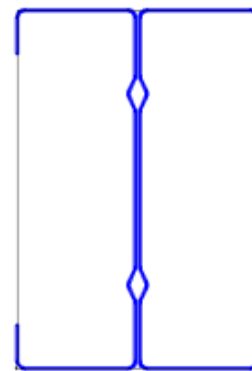


Figure 16. Coupled profile PN200–50–1.5.

Below are the graphs of the distribution of the bimoments and warpings along the columns and the crossbar for the rigid joint without considering the coefficient K_ω (Fig. 17, Fig. 19).

Further the K_ω is assumed as for the rigid connection with the value of 0.184. This value of the coefficient is referred to as the cosine of the rotation and is exceptionally applied to two finite column elements, adjacent to the crossbar.

Graphs of the distribution of the bimoments and warpings along the columns and the crossbar for the rigid joint with the coefficient $K_\omega = 0.184$ are presented below (Fig. 18, Fig. 20).

For the calculation with the rotation coefficient the obtained bimoments are neglected on the ends of the columns, adjoit to the crossbar, since the area is within the joint connection.

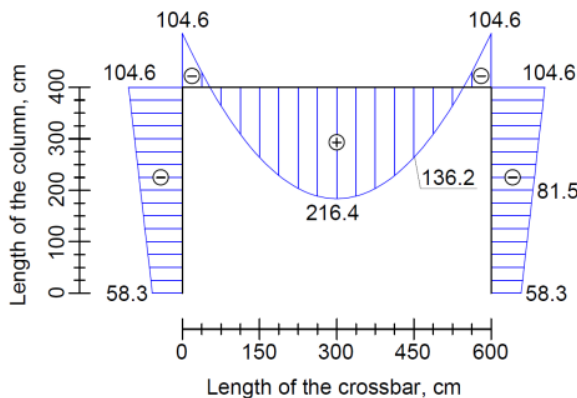


Figure 17. Distribution of the bimoment (daN·cm²) without considering the K_ω .

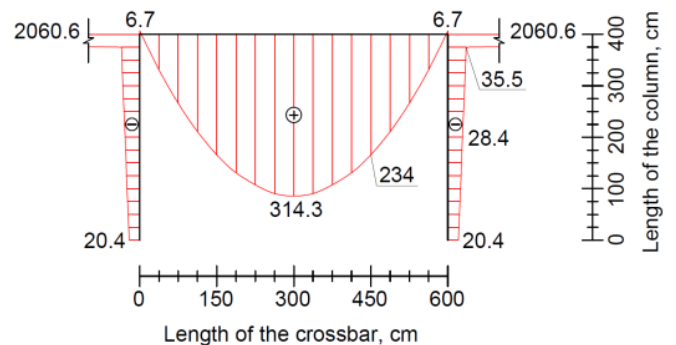


Fig. 18. Distribution of the bimoment (daN·cm²) with the $K_\omega = 0.184$

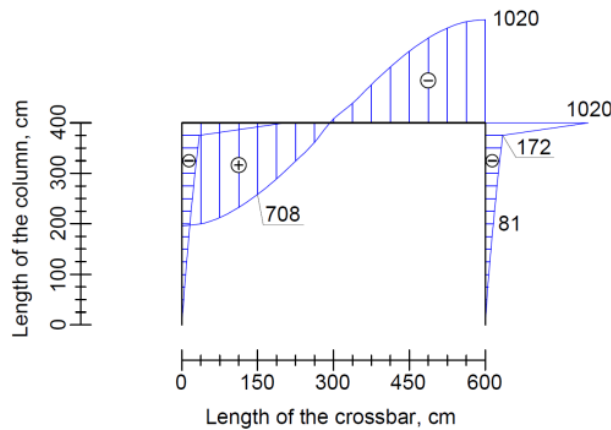


Figure 19. Distribution of the warping (10^{-7} cm^{-1}) without considering the K_{ω} .

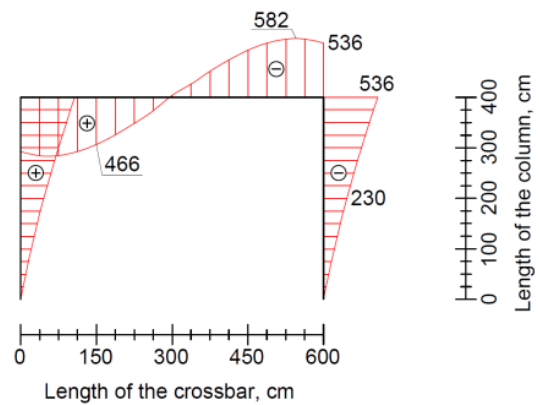


Figure 20. Distribution of the warping (10^{-7} cm^{-1}) with the $K_{\omega} = 0.184$.

Observing the graphs of the distribution of the bimoments (Fig. 18, Fig. 19) it is important to make next notes.

1) Adding moduli of maximum and minimum values of the bimoment distributed along the crossbar for the calculations with and without the rotation coefficient and equating the obtained values, the next expression is derived:

$$\begin{aligned} (|104.6| + |216.4|) \text{ daN} \cdot \text{cm}^2 &= (|314.3| + |6.7|) \text{ daN} \cdot \text{cm}^2 \\ 321 \text{ daN} \cdot \text{cm}^2 &= 321 \text{ daN} \cdot \text{cm}^2 \end{aligned} \quad (4)$$

The identity of the shape and dimensions (4) of the distribution of the bimoment diagrams along the crossbar indirectly confirms the correctness of the obtained results.

2) Comparing the maxima of the bimoments distributed along the crossbar for the calculations with and without the rotation coefficient, one is observed that the maximum value of the bimoment for the calculation considering the rotation coefficient is 31 % higher than the maximum value without considering the rotation coefficient (5).

$$216.4 \text{ daN} \cdot \text{cm}^2 < 314.3 \text{ daN} \cdot \text{cm}^2 \quad (5)$$

Such a difference in the obtained results (5) may affect the correctness of the calculated strength of the structure.

4. Conclusion

1. The Tusnín theory of the warping identity of all intersecting in a joint bars does not apply to the calculation of the cross-sectional axis rotation of the thin-walled profiles.

2. The values of normal stresses and the corresponding bimoments are changed considerably with the rotation of the cross-sectional axis (4.3–5.8 times).

3. The coefficient of the cross-sectional axis rotation linearly depends on the change of the geometric parameters of the connecting plate.

4. The change of the thickness of thin-walled profiles negligibly contributes to the value of the coefficient of rotation of the cross-sectional axis.

5. For the observed rigid connection the value of the bimoment with the consideration of the coefficient of the rotation along the column length is 2.86 times reduced in comparison to the calculation without the rotation coefficient. At the same time the value of the bimoment in the joint directly increases by 19.7 times.

6. The maximum value of the bimoment with the consideration of the coefficient of the rotation along the crossbar length is 1.45 times bigger than the one obtained without considering the rotation coefficient.

7. The shape and the dimensions of the distribution of the bimoment diagrams along the crossbar are identical for the calculation with and without the rotation coefficient, which confirms the correctness of the calculations.

References

1. Rybakov, V., Sovetnikov, D., Jos, V. Cross-Sectional Warping of Thin-Walled Rods at Plane Frame Joints. Proceedings of EECE 2019. Lecture Notes in Civil Engineering. 2020. Vol. 70. Pp. 241–243. DOI: 10.1007/978-3-030-42351-3_20
2. Slivker, V.I. Stroitel'naya mekhanika. Variatsionnye osnovy. [Structural mechanics. Variational basis]. Moscow: ASV, 2005. 710 p. (rus)
3. Lalin, V., Rybakov, V., Sergey, A. The finite elements for design of frame of thin-walled beams. Applied Mechanics and Materials. 2014. Vol. 578-579. Pp. 858–863.
4. Lalin, V.V., Rybakov, V.A., Diakov, S.F., Kudinov, V.V., Orlova, E.S. The semi-shear theory of V.I. Slivker for the stability problems of thin-walled bars. Magazine of Civil Engineering. 2019. 87(3). Pp. 66–79. DOI: 10.18720/MCE.87.6
5. Crisfield, M.A. Non-linear Finite Element Analysis of Solids and Structures. Vol. 2. Wiley: Chichester, 1977.
6. Lalin, V.V., Zdanchuk, E.V., Kushova, D.A., Rozin, L.A. Variational formulations for non-linear problems with independent rotational degrees of freedom. Magazine of Civil Engineering. 2015. 56(4). Pp. 54–65. (rus). DOI: 10.5862/MCE.56.7
7. Tushina, O. A finite element analysis of cold-formed Z-purlins supported by sandwich panels. Applied Mechanics and Materials. 2014. Vol. 467. Pp. 398–403.
8. Tushina O. An influence of the mesh size on the results of finite element analysis of Z-purlins supported by sandwich panels. Applied Mechanics and Materials. 2014. Vol. 475–476. Pp. 1483–1486.
9. Hsiao, K.M., Lin, J.Y., Lin, W.Y. A consistent co-rotational finite element formulation for geometrically nonlinear dynamic analysis of 3-D beams. Computer Methods in Applied Mechanics and Engineering. 1999. 169 (1). Pp. 1–18.
10. Kibkalo, A., Lebedeva, M., Volkov, M. Methods of Parametric Optimization of Thin-Walled Structures and Parameters which Influence on it. MATEC Web of Conferences 53. 2016. No. 01051.
11. Degtyarev, V.V., Degtyareva, N.V. Finite element modeling of cold-formed steel channels with solid and slotted webs in shear. Thin-Walled Structures. 2016. Vol. 103. Pp. 183–198. DOI: 10.1016/j.tws.2016.02.016
12. Degtyarev, V.V., Degtyareva, N.V. Numerical simulations on cold-formed steel channels with longitudinally stiffened slotted webs in shear. Thin-Walled Structures. 2018. Vol. 129. Pp. 429–546. DOI: 10.1016/j.tws.2018.05.001
13. Degtyarev, V.V., Degtyareva, N.V. Numerical simulations on cold-formed steel channels with flat slotted webs in shear. Part I: Elastic shear buckling characteristics. Thin-Walled Structures. 2017. Vol. 119. Pp. 22–32. DOI: 10.1016/j.tws.2017.05.026
14. Degtyarev, V.V., Degtyareva, N.V. Numerical simulations on cold-formed steel channels with flat slotted webs in shear. Part II: Ultimate shear strength. Thin-Walled Structures. 2017. Vol. 119. Pp. 211–223. DOI: 10.1016/j.tws.2017.05.028
15. Basaglia, C., Camotim, D., Silvestre, N. GBT-based local, distortional and global buckling analysis of thin-walled steel frames. Thin-Walled Structures. 2009. Vol. 47. Pp. 1246–1264. DOI: 10.1016/j.tws.2009.04.003
16. Basaglia, C., Camotim, D., Silvestre, N. Global buckling analysis of plane and space thin-walled frames in the context of GBT. Thin-Walled Structures. 2008. Vol. 46. Pp. 79–101. DOI: 10.1016/j.tws.2007.07.007
17. Basaglia, C., Camotim, D., Silvestre, N. Post-buckling analysis of thin-walled steel frames using generalised beam theory (GBT). Thin-Walled Structures. 2013. Vol. 62. Pp. 229–242. DOI: 10.1016/j.tws.2012.07.003
18. Manta, D., Gonçalves, R., Camotim, D. Combining shell and GBT-based finite elements: Linear and bifurcation analysis. Thin-Walled Structures. 2020. Vol. 152. 106665. DOI: 10.1016/j.tws.2020.106665
19. Pignataro, M., Rizzi, N., Ruta, G., Varano, V. The effects of warping constraints on the buckling of thin-walled structures. Journal of Mechanics of Materials and Structures. 2009. Vol. 4. Pp. 1711–1727. DOI: 10.2140/jomms.2009.4.1711
20. Atavin, I.V., Melnikov, B.E., Semenov, A.S., Chernysheva, N.V., Yakovleva, E.L. Influence of stiffness of node on stability and strength of thin-walled structure. Magazine of Civil Engineering. 2018. 80(4). Pp. 48–61. DOI: 10.18720/MCE.80.5
21. Garifullin, M., Pajunen, S., Mela, K., Heinisuo, M., Havula, J. Initial in-plane rotational stiffness of welded RHS T joints with axial force in main member. Journal of Constructional Steel Research. 2017 Vol. 139. Pp. 353–362.
22. Garifullin, M., Vatin, N., Jokinen, T., Heinisuo, M. Numerical solution for rotational stiffness of RHS tubular joints. Advances and Trends in Engineering Sciences and Technologies II – Proceedings of the 2nd International Conference on Engineering Sciences and Technologies. 2017. Vol. 165. Pp. 1643–1650.
23. Garifullin, M., Bronzova, M., Pajunen, S., Mela, K., Heinisuo, M. Initial axial stiffness of welded RHS T joints. Journal of Constructional Steel Research. 2019. Vol. 153. Pp. 459–472.
24. Rybakov, V.A., Sergey, A. Mathematical analogy between non-uniform torsion and transverse bending of thin-walled open section beams. Applied Mechanics and Materials. 2015. Vol. 725-726. Pp. 746–751.
25. Horacek, M., Melcher, J., Balazs, I., Pesek, O. On Problem of Torsional Characteristics of Thin-walled Steel Beams with Web Openings. IOP Conference Series: Materials Science and Engineering. 2019. Vol. 471. 052040. DOI: 10.1088/1757-899X/471/5/052040
26. Perelmuter, A., Yurchenko, V. On the issue of structural analysis of spatial systems from thin-walled bars with open profiles. Metal constructions. 2014. Vol. 20. No. 3. Pp. 179–190.
27. Tushin, A.R. Finite element for numeric computation of structures of thin-walled open profile bars. Metal constructions. 2009. Vol. 15. No. 1. Pp. 73–78.
28. Tushin, A.R. Features of numerical calculation of designs from thin-walled bars of an open profile. Industrial and Civil Engineering. 2010. No. 11. Pp. 60–63.
29. Rybakov, V.A. Metodi resheniya nauchno-tekhnicheskikh zadach v stroitel'stve. Chislennye metody rascheta tonkostennih sterzhnei. [Methods for solving scientific and technical problems in construction. Numerical methods for calculating thin-walled rods]. Saint Petersburg: SPbPU, 2013. 167 p. (rus)
30. Vlasov, V.Z. Thin-walled elastic beams. Israel Program for Scientific Translation. Jerusalem, 1961. 493 p.

Contacts:

Vladimir Rybakov, fishermanoff@mail.ru

Daniil Sovetnikov, sovetnikov.daniil@gmail.com

Vladislav Jos, jos_vlad@mail.ru



DOI: 10.18720/MCE.99.10

Behavior of B-C connections damaged by thermal shock

R. Al-Rousan*

Jordan University of Science and Technology, Irbid, Jordan

* E-mail: rzalrousan@just.edu.jo

Keywords: reinforced concrete, thermal shock, structural strength, horizontal load, fiber reinforced polymer, nonlinear, finite element analysis.

Abstract. The behavior of beam-column (B-C) connections received thorough investigation during the past decades focusing on critically-detailed connections before and after strengthening. Exposure of such B-C connections to thermal shock due to subjected to cycles of heating-cooling such as in chimneys, concrete foundations for launching rockets carrying spaceships, concrete near to furnace, clinker silos and nuclear power plants, or those subjected to fire then extinguished using water would aggravate the weakness of the high joint zone. In this study, systematic nonlinear finite element analyses (NLFEA) were conducted using ANSYS to evaluate the effects of the level of the column axial load and thermal shock impact which is a parameter difficult to evaluate experimentally due to limitations in loading machines and requirement for complicated testing setups. A total of eight NLFEA models were created, calibrated and properly verified with reputable experimental literature results. The NLFEA results showed that both level of the column axial load and thermal shock impact significantly affect the cracks distribution, failure mode, ultimate load capacity, and ductility of the B-C connection. Column axial load levels up to 75 % were advantageous to the behavior of virgin B-C connections. The lateral load capacities, net drifts, hysteresis loops, cracks distribution, energy dissipation, and failure modes were presented.

1. Introduction

One of the main reasons for collapsing of reinforced concrete frame structures is the failure of the B-C connections by shearing of the joint or column. Critical beam-column (B-C) connection details common in buildings constructed before 1970s and still used in third-world countries include: discontinuous bottom beam reinforcement, lap-splicing of the column bars just above the joint, and lack of joint confinement. Proper strengthening of the B-C joint results in improved structural behavior and failure mode transformation [1]. Failure of the joint or the column is sudden and accompanied with low ductility and energy dissipation. It leads to dangerous local collapses that may cause progressive total collapse of the structure. The other failure mode is a desired ductile one in the beam typically at short distance from the face of the column. It is important when analyzing the B-C connections to consider all the aforementioned failure modes.

Recent studies focused on creating numerical simulations and modeling of the B-C joint under seismic loading. Researchers proposed three types of B-C joint models such as: rotational hinge models [2]; component models [3–5], and nonlinear finite element analysis (NLFEA) [6]. Each model has advantages and limitations, and there is no scientific agreement on a model that is optimal for all applications. However, NLFEA that takes into consideration materials and geometric nonlinearities provides accurate results if properly simulated, calibrated, and validated with reputable experimental results. It also saves tremendous amount of time and cost compared with experimental testing [6–7]. Using a strut-and-tie model, Sasmal et al. [8] found that most of the energy was dissipated through the development of damage in the joint region, which not safe for the stability of the entire structure. Venkatesana et al. [6] carried out experimental tests and numerical simulations using ANSYS software for the seismic performance of exterior B-C joints before and after strengthening with ferrocement jackets, and found that the analytical shear strength predictions were in line with the test results. Sasmal and Nath [7] introduced a steel bracing technique to strengthen poorly designed B-C joints, and their NLFEA using ATENA package demonstrated the improvement in crack patterns, ultimate load, energy dissipation, and ductility after strengthening. Lima et al. [9] modeled the exterior B-C joints as nonlinear rotational spring elements, and their results confirmed that neglecting the effects of joints damage



might potentially lead to non-conservative seismic assessment of existing reinforced concrete framed structures. Ibrahim et al. [10] carried out finite element modeling of exterior beam-column joints strengthened by ferrocement under cyclic loading found that the effect of orientation angle became less significant on the ductility with increasing the number of ferrocement layers used for strengthening. More recent studies were published [11–14] and provided good information toward better understanding of the behavior of the B-C joints, which considered essential for future calibration of the design codes as well as repairing techniques.

Elevated temperatures cause severe damage for reinforced concrete (RC) structures, such as RC beams. RC beams have been reported to loss strength and stiffness with relatively large permanent deformations because of exposure to high temperatures [15]. These harmful effects could be attributed to the deterioration of mechanical characteristics of concrete and steel rebars and the redistribution of stresses within the beam due to the elevated temperatures [15, 16]. Currently, the most used technique to repair the heat-damaged RC beams is using carbon fiber reinforced polymer (CFRP) composites. These sheets are advanced materials that can be easily applied on the structures and characterized by outstanding mechanical and corrosion resistance characteristics. Various studies were performed to investigate the flexural behavior of RC beams wrapped with CFRP. The results showed that externally bonded carbon FRP (CFRP) sheets and laminates can enhance the flexural behavior of the beams and recover, to certain limit, the flexural strength of heat-damaged beams. Strengthening level or recovery depends on several factors such as fire resistance [17], elevated temperature [18, 19], fiber type [20–23], analysis type [24–28], energy integrity resistance [29], anchored system [30], heating condition [31–33], degree of beam's damage and geometry and type of fiber sheet [34], and safety factors for CFRP strengthening of bridges [35].

Reinforcing concrete structures are often subjected to cycles of heating–cooling such as in chimneys, concrete foundations for launching rockets carrying spaceships, concrete near to furnace, clinker silos and nuclear power plants, or those subjected to fire then extinguished using water. Temperature cycles are critical to the stability of concrete structures and require considerations upon design [36, 37]. As well stipulated, the mechanical properties of concrete are preserved for exposure temperatures below 300 °C, yet are decreased considerably as temperature exceeds 500 °C. Additional damage results from rapid cooling such as in the case of distinguishing of fire with cool water due to creation of temperature gradient between concrete core and its surface. This results in tensile stresses on the concrete surface that are high enough to crack concrete and this considered as another source of damage results from incompatible expansion and contraction of aggregate and surrounding cement paste. The magnitude of damage is influenced by many factors such as the size of concrete members, the type of cement and aggregate, the concrete moisture content and the predominant environmental factors, Those are represented in heating exposure time and rate, type of cooling, and maximum temperature attained [38]. Different types of materials and techniques were used in strengthening and retrofitting of existing concrete structures such as steel plates bolting, reinforced concrete jackets, pre-stressed external tendons, and most recently FRP composite which has been used on a large scale in different countries. FRP composites have many advantages over conventional methods represented in ease of application, high strength-to-weight ratio, excellent mechanical strength, and good resistance to corrosion, especially that most structures are damaged due to dynamic loads, corrosion of steel, and freeze-thaw cycles [39, 40].

Many reinforced concrete bridges are deteriorating due to problems related to environment and increase in load of trucks. Also, the impact of thermal shock on the behavior of deficient reinforced concrete B-C connections must receive miniature consideration. The scientific problem considered in the study is indeed one of the problems in the modern theory of deficient reinforced concrete B-C connections. A lack of literature regarding behavior of deficient columns damaged by thermal shock necessitated conducting the present investigation. In this study, NLFEA program were carried out to find the improvements in the strength and ductility behavior of reinforced concrete (RC) B-C connections damaged by thermal shock. This parametric study provides systematic nonlinear FEA using ANSYS software addressing key parameters related to the behavior of B-C connections under cyclic loading. The study takes into consideration.

The study is aimed at establishing the impact of thermal shock on the structural behavior of reinforced concrete B-C connections. As a result of the work carried out, the following tasks were solved: (1) the effect of the column axial load up to high levels (0, 25 %, 50 %, and 75 %), which is a parameter difficult to evaluate experimentally due to limitations in the loading machines and requirement of a special setup; (2) the significant reduction in strength and ductility of B-C connection due to thermal shock; (3) the impact of thermal shock on the lateral load capacities, net drifts, hysteresis loops, cracks distribution, energy dissipation, and failure modes. Eight NLFEA models were created, calibrated, and properly verified with the experimental results published by Shannag and Alhassan [1]. The actual loading setup, dimensions, reinforcement details, materials properties for the concrete and steel were considered in the NLFEA models.

2. Methods

ANSYS V16 software is an effective numerical method and important tool in the analysis of complex structures. The main benefits that NLFEA include: 1) substantial savings in the cost, time, and effort compared

with the fabrication and experimental testing of structure elements; 2) allows to change any parameter of interest to evaluate its influence on the structure, such as the concrete compressive strength; 3) allows to see the stress, strain, and displacement values at any location and at any load level. Eighteen full-scale models strengthened using CFRP are developed to carry out different investigated parameters.

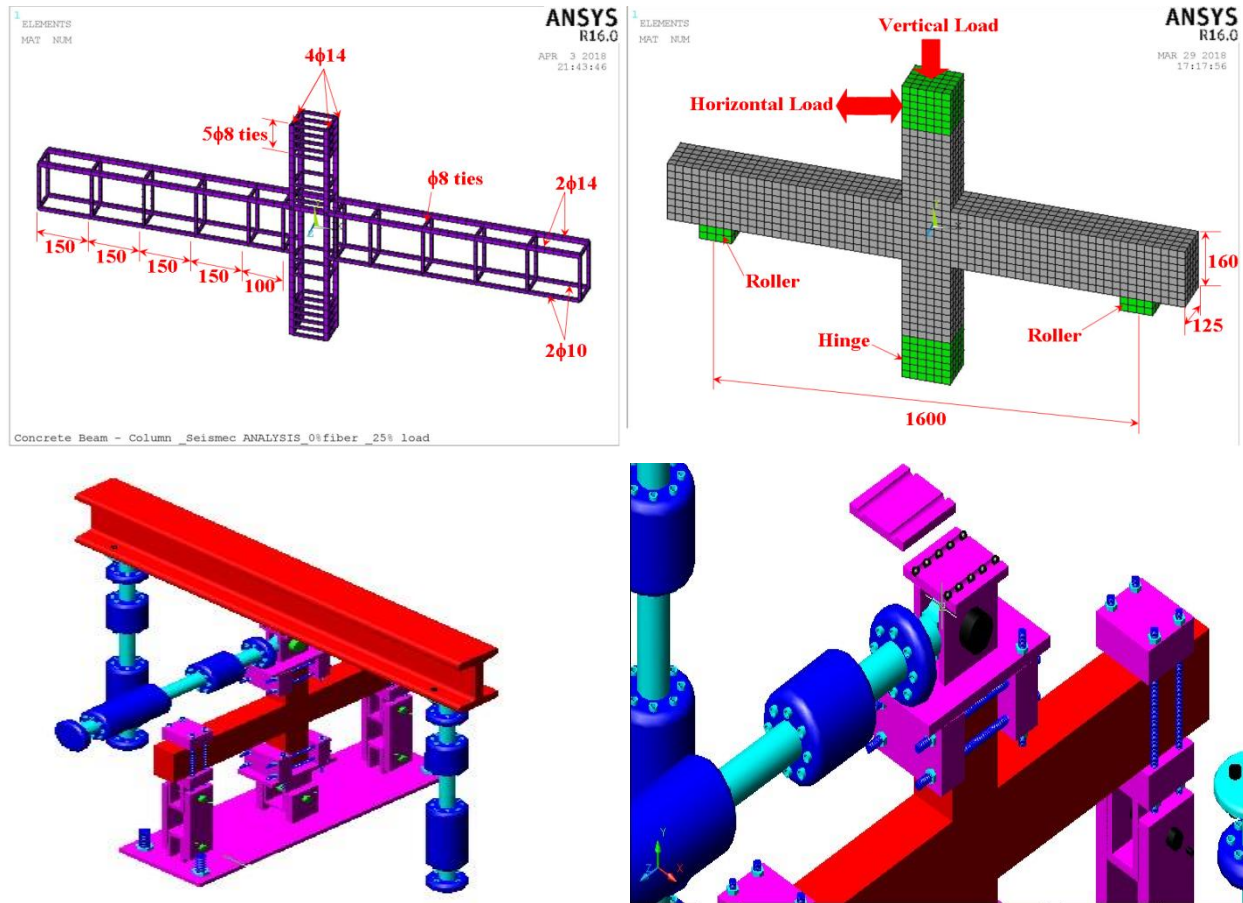


Figure 1. Specimen geometry, steel detailing, and schematic of applied loads setup (dimensions are in mm) [1].

2.1. Experimental Work Review

The validation process of the finite element model is based on the experimental work performed by Shannag and Alhassan [1]. The experimental work used in this paper was conducted by Shannag and Alhassan [6] and the basic NLFEA models were calibrated based on that tested specimens. A total of ten nonlinear NLFEA models were created, calibrated, and properly verified with reputable experimental results, therefore the actual member's dimensions and reinforcement details as shown in Fig. 1. The column was rectangular with dimension 125×150 mm and 750 mm in cross-section and length, while the beam was rectangular with 200×125 mm and 1600 mm in cross section and length. The support was hinged at the bottom end of the column while kept free at the other end to allow for relative drift; simple rollers supported the beams-ends as shown in (Fig. 1).

2.2. Description of Non-linear Finite Element Analysis (NLFEA)

Concrete is non-homogenous and brittle material and has different behavior in tension and compression. SOLID 65 element is capable to predict the nonlinear behavior of concrete materials by using a smeared crack approach by ultimate uniaxial tensile and compressive strengths. The average compressive strength of the cylinders before and after being damaged by thermal shock were 25.8 and 10 MPa, respectively, and the average splitting tensile strength of the cylinders before and after being damaged by thermal shock were 3.1 and 0.7 MPa, respectively [41]. Poisson's ratio of 0.2 and shear transfer coefficient (β_t) of 0.2 for β_t was used in this study. Fig. 2(a) shows the stress-strain relationship for unconfined concrete which describes the post-peak stress-strain behavior.

LINK180 element was used to model the steel reinforcement. The 3-D spar element is a uniaxial tension-compression element with three degrees of freedom at each node with translations in the nodal x, y, and z directions. The element is also capable of plastic deformation. The steel in simulated models was assumed to be an elastic-perfectly plastic material and the same in compression and tension. There are two types of steel reinforcement in column, longitudinal bars (axial) with 14 mm-diameter and lateral bars (stirrups)

with 8 mm-diameter and spacing of 250 mm, and there are two types of steel reinforcement in beam, longitudinal bars (axial) with 14, 10 mm-diameter and lateral bars (stirrups) with 8 mm-diameter and spacing of 150 mm. Poisson's ratio of 0.3 and the yield stress of undamaged and damaged columns were 300 MPa and $0.78f_y$ [42], respectively, as well as the elastic modulus were 200 GPa and $0.6E_s$ [32], respectively, were used for the steel reinforcement. Fig. 2(b) shows the idealized stress-strain relationship. The steel plates were assumed to be linear elastic materials with a Poisson ratio and elastic modulus of 0.3 and 200 GPa, respectively.

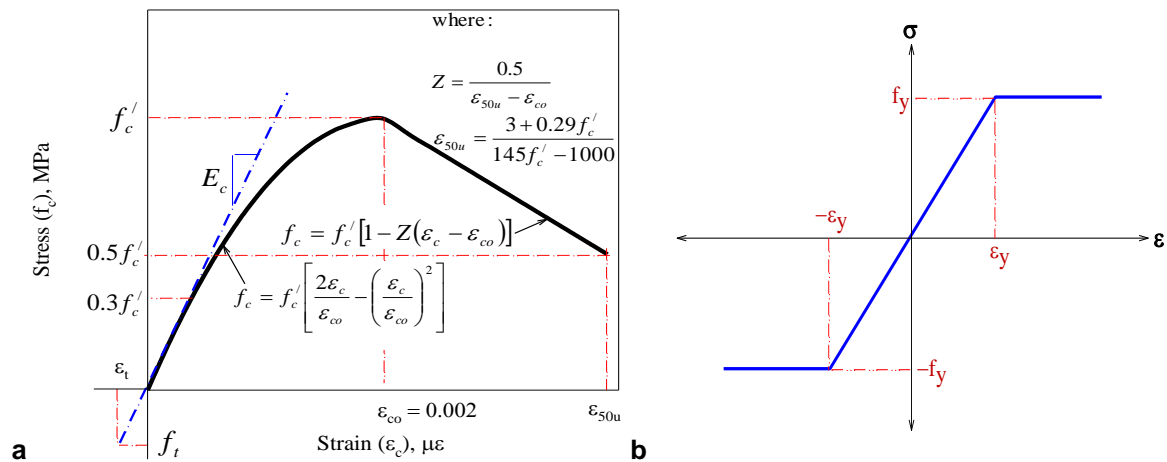


Figure 2. Stress-strain curves for: a. unconfined concrete [41] and b. steel reinforcement [42].

Table 1. Maximum loads and drifts under cyclic loading.

| Group | Specimen | Axial load, % | Un-damaged/ Damaged | Maximum horizontal load, kN | Maximum horizontal net drift, mm |
|-------|----------|---------------|------------------------|--------------------------------|-------------------------------------|
| I | BC0J-UD | 0 | Un-damaged | 14.5 | 7.67 |
| | BC25J-UD | 25 | | 21.8 | 15.05 |
| | BC50J-UD | 50 | | 26.2 | 22.51 |
| | BC75J-UD | 75 | | 27.6 | 26.52 |
| II | BC0J-D | 0 | Damaged | 9.2 (0.63) | 6.19 (0.81) |
| | BC25J-D | 25 | | 14.7 (0.67) | 11.85 (0.79) |
| | BC50J-D | 50 | | 18.2 (0.69) | 17.21 (0.76) |
| | BC75J-D | 75 | | 20.4 (0.74) | 20.86 (0.74) |

Note: C: Column, UD: un-damaged, D: Damaged

Full model was simulated to study the behavior of the control reinforced concrete B-C connection. The bond between the concrete and reinforcing bars was assumed to be perfect (no slippage). Also, full bond was assumed between the concrete and HPCJ to simulate strong contact interface, so coincide nodes were merged into single node with an appropriate tolerance. A convergence study was conducted to specify the optimum mesh size with 25 mm element meshing size as shown in Fig. 1. The boundary conditions at the two ends of the beam were constrained vertically $U_y = 0$, whereas the bottom end of the column was modeled as hinge support. The column axial load was applied at first loading step, and then the horizontal load was applied as displacement-controlled loading to ensure that the descending part of the load-displacement response curve is involved. This loading was applied incrementally to avoid sudden failure (solution divergence); the more the load sub-steps within a loading step, the more stable is the analysis process. ANSYS can automatically divide the loading into steps, but the number of sub-steps must be inserted manually. For each loading increment, the stiffness matrix of each element is updated each iteration to achieve the nonlinear response convergence using Newton-Raphson equilibrium iterative method with a tolerance of 0.001.

2.3. Investigated Parameters

The ANSYS program package was used to simulate the actual seismic structural behavior of the validated specimens as shown in Table 1. After that the simulated models were expanded to provide a parametric study in terms of the effect of column axial load level (0 %, 25 %, 50 %, and 75 %) and thermal shock damaged (un-damaged control B-C connection damaged B-C connection). A full description of the finite element modeling groups is shown in Table 1.

2.4. Validation Process

The basic NLFEA models were calibrated based on the tested specimens by Shannag and Alhassan [1] and therefore the actual members' dimensions and reinforcement details (Fig. 1) as well as materials properties for the concrete and steel (Fig. 2) were considered in the NLFEA models. Proper calibration was ensured using proper mesh size, boundary conditions, rate of loading, and considering materials' nonlinearities. Fig. 3 (top) shows the experimental load-drift hysteresis results for a virgin (top left) and strengthened (top right) B-C connections tested by Shannag and Alhassan [1]. Fig. 4 also shows the NLFEA results of this study for companion models. It can be clearly seen that the agreement is very good between the experimental and NLFEA results in terms of the ultimate load, ultimate drift, stiffness, degradation during the pushing and pulling stages of the loading. The cracking patterns, deformed shapes, and failure modes generated from the NLFEA were logical and in good agreement with the experimental results (Fig. 5).

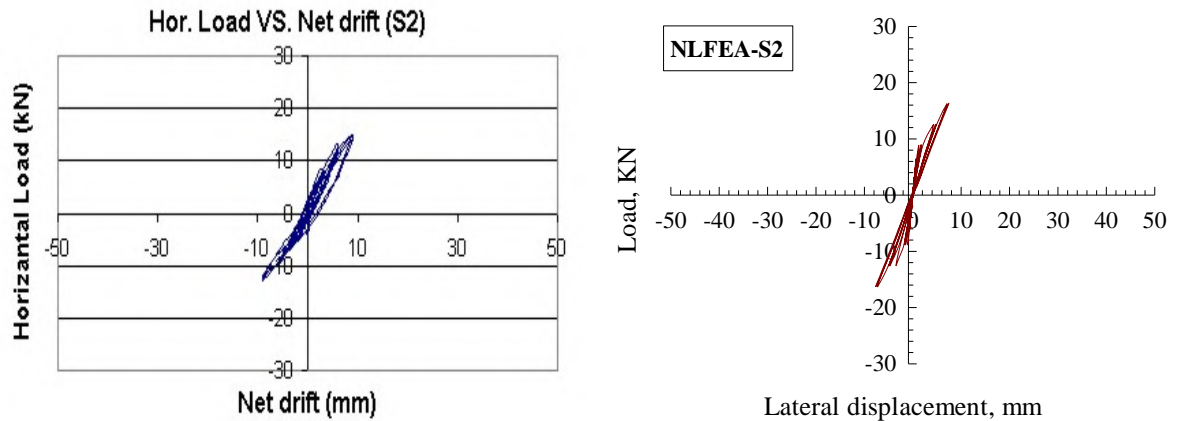


Figure 4. Validation of the NLFEA results with Shannag and Alhassan [1] results.

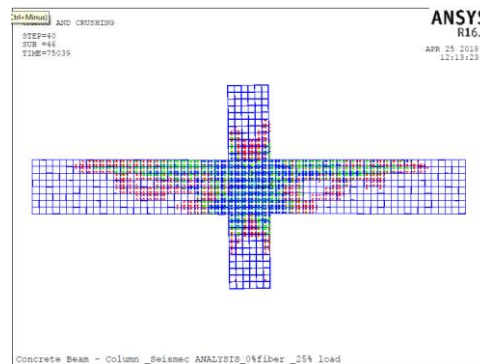


Figure 5. Typical cracks patterns.

3. Results and Discussion

3.1. Failure Mode

Fig. 5 shows the crack patterns and the brittle failure modes of the simulated beam-column connections. The first crack in control beam-column connection occurred in the top and the bottom of the diagonal joint area in the pushing part of the loading while in the pulling part crack begin to appear at the top and the bottom of the another diagonal side. Therefore, when the displacement increased the initial cracks extended from the joints side corner diagonally and also extended in the third direction due to the cyclic load that leads to open and closed these crack so for that reason the strength decreased. With further load increase, the cracks extended toward the beam and column and this caused a crushing failure in the concrete. Prior to failure, the control beam-column connection exhibited a yielding in the tension steel reinforcement at an ultimate horizontal load of 19.0 kN and the corresponding horizontal net drift of 9.1 mm. Fig. 6 shows the stress contours in the concrete and steel generated from ANSYS for each model. Comparing the stress contours for the specimens of each group show that as the column axial load increases, the intensity of the tensile stress within the joint area are is reduced and the yielding spreads more into the beam main steel. This indicates that the column axial load is advantageous for transforming the failure from brittle one in the joint into a ductile one in the beam, which reflects a strong column-weak beam action.

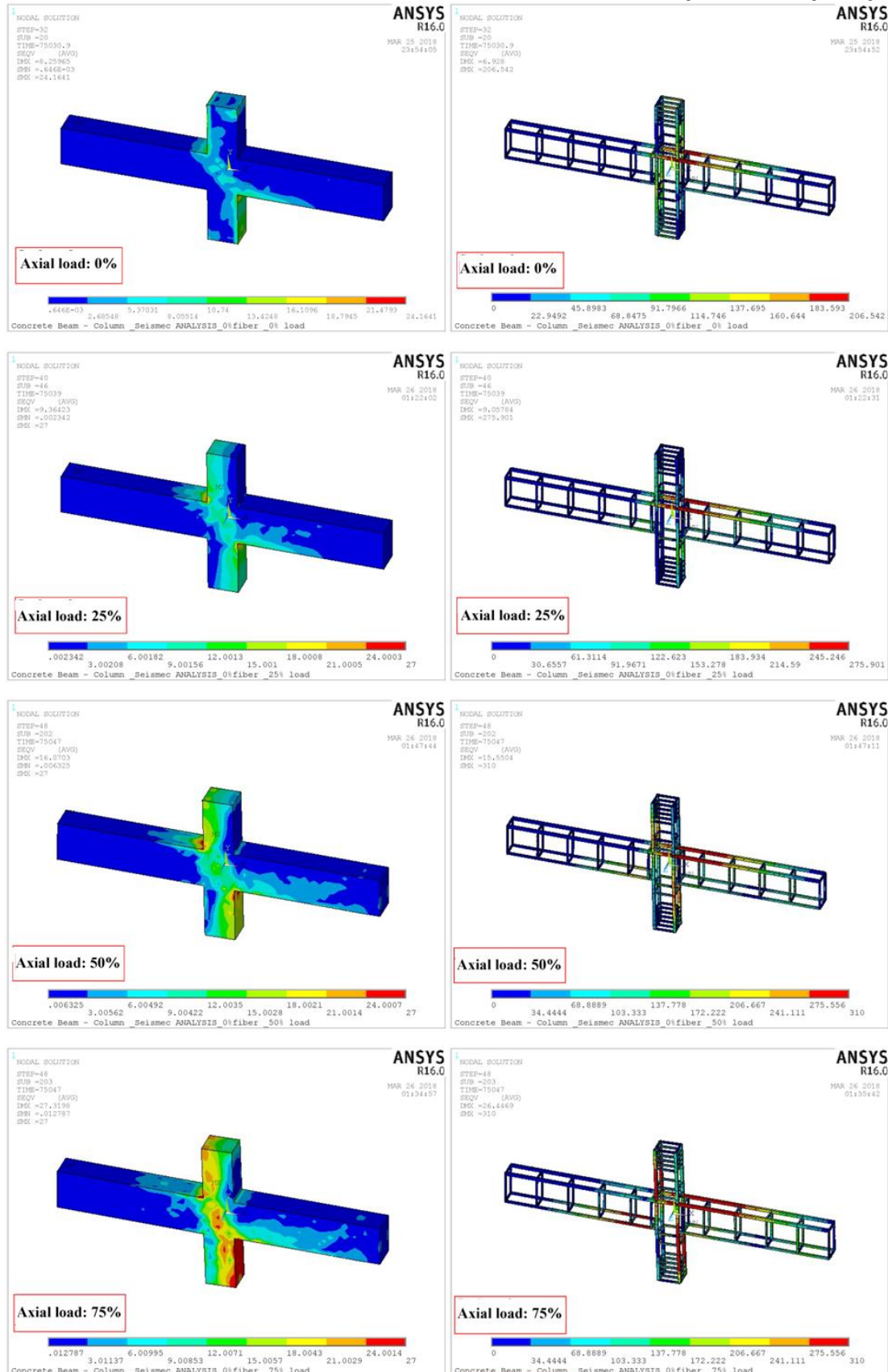


Figure 6. Typical Stress contours in concrete and steel.

3.2. Horizontal load-displacement hysteretic loops

The horizontal load-displacement hysteretic loops for all simulated B-C joints are shown in Fig. 7 (un-damaged) and Fig. 8 (Damaged). Inspection of Fig. 8 reveals that joint BC0J-D (axial load of 0 %, Damaged) exhibited minimum horizontal load and displacement. Joint BC0J-UD (axial load of 0 %, Un-damaged) (Fig. 7) exhibited higher strength and displacement than joint BC0J-D (Fig. 8) although the imposed

lateral reinforcement in these joint region is still inadequate to transmit the failure mechanism to the RC beam. Horizontal load-displacement loops of un-damaged joint show a considerable enhancement in the performance in terms of horizontal load and displacement (Fig. 7 and Fig. 8) because of the un-damaged system provided confinement to the joint rejoin by providing external cracks arresting mechanism and improving the post cracking ductility after reaching the ultimate load capacity and displacement. Also, the axial load level had a strong impact on the Horizontal load-displacement loops (Fig. 7 and Fig. 8) because the compressive stress in the column increased with the increasing of axial load which leads to the initiation of joint tensile concrete cracks that cause reduction in joint strength and maintaining the integrity of the joint connections.

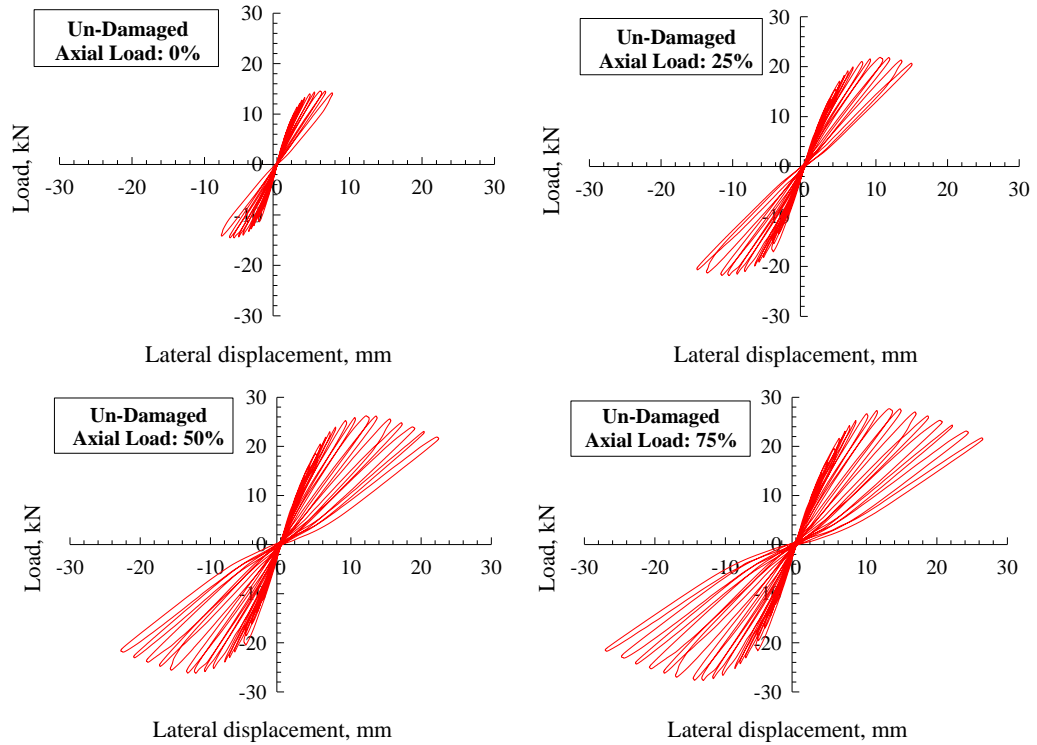


Figure 7. Horizontal load-net drift hysteresis loops for the un-damaged B-C connections.

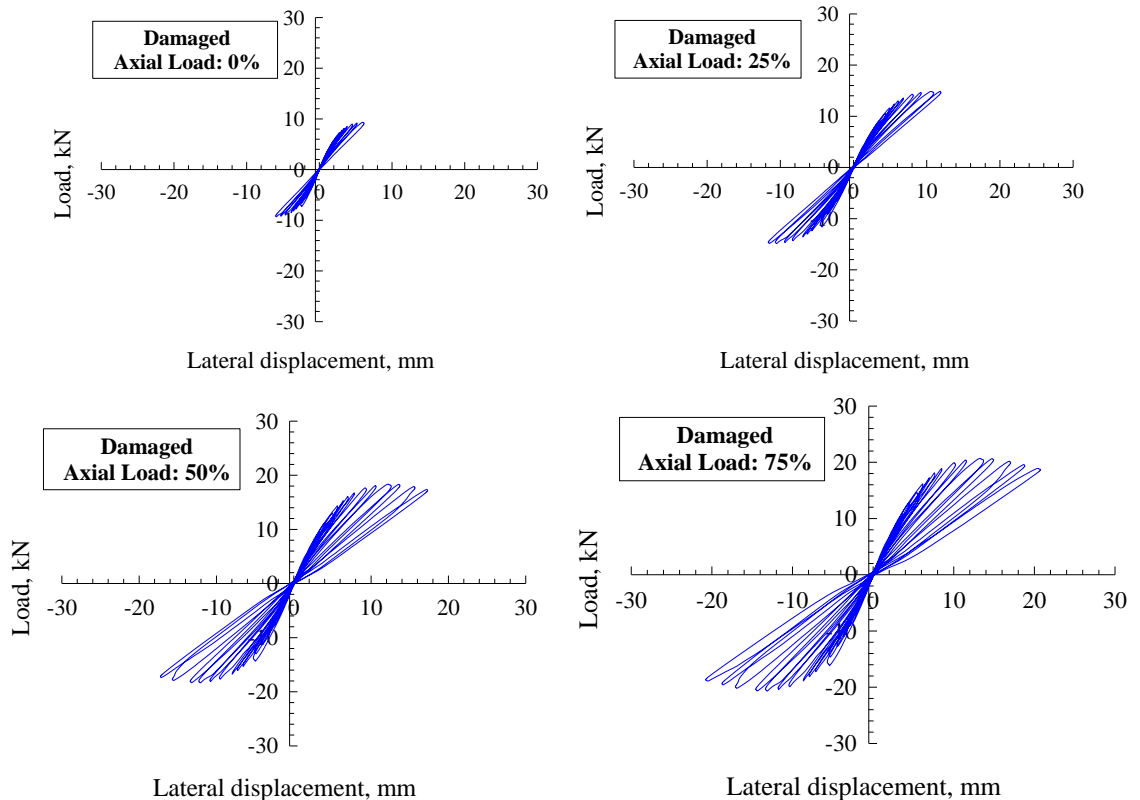


Figure 8. Horizontal load-net drift hysteresis loops for the damaged B-C connections.

3.3. Horizontal load-displacement envelopes

Fig. 9 shows the load-displacement envelopes for all simulated B-C joints were the maximum loads and corresponding displacements attained in each half cycle (pushing and pulling). Inspection of Fig. 9 reveals that the load and displacement increased with the increase of axial load percentage as well as the thermal shock had a helpful impact on both load and displacement.

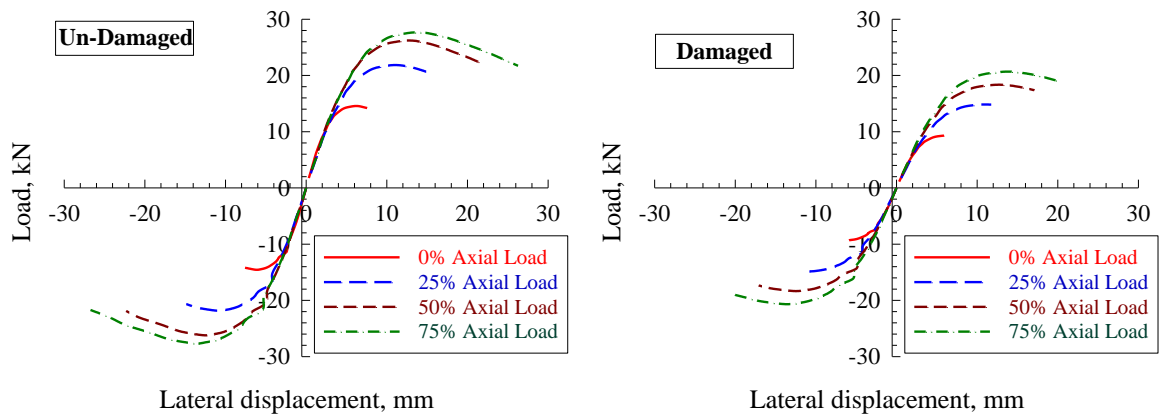


Figure 9. Horizontal load-displacement envelopes of B-C connections.

3.4. Ultimate horizontal load corresponding net drift displacement

The assessment of beams for horizontal load corresponding net drift displacement shows the excellent performance of B-C connections. For B-C connections, horizontal load corresponding net drift displacement can be related to the serviceability and ultimate load limit states, respectively, as shown in Table 1. The horizontal load corresponding net drift displacement percentages are defined as the horizontal load corresponding net drift displacement, respectively, of damaged B-C connections divided by the horizontal load corresponding net drift displacement, respectively, of un-damaged B-C connections as shown in Table 1. The drift displacement indicates how much the un-damaged B-C connections can sustain deformations without failure. Strength ratio also predicts the increase of load that the model can sustain.

Fig. 10 and 11 show the horizontal load corresponding net drift displacement with respect to un-damaged B-C connections, respectively, for all simulated models. Inspection of Fig. 10 reveals that the average enhancement percentage in horizontal load for the un-damaged is 50 %, 81 %, and 90 % for axial load of 25 %, 50 %, and 75 %, respectively. This reflected that the ultimate horizontal load increased with the increase of axial load percentages. Also, the average reduction percentage in horizontal load for the damaged with respect to un-damaged is 37 % is 33 %, 31 %, and 26 % for axial load of 0 %, 25 %, 50 %, and 75 %, respectively. Fig. 11 reveals that the average enhancement percentage in horizontal net drift for the un-damaged is 96 %, 193 %, and 245 % for axial load of 25 %, 50 %, and 75 %, respectively. Also, the average reduction percentage in horizontal net drift for the damaged with respect to un-damaged is 19 % is 21 %, 24 %, and 25 % for axial load of 0 %, 25 %, 50 %, and 75 %, respectively.

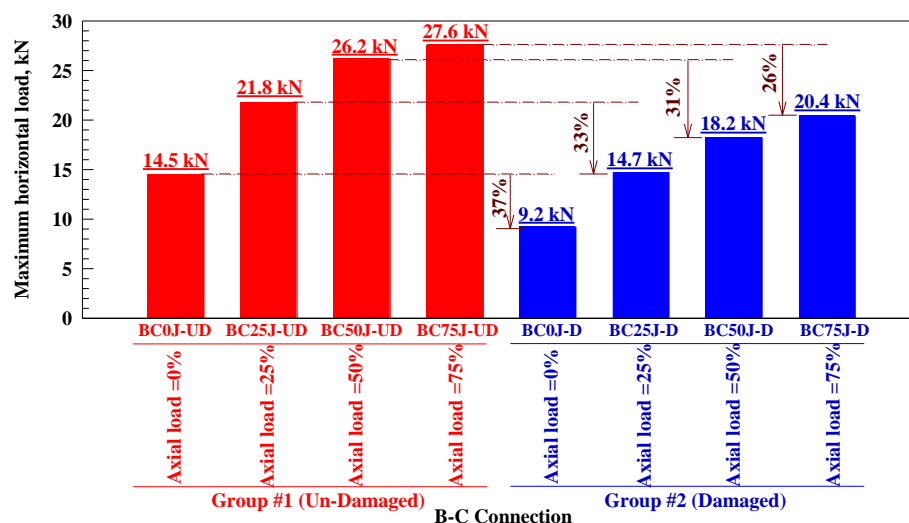


Figure 10. Ultimate horizontal load of B-C connections.

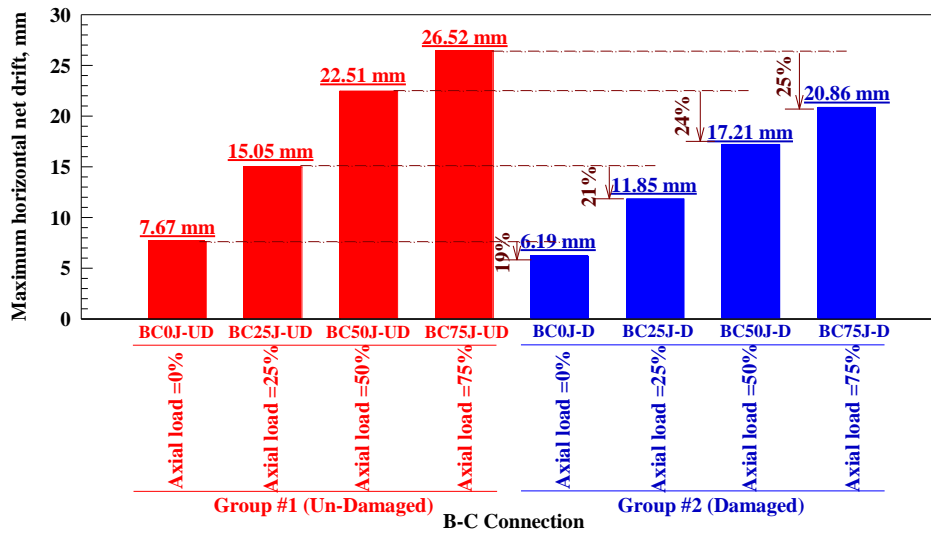


Figure 11. Ultimate horizontal net drift displacement of B-C connections.

3.5. The displacement ductility

The displacement ductility of the B-C connections was calculated from the ratio between the maximum and yield displacements (d_m/d_y). Table 2 shows the maximum and yield displacements which obtained from NLFEA results. Inspection of Table 2 reveals that the un-damaged connections BC0J-UD and BC25J-UD exhibited poor seismic performance and due to that the joint panel failed before the beam yielding of steel reinforcement. In contrast, BC50J-UD and BC75J-UD exhibited high displacement ductility values because of the excellent confinement to the joint-column region by higher axial load percentage which forced the joint to fail in a ductile behavior through formation of the plastic hinge in the beam. Also, Table 2 shows that the displacement ductility increased with the increased of axial load. While, all damaged connections exhibited poor seismic performance due to that the joint panel failed before the beam yielding of steel reinforcement.

Table 2. Displacement ductility values, energy dissipation, and steel strain.

| Group | Specimen | Steel strain, $\mu\epsilon$ | Yield displacement d_y , mm | Maximum displacement d_m , mm | Displacement ductility d_m/d_y | Energy dissipation, kN.mm |
|-------|----------|-----------------------------|-------------------------------|---------------------------------|----------------------------------|---------------------------|
| I | BC0J-UD | 916.75 | Not yielded | 7.29 | NA | 165 |
| | BC25J-UD | 1375.6 | Not yielded | 14.30 | NA | 498 |
| | BC50J-UD | 1651.1 | 2.636 | 21.39 | 8.5 | 918 |
| | BC75J-UD | 1742.3 | 2.164 | 25.19 | 12.3 | 1150 |
| II | BC0J-D | 601.35 | Not yielded | 5.86 | NA | 75 |
| | BC25J-D | 958.55 | Not yielded | 11.35 | NA | 250 |
| | BC50J-D | 1183.7 | Not yielded | 16.44 | NA | 481 |
| | BC75J-D | 1333.8 | Not yielded | 19.73 | NA | 654 |

Note: C: Column, UD: un-damaged, D: Damaged

3.6. Energy dissipation

The energy dissipation is defined as the area under the hysteretic loop for each cyclic load so when the building subjected to lateral loading a higher energy dissipation capability to absorb more energy. Fig. 12 shows the energy dissipation versus investigated parameter of simulated beam-column connections. Inspection of Fig. 12 reveals that the average enhancement percentage in energy dissipation for the un-damaged is 202 %, 458 %, and 598 % for axial load of 25 %, 50 %, and 75 %, respectively. This reflected that the energy dissipation increased with the increase of axial load percentages. Also, the average reduction percentage in energy dissipation for the damaged with respect to un-damaged is 46 % is 50 %, 53 %, and 57 % for axial load of 0 %, 25 %, 50 %, and 75 %, respectively.

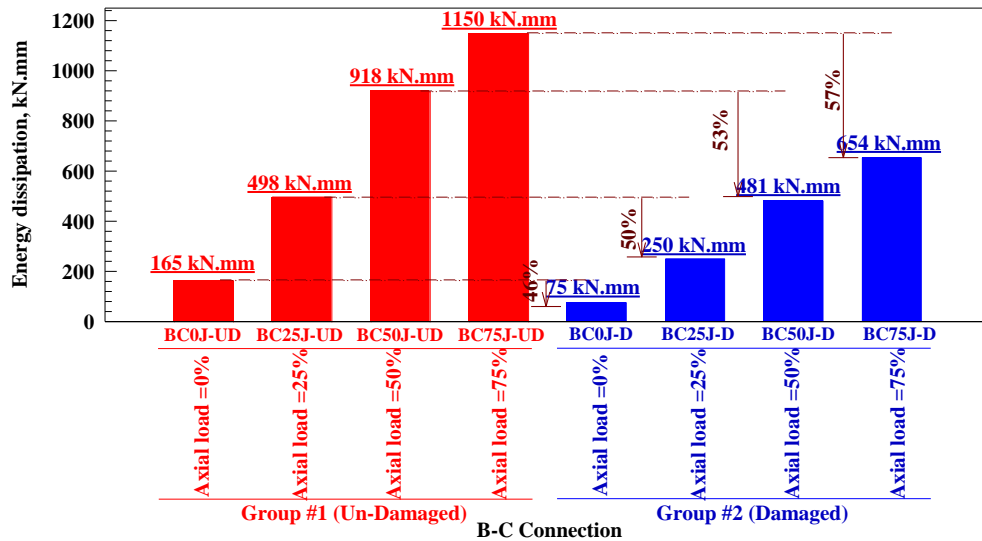


Figure 12. Energy dissipation of B-C connections.

3.7. Secant stiffness degradation

The secant stiffness degradation of the B-C connections is considered as a qualitative measure of the secant stiffness in each cycle. The method of stiffness degradation calculation involved: plotting the horizontal load-displacement hysteretic loops envelopes of each connection and then the secant stiffness for each cycle was calculated by dividing the summation of the maximum pushing and pulling loads on the summation of the maximum pushing and pulling corresponding displacements (the slope of the line between the maximum pulling and pushing and loads in each cycle) as shown in Fig. 13. Inspection of Fig. 13 reveals that the sharp reduction in secant stiffness values for damaged connections because the first crack initiated at initial stages of loading due to connection critical reinforcement details which caused concrete strength reduction and softening. While the stabilized reduction in secant stiffness values is clearly shown in un-damaged connections because the high strength concrete prevented the formation of main cracks to the joint-column region. Also, the un-damaged concrete considerably increased the initial secant stiffness of the connections and number of cycles. The effect of the column axial load percentage on increasing initial stiffness, stabilizing stiffness degradation, and increasing number of cycles is clear due to the increase in column compressive stress and reduces of the diagonal tensile stresses with the increasing of axial load. In addition, Fig. 13 shows that the secant stiffness degradation slightly increased when the axial load increased with a percentage of 4, 7, and 10 for axial load of 25 %, 50 %, and 75 %, respectively, with respect to un-damaged connection subjected to 0 % axial load. In addition, the thermal shock had an average reduction in the secant stiffness degradation of 39 %.

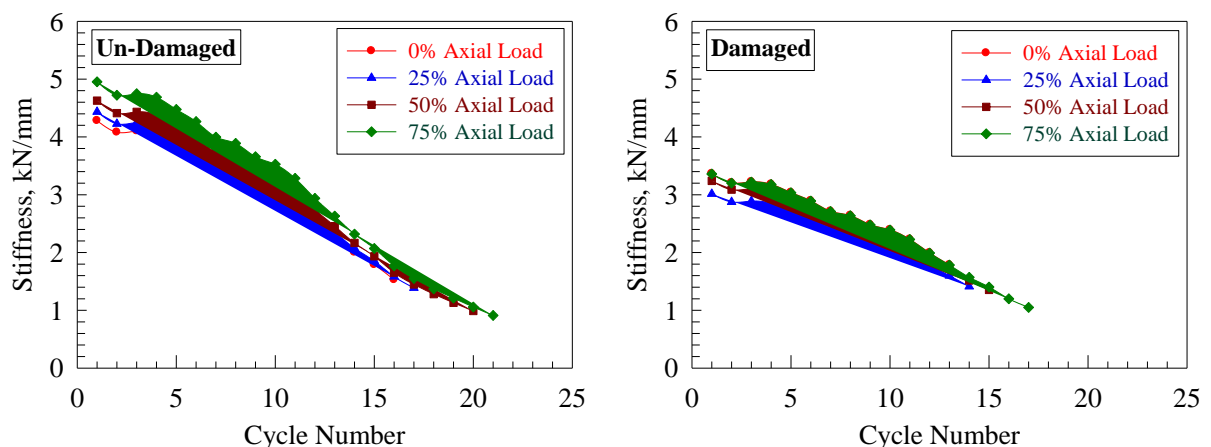


Figure 13. Secant stiffness degradation of simulated connection.

3.8. Comparison of NLFEA with other results

Comparison of NLFEA with Alhassan et al. [43], in virgin B-C connections, column axial load levels up to 75 % of its ultimate capacity were advantageous to its structural performance and substantially improve its lateral load capacity and ultimate net drift as a result of the induced axial compressive stresses in the joint region that alleviate the induced shear stresses by lateral loading which experienced similar behavior of NLFEA. The use of a higher axial load results in increase in the number of hysteretic loops indicating higher energy dissipation, enhanced ductility, and more stabilized stiffness degradation. The intensity of the stresses

within the joint decreases and yielding of steel spreads more to the beam main steel is almost the same performance as the NLFEA.

4. Conclusions

1. The performance of damaged beam-column connection was poor under cyclic loading simulating earthquake excitation, while the un-damaged beam-column connection had a significant enhancement on the seismic behavior of the weak connections. Higher horizontal load levels and larger horizontal drift displacements were attained and higher energy dissipation were achieved, and a significant increase in the joint strength was recorded.

2. In general, the higher axial load percentage results in increase in the number of hysteresis loops indicating higher energy dissipation, enhanced ductility, and more stabilized stiffness degradation. The intensity of the stresses within the joint decreases and yielding of steel spreads more to the beam main steel.

3. The energy of un-damaged beam-column connections could be dissipated by the joint before the system loses its stability as well as it is an indication of the joint maximum capacity to be stressed until failure.

4. Thermal shock has a significant impact on the behavior of beam-column connections. The increase in ductility is directly related to a decrease of compressive strength due to thermal shock.

References

- Shannag, M., Alhassan, M. Seismic Upgrade of Interior Beam-Column Subassemblages with High-Performance Fiber Reinforced Concrete Jackets. *ACI Structural Journal*. 2005. 102(1). Pp. 131–138. DOI: 10.14359/13538
- Shin, M., LaFave, J. Modeling of Cyclic Joint Shear Deformation Contributions in RC Beam-Column Connections to Overall Frame Behavior. *Structural Engineering Mechanics*. 2004. 18(5). Pp. 645–669. DOI: 10.12989/sem.2004.18.5.645
- Ghobarah, A., Youssef, M. Modeling of RC Beam-Column Joints and Structural Walls. *Journal of Earthquake Engineering*. 2001. 5(1). Pp. 91–111. DOI: 10.1080/13632460109350387
- Lowes, L., Altoontash, A. Modeling Reinforced Concrete Beam-Column Joints Subjected to Cyclic Loading. *Journal of Structural Engineering*. 2003. 129(12). Pp. 1686–97. DOI: 10.1061/(ASCE)0733-9445(2003)129:12(1686)
- Mitra, N., Lowes LN. Evaluation, Calibration, and Verification of a Reinforced Concrete Beam-Column Joint Model. *Journal of Structural Engineering*. 2007. 133(1). Pp. 105–20. DOI: 10.1061/(ASCE)0733-9445(2007)133:1(105)
- Venkatesan, B., Ilangoan, R., Jayabalan, P., Mahendran, N., Sakthieswaran, N. Finite Element Analysis (FEA) for the Beam-Column Joint Subjected to Cyclic Loading as Performed Using ANSYS. *Circuits Systems*. 2016. 7(1). Pp. 1581–1597. DOI: 10.4236/cs.2016.78138
- Sasmal, S., Nath, D. Evaluation of Performance of Non-Invasive Upgrade Strategy for Beam-Column Sub-Assemblages of Poorly Designed Structures Under Seismic Type Loading. *Earthquake Engineering Structural Dynamics*. 2016. 45(1). Pp. 1817–1835. DOI: 10.1002/eqe.2730
- Sasmal, S., Ramanjaneyulu, K., Novák, B., Lakshmanan, N. Analytical and Experimental Investigations on Seismic Performance of Exterior Beam-Column Sub-Assemblages of Existing RC-Framed Building. *Earthquake Engineering Structural Dynamics*. 2013. 42(1). Pp. 1785–1805. DOI: 10.1002/eqe.2298
- Lima, C., Martinelli, E., Macorini, L., Izzuddin B. Modelling Beam-to-Column Joints in Seismic Analysis of RC Frames. *Earthquakes Structures*. 2017. 12(1). Pp. 119–133. DOI: 10.12989/eas.2017.12.1.119
- Ibrahim, G., Shaaban, M. Finite element modeling of exterior beam-column joints strengthened by ferrocement under cyclic loading. *Case Studies in Construction Materials*. 2018. 8(1). Pp. 333–346. DOI: 10.1016/j.cscm.2018.02.010
- Roy, B., Aminul, I. Cyclic Performance of Beam-Column Subassemblies with Construction Joint in Column Retrofitted with GFRP. *Structures*. 2018. 14(1). Pp. 290–300. DOI: 10.1016/j.istruc.2018.04.002
- Marthong, C., Sangma, A., Choudhury, S., Pyrbot, R., Tron, S., Mawroh, L., Bharti, G. Structural Behavior of Recycled Aggregate Concrete Beam-Column Connection in Presence of Micro Concrete at Joint Region. *Structures*. 2017. 11(1). Pp. 243–251. DOI: 10.1016/j.istruc.2017.07.001
- Marthong, C., Marthong, S. An experimental study on the Effect of PET Fibers on the Behavior of Exterior RC Beam-Column Connection Subjected to Reversed Cyclic Loading. *Structures*. 2016. 5(1). Pp. 175–185. DOI: 10.1016/j.istruc.2015.11.003
- Baji, H., Eslami, A., Ronagh, H. Development of a Nonlinear FE Modelling Approach for FRP-Strengthened RC Beam-Column Connections. *Structures*. 2015. 3(1). Pp. 272–281. DOI: 10.1016/j.istruc.2015.06.003
- Kodur, V., Agrawal, A. An approach for evaluating residual capacity of reinforced concrete beams exposed to fire. *Engineering Structures*. 2016. 110(1). Pp. 293–306. DOI: 10.1016/j.engstruct.2015.11.047
- Al-Ostaz, A., Irshidat, M., Tenkhoff, B., Ponnappalli, P. Deterioration of bond integrity between repair material and concrete due to thermal and mechanical incompatibilities. *Journal of Materials in Civil Engineering*. 2010. 22(2). Pp. 136–144. DOI: 10.1061/(ASCE)0899-1561(2010)22:2(136)
- Nedviga, E., Beresneva, N., Gravit, M., Blagodatskaya, A. Fire Resistance of Prefabricated Monolithic Reinforced Concrete Slabs of “Marko” Technology. *Adv. Intell. Syst. Comput.* 2018. 692(1). Pp. 739–749. DOI: 10.1007/978-3-319-70987-1_78
- Hezhev, T., Zhurtov, A., Tshipinov, A., Klyuev, S. Fire resistant fibre reinforced vermiculite concrete with volcanic application. *Mag. Civ. Eng.* 2018. 80(1). Pp. 181–194. DOI: 10.18720/MCE.80.16
- Goremikins, V., Blesak, L., Novak, J., Wald, F. Experimental investigation on SFRC behaviour under elevated temperature. *J. Struct. Fire Eng.* 2017. 8(1). Pp. 287–299. DOI: 10.1108/JSFE-05-2017-0034
- Purkiss, J. Steel fibre reinforced concrete at elevated temperatures. *International Journal of Cement Composites and Lightweight Concrete*. 1984. 6(3). Pp. 179–184. DOI: 10.1016/0262-5075(84)90006-X. DOI: 10.14311/asfe.2015.055
- Blesak, L., Goremikins, V., Wald, F., Sajdlova, T. Constitutive model of steel fibre reinforced concrete subjected to high temperatures. *Acta Polytech.* 2016. 56(1). Pp. 417–424. DOI: 10.14311/AP.2016.56.0417

22. Korsun, V., Vatin, N., Franchi, A., Korsun, A., Crespi, P., Mashtaler, S. The strength and strain of high-strength concrete elements with confinement and steel fiber reinforcement including the conditions of the effect of elevated temperatures. *Procedia Eng.* 2015. 117(1). Pp. 970–979. DOI: 10.1016/j.proeng.2015.08.192
23. Goremikins, V., Blesak, L., Novak, J., Wald, F. Experimental method on investigation of fibre reinforced concrete at elevated temperatures. *Acta Polytech.* 2016. 56(1). Pp. 258–264. DOI: 10.14311/AP.2016.56.0258
24. Selyaev, V., Nizina, T., Balykov, A., Nizin, D., Balbalin, A. Fractal analysis of deformation curves of fiber-reinforced fine-grained concretes under compression. *PNRPU Mech. Bull.* 2016. 1(1). Pp. 129–146. DOI: 10.15593/perm.mech/2016.1.09
25. Petr Bílý, Alena Kohoutková. A Numerical Analysis of the Stress-strain Behavior of Anchorage Elements and Steel Liner of a Prestressed Concrete Containment Wall. *Structures.* 2017. 12(1). Pp. 24–39. DOI: 10.1016/j.istruc.2017.07.003
26. Bílý, P., Kohoutková, A. Sensitivity analysis of numerical model of prestressed concrete containment. *Nucl. Eng. Des.* 2015. 295(1). Pp. 204–214. DOI: 10.1016/j.nucengdes.2015.09.027
27. Al-Rousan, R. Behavior of two-way slabs subjected to drop-weight. *Magazine of Civil Engineering.* 2019. 90(6). Pp. 62–71. DOI: 10.18720/MCE.90.6
28. Al-Rousan, R. The impact of cable spacing on the behavior of cable-stayed bridges. *Magazine of Civil Engineering.* 2019. 91(7). Pp. 49–59. DOI: 10.18720/MCE.91.5
29. Krishan, A., Rimshin, V., Erofeev, V., Kurbatov, V., Markov, S. The energy integrity resistance to the destruction of the long-term strength concrete. *Procedia Eng.* 2015. 117(1). Pp. 211–217. DOI: 10.1016/j.proeng.2015.08.143
30. Hyo-Gyoung, Kwak, Jae, Hong Kim. Numerical models for prestressing tendons in containment structures. *Nuclear Engineering and Design.* 2006. 236(1). Pp. 1061–1080. DOI: 10.1016/j.nucengdes.2005.10.010
31. Korsun, V., Vatin, N., Korsun, A., Nemova, D. Physical-mechanical properties of the modified fine-grained concrete subjected to thermal effects up to 200°S. *Appl. Mech. Mater.* 2014. 633–634. Pp. 1013–1017. DOI: 10.4028/www.scientific.net/AMM.633-634.1013
32. Korsun, V., Korsun, A., Volkov, A. Characteristics of mechanical and rheological properties of concrete under heating conditions up to 200°C. *MATEC Web Conf.* 2013. 6(1). Pp. 07002. DOI: 10.1051/mateconf/20130607002
33. Petkova, D., Donchev, T., Wen, J. Experimental study of the performance of CFRP strengthened small scale beams after heating to high temperatures. *Construction and Building Materials.* 2014. 68(1): Pp. 55–61. DOI: 10.1016/j.conbuildmat.2014.06.014
34. Ji, G., Li, G., Alaywan, W. A new fire resistant FRP for externally bonded concrete repair. *Construction and Building Materials.* 2013. 42(1). Pp. 87–96. DOI: 10.1016/j.conbuildmat.2013.01.008
35. Trentin, C., Casas, J. Safety factors for CFRP strengthening in bending of reinforced concrete bridges. *Composite Structures.* 2015. 128(1). Pp. 188–198. DOI: 10.1016/j.compstruct.2015.03.048
36. Ferrari, V., Hanai, J., Souza, R. Flexural strengthening of reinforcement concrete beams using high performance fiber reinforcement cement-based composite (HPFRCC) and carbon fiber reinforced polymers (CFRP). *Construction and Building Materials.* 2013. 48(1). Pp. 485–498. DOI: 10.1016/j.conbuildmat.2013.07.026
37. Attari, N., Amziane, S., Chemrouk, M. Flexural strengthening of concrete beams using CFRP, GFRP and hybrid FRP sheets. *Construction and Building Materials.* 2012. 37(1). Pp. 746–757. DOI: 10.1016/j.conbuildmat.2012.07.052
38. Kara, I., Ashour, A., Köroğ'lu, M. Flexural behavior of hybrid FRP/steel reinforced concrete beams. *Composite Structures.* 2015. 129(1). Pp. 111–121. DOI: 10.1016/j.compstruct.2015.03.073
39. Kolchunov, V., Dem'yanov, A. The modeling method of discrete cracks in reinforced concrete under the torsion with bending. *Magazine of Civil Engineering.* 2018. 81(5). Pp. 160–173. DOI: 10.18720/MCE.81.16
40. Travush, V., Konin, D., Krylov, A. Strength of reinforced concrete beams of high-performance concrete and fiber reinforced concrete. *Magazine of Civil Engineering.* 2018. No. 77(1). Pp. 90–100. DOI: 10.18720/MCE.77.8
41. Al-Rousan, R. Behavior of CFRP Strengthened Columns Damaged by Thermal Shock. *Magazine of Civil Engineering.* 2020. 95(3). Pp. 48–62. DOI: 10.18720/MCE.95.3
42. Zhang, YX, Bradford, MA. Nonlinear analysis of moderately thick reinforced concrete slabs at elevated temperatures using a rectangular layered plate element with Timoshenko beam functions. *Engineering Structures.* 2007. 29(10). Pp. 2751–2761. DOI: 10.1016/j.engstruct.2007.01.016
43. Alhassan, MA, Al-Rousan, RZ, Amaireh, LK, Barfed, MH. Nonlinear Finite Element Analysis of B-C Connections: Influence of the Column Axial Load, Jacket Thickness, and Fiber Dosage. *Structures.* 2018. 16(1). Pp. 50–62. DOI: 10.1016/j.istruc.2018.08.011

Contacts:

Rajai Al-Rousan, rzalrousan@just.edu.jo



DOI: 10.18720/MCE.99.11

The effect of formworks on the temperature regime in the mass concrete

N.A. Aniskin, T.C. Nguyen*

National Research Moscow State Civil Engineering University, Moscow, Russia

* E-mail: ntchuc.mta198@gmail.com

Keywords: temperature regime, thermally stressed state, concrete mass, temperature crack formation, formwork.

Abstract. This paper presents the results of numerical studies about the temperature regime and thermal stress state of an erected concrete block with various design forms of formwork. The influence of formwork on the formation of the temperature regime is considered taking into account the influence of the main factors: the air temperature, the cement consumption per cubic meter of concrete and its maximum heat dissipation. An assessment of the risk of temperature cracks is given for three formwork cases: metal (steel) and wooden without thermal insulation and with insulation. Based on the results obtained, nomograms are constructed in order to estimate the temperature difference between the center of the concrete mass and its surface, depending on the values of the factors. It is shown that under the considered conditions during construction from the point of view of temperature crack formation, wooden formwork is more preferable than metal (steel). Thus, when concreting in the cold season and using a large amount of cement or large-heat cement then formwork insulation is necessary. In this work, results from the nomograms are obtained may be used as reference material in the design and construction of mass concrete structures such as dams, foundations, bridge supports, etc.

1. Introduction

The heat release due to cement hydration during the construction of massive structures often leads to significant heating of the inner zones of the concrete structure and the development of a large volume change [1–4]. There is a large temperature difference between the outer surface and the inner zone of the concrete mass. When this difference exceeds the allowable value then tensile stresses and cracks were formed in the concrete structure [5–7]. Concrete is a material with a sufficiently low thermal conductivity, so the release of heat to the outside of concrete blocks is quite slow and can last for months or years [8].

For the problem control temperature regime during construction massive concrete is very much interested scientists [9]. The formation temperature during construction mass concrete was affected by a large number of factors: the cement consumption per cubic meter of concrete and its maximum heat release, the intensity of concreting, layer thickness and concrete block sizes, the temperature of the concrete to be laid, etc. [10, 11].

In the construction period, there are many methods are used in order to control the temperature in the mass concrete such as cooling mass - through external watering cold water or using the Internal cooling system by cooling pipe [12]. A large temperature difference can be avoided by thermal insulation on the surface of mass concrete, which prevents the cooling of surfaces in the winter and their heating in the summer. The structural thermal insulation that can be used by formwork is necessary during construction. To enhance its thermal insulation properties, materials with low thermal conductivity can be used [13].

Currently, in the construction of concrete structures, there are several types of formwork made of different materials and are used in many applications. Common types of formwork such as wooden formwork, metal formwork, plastic formwork and, combined formwork, etc. [14].

The traditional and oldest in-use time is the wooden formwork, currently performed using laminated plywood. Wooden formwork is a rather time-consuming type with high costs for its manufacture. In addition,

Aniskin, N.A., Nguyen, T.C. The effect of formworks on the temperature regime in the mass concrete. Magazine of Civil Engineering. 2020. 99(7). Article No. 9911. DOI: 10.18720/MCE.99.11



This work is licensed under a CC BY-NC 4.0

wooden formwork often cannot be reused multiple times. The development of concrete technology has led to the appearance of metal formwork, which is reused many times during construction [15, 16]. Currently, reusable plastic formwork has many applications in the construction industry and is widely used.

The choice of formwork is carried out for each specific case with an assessment of its manufacturability and cost. Formwork is often used not only to obtain the shape of the structure but also to control the temperature regime in the mass concrete structure. It protects the surface of the concrete block from cooling in the winter and heating in the summer. In order to increase the thermal insulation properties of the formwork, various types of thermal insulation materials are used [17].

The issue of using insulated formwork to control the temperature regime and the thermal stress state in the mass concrete structures were considered in many works [18]. However, today a full-fledged analysis of the impact of this technological measure in conjunction with other factors acting on the state of the concrete structure during construction has not been completed. This paper presents some research results on the influence of the formwork type and the main factors acting on the temperature regime in the mass concrete during the construction period. Besides, this study assesses the possibility of the formation of thermal cracks in the mass concrete depending on the combination of factors used in numerical experiments.

2. Materials and Methods

2.1. Mathematical foundations of numerical modeling for solving the temperature problem

Numerical modeling of the temperature non-stationary problem taking into account heat release during cement hydration is based on the solution of the well-known equation of the theory of thermal conductivity [19–21]:

$$k\nabla^2 T + q = \rho c \frac{\partial T}{\partial t} \quad (1)$$

where T is temperature function, °C;

k is the thermal conductivity of the material, m²/s;

c is the specific heat of the material, kJ/kg.°C;

ρ is the density of the material, kg/m³;

q is the heat released during the hydration process, kJ/m³;

t is time, days.

Equation (1) can be written as follows:

$$\frac{k}{c\rho} \nabla^2 T + \frac{q}{c\rho} = \frac{\partial T}{\partial t} \quad (2)$$

The International Conference on Structural Analysis by finite element method in 1985 in Tokyo – Japan, Tanabe was proposed to determine heat source due to cement hydration given by formulas (3) and (4). In 1986 the American Society of Civil Engineers – ASCE was agreed with the formula of Tanabe [22].

$$q = \frac{1}{24} \rho c K e^{\frac{-\alpha t}{24}} \quad (3)$$

$$T(t) = K(1 - e^{-\alpha t}) \quad (4)$$

where CC is the cement consumption per cubic meter of concrete, kg/m³;

E is the maximum heat release of cement, kJ/kg;

K is the maximum temperature in concrete under adiabatic conditions, $K = CC * E / c * \rho$, °C;

α is the degree of hydration (ranges from 0 to 1).

The degree of hydration (α) depends on many factors such as cement content, the initial temperature of concrete mixture, age of concrete etc. It is defined as the ratio of the heat generated from the beginning of hydration to the time t , and the total heat generated by hydration of cement.

The boundary condition for the case of convective heat transfer on the surface of a concrete block can be written in the form [23]:

$$q = h(T_s - T_a) \quad (5)$$

where q is the heat flux per unit area, W/m^2 ;

T_s and T_a are the temperatures at the surface of the block and the ambient air, respectively, °C;

h_{eq} is equivalent convection coefficient, $W/(m^2 \cdot ^\circ C)$ (depends on the type and design of the formwork).

The equivalent convection coefficient, taking into account the type and design of the formwork, was determined by the formula [24]:

$$h_{eq} = \left(\frac{1}{hA} + \sum_{i=1}^n \frac{L_i}{k_i A} \right)^{-1} \quad (6)$$

where h is the heat transfer coefficient between the concrete surface and the environment ($9.9-17.9 W/(m^2 \cdot ^\circ C)$);

A is unit through which heat transfer is occurring, and for the i -th layer;

L_i is the thickness;

k_i is the thermal conductivity coefficient for the i -th layer.

In the study to solve temperature problems taking into account the influence of formwork on the temperature regime in the mass concrete, a numerical method for solving differential equation (1) was used – the finite element method (FEM) [25]. All tasks in this work were solved using the Midas civil 2011 software package [26, 27].

2.2. Relationship of thermal stress and temperature field in concrete mass

According to research [28, 29] indicates that the relationship between thermal stress and temperature in mass concrete is determined by equation (7):

$$\sigma = R \times E(t) \times \alpha \times \Delta T, \quad (7)$$

where σ is thermal-stresses, MPa;

R is restraint ($0 < R < 1$), the restraint coefficient which is dependent on the size of the concrete mass and the ratio of elastic module of concrete and foundation: $R \in f(V; Ec/Ef)$ and can be calculated using the computer program Midas Civil;

α is coefficient of thermal expansion, $1/^\circ C$;

$E(t)$ is concrete elasticity modulus, MPa;

ΔT is temperature drop, °C.

Data for example, according to standards ACI 209.2R-08 "Guide for Modeling and Calculating Shrinkage and Creep in Hardened Concrete". A creep coefficient and an unrestrained shrinkage strain at any time depend on [30]: age of concrete when drying starts, usually taken as the age at the end of moist curing, days; age of concrete at loading, days; curing method; ambient relative humidity expressed as a decimal; volume-surface ratio or average thickness, m; concrete slump, m; fine aggregate percentage, %; cement content, kg/m^3 ; air content of the concrete expressed in percent, %; and cement type.

The compliance function $J(t, t_0)$ that represents the total stress-dependent strain by unit stress is given by equation (8):

$$J(t, t_0) = \frac{1 + \phi(t, t_0)}{E_{cm(t_0)}}, \quad (8)$$

where $E_{cm(t_0)}$ is the modulus of elasticity at the time of loading to, MPa;

$\phi(t, t_0)$ is the creep coefficient as the ratio of the creep strain to the elastic strain at the start of loading at the age t_0 .

The secant modulus of elasticity of concrete E_{cmto} at any time to of loading is given by equation (9):

$$E_{cmto} = 0.043\gamma_c^{1.5} \sqrt{f_{cmto}} \quad (9)$$

where γ_c is the unit weight of concrete, kg/m³;

f_{cmto} is the mean concrete compressive strength at the time of loading, MPa.

The general equation for predicting compressive strength at any time t is given by equation (10):

$$f_{cmto} = \left[\frac{1}{a + bt} \right] f_{cm28} \quad (10)$$

where f_{cm28} is the concrete mean compressive strength at 28 days, MPa; a , b are functions of both the type of cement used and the type of curing employed.

2.3. Evaluation criteria for thermal cracking in mass concrete

Currently, both in Russia and in various countries of the world, there are many standards for controlling the formation of temperature cracks in the mass concrete during construction. Each standard presents different criteria to match the climatic conditions and construction technology in the countries' respective.

Currently, when laying concrete the possible temperature difference ΔT between the surface and the central zone of the structure is limited. The common temperature difference in the type of concrete is usually equal to 20 °C [30].

A number of Russian regulatory documents [31, 32] somewhat share the requirements for temperature differences. So, for example, in accordance with the standard SP 357.1325800.2017 [33] in the contact zone, the ΔT drop should be no more than (16–18) °C when concreting with long blocks and (20–27) °C when using columnar. The contact zone means a zone of construction at the base with a height equal to 0.2 of the largest block size in the plan. In the contact, the zone is not allowed to supercooling concrete below the calculated lowest temperatures. For concrete in the free region, the temperature difference between the core and the surfaces of the mass concrete ΔT is allowed no more than (20–25) °C.

Similar requirements for the temperature regime in the mass concrete during construction are imposed in the international construction practice. So, according to the Vietnamese norms and standard 305.2004 "mass concrete blocks, inspection and production", two factors are controlled during the construction of massive concrete structures, which influence the appearance of cracks in the mass concrete. The first factor is the temperature difference between the center of the mass concrete and its surface ΔT . In order to avoid cracking, the following condition is necessary $\Delta T < 20$ °C. The second factor is the temperature gradient, the value of which should be $M_T \leq 50$ °C/m [34].

In Japan, the assessment of crack formation in the mass concrete is performed using the index of thermal cracking and defined as follows [35, 36]. The cracking tendency is estimated by the value of the thermal crack index based on the criteria values presented in Table 1.

$$I_{cr} = \frac{f_{sp}(t)}{f_t(t)} \quad (11)$$

where: I_{cr} is the index of thermal cracking;

$f_t(t)$ is tensile strength, respectively, the "age" of concrete t;

$f_{sp}(t)$ – maximum temperature stress caused by the process of cement hydration per day t.

Table 1. Criteria for controlling the cracking tendency in the mass concrete.

| Controlled Cracking Criteria | Temperature crack index (I_{cr}) |
|-------------------------------------|--------------------------------------|
| To prevent any temperature cracks | $I_{cr} \geq 1.5$ |
| Limited cracking possible | $1.2 \leq I_{cr} \leq 1.5$ |
| The possibility of dangerous cracks | $0.7 \leq I_{cr} \leq 1.2$ |

In accordance with the criterion for evaluation of cracking CIRIA C600 (Great Britain) standard, the maximum temperature difference between the inner zone of the concrete mass and its external surface ΔT_{max} is defined by the formula [37, 38]:

$$\Delta T_{max} = \frac{3.7\varepsilon}{\alpha} \quad (12)$$

where ε is ultimate tensile strength of early-age concrete;

α is the coefficient of thermal expansion of concrete.

After substituting the known values $\alpha = 13 \cdot 10^{-6}$ and $\varepsilon = 70 \cdot 10^{-6}$ into expression (12), we obtain the value of the maximum allowable difference $\Delta T_{max} = 19.9 \text{ }^\circ\text{C}$.

Thus, all the above requirements for the temperature regime in the mass concrete during construction are reduced to one general requirement: the temperature difference between the center and the surface of the concrete mass should not exceed $20 \text{ }^\circ\text{C}$. The given requirements for temperature differences are based on the practice during construction and do not always take into account the features of the process. In more detail, the requirements for the temperature regime in the mass concrete during construction are established on the basis of calculations of temperature fields and the thermal stress state of the constructed concrete structures.

3. Results and Discussion

3.1. Object of study

In this paper, we examined the influence of the formwork type on the temperature regime of the concrete block during construction. A concrete block of size $8 \times 6 \times 3 \text{ m}$ is placed on the foundation with dimensions $16 \times 12 \times 4 \text{ m}$. The structure of the studied is shown in Fig. 1a. We considered three cases for formwork on the surfaces of a concrete block: wooden, metal (steel) and combined with thermal insulation (polystyrene foam) (Fig. 1b).

In studies, for standard formwork thicknesses were considered: wooden – 2.5 cm, metal (steel) – 2 mm. For the accepted thicknesses, the equivalent convection coefficient calculated by the formula (6) is: $h_{eq} = 9.9 \text{ W}/(\text{m}^2 \cdot ^\circ\text{C})$ for steel formwork $h_{eq} = 2.6 \text{ W}/(\text{m}^2 \cdot ^\circ\text{C})$ for wooden formwork [24]. The combined formwork (Fig. 1b) is made of wooden boards 2.5 cm thick and 3 cm thick polystyrene foam. The physical characteristics of the materials used in the calculations are presented in Table 2.

The studies also examined the influence of the main factors in order to determine the temperature regime of a concrete block: air temperature, cement consumption (CC) and its maximum heat dissipation (E). There are different climate factors that must be considered: during construction in North Vietnam in summer (with an average temperature of $26.5 \text{ }^\circ\text{C}$); during construction in North Vietnam in winter (an average temperature of $17.0 \text{ }^\circ\text{C}$); during construction in mountainous Vietnam (an average temperature of $5 \text{ }^\circ\text{C}$).

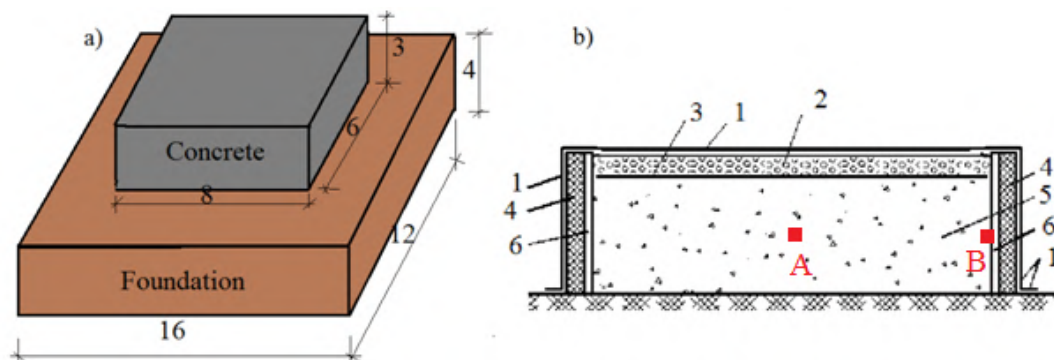


Figure 1. Diagrams for concrete blocks a – Dimensions of the computational domain; b – Formwork installation of formwork combined with thermal insulation; 1, 3 – polyethylene coating; 2 – mineral wool thickness of 10 cm; 4 – 3 cm thick polystyrene; 5 – concrete; 6 – wooden formwork 2.5 cm thick.

Table 2. The estimated physical characteristics of the materials.

| Characteristics, units | Values | | |
|--|----------------------|----------------------|---------------------|
| | Concrete | Foundation | Polystyrene foam |
| The coefficient of thermal conductivity (W/(m.°C)) | 2.60 | 2.00 | 0.029 |
| Specific heat (kJ/kg.°C) | 0.95 | 0.84 | 1.13 |
| Density of the material (kg/m ³) | 2400 | 2650 | 20 |
| The coefficient of convective heat transfer (W/m ² .°C) | 12.0 | 14.0 | 0.93 |
| Modulus of elasticity (N/m ²) | 2.7×10 ¹⁰ | 1.8×10 ¹⁰ | 3.0×10 ⁹ |
| The coefficient of linear expansion (1/°C) | 1×10 ⁻⁶ | 1×10 ⁻⁵ | 1×10 ⁻⁵ |
| Poisson's ratio | 0.18 | 0.20 | 0.20 |

The initial temperature of the concrete mixture depends on the temperature of the aggregate component. The change in the initial temperature of the concrete mixture by changing the temperature of the aggregate components. In this study, the initial temperature of the concrete mixture is assumed to be constant and equal to 25 °C. Besides that, the cement consumption (CC) was considered in the range of (200–450) kg/m³, maximum heat emission of cement E_{max} in the range of (120–350) kJ/kg. Using the Midas civil 2011 software package, for all design cases and combinations of the factors considered in order to determine the temperature regimes, maximum temperature and, the temperature difference between the center of the block and its surface during construction.

3.2. Research results

3.2.1. The temperature differential in mass concrete for different types of formwork

The results of numerical experiments under the form of the temperature difference between the center (location A) of the concrete block and its surface (location B) (see Fig. 1) for two formwork cases (wood and metal) under various external temperature influences are presented in Tables 3-5. In these tables, color indicates cases for which the temperature difference exceeds the value of the temperature allows 20°C. From the results obtained, the following features can be noted.

When pouring concrete in the summer (air temperature $T_{air} = 26.5$ °C), the use of wooden formwork for almost all the considered cases for cement consumption and its maximum heat generation do not exceed the allowable temperature value of 20°C. The only exceptions are the cases with the maximum cement consumption in (400–450) kg/m³ and the maximum heat release of 350 kJ/kg, the temperature difference is in the range of (20.2–23.7) °C. Metal formwork has a much lower heat-insulating ability compared to wood. It contributes more cooling on the surface of concrete blocks. Therefore, the results lead to an increase the temperature difference between the surface and the center of mass concrete block.

Table 3. The temperature difference in the mass concrete when $T_{air} = 26.5$ °C.

| E_{max} kJ/kg | Wood formwork | | | | | | Metal formwork | | | | | |
|--------------------|--|-------|-------|-------|-------|-------|--|-------|-------|-------|-------|-------|
| | CC is the consumption of cement, kg/m ³ | | | | | | CC is the consumption of cement, kg/m ³ | | | | | |
| | 200 | 250 | 300 | 350 | 400 | 450 | 200 | 250 | 300 | 350 | 400 | 450 |
| 120 | 3.08 | 4.01 | 4.94 | 5.86 | 6.79 | 7.72 | 5.56 | 7.22 | 8.88 | 10.54 | 12.19 | 13.85 |
| 180 | 4.94 | 6.32 | 7.72 | 9.11 | 10.49 | 11.89 | 8.88 | 11.36 | 13.85 | 16.32 | 18.80 | 21.29 |
| 240 | 6.79 | 8.64 | 10.49 | 11.35 | 14.20 | 16.06 | 12.2 | 15.49 | 18.80 | 22.11 | 25.43 | 28.74 |
| 300 | 8.64 | 10.96 | 13.28 | 15.59 | 17.91 | 20.23 | 15.5 | 19.63 | 23.77 | 27.91 | 32.05 | 36.19 |
| 350 | 10.2 | 12.89 | 15.59 | 18.30 | 21.00 | 23.70 | 18.3 | 23.08 | 27.91 | 32.74 | 37.56 | 42.43 |

As can be seen from Table 3, a much larger number of cases has an excess of the permissible temperature difference. When concreting under the air temperature of 17 °C, temperatures across the surface of a concrete block will drop sharply due to the influence of air temperature. Therefore, it increases the temperature difference between the center and the surface of the concrete block. As can be seen from Table 4, wooden formwork creates a safe temperature difference for most cases.

When using metal formwork, the temperature difference is in the permissible range only for cases with low cement content and low heat cement. For cases with cement content in the range of (200–450) kg/m³ and its maximum heat release from 240 to 350 kJ/kg, the temperature difference between the center of the block and its surface significantly exceeds the permissible value and is in the range of (30.2–48.9) °C.

Table 4. The temperature difference in the mass concrete when $T_{air} = 17.0\text{ }^{\circ}\text{C}$.

| E_{max} kJ/kg | Wood formwork | | | | | | Metal formwork | | | | | |
|--------------------|---|-------|-------|-------|-------|-------|---|-------|-------|-------|-------|-------|
| | CC – The consumption of cement, kg/m ³ | | | | | | CC – The consumption of cement, kg/m ³ | | | | | |
| | 200 | 250 | 300 | 350 | 400 | 450 | 200 | 250 | 300 | 350 | 400 | 450 |
| 120 | 6.76 | 7.68 | 8.61 | 9.53 | 10.45 | 11.38 | 12.1 | 13.72 | 15.37 | 17.02 | 18.67 | 20.32 |
| 180 | 8.61 | 9.99 | 11.38 | 12.77 | 14.15 | 15.54 | 15.4 | 17.85 | 20.32 | 22.77 | 25.25 | 27.73 |
| 240 | 10.5 | 12.30 | 14.15 | 16.00 | 17.86 | 19.71 | 18.7 | 21.95 | 25.25 | 28.57 | 31.88 | 35.19 |
| 300 | 12.3 | 14.61 | 16.93 | 19.25 | 21.56 | 23.88 | 22.0 | 26.08 | 30.22 | 34.36 | 38.50 | 42.64 |
| 350 | 13.8 | 16.54 | 19.25 | 21.95 | 24.65 | 27.35 | 24.7 | 29.53 | 34.36 | 39.19 | 44.02 | 48.89 |

Concreting under conditions of lowest ambient temperatures was considered. So, this worsens the temperature regime in mass concrete and is presented in Table 5. For all cases with metal formwork, the temperature difference in concrete blocks reaches a large value and exceeds the allowed temperature difference. Approximately half of the cases obtained a temperature difference exceeding 30.5°C. Opposite, when using wooden formwork was obtained satisfactory results in all cases. Only for cases with the high cement content and high maximum heat dissipation, the temperature difference was obtained, varying from 21.3 °C to 32.1 °C.

Table 5. The temperature difference in the mass concrete when $T_{air} = 5.0\text{ }^{\circ}\text{C}$

| E_{max} kJ/kg | Wood formwork | | | | | | Metal formwork | | | | | |
|--------------------|---|-------|-------|-------|-------|-------|---|-------|-------|-------|-------|-------|
| | CC – The consumption of cement, kg/m ³ | | | | | | CC – The consumption of cement, kg/m ³ | | | | | |
| | 200 | 250 | 300 | 350 | 400 | 450 | 200 | 250 | 300 | 350 | 400 | 450 |
| 120 | 11.51 | 12.43 | 13.36 | 14.28 | 15.21 | 16.13 | 20.48 | 22.10 | 23.73 | 25.38 | 27.03 | 28.68 |
| 180 | 13.36 | 14.74 | 16.13 | 17.52 | 18.90 | 20.29 | 23.73 | 26.20 | 28.68 | 31.12 | 33.60 | 36.07 |
| 240 | 15.21 | 17.05 | 18.90 | 20.75 | 22.60 | 24.45 | 27.01 | 30.30 | 33.60 | 36.89 | 40.19 | 43.48 |
| 300 | 17.05 | 19.36 | 21.67 | 23.98 | 26.30 | 28.61 | 30.30 | 34.42 | 38.54 | 42.66 | 46.78 | 50.89 |
| 350 | 18.60 | 21.29 | 23.98 | 26.68 | 29.38 | 32.08 | 33.05 | 37.85 | 42.66 | 47.46 | 52.27 | 57.14 |

In order to quickly assess the temperature differences depending on the considered climatic conditions, the type of formwork, and the factors (CC, E), nomograms were constructed to predict (Fig. 2).

The matrix of the relationship between the cement content and maximum heat emission of cement E_{max} combined with the approximate evaluation criteria (temperature difference according to CIRIA C600 of Great Britain standard) can give the following notes:

- The use of nomograms in order to determine the maximum temperature difference between the center and the surface of concrete blocks is made by the vertical lines from the ox (the consumption of cement) and from the horizontal line oy (the maximum heat release) (see Fig. 2).

For example, when $T_{air} = 26.5\text{ }^{\circ}\text{C}$; $CC = 375\text{ kg/m}^3$ and $E = 250\text{ kJ/kg}$:

Use wooden formwork: $\Delta T \approx 13.40\text{ }^{\circ}\text{C}$; use steel formwork: $\Delta T \approx 25\text{ }^{\circ}\text{C}$.

- Preliminary prediction about the risk of forming cracks due to temperature difference in excess of the allowable value (20 °C).

- The use of wooden formwork can help to adequately control temperature difference values in most climatic conditions. The exception is the cases with high cement content and high maximum heat dissipation. For example, when $CC = 450\text{ kg/m}^3$ and $E = 350\text{ kJ/kg}$, the temperature difference is 23.7 °C, 27.4 °C and 32.1 °C at air temperatures of 26.5 °C, 17.0 °C and 5.0 °C, respectively.

- In order to accurately assess the formation of cracks in mass concrete, it is necessary to determine the tensile stress at any time t and compare with the permissible tensile stress.

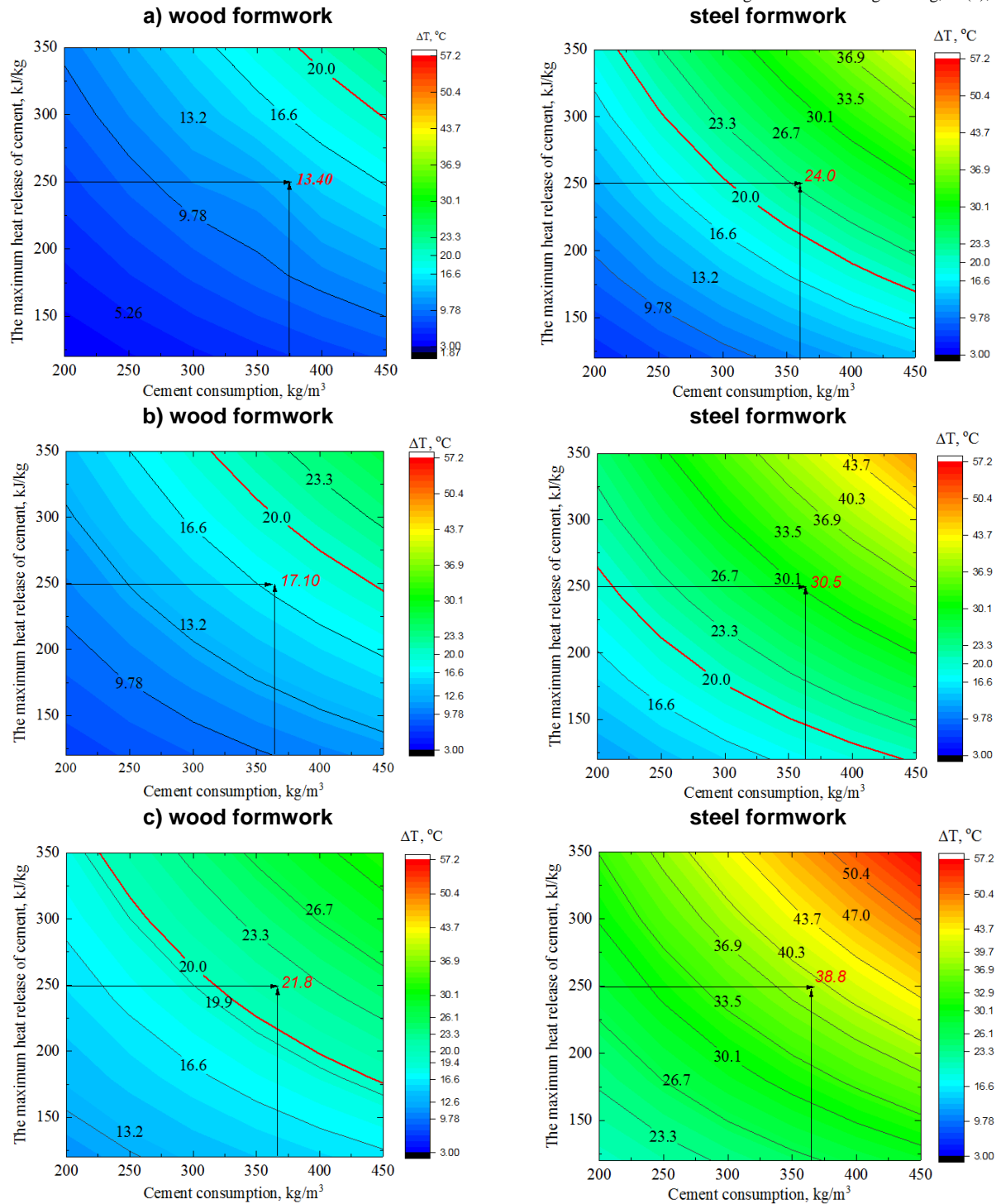


Figure 2. Nomograms in order to determine the temperature difference between the center of the block and its surface, which depending on the consumption of cement and its maximum heat release when: a) $T_{air} = 26.5\text{ }^{\circ}\text{C}$; b) $T_{air} = 17.0\text{ }^{\circ}\text{C}$; c) $T_{air} = 5.0\text{ }^{\circ}\text{C}$.

3.2.2. The use of insulated formwork to reduce the risk of cracking in the mass concrete

Obviously, the measure to reduce the temperature difference in these cases, it is necessary to use a formwork with thermal insulation. That will prevent the heat transfer of concrete to the air environment while increasing the temperature on the surface of the concrete block. Calculations were performed for the case with insulated formwork (Fig. 1b) for the case of the concrete block with the values of the factors $CC = 450\text{ kg/m}^3$, $E_{max} = 350\text{ kJ/kg}$. Fig. 3 shows the temperature changes of the center point and surface point of concrete blocks with air temperature conditions of $26.5\text{ }^{\circ}\text{C}$ (Fig. 3a) and $5\text{ }^{\circ}\text{C}$ (Fig. 3b). As is seen in Fig. 3, the change in the temperature difference between the center and the surface of the block is also shown. The values of the maximum temperature T_{max} in the center of the block and the temperature difference ΔT for all the considered formwork cases with values of factors $CC = 450\text{ kg/m}^3$, $E_{max} = 350\text{ kJ/kg}$ are presented in Table 6.

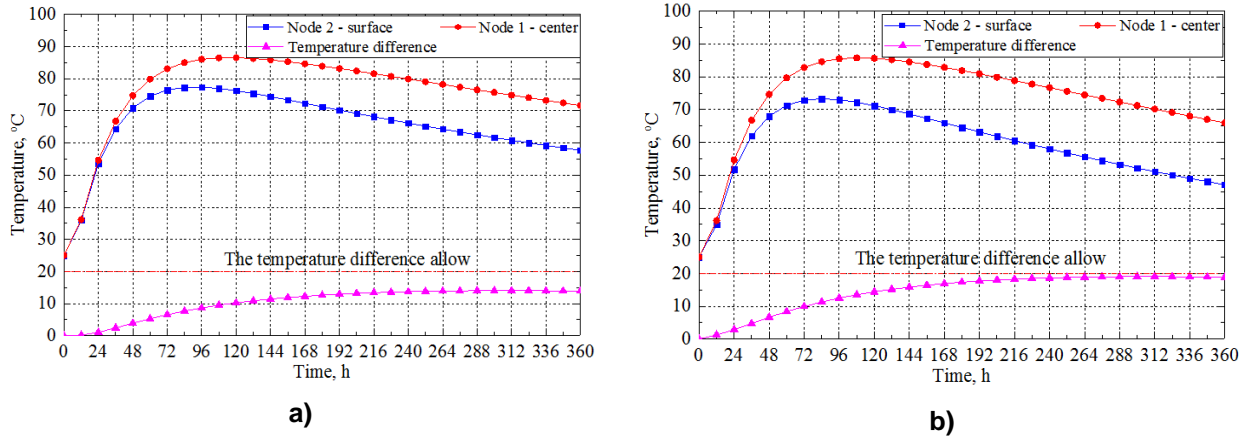


Figure 3. The temperature at the center and the surface of the concrete block and their temperature difference changes over time: a – when the air temperature $T_{air} = 26.5\text{ }^{\circ}\text{C}$, b – when the air temperature $T_{air} = 5.0\text{ }^{\circ}\text{C}$.

Analyzing the results, we can note the following. The temperature in the center of the mass concrete depends little on the ambient temperature. That is explained that mass concrete blocks have a large volume of concrete and low thermal conductivity of concrete mix. The difference between the maximum temperatures in the center of the mass concrete for all air temperature cases and formwork types does not exceed $3.4\text{ }^{\circ}\text{C}$ (~ 4 %). Opposite, the surface temperature of concrete blocks depends largely on air temperature and especially depends on the type of formwork used. This is illustrated by the values of the temperature difference (Table 6). Therefore, from a cracking point of view, concreting in the coldest period is the most dangerous state with the following temperature difference values: for metal formwork – $\Delta T_{max} = 57.14\text{ }^{\circ}\text{C}$; for wooden formwork – $\Delta T_{max} = 32.08\text{ }^{\circ}\text{C}$; for formwork with thermal insulation – $\Delta T_{max} = 19.06\text{ }^{\circ}\text{C}$. Thus, for the case under consideration with high heat release ($CC = 450\text{ kg/m}^3$, $E_{max} = 350\text{ kJ/kg}$), only the use of thermal insulation of the formwork with polystyrene thickness of 3 cm to obtain the temperature difference does not exceed the allowable temperature difference for all air temperatures.

Table 6. Maximum temperature and temperature difference of the concrete block.

| Air temperature | Wood formwork | | Steel formwork | | Thermally insulated formwork | |
|--|---------------|------------------|----------------|------------------|------------------------------|------------------|
| | T_{max} | ΔT_{max} | T_{max} | ΔT_{max} | T_{max} | ΔT_{max} |
| $T_{air} = 26.5\text{ }^{\circ}\text{C}$ | 84.68 | 23.70 | 84.76 | 42.43 | 86.52 | 14.04 |
| $T_{air} = 17.0\text{ }^{\circ}\text{C}$ | 83.97 | 27.35 | 84.05 | 48.89 | 86.12 | 16.21 |
| $T_{air} = 5.0\text{ }^{\circ}\text{C}$ | 83.15 | 32.08 | 83.21 | 57.14 | 85.76 | 19.06 |

In order to assess the formation of cracks, it is necessary to determine the maximum thermal stress appearing at the center and surface of concrete blocks. Calculations of the maximum thermal stress of the concrete block confirm these results (see Fig. 4). Fig. 4 shows the change in maximum thermal stress at the surface and center points of the concrete block for three variants of air temperature. Also shown is a graph of the change in permissible tensile stress, it is possible to assess the possibility of temperature cracks developing in the concrete.

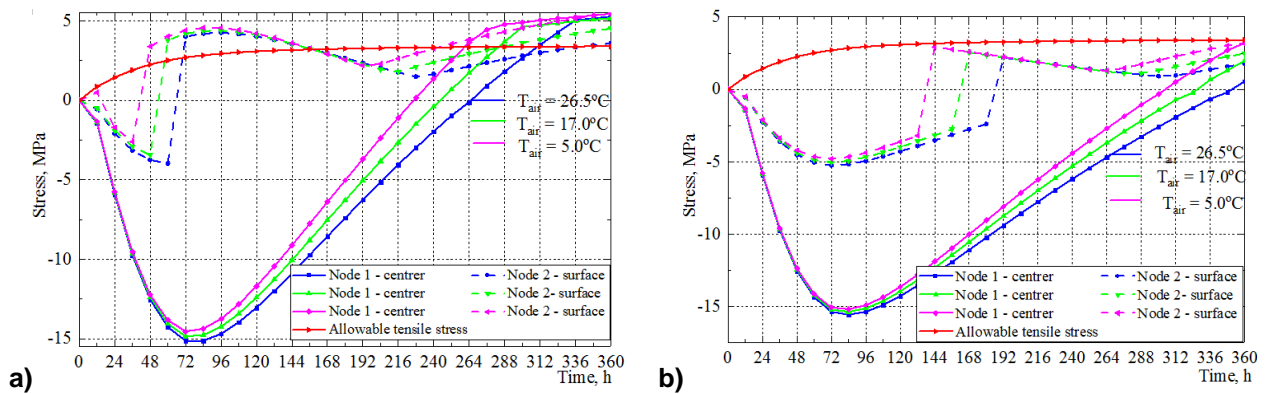


Figure 4. Changes in temperature stresses in the center and surface of the concrete block: a – for wood formwork; b – for insulated formwork.

It can be seen on the chart that: when using wooden formwork (Fig. 4a), the possibility of forming cracks due to stresses on the surface of concrete blocks exceeds the permissible tensile stresses. At the same time, the wooden insulation formwork with polystyrene foam 3 cm thick helps to completely eliminate the appearance of thermal cracks in the mass concrete blocks (Fig. 4b).

It is obvious that after removing the formwork, the surface stress increases (due to the temperature difference between the center and the surface increases) and then decreases over time.

4. Conclusions

Based on the studies and the results obtained, the following conclusions can be drawn:

1. The use of formwork in order to reduce the risk of temperature cracking during the construction of massive concrete structures is an affordable and economical tool. In this sense, metal (steel) formwork is much less effective than wood formwork.
2. The use of insulated formwork is necessary not only for concreting at low temperatures but also to prevent cracking of concrete blocks with the high cement content and high maximum heat dissipation.
3. The research results and the nomograms are obtained may be used as a reference in the design and construction of mass concrete such as dams, foundations, bridge supports, etc.
4. It can further study the effect of the erection of formwork and their materials on the thermal regime in the mass concrete blocks.

References

1. ACI 207.1R-05. Guide to mass concrete. America. 2005. 30 p.
2. Korean Concrete Institute. Thermal crack control of mass concrete, concrete practices Manual. Korean. 2010. 70 p.
3. Rasskazov, L.N., Orekhov, V.G., Aniskin, N.A., Malakhanov, V.V., Bestuzheva, A.S., Sainov, M.P., Soldatov, P.V., Tolstovkov, V.V. Hydraulic structures. Moscow. 2011. Part 2. 586 p.
4. Bushmanova, A.V., Videnkov, N.V., Semenov, K.V., Barabanshchikov, Yu.G., Dernakova, A.V., Korovina, V.K. The thermo-stressed state in massive concrete structures. Magazine of Civil Engineering. 2017. No. 71(3). Pp. 51–60. DOI: 10.18720/MCE.71.6
5. Struchkova, A.Y., Barabanshchikov, Yu.G., Semenov, K.S., Shaibakova, A.A. Heat dissipation of cement and calculation of crack resistance of concrete massifs. Magazine of Civil Engineering. 2018. 78(2). Pp. 128–135. DOI: 10.18720/MCE.78.10
6. Nguyen, C.T., Aniskin, N.A. Temperature regime during the construction massive concrete with pipe cooling. Magazine of Civil Engineering. 2019. 89(5). Pp. 156–166. DOI: 10.18720/MCE.89.13
7. Barbara, K., Agnieszka, K.W. Early age thermal and shrinkage cracks in concrete structures – description of the problem. Architecture, Civil Engineering, Environment. 2011. Vol. 2. Pp. 35–48.
8. Worapong, S., Hikaru, N., Minoru, K., Yasuaki, I. Analysis of crack propagation due to thermal stress in concrete considering solidified constitutive model. Journal of Advanced Concrete Technology. 2017. Vol. 5. No. 1. Pp. 99–112. <https://doi.org/10.3151/jact.5.99>
9. Zhineng, Tong. Cause and influence of mass concrete crack. International Conference on Chemical, Material and Food Engineering. 2015. Pp. 497–499.
10. Aniskin, N.A., Nguyen, T.C. Mathematical model of temperature regime and thermal stress state of roller-compacted concrete gravity dam. IOP Conf. Series: Journal of Physics: Conf. Series. 2019. Vol. 1425. No. 2020. 9 p. DOI: 10.1088/1742-6596/1425/1/012051
11. Aniskin, N.A. Temperature regime gravity dams of the rolled concrete. Hydraulic engineering. 2005. Vol. 12. Pp. 13–17.
12. Sheng-hong Chen, Peifang Su, Isam Shahrouh. Composite element algorithm for the thermal analysis of mass concrete Simulation of cooling pipes. International Journal of Numerical Methods for Heat & Fluid Flow. 2011. Vol. 21. No. 4. Pp. 434–447. <https://doi.org/10.1108/09615531111123100>
13. Yuan-Yuan, Chen, Ssu-Yu, Chen, Chien-Jou, Yang, Hei-Tao, Chen. Effects of insulation materials on mass concrete with Pozzolans. Construction and Building Materials. 2017. Vol. 137. Pp. 261–271. <https://doi.org/10.1016/j.conbuildmat.2017.01.059>
14. Zhang, Xiao-fei, Li, Shou-yi, Li, Yan-long, Ge, Yao, Li, Hui. Effect of superficial insulation on roller-compacted concrete dams in cold regions. Advances in Engineering Software. 2011. Vol. 42. No. 11. Pp. 939–943. DOI: 10.1016/j.advengsoft.2011.06.004
15. Elemuo Peter Onyekachukwu, Puneet Sharma, Jagdeep Singh. Review work on plastic formwork. International Journal of Civil Engineering and Technology (IJCIET). 2017. Vol. 8. No. 7. Pp. 1141–1146.
16. Metin Arslan, Osman Şimşek, Serkan Subaş. Effects of formwork surface materials on concrete lateral pressure. Construction and Building Materials. 2005. Vol. 19. No. 4. Pp. 319–325. DOI: 10.1016/j.conbuildmat.2004.07.007
17. John Gajda, Martha Vangeem. Controlling temperatures in mass concrete. Concrete international. 2002. Pp. 59–62.
18. ACI 207.2R-95. Effect of restraint, volume change, and reinforcement on cracking of mass concrete. America. 1995. 26 p.
19. Lee, M.H., Khil, B.S., Yun, H.D. Influence of cement type on heat of hydration and temperature rise of the mass concrete. Indian Journal of Engineering & Materials Sciences. 2014. Vol. 8. No. 5. Pp. 536–542.
20. Havlásek, P., Šmilauer, V., Hájková, K., Baquerizo, L. Thermo-mechanical simulations of early-age concrete cracking with durability predictions. Materials Science and Engineering. 2017. Vol. 236. 8 p. DOI: 10.1088/1757-899X/236/1/012052
21. Rahimi, A., Noorzai, J. Thermal and structural analysis of roller compacted concrete (R.C.C) dams by finite element code. Australian Journal of Basic and Applied Sciences. 2011. Vol. 5. No. 12. Pp. 2761–2767.
22. Bamforth, P.P., Chisholm, D., Gibbs, J., Harrison, T. Properties of concrete for use in Eurocode 2. The Concrete centre.
23. Wenchao, Liu, Wanlin, Cao, Huiqing, Yan, Tianxiang, Ye, Wang, Jia. Experimental and numerical studies of controlling thermal cracks in mass concrete foundation by circulating water. Applied sciences. 2016. Vol. 6. No. 110. 18 p. DOI: 10.3390/app6040110

24. Xian, Liu, Yong, Yuan, Quanke, Su. Sensitivity analysis of the early-age cracking risk in an immersed tunnel. *Structural Concrete*. 2014. Vol. 15. No. 2. Pp. 179–190. <https://doi.org/10.1002/suco.201300064>
25. Lewis, R.W., Nithiarasu, P., Seetharamu, K.N. *Fundamentals of the finite element method for heat and fluid flow*. John Wiley & Sons. 2004. 356 p.
26. Li, F., Shen, Y. Full-scale test of the hydration heat and the curing method of the wet joints of a precast segmental pier of a bridge. *European Journal of Environmental and Civil Engineering*. 2015. Vol. 21. No. 3. Pp. 348–370. <https://doi.org/10.1080/196481-89.2015.1119063>
27. Bingqi, L., Zhenhong, W., Yunhui, J. Temperature control and crack prevention during construction in steep slope dams and stilling basins in high-altitude areas. *Advances in Mechanical Engineering*. 2018. Vol. 10. No. 1. Pp. 1–15. DOI: 10.1177/1687814017752480
28. Hai, T.H., Thuc, L.V. The effect of splitting concrete placement on controlling thermal cracking in mass concrete. *Journal of science and technology in civil engineering*. 2017. Vol. 11. No. 6. Pp. 22–28. <http://stce.nuce.edu.vn/index.php/en/article/view/932>
29. Abeka, H., Agyeman, S., Adom-asamoah, M., Hussain, R.R. Thermal effect of mass concrete structures in the tropics: experimental, modelling and parametric studies. *Journal Cogent Engineering*. 2017. Vol. 4. No. 1. Pp. 185–192
30. ACI 209.2R-08. Guide for modeling and calculating shrinkage and creep in hardened concrete. American Concrete Institute. 2008. 48 p.
31. Krat, T.Yu., Rukavishnikova, T.N. Assessment of temperature regime and thermal stress state of concrete blocks under different conditions concreting. *News VNIIG 2007*. 248. Pp. 77–85.
32. Teleshev, V.I. *Foundations and Methods of Concrete Dam Design and Construction in Severe Climatic Conditions*. Doctoral Thesis. 2003, St. Peterburg, SpbGPU Publ., 217 p.
33. SP 357.1325800.2017. Concrete constructions of hydraulic structures. Rules of works and acceptance of works. Ministry of construction and housing and communal services of the Russian Federation. 2016. 77p.
34. Do, T.M.D., Lam, T.Q.K. Solutions to improve the quality of mass concrete construction in climate conditions of Southern Vietnam. *International Journal of Innovative Technology and Exploring Engineering (IJITEE)*. 2019. Vol. 8. No. 6 C2. Pp. 188–192.
35. Zhong, R., Hou, G.-P., Qiang, S. An improved composite element method for the simulation of temperature field in massive concrete with embedded cooling pipe. *Applied Thermal Engineering*. 2017. Vol. 124. Pp. 1409–1417. DOI: 10.1016/j.applthermaleng.2017.06.124
36. Nguyen, T.C., Tang, V.L., Bulgakov, B.I. Designing the composition of concrete with mineral additives and assessment of the possibility of cracking in cement concrete pavement. *Materials Science Forum*. 2018. Vol. 931. Pp. 667–673. DOI: 10.4028/www.scientific.net/MSF.931.667
37. Ju-Hyung, Ha, Youn su, Jung, Yun-gu, Cho. Thermal crack control in mass concrete structure using an automated curing system. *Automation in Construction*. 2014. Vol. 45. Pp. 16–24. DOI: 10.1016/j.autcon.2014.04.014
38. Bamforth, P.B. *Early-age thermal crack control in concrete*. CIRIA C660. London. 2007. 113 p.

Contacts:

Nikolay Aniskin, nikolai_aniskin@mail.ru

Trong Chuc Nguyen, ntchuc.mta198@gmail.com

© Aniskin, N.A., Nguyen, T.C., 2020



DOI: 10.18720/MCE.99.12

Flange connections with high-strength bolts with technological heredity of bolts

N. Vatin^{a*}, R.G. Gubaydulin^b, A. Tingaev^b

^a Peter the Great St. Petersburg Polytechnic University, St. Petersburg, Russia

^b South Ural State University, Chelyabinsk, Russia

* E-mail: vatin@mail.ru

Keywords: delayed brittle fracture, finite element method, flanges, high-strength bolts, joints, non-metallic inclusions, steel structures, stiffness, stress-strain state, structure

Abstract. Tubular truss and column members with bolted connections widely used in construction. The object of this research was the flange joint of a truss bottom chord. The flange joint coaxially connects two cold-formed closed welded rectangular hollow section profiles. The flange connects with high-strength bolts of strength class 10.9. The stress-strain state of the joint was numerically and experimentally investigated. Experimental studies were performed on a full-size sample of a flange joint using strain gauges. Numerical calculations were performed at ANSYS. The bilinear isotropic hardening model simulated the metal elements performance of the joint. The “Frictional” model was chosen for the friction forces between the flanges. The microstructure of the bolt material was studied using an optical microscope. The study results showed that the model solution for a flanged provides a uniform distribution of stresses at the junction due to its spatial rigidity. The presence of stiffener ribs provides the absence of the clearance between the flanges and promotes the joint performance of welded units and high-strength bolts. The design of the flange joint using the developed finite element model indicates that the results of numerical and experimental studies are sufficient for practical application. The difference between finite element model calculations and experimental data in the most loaded elements of flange joints does not exceed 10 %. It is proposed for high-strength bolts of strength class 10.9 and higher to introduce regulatory restrictions on the number and size of non-metallic inclusions that affect the delayed brittle fracture of bolts. To improve the performance that bolts, it is proposed to use steel grades with a bainitic or bainitic-martensitic structure, which are formed by microalloying them with molybdenum, vanadium, niobium, titanium, boron and heat treatment.

1. Introduction

Bolted joints have been widely used in steel structures of buildings. One of the most effective of them is bolted-flange connections with high-strength bolts. The advantages of these joints include the simplicity of assembly, the possibility of work in any climatic conditions, high reliability, and the ability to disassemble them without damage to structural elements [1–6]. Bolted joints may be subject to the combined action of axial compression, bending moments and shearing under the combination of dead, live, wind loads or earthquake action.

Flange connections in structures are subject to tension, compression, tensile bending, seismic actions, and vibration loads with the number of cycles of constant loading up to 105 with an asymmetry coefficient of at least 0.8 [4, 7].

The disadvantages of flange connections include high requirements for the accuracy of their manufacture since this type of connections does not have a proper compensating ability. In particular, experience with flange connections indicates that combinations of unfavorable structural and technological deviations, such as non-planarity of matching surfaces, displacement of hole axes, misalignment of nut and bolt bearing surfaces, etc., increase the likelihood of their failure, especially when using bolts of the strength class 10.9 and higher [8–10].



The design of flange connections is a rather complicated task [10, 3, 11]. As a result, the main provisions of the regulatory methods for calculating flange joints are formulated, which establish three types of design models (rigid, semi-rigid and flexible), which differ in the development of fracture mechanism [12, 13].

In the case of using flexible flanges, the destruction of the joint occurs due to the development of significant plastic deformations in the flange. The bearing capacity of the connection in this case is determined by the bearing capacity of the flange itself, while the forces acting in the bolts do not reach their ultimate state. When using semi-rigid flanges, their bending stiffness increases, and the destruction of the joint occurs due to the destruction of the bolts during the partial development of plastic deformations in the flanges. For joints with rigid flanges, the ultimate state is the destruction of a high-strength bolt, while the stress-strain state of the remaining elements of the flange is characterized by the elastic behavior of the material. The flange thickness has a considerable impact on the connection properties, while the bolt edge distance and the flange edge width were found to have a smaller effect [4, 5, 14, 15].

The design rules for calculating flange joints are mainly based on the experimental results of T-shaped joints' models, which have been tested and refined concerning specific types of joints. For example, in the EU countries, flanged joints with double and four-row arrangement of bolts without stiffeners are widely used, which are more technologically advanced and less demanding to manufacture [12], however, they are unbeneficial in terms of strength and stiffness when compared to flange joints with additional stiffening ribs. In particular, flanged joints without stiffeners with a double-row arrangement of bolts can provide only 30...40 % of the profile strength of the connected elements, and with a four-row arrangement can provide 60...70 % of the profile strength [16].

It should be noted that the design rules for flange joints are valid for certain types of structural solutions and for a limited range of flange thicknesses, which does not allow us to use them in the design of flange joints for technically complex and unique structures. In this regard, the most universal tool for determining the stress-strain state of flange joints, considering the combined behavior of its elements (flanges, bolts and welded joints), is the finite element method. The use of the finite element method allows us to avoid using idealized models and standard design models and to examine in more detail the behavior of individual elements of flange joints considering their geometric and physical nonlinearity.

The effectiveness of applying the finite element method to consider the influence of structural factors on the stress-strain state of flange joints is doubtless [17, 18]. At the same time, it should be noted that to ensure the accuracy of the calculation of the stress-strain state of flange joints, it is necessary to use finite element models validated with experimental tests. The absence of such models is one of the main factors restraining the use of the finite element method as a method for calculating flange joints.

The calculation of the stress-strain state of a flange joint is a necessary but not sufficient condition for ensuring its safe behavior, especially for cases in which its ultimate state is the destruction of high-strength bolts. Single-direction high-strength bolts are mostly used in column-beam joints and conventional high-strength bolts are mostly used in flange connections. Experimental results show that two types of the bolt have different failure models [19]. The failure of the single-direction high-strength bolt is due to the pullout of the bolt, which is caused by the extrusion bending deformation of its outer sleeve [19].

In flange joints, conventional high-strength bolts of strength class 10.9 and higher are characterized by an increased tendency to hydrogen embrittlement [20, 8], in which relatively insignificant changes in the structure, properties and stress-strain state of the bolt, if the combination is unfavorable, can initiate the process of delayed brittle fracture.

Delayed brittle fracture of high-strength bolts is one of the most difficult to predict types of ultimate state [21–26], for which no design rules have yet been developed. Therefore, to reduce the risk of its occurrence, the standard [27] recommends using experimental methods for assessing resistance to delayed brittle fracture, which allows building designers to properly choose a material, manufacturing technology, and anticorrosive protection of bolts.

It follows from the review that the connections of steel structures with rigid flanges, stiffening ribs and high-strength bolts have not been adequately studied. In particular, there is no analysis of the influence of the technological heredity of high-strength bolts on the general characteristics of the flange connection. Technological heredity is the transfer to the finished product in the process of manufacturing errors, mechanical and physical and chemical properties of the original billet or properties and errors formed in the billets in individual operations of manufacturing the product [28].

The work aims to develop recommendations for improving the design of flange joints, as well as recommendations for improving the standards for the quality of high-strength bolts with the risk of delayed brittle fracture.

The objectives of the study are:

1. Analysis of the effectiveness of a typical solution of flange joints according to the results of experimental and numerical studies of the stress-strain state.
2. Studies to assess the influence of technological heredity factors on the performance of high-strength bolts, develop proposals for regulatory restrictions on the number and size of non-metallic inclusions that affect delayed brittle fracture of bolts, develop proposals for the selection of steel grades for the manufacture of bolts.

2. Methods

2.1. The investigated flange joints

This paper experimentally investigated the flanged joint of the truss bottom chord. The flanges were connected by high-strength bolts with a diameter of 24 mm, strength class 10.9 (Fig. 1). The section of the bottom truss chord is made of a cold-formed closed welded rectangular hollow section profile 140×140×4 mm of the S345-3 steel grade according to Russian State Standard GOST 30245-2012 "Steel bent closed welded square and rectangular section for building. Specifications".

The connection flange is made of 30 mm thick sheet steel of the same grade S345-3 steel grade. The S345-3 steel grade is specified by Russian State Standard GOST 27772-2015 "Hot-rolled steel for building steel structures. General specifications". The properties of S345-3 steel are given in Tables 1, 2.

Table 1. The S345-3 steel grade chemical decomposition.

| Steel grade | Mass fraction, % | | | | | | | | |
|-------------|------------------|-----------|--------|--------|--------|--------|------------|---------|---------|
| | C | Mn | Si | Cr | Ni | Cu | Al | S | P |
| S345-3 | ≥ 0.15 | 1.30–1.70 | ≥ 0.80 | ≥ 0.30 | ≥ 0.30 | ≥ 0.30 | 0.015–0.06 | ≥ 0.025 | ≥ 0.030 |

Table 2. The S345-3 steel grade mechanical properties.

| Steel grade | Thickness [mm] | Yield strength σ_y [MPa] | Ultimate strength σ_u [MPa] | Elongation A_5 [%] | Impact strength KCV^{40} [J/cm ²] |
|-------------|----------------|---------------------------------|------------------------------------|----------------------|---|
| S345-3 | 4-10 | ≥ 345 | ≥ 490 | ≥ 21 | ≥ 34 |
| | 20-40 | ≥ 305 | ≥ 460 | ≥ 21 | ≥ 34 |

The connection of the chord (Tag No. 287) with the flange (Tag No. 34) is made by equal-angle fillet welds with a 4 mm leg (Fig. 2). The stiffeners (Tag No. 75) are connected to the chord by equal-angle fillet welds with a 5 mm leg. All welds are made by mechanized welding in a protective gas medium with welding steel wire of the steel grade Sv-08G2S with a diameter of 1.2 mm. The welding steel wire is specified by Russian State Standard GOST 2246-70 "Welding steel wire. Technical specifications". The quality of the welds is confirmed by visual, measuring, and ultrasonic testing.

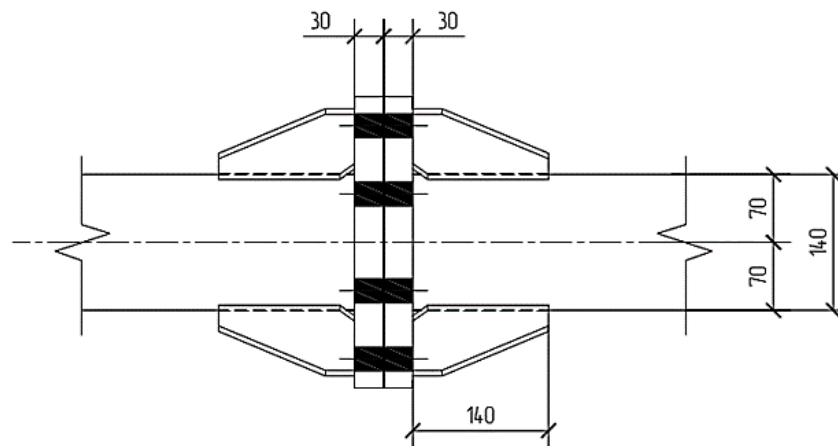


Figure 1. Analyzed joint.

2. The external load was uniformly distributed between the bolts.
3. The analytical model cannot be represented in the form of a flat beam system. Therefore, it is necessary to take into account the spatial behavior of the joint in two orthogonal planes.
4. The stress-strain state of the flange and bolts depends on the ratio of the stiffness properties of the connected elements.

To take these features into account, the following assumptions were made:

1. A tensile force is applied along the centerline of the chord.
2. The bolt is modeled by a cylinder. The cross-sectional area of the cylinder in the bolt's thread segment is equal to the net area of the bolt. The cross-sectional area of the cylinder out of the bolt's thread segment is equal to the gross area of the bolt.
3. The contact between the surfaces of the flanges is a tight connection of two surfaces. A shift of one surface along another causes a friction force.
4. The contact of the inner surface of the bolt head and the outer surface of the flange does not interrupt during loading. The friction of one surface relative to another is allowed.
5. To describe the nonlinear properties of the material, a bilinear model with isotropic hardening was chosen. The model establishes the following relationship between load σ and strain ε . The transition from an elastic to a plastic state is determined by the von Mises criterion.

$$\sigma = \begin{cases} E \cdot \varepsilon, & \text{when } \varepsilon \leq \sigma_y / E \\ \sigma_y + E_T (\varepsilon - \sigma_y / E), & \text{when } \varepsilon > \sigma_y / E \end{cases}$$

where ε is the current value of the relative deformation of the specimen, σ_y is yield strength, E_T is the tangent module of elasticity, E is Young's modulus. The values of the tangential modulus of elasticity E_T and Young's modulus E for steel grade C345-3 are taken equal to 0.92 GPa and 206 GPa, respectively, the remaining values are taken from Table 2.

In numerical modeling of flange joints, it is important to choose the models of the contact parts of the joint [30], [33]. ANSYS allows users to set different models for each contact pair, which are based on different physical and mechanical conditions for the interaction of real objects. In this study, the contact between the flanges in the joint is described using the "Frictional" model, which takes into account the sliding friction force proportional to the magnitude of the normal reaction with a friction coefficient of 0.25. The inner face of the bolt head and the upper face of the flange are connected by the "Bonded" contact, preventing them from moving along the axis of the bolt. In the model of flange joint, solid finite elements with a sampling interval of 10 mm were used. The number of finite elements in the model is 130630. The number of nodes is 224048 (Fig. 4).

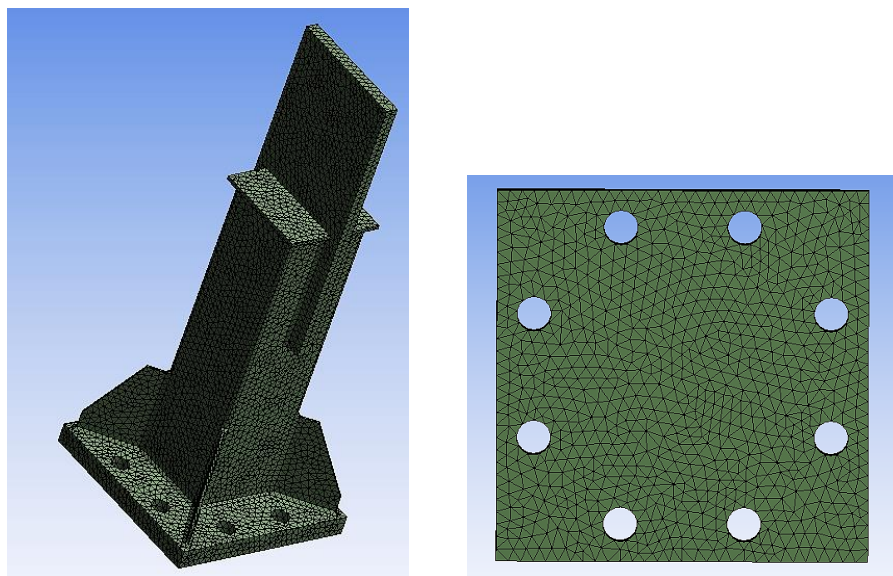


Figure 4. FE model of the joint.

The calculation of the model was carried out in a geometrically and physically nonlinear formulation in the following sequence. Initially, the force of the preliminary tension of the bolts was created, then this state

was fixed, and only after that, the design load equal to 451 kN was applied to the joint. The calculated load was applied with a uniform distribution over the cross-sectional area of the square section profile of the test joint. The restriction on all degrees of freedom as boundary conditions was used on the opposite side of the joint, i.e., the opposite side of the joint was absolutely rigid fixed.

2.4. Metallographic test of bolts

At the third stage of the research, metallographic studies were carried out to assess the effect of non-metallic inclusions on the performance of high-strength bolts. Non-metallic inclusions are a factor in the technological heredity of bolt stock. The typical non-metallic inclusions are oxides and sulfides. At present, non-metallic inclusions are not regulated and are not a defect in assessing the quality of high-strength bolts. A significant fraction of the failure of high-strength bolts is associated with contamination of steel by non-metallic inclusions [34, 35].

The microstructure of the bolt material was studied using an Axio Observer D1.m optical microscope equipped with a Thixomet Pro hardware-software complex for image analysis. The Estimation of the amount and shape of non-metallic inclusions was studied on etched thin sections. To identify the microstructure, the bolt samples were etched in a 4 % solution of nitric acid in ethanol. The hardness was measured by FM-800 microhardness tester with a load of 300 g and by Rockwell hardness tester TP 5014.

3. Results and Discussion

3.1. . Experimental and numerical studies

The results of experimental and numerical studies of the stress-strain state of the analyzed joint are compared in Fig. 5–10. In these figures, the numerator shows the results of the experiment, and the denominator shows the results of numerical calculation.

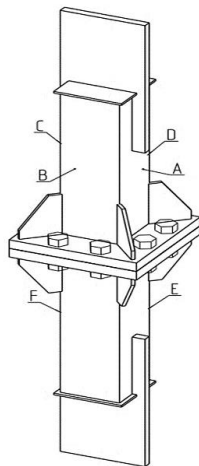


Figure 5. Scheme for marking the surfaces of the sample.

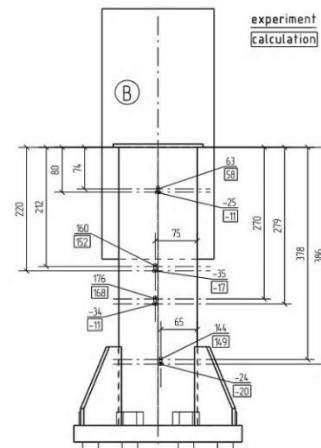


Figure 6. Stress values on surface B, MPa.

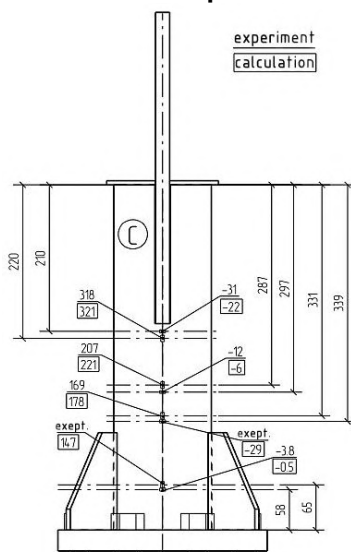


Figure 7. Stress values on surface C, Mpa.

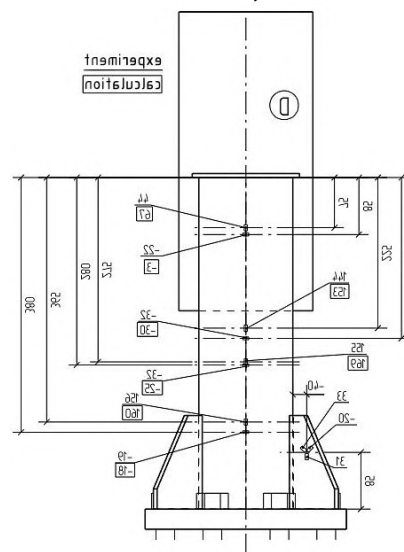


Figure 8. Stress values on surface D, Mpa.

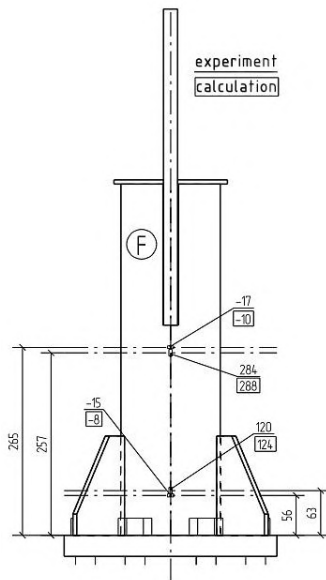


Figure 9. Stress values on surface F, MPa.

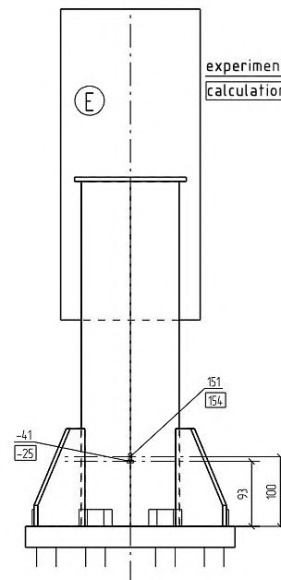


Figure 10. Stress values on surface E, Mpa.

Fig. 7–10 show that tensile forces act in along direction on the part of the chord which is above the stiffening ribs. Those forces create stresses of 160–220 MPa. Compressive forces act in the transverse direction to the chord. The compressive forces create stresses of up to 35 MPa. On the transition area from the free chord to the area with stiffening ribs, the tensile stresses decreased to 120–160 MPa. In this case, the stress created by the compressive forces remains at approximately the same level. Partial unloading of the chord in this section is due to the performance of stiffening ribs, which are in the complex stress state.

It should be noted here that the main stress plates in this case do not coincide with the axes of the strain gauges glued to the stiffening rib. Therefore, the stress values shown in Fig. 7 are somewhat different from the stresses acting in the main stress plates. In particular, the main tensile stresses at this point are 75 MPa, and compressive – 15 MPa. In the other areas, where the rosette of the sensor sticker was used, no significant differences were found.

Maximum stresses in the flange occur in areas under the head and nut of high-strength bolts. The magnitude of these stresses is about 170 MPa (Fig. 11) and is due to the preliminary tension of the bolts. In other parts of the flange, the stress level is much lower and does not exceed 35 MPa. The maximum clearance between the flanges is observed at the installation site of the stiffening ribs, and is 0.2 mm. Under the square section profile, it is slightly smaller and does not exceed 0.15 mm.

The external force applied at one bolt is much less than the force of its preliminary tension. So, for example, when a load of 608 kN is applied to the assembly, only 76 kN falls on one bolt, which is 3.51 times less than the force of its preliminary tension. Due to this fact, any significant changes in the stress-strain state of the bolts were detected neither by experimental nor numerical methods. The clearance between the flanges under the bolts did not appear. The maximum stresses arise in the body of the bolt and is about 600 MPa (Fig. 12).

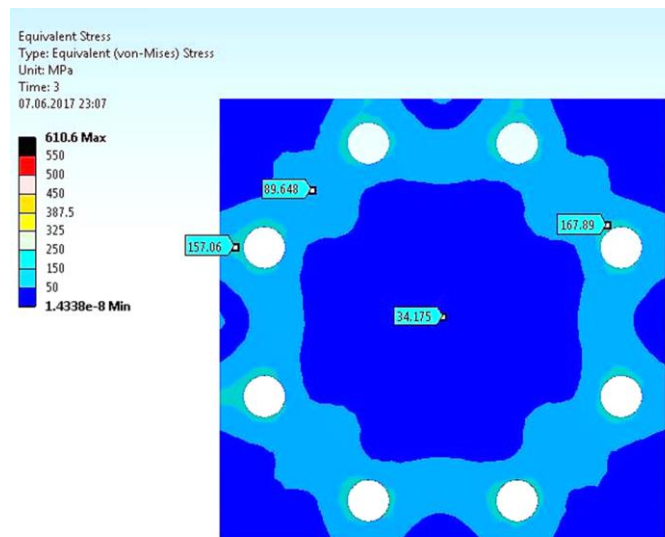


Figure 11. von Mises equivalent stresses on the flange surface [MPa].

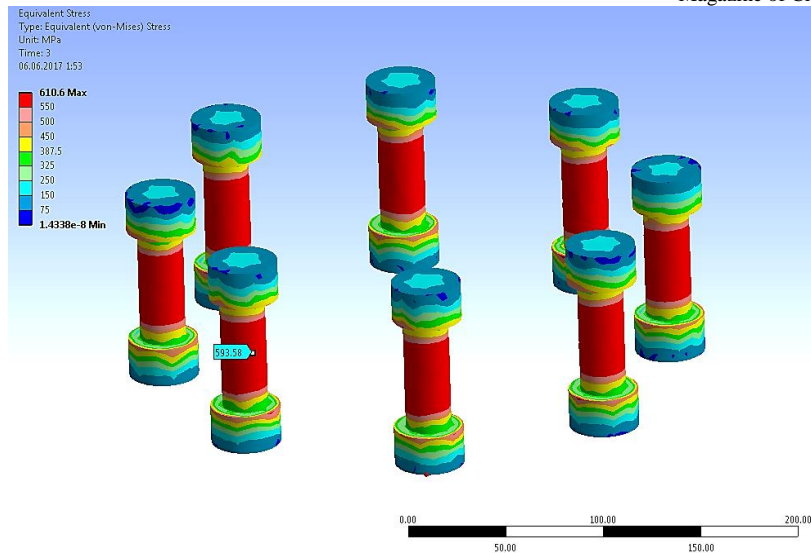


Figure 12. von Mises equivalent stresses in Fasteners [MPa].

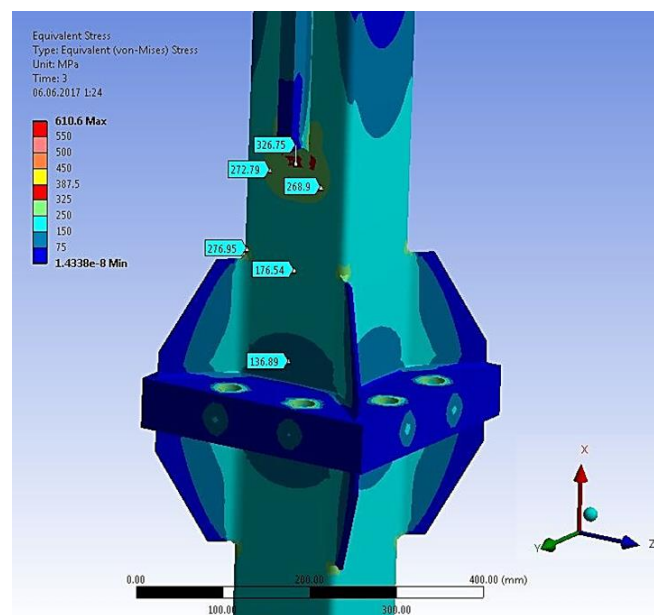


Figure 13. von Mises equivalent stresses in the joint [MPa].

From the analysis of the stress-strain state, it follows that the joint has a large safety margin of strength and that the stress-strain state is non-optimal by the distribution. For example, the most part of flanges and stiffening ribs turned out to be unloaded in comparison with the square section profile. In the chord itself, in the area where the stiffening ribs are adjacent to the profile, in its upper part, the stress is 1.5 times greater than in the rest of the section (Fig. 13).

In most elements, the calculated and experimental values of stresses practically coincide. The maximum difference between them in the most loaded elements does not exceed 10 %. To illustrate the capabilities of the developed finite element model in the studied unit, the thickness of the flanges and the diameter of the bolts was reduced to 20 mm, and the height of the stiffening ribs was increased to 210 mm. From the calculation results it follows that when the design load is applied, the clearance between the flanges under the bolts did not appear, the material of the flange joints behaves elastically.

The increase in the height of the stiffening ribs (L) to the value recommended in [36] with $L > 1.5 H$, but not less than 200 mm, did not significantly affect the stress-strain state of the horizontal cross-section (Fig. 14). Where H is the cross-sectional depth of the horizontal cross-section.

The decrease in the thickness of the flanges led to an increase in the equivalent stresses in them under the hydraulic fracturing to 62 MPa (Fig. 15), and the clearance between flanges increased to 0.3 mm. The clearance between the flanges under the stiffening ribs has not changed. Thus, it can be stated that the optimized assembly is in a completely operable state and provides material savings and a reduction in the diameter of the bolts.

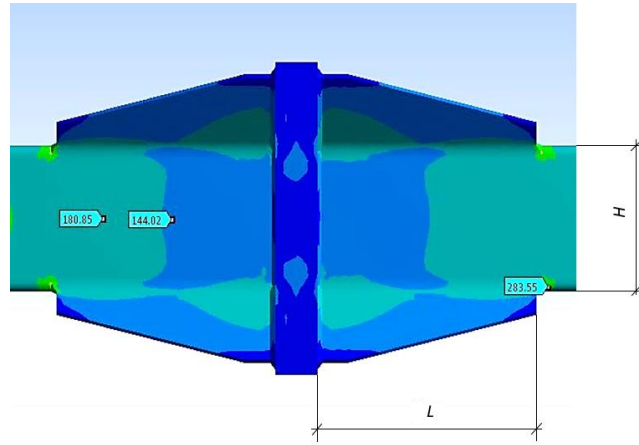


Figure 14. von Mises equivalent stresses in a modified joint [MPa].

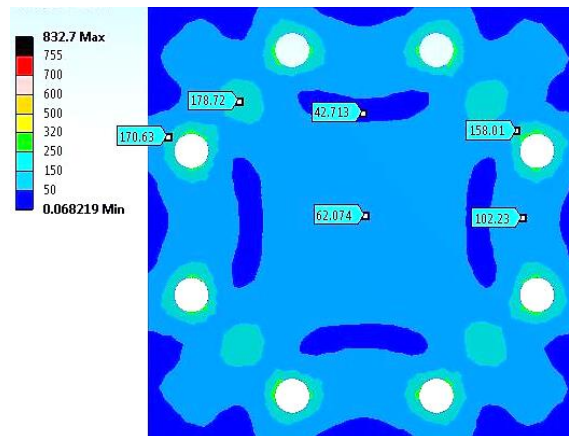


Figure 15. von Mises equivalent stresses on the surface of a modified joint flange [MPa].

3.2. Metallographic studies

The performance of a flange joint depends on the bearing capacity of high-strength bolts. Bolts are critical elements for this type of flange connection. The determination of the bearing capacity of a bolt during its viscous destruction is regulated by current regulatory documents and does not cause difficulties. Problems arise when evaluating the performance of a bolt in the presence of a risk of delayed brittle fracture. Such destruction depends on the saturation of the metal with hydrogen diffusion, the magnitude of tensile stresses, the structure of the steel, and the contamination of its non-metallic inclusions.

Delayed brittle fracture of high-strength bolts is a dangerous type of fracture. It occurs at nominal stresses below the creep limit of the material and is determined by the strength of the grain boundaries in the metal. The state of metal grains depends on several internal factors and varies over time. The main causes of damage are non-metallic inclusions, the size and quantity of which are not regulated by the current regulatory documents for the manufacture of high-strength bolts [34, 35].

Fig. 16 shows the surface crack formed under the head of the M30×160 10.9 bolt. The bolt was made of steel of the Russian grade 40X (Table 3). The crack was detected by visual inspection of the quality of the anti-corrosion coating applied by electrolytic galvanizing.

Table 3. The chemical composition of the steel according to Russian State Standard GOST 4543-2016 “Metal products from structural alloy steel. Technical specifications”.

| Steel grade | Mass percentage, % | | | | | | | |
|-------------|--------------------|---------|-----------|---------|-------|-------|--------|--------|
| | C | Mn | Si | Cr | Ni | Cu | S | P |
| 40X | 0.36–0.44 | 0.5–0.8 | 0.17–0.37 | 0.8–1.1 | ≥0.30 | ≥0.30 | ≥0.035 | ≥0.035 |

From the results of metallographic studies, it was found that the microstructure of the bolt material is troostosorbite tempering, which preserves the needle orientation of martensite (Fig. 17). The steel at the crack is not decarburized, the hardness of the bolt meets the requirements of ISO 898-1-2014. The bolt’s crack is radial, sinuous, and runs along the grain boundaries. Opened and closed cavity cracks are associated with sulfide inclusions lines. The beginning of the crack lies on the surface of the bolt rod.

The studies of non-etched samples taken from the bolt showed the presence in it of many sulfide inclusions lines. The inclusions identified by Russian State Standard GOST 1778-70 "Steel. Metallographic methods for the determination of non-metallic inclusions" as 2-3 points (Fig. 18, inclusions type 1). Most of these inclusions are located near the crack. In the remaining fields of view of the sample, mainly point oxides and sulfides are present and identified as 2 points (Fig. 18, inclusions type 2).

It can be assumed that crack formation occurred during bolt hardening as a result of the separation of grain-boundary sulfides from the metal matrix under the action of tensile stresses. The final crack opening appeared, most likely, at the stage of electrolytic galvanizing of the bolt due to diffusion of atomic hydrogen into the prefracture zone, which led to a decrease in the cohesive strength of the interphase boundaries between the metal matrix and nonmetallic inclusions.

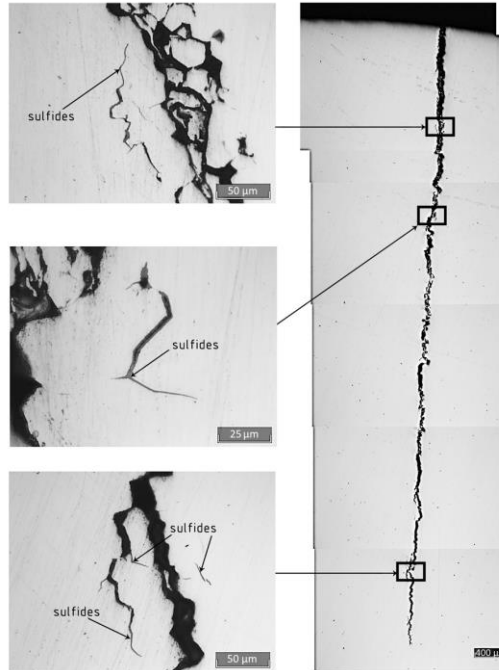


Figure 16. Crack panorama.

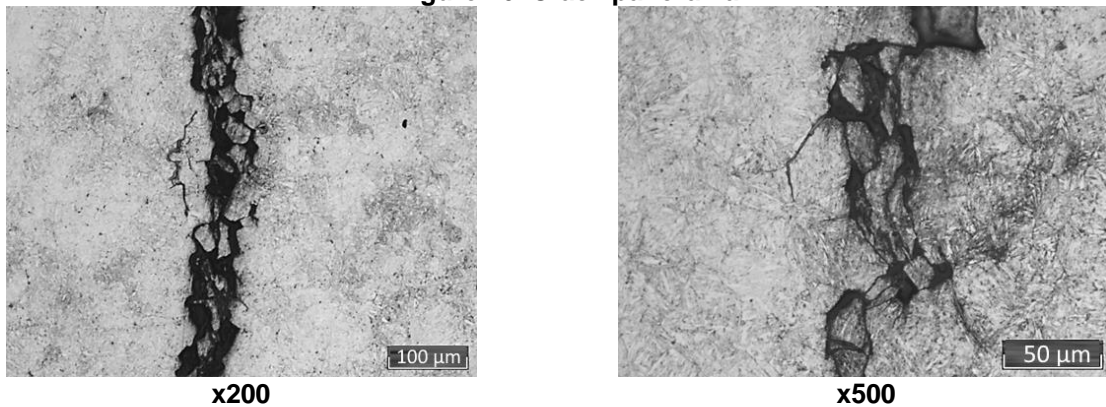


Figure 17. The microstructure of the bolt with a crack passing through the grain boundary inclusions.

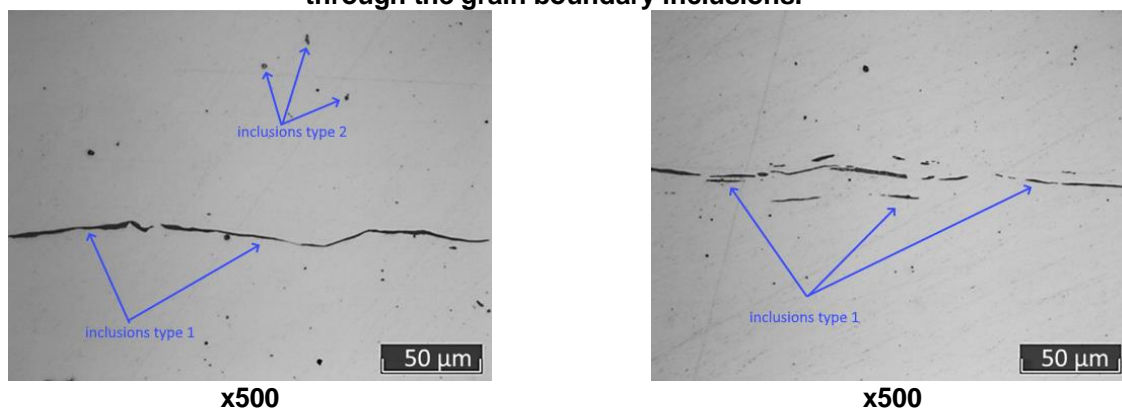


Figure 18. Sulfide inclusions lines under the head of a bolt on a longitudinal non-etched section.

Fig. 19 shows a photograph of the fracture surfaces of bolts M30-6gx160 of strength class 10.9 made of steel 40X. The destruction occurred as a result of the separation of the heads in the process of tensioning the bolts with a force less than the designed.

Studies have shown that the main reason for the failure of bolts is the low quality of bolt stock, namely the presence of large precipitates of sulfides along grain boundaries (Fig. 20). Initially, after rolling, the sulfides are oriented in the rolling direction, which coincides with the axis of the bolt shaft. This is not critical for the given scheme of loading the bolt in the seam assembly. However, during stamping of the bolt head, non-metallic inclusions were deformed along with it and, repeating the configuration of the head, extended in the direction perpendicular (with respect to the initial state). When a bolt is tensioned with inclusions oriented perpendicular to the axis of the bolt, grain-boundary sulfides detach from the metal matrix at voltages lower than the design ones (Fig. 21).



Figure 19. Fracture surfaces of severed bolt heads.

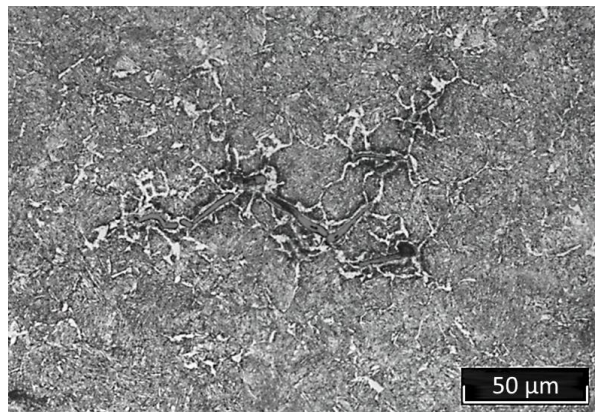


Figure 20. Sulfide precipitation along austenitic grain boundaries.



Figure 21. Cavities and cracks oriented perpendicular to the bolt axis under the bolt fracture surface, x50.

The examples of fracture of high-strength bolts discussed above show the need to consider delayed brittle fracture in regulatory documents for the design, manufacture, and assembly of flange joints. The quality of steel for non-metallic inclusions can be ensured by various types of out-of-furnace processing of steel, during which the quantity, size, and shape of non-metallic inclusions are optimized.

For bolts of strength class 10.9 and higher, it is necessary to use microalloyed steel with vanadium, niobium, titanium, and boron. The presence of these elements prevents the growth of austenitic grain during steel hardening, and under certain heat treatment conditions, it allows the formation of a finely dispersed bainitic or bainitic-martensitic structure [9, 37–40]. Such steels have high strength and toughness, better resist delayed brittle fracture, and are not so sensitive to stress concentrators.

Considering the influence of technological heredity on the bearing capacity of high-strength bolts requires more in-depth study and proper reflection in regulatory documents. For example, in the current regulatory documents for the manufacture of bolts, the shape of the hollows of the thread is not regulated and can be either rounded or flat-cut. For high-strength bolts with a strength class of 10.9 and higher, a thread with a rounded hollow profile is preferable, since it has a lower concentration of stresses and better resists crack nucleation [9, 41]. The presence of a small and unregulated transition radius at the base of the depression of a plane-cut profile contributes to the formation of microcracks at medium voltages less than design.

Fig. 22 shows macro slices of a flat-section profile of a threaded cavity of a high-strength stud of strength class 10.9 made of steel 30KhGSA in the initial state and after the destruction. The hollow of the thread shown in Fig. 21b was in the third from the place of destruction of the pin, which collapsed after 45 days after its installation.

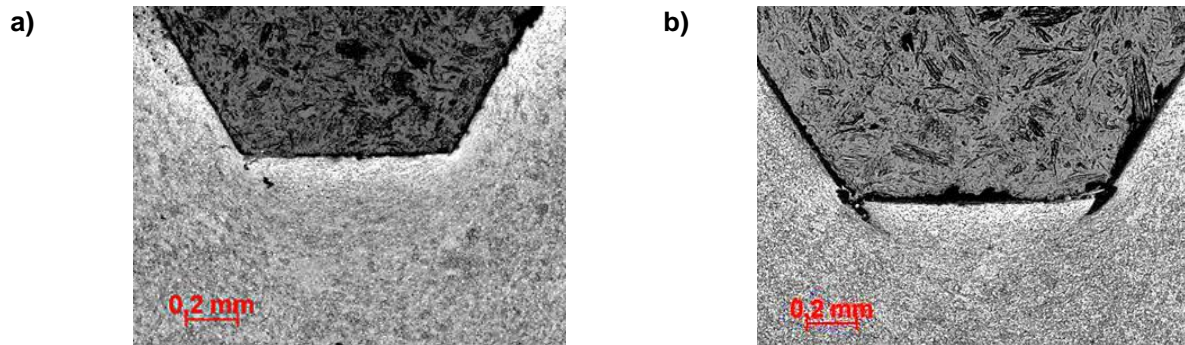


Figure 22. Flat-cut profile of the thread cavity of the stud 2M48-6gx500 10.9 before (a) and after (b) fracture.

4. Conclusions

The flanged joint of the bottom chord of a truss made of a cold-formed closed welded square profile is studied. The joint included rigid flanges with stiffening ribs and high-strength bolts. The stress-strain state of the flange joint was determined by strain gauges testing the full-scale unit. The numerical simulation was performed in ANSYS. Studies of the technological heredity of high-strength bolts were carried out by metallographic and durometric methods.

The results obtained allow to draw the following conclusions:

1. The model solution for a flanged coaxial connection of two square section bent closed welded strip profiles (Fig. 1, 2) provides for the most part a uniform distribution of stresses at the junction due to its spatial rigidity. The presence of stiffening ribs provides the absence of the clearance between the flanges and promotes the joint performance of welded units and high-strength bolts.
2. The disadvantages of this connection include the incomplete loading of flanges and stiffeners in comparison with a square section bent closed welded strip profiles. Stresses in flanges and stiffeners do not exceed 50 MPa. The field tests of full-size flange joints showed that the destruction of such joints occurs along the body of a section not reinforced with stiffening ribs.
3. The calculation of the flange joint using the developed finite element model indicates that the results of the numerical and experimental studies are sufficient for practical application. The difference between them in the most loaded elements of flange joints does not exceed 10 %.
4. To ensure the bearing capacity of high-strength bolts of strength class 10.9 and higher, which are part of rigid flange joints, it is proposed to introduce regulatory restrictions on the number and size of non-metallic inclusions that affect the delayed brittle fracture of bolts.
5. To improve the performance of high-strength bolts of strength class 10.9 and higher, it is proposed to use steel grades with a bainitic or bainitic-martensitic structure, which are formed by microalloying them with molybdenum, vanadium, niobium, titanium, boron and heat treatment. The strength of such steels reaches 1400–1600 MPa, while their toughness, fracture toughness, as well as resistance to delayed brittle fracture increases.

5. Acknowledgements

The research is partially funded by the Ministry of Science and Higher Education of the Russian Federation as part of World-class Research Center program: Advanced Digital Technologies (contract No. 075-15-2020-934 dated 17.11.2020).

Field tests of flanges were carried out under an agreement with CJSC INSI, Chelyabinsk, Russia. The authors thank master students V.A. Stabel and K.A. Patlusova of the South Ural State University for help in this work.

References

1. Liu, X.-C., Cui, F.-Y., Jiang, Z.-Q., Wang, X.-Q., Xu, L., Shang, Z.-X., Cui, X.-X. Tension–bend–shear capacity of bolted-flange connection for square steel tube column. *Engineering Structures*. 2019. 201. DOI: 10.1016/j.engstruct.2019.109798
2. Willibald, S. *Bolted Connections for Rectangular Hollow Sections under Tensile Loading*. Universität Fridericiana zu Karlsruhe, 2003.
3. Yamaguchi, T. *Fundamental Study on High Strength Bolted Tensile Joints*. Kyoto University, 1996.
4. Leong, S.H., Sulong, N.H.R., Jameel, M. Bolted connections to Tubular columns at ambient and elevated temperatures – A review. *Steel and Composite Structures*. 2016. 21(2). Pp. 303–321. DOI: 10.12989/scs.2016.21.2.303
5. Liu, X.C., He, X.N., Wang, H.X., Zhang, A.L. Compression-bend-shearing performance of column-to-column bolted-flange connections in prefabricated multi-high-rise steel structures. *Engineering Structures*. 2018. 160. Pp. 439–460. DOI: 10.1016/j.engstruct.2018.01.026
6. Liu, X.C., Pu, S.H., Zhang, A.L., Zhan, X.X. Performance analysis and design of bolted connections in modularized prefabricated steel structures. *Journal of Constructional Steel Research*. 2017. 133. Pp. 360–373. DOI: 10.1016/j.jcsr.2017.02.025
7. Hoang, V.L., Jaspert, J.-P., Demonceau, J.-F. Behaviour of bolted flange joints in tubular structures under monotonic, repeated and fatigue loadings I: Experimental tests. *Journal of Constructional Steel Research*. 2013. 85. Pp. 1–11. DOI: 10.1016/j.jcsr.2013.02.011
8. Álvarez, J.A., Lacalle, R., Arroyo, B., Cicero, S., Gutiérrez-Solana, F. Failure analysis of high strength galvanized bolts used in steel towers. *Metals*. 2016. 6(7). DOI: 10.3390/met6070163
9. Tingaev, A.K., Gubayduln, R.G., Shaburova, N.A. Causes of Failure of High-Tensile Stud Bolts Used for Joining Metal Parts of Tower Crane. *IOP Conference Series: Materials Science and Engineering*. 2017. 262(1). DOI: 10.1088/1757-899X/262/1/012058
10. Willibald, S., Packer, J.A., Puthli, R.S. Experimental study of bolted HSS flange-plate connections in axial tension. *Journal of Structural Engineering*. 2002. 128(3). Pp. 328–336. DOI: 10.1061/(ASCE)0733-9445(2002)128:3(328)
11. Kato, B., Mukai, A. Bolted tension flanges joining square hollow section members. *Journal of Constructional Steel Research*. 1985. 5(3). Pp. 163–177. DOI: 10.1016/0143-974X(85)90001-X
12. EN 1993-1-8: Eurocode 3: Design of steel structures – Part 1-8: Design of joints.
13. *Standard Specifications for Steel and Composite Structures*. English version Tokyo, 2009.
14. Wang, X., Wang, Y., An, Q. Moment Resistance and Stiffness of an Assembled Beam-Column Joint with High-Strength Bolt and External Diaphragm | 装配式梁柱外环板高强螺栓连接节点抗弯承载力及节点刚度研究. *Tianjin Daxue Xuebao (Ziran Kexue yu Gongcheng Jishu Ban)/Journal of Tianjin University Science and Technology*. 2019. 52. Pp. 75–82. DOI: 10.11784/tdxbz201904086
15. Liu, X., He, X., Zhang, A., Wang, H., Zhan, X., Xu, L. Bearing performance of bolted-flange connection of square steel tubular column under tension-bend-shearing combination | 拉-弯-剪组合作用下法兰连接方钢管柱受力性能研究. *Jianzhu Jiegou Xuebao/Journal of Building Structures*. 2018. 39(6). Pp. 69–80. DOI: 10.14006/j.jzjgxb.2018.06.008
16. Nadolski, V. Calculation and Construction of the Flange Connection of Rectangular Elements Subjected to the Axial Tension. *Vestnik of PSU. Part F. Constructions. Applied Sciences*. 2018. (8). Pp. 121–130.
17. Ismail, R.E.S., Fahmy, A.S., Khalifa, A.M., Mohamed, Y.M. Numerical study on ultimate behaviour of bolted end-plate steel connections. *Latin American Journal of Solids and Structures*. 2016. 13(1). Pp. 1–22. DOI: 10.1590/1679-78251579
18. Tarleton, E. Incorporating hydrogen in mesoscale models. *Computational Materials Science*. 2019. 163. Pp. 282–289. DOI: 10.1016/j.commatsci.2019.03.020
19. Wang, Y., Jia, S., Chai, W. Experimental Study and Numerical Analysis of T-Stub Connections with Single Direction High Strength Bolts | 单边高强螺栓 T 型件连接节点试验研究及数值模拟. *Tianjin Daxue Xuebao (Ziran Kexue yu Gongcheng Jishu Ban)/Journal of Tianjin University Science and Technology*. 2018. 51. Pp. 78–85. DOI: 10.11784/tdxbz201804057
20. Brahim, S.V., Yue, S., Sriraman, K.R. Alloy and composition dependence of hydrogen embrittlement susceptibility in high-strength steel fasteners. *Philosophical Transactions of the Royal Society A: Mathematical, Physical and Engineering Sciences*. 2017. 375(2098). DOI: 10.1098/rsta.2016.0407
21. Akiyama, E. Evaluation of delayed fracture property of high strength bolt steels. *ISIJ International*. 2012. 52(2). Pp. 307–315. DOI: 10.2355/isijinternational.52.307
22. Hagihara, Y. Evaluation of delayed fracture characteristics of high-strength bolt steels by CSRT. *ISIJ International*. 2012. 52(2). Pp. 292–297. DOI: 10.2355/isijinternational.52.292
23. Major, I., Major, M., Kuliński, K. The influence of high-strength bolts stiffening on flange connection behaviour. *Engineering Transactions*. 2019. 67(2). Pp. 199–211. DOI: 10.24423/EngTrans.1006.20190405
24. Bao, W., Jiang, J., Yu, Z., Zhou, X. Mechanical behavior of high-strength bolts in T-stubs based on moment distribution. *Engineering Structures*. 2019. 196. Pp. 109334. DOI: 10.1016/j.engstruct.2019.109334
25. Tuan, L.A. Behavior of ring flange – Bolts joint under complex bearing forces. *International Journal of Engineering and Advanced Technology*. 2019. 9(1). Pp. 7352–7358. DOI: 10.35940/ijeat.A2224.109119
26. Shafaray, K., Shafaray, S. Work flange connections of structural elements of an open profile on high-strength bolts. *Journal of Physics: Conference Series*. 1425(1) 2020. Pp. 012072.
27. ISO 16573:2015, Steel — Measurement method for the evaluation of hydrogen embrittlement resistance of high strength steels.
28. Popov, A., Babak, S. Effect of cutting modes and tool wear on the microhardness of the surface layer after face milling of structural and stainless steels. *Manufacturing Technology*. 2018. 18(6). Pp. 1011–1014. DOI: 10.21062/ujep/216.2018/a/1213-2489/mt/18/6/1011
29. Couchaux, M., Hjjaj, M., Ryan, I., Bureau, A. Effect of contact on the elastic behaviour of tensile bolted connections. *Journal of Constructional Steel Research*. 2017. 133. Pp. 459–474. DOI: 10.1016/j.jcsr.2016.10.012
30. Couchaux, M., Hjjaj, M., Ryan, I., Bureau, A. Tensile resistances of bolted circular flange connections. *Engineering Structures*. 2018. 171. Pp. 817–841. DOI: 10.1016/j.engstruct.2018.04.004

31. Semenov, A.A., Malyarenko, A.A., Porivaev, I.A., Safiullin, M.N. Stress-strain behavior investigation of friction grip bolts in flange joints of trusses. *Magazine of Civil Engineering*. 2014. 49(5). Pp. 54–62, 131–132. DOI: 10.5862/MCE.49.6
32. Priadko, I.N., Mushchanov, V.P., Bartolo, H., Vatin, N.I., Rudnieva, I.N. Improved numerical methods in reliability analysis of suspension roof joints. *Magazine of Civil Engineering*. 2016. 65(5). Pp. 27–41. DOI: 10.5862/MCE.65.3
33. Kim, J., Yoon, J.-C., Kang, B.-S. Finite element analysis and modeling of structure with bolted joints. *Applied Mathematical Modelling*. 2007. 31(5). Pp. 895–911. DOI: 10.1016/j.apm.2006.03.020
34. Álvarez, J.A., Lacalle, R., Arroyo, B., Cicero, S., Gutiérrez-Solana, F. Failure analysis of high strength galvanized bolts used in steel towers. *Metals*. 2016. 6(7). Pp. 163. DOI: 10.3390/met6070163
35. Brahim, S.V., Yue, S., Sriraman, K.R. Alloy and composition dependence of hydrogen embrittlement susceptibility in high-strength steel fasteners. *Philosophical Transactions of the Royal Society A: Mathematical, Physical and Engineering Sciences*. 2017. 375(2098). Pp. 20160407. DOI: 10.1098/rsta.2016.0407
36. Kalenov, V.V. Eksperimentalno-teoreticheskoe issledovanie i sovershenstvovanie metodov proektirovaniia boltovykh montazhnykh soedinenii stalnykh stroitelnykh konstruktsii [Experimental and theoretical research and improvement of design methods for bolted mounting joint. Melnikov Central Research and Design Institute of Steel Structures, Moscow, Russia, 1995.
37. Ooi, S.W., Ramjaun, T.I., Hulme-Smith, C., Morana, R., Drakopoulos, M., Bhadeshia, H.K.D.H. Designing steel to resist hydrogen embrittlement Part 2—precipitate characterisation. *Materials Science and Technology (United Kingdom)*. 2018. 34(14). Pp. 1747–1758. DOI: 10.1080/02670836.2018.1496536
38. Ramjaun, T.I., Ooi, S.W., Morana, R., Bhadeshia, H.K.D.H. Designing steel to resist hydrogen embrittlement: Part 1—trapping capacity. *Materials Science and Technology (United Kingdom)*. 2018. 34(14). Pp. 1737–1746. DOI: 10.1080/02670836.2018.1475919
39. Das, T., Sriraman, K.R., Brahim, S.V., Song, J., Yue, S. A study on the susceptibility of high strength tempered martensite steels to hydrogen embrittlement (HE). *ICF 2017 – 14th International Conference on Fracture*. 2017. Pp. 974–976.
40. Das, T., Rajagopalan, S.K., Brahim, S.V., Wang, X., Yue, S. A study on the susceptibility of high strength tempered martensite steels to hydrogen embrittlement (HE) based on incremental step load (ISL) testing methodology. *Materials Science and Engineering A*. 2018. 716. Pp. 189–207. DOI: 10.1016/j.msea.2018.01.032
41. Eder, M.A., Haselbach, P.U., Mishin, O.V. Effects of Coatings on the High-Cycle Fatigue Life of Threaded Steel Samples. *Journal of Materials Engineering and Performance*. 2018. 27(6). Pp. 3184–3198. DOI: 10.1007/s11665-018-3399-2

Contacts:

Nikolai Vatin, vatin@mail.ru

Rafkat Gubaydulin, gubaidulinrg@susu.ru

Aleksandr Tingaev, tingaevak@susu.ru

© Vatin, N., Gubaydulin, R.G., Tingaev, A., 2020



DOI: 10.18720/MCE.99.13

Deformations during drying of wooden corner elements of I-beams

A.S. Toropov^a, V.E. Byzov^{b*}, V.I. Melekhov^c

^a Saint Petersburg State Forest Technical University under name of S.M Kirov, St. Petersburg, Russia

^b St. Petersburg State University of Architecture and Civil Engineering, St. Petersburg, Russia

^c Northern (Arctic) Federal University named after M.V. Lomonosov, Arkhangelsk. Russia

*E-mail: mapana@inbox.ru

Keywords: core rot, the round assortments, drying of lumber, angular cross-sectional elements, supporting building structures, lateral warping of lumber

Abstract. At present, environmental degradation is occurring, which affects forests. Increasingly, in the trunks of conifers there is core (sound) rot. Round timber with sound rot is left in the forest, which does not contribute to improving the environmental situation. A new technological process is proposed for producing lumber from round timber with sound rot for the manufacture of structural elements for construction. In the process of cutting, the rot is removed, and the elements of the angular cross section are obtained. In the future, they are used for the manufacture of I-beams. A method of drying elements of an angular cross section in convection chambers of periodic action is considered. Samples were made in which the change in the angles of the inner quarter was measured. Samples were dried to a moisture content of $6 \pm 2\%$. During drying, the samples were fixed in pairs using clamps (clamps). It is established that the deviation of the angles of the side of the quarter of the bar of the angular cross section increases with increasing size of the quarter. The transverse warping of the pressed samples is much less than that of the samples without pressure. The optimal size of the core (core) rot should be 30-35% of the diameter of the round assortment at the top. Such rot sizes at the corresponding quarter sizes do not lead to significant allowances for machining and loss of volumes of high-quality structural wood.

1. Introduction

Currently, construction lumber is widely used in construction. This lumber is used in the manufacture of elements of load-bearing building structures for industrial, agricultural construction and low-rise housing construction. For the manufacture of structural elements, softwood, usually pine or spruce, is used.

Recently, however, environmental degradation has been occurring, which affects, among other things, forest areas. Increasingly, in the trunks of conifers there is core (central) rot [1]. The presence of sound rot in lumber for the manufacture of elements of load-bearing building structures is not allowed, therefore, the technological process of cutting tree trunks with rot into sawing logs involves the removal of sections of the trunk with rot. Sound rot primarily affects the part of the trunk located near the root system, and this section of the trunk has the largest diameter. In this part of the tree trunk, in addition to the presence of rot, there is a significant amount of sapwood with high strength characteristics.

Typically, the removal of rot occurs at the stage of harvesting round timber. At the same time, a healthy sapwood is removed together with the wood affected by rot. As a result, a large amount of quality wood remains in the forest. This leads not only to loss of harvested wood. In addition, wood left in the forest leads to the formation of sound rot in growing trees. The rot remaining in the sawn timber assortment supplied to the sawmills is removed in the process of cutting and obtaining sawn timber. The use of existing cutting schemes for sawing assortments with sound rot results in large losses of wood [2]. Recently, technological processes have been developed for the efficient cutting of assortments with the presence of rot. This is a method which consists in the following. Preliminary longitudinal sawing of short round timber is carried out. Perform one or more longitudinal cuts. From the parts of timber obtained after sawing, the core layer is removed, according to the dimensions of the voids formed in these parts, connecting blanks are made of wood. After drying, long timber is formed from the obtained parts of timber and connecting blanks, while the ends of the contact of



parts of the wood are displaced one relative to the other along the length of the formed timber [3]. In addition, there is a technological process to produce glued beams from elements of angular cross-section [4]. However, the proposed methods do not provide for lumber for construction purposes for construction.

We have a fundamentally new way of obtaining elements of building structures from round timber with sound rot. Production is carried out according to the following scheme. Cutting is done according to the timber scheme. On the first pass, a two-edged beam with core rot and lateral unedged thin lumber are obtained. On the second pass, two bars with core rot, as well as side unedged lumber, are obtained. Then, rot is removed by milling. After milling, the bars have a corner profile. The casts of the angle profile are subjected to chamber drying with mild regimes and their moisture content is adjusted to $14 \pm 2\%$. The bars are sorted so that the quality of the wood corresponds to grade 2 according to GOST 8486, which roughly corresponds to C24 strength class according to European standard EN 338-2011 "Structural wood. Strength classes". The bars are glued in such a way as to obtain an I-beam. The priority for this method is fixed by the patent for the invention of the Russian Federation [5].

I-beams made of wood are currently widely used in the construction of buildings and structures. Modern construction experience shows the feasibility of using I-beams for flights from 2 to 6 m [6]. High installation speed and ease of assembly increase the manufacturability of the construction of buildings and structures [7-14]. After processing with special compounds, the wood of the beams has the necessary fire resistance, anti-decay and insect damage. There is a great need for such beams in seismically dangerous areas of construction.

Sawing round timber with sound rot and manufacturing lumber for load-bearing building structures reduces the amount of wood with rot left in the forest. This helps to improve the environmental situation. Therefore, structural lumber obtained from such timber will be hereinafter referred to as ecological structural lumber.

The greatest difficulty in applying this method is the drying of the corner elements to operational humidity. Drying is accompanied by lateral warping, which increases the loss of wood during further processing. The warping of lumber in the transverse direction has been an object of research for a long time. As early as 1878, P.A. Afanasyev [15] in his work describes the possible types of contortion, the reasons for its appearance and factors affecting the decrease in its size. He proposed a formula for calculating the maximum deflection boom for lateral warping of lumber:

$$f_{\max} = \frac{\pi}{2} (W_{n.n} - W_{\kappa}) (K_t - K_r) \frac{B}{2}, \text{mm} \quad (1)$$

where W_s is saturation limit of wood cell walls, %; W_f is final wood moisture, %; K_t , K_r are tangential and radial shrinkage coefficients; B is lumber width, mm.

The maximum deflection arrow will be at the board, on the lower face of which there is a core. That is, the deflection will be the greater, the closer the sawn boards are located closer to the core of the round assortment. From equation (1) it follows that all boards, except for radial ones, after drying will have a grooved shape.

In 1971, G.G. Petrukhin obtained an approximate solution to the problem of structural warping of the cross section of lumber [16]. The solution was obtained on the basis of the provisions of the theory of deformations and the theory of elasticity. The author believes that the solutions to this problem obtained earlier by P.A. Afanasyev, K.I. Kolenchuk, V.A. Shevchenko, M.N. Feller and the solutions contain several incorrect assumptions and give various numerical results. He obtained equations for determining the cross-sectional shape of warped boards:

$$u = -\Delta W \left[K_r x - (K_r - K_t) y \cdot \arctg \left(\frac{x}{y} \right) \right], \text{mm} \quad (2)$$

$$v = -\Delta W \left[K_r y - (K_r - K_t) x \cdot \arctg \left(\frac{x}{y} \right) \right], \text{mm} \quad (3)$$

where u , v are components of the movement of the points of the cross section of the assortment after drying, mm; x , y are coordinates of points before drying, mm; K_r , K_t are radial and tangential shrinkage coefficients; $\Delta W = W_s - W_f$ is moisture difference between the saturation limit of the cell walls of wood and the final humidity (hygroscopic humidity), %.

Formulas (2) and (3) are obtained in a rectangular coordinate system x , y with the beginning in the center of the cross section of a round assortment.

It is known that the main cause of warpage of lumber is the anisotropy of shrinkage due to the anisotropy of the elastic characteristics of wood. Anisotropies of the elasticity characteristics of wood are considered in detail in the works of E.K. Ashkenazi [17] and N.L. Leontyev [18] and others. In particular, E.K. Ashkenazi considers wood as an orthotropic material (Fig. 1).

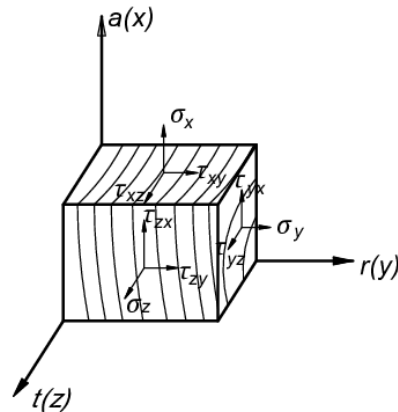


Figure 1. The stress state of the triaxial equal compression hydrostatic pressure.

The magnitude of the deformation depends not only on the magnitude of the acting stresses, but also on the direction of their action in the material. The author presents Hooke's law at first in the case of a triaxial stress state, i.e., stress and strain components are assigned to some Cartesian coordinate axes x , y , z and the elastic properties are determined by the characteristics of the elastic modulus E , transverse strain coefficient μ and shear modulus G . Then, if Cartesian coordinates with the directions of the axes of symmetry. Then the quantities E , μ , G have their own meaning for each direction in the material, which is expressed in the formula 4:

$$\begin{aligned}\varepsilon_x &= \frac{\sigma_x}{E_x} - \frac{\mu\sigma_y}{E_y} - \frac{\mu\sigma_z}{E_z} \\ \varepsilon_y &= -\frac{\mu\sigma_x}{E_x} + \frac{\sigma_y}{E_y} - \frac{\mu\sigma_z}{E_z} \\ \varepsilon_z &= -\frac{\mu\sigma_x}{E_x} - \frac{\mu\sigma_y}{E_y} + \frac{\sigma_z}{E_z} \\ \gamma_{xy} &= \frac{\tau_{xy}}{G}; \gamma_{yz} = \frac{\tau_{yz}}{G}; \gamma_{zx} = \frac{\tau_{zx}}{G}\end{aligned}\quad (4)$$

where τ is shear stress applicable on the sites, MPa; γ is angular deformations.

It was noted that the formulas indicate experimentally established features of the elastic deformation of anisotropic bodies. This fact will have a negative value in the future. The full set of characteristics of the elastic deformation of an orthotropic material consists of nine independent quantities (elastic constants). These include lateral strain coefficients, shear moduli, and elastic modulus when the coordinate system rotates through an angle of 45° around z axis. The author took the advantage of the rotation of the system at an angle of 45° alternately around each of the axes. This is necessary to obtain equations that calculate the elastic constants.

A significant amount of research on solving the issues of transverse warping was performed by Professor of Saint Petersburg University of Architecture and Civil Engineering V.N. Glukhikh. In [19] V.N. Glukhikh believes that the formulas for calculating the elastic constants are difficult due to the use of a number of experimentally determined quantities. It is known that the elastic deformation of wood is characterized by the reciprocal of the elastic modulus and varies depending on the angle of inclination of the annual layer to the face. The author suggests determining E_{xy}^{45} elastic modulus theoretically and believes that this would greatly simplify the task of studying the deformability of wood across the fibers. The author concludes that " E_{xy}^{45} modulus is equal to the elastic modulus in the tangential direction". Or in other words, at an annual layer inclination angle of 45° , the elastic modulus in the direction of x axis is equal to the elastic modulus in the tangential direction. To study the deformability of lumber, he suggests using the function:

$$\frac{1}{E_x} = \frac{\cos^4 \theta}{E_r} + \frac{\sin^4 \theta}{E_t} + \frac{3-a^2}{E_t} \sin^2 \theta \cdot \sin^2 \theta \quad (5)$$

where $a^2 = \frac{E_t}{E_r}$; θ is annual ring slope; E_r , E_t are modulus of elasticity of wood in the radial and tangential directions, GPa.

For convenience, expression (4) is written in Cartesian coordinates:

$$\frac{1}{E_x} = \frac{a^2 x^4 + (3-a^2)x^2 y^2 + y^4}{E_t (x^2 + y^2)^2} \quad (6)$$

The results of calculations by formula (5) show that for boards with a symmetry axis of the cross section coinciding with Y axis (Fig. 2), the least deformability takes place in the middle of the face width. From the middle to the edges of the face, the deformability increases, reaches its maximum value, and then decreases, tending in the limit to the reciprocal of the elastic modulus in the radial direction.

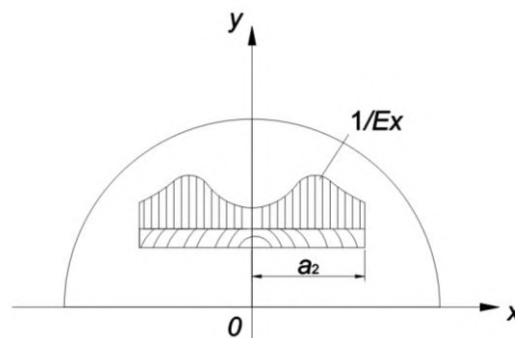


Figure 2. Deformability along the width of the boards of a semi-radial cut:
 $1/E_x$ is change in the value of deformability along the width of the board;
 a_2 is half the width of the board, mm.

The work also noted that “deformability of the radial boards along the width of the face changes imperceptibly, excluding a narrow local area adjacent to the middle of the width of the board”. For tangential boards, the deformability along the face also changes imperceptibly. According to the seam of semi-radial boards, the deformability varies from the smallest values along the edges to the maximum value in the middle.

This, as well as a slightly higher tensile strength in the radial direction compared with the tangential, ensures the absence of reservoir cracks during drying. The aim of this study is to develop a methodology for compiling individual patterns for cutting round timber into sawn timber, which excludes the negative influence of the anisotropy factor of wood during subsequent drying. The methodology for determining the greatest deformability of the board in cross section allows you to analyze any pattern of cutting logs. In [20] V.N. Glukhikh concludes that warping can be reduced by rationally sawing logs, since the deflection arrow in lateral warping depends on the size of the sawn timber, the anisotropy of drying, and the moisture content of the wood. In another work [12] V.N. Glukhikh gives a theoretical calculation and diagrams for determining the favorable sizes of lumber and their location in the section of sawing logs. Based on the calculations, an analysis is made of the options for cutting logs in which the quality of lumber does not suffer during drying.

Later studies [21, 22] showed that lateral warping is influenced not only by the width, but also the thickness of the lumber. A formula was obtained for calculating the magnitude of the transverse warpage, provided that the moisture distribution over the board section was evenly distributed (final drying period):

$$b_k = \frac{b^2 \Delta W (\alpha_2 - \alpha_1)}{4S}, mm \quad (7)$$

where b is board width, mm; S is board thickness, mm; ΔW is difference between the hygroscopicity limit and final moisture content of wood during drying, %; α_1 , α_2 are shrinkage coefficients of the inner and outer faces of the board.

Summarizing the results of the research, the following conclusions can be drawn. The resistance of lumber to warping increases in proportion to the square of their thickness, depends linearly on the difference in the coefficients of drying of the layers and is in a complex dependence on their width. The farther the board is cut from the center of the round assortment, the less its warpage.

Studies [23–25] showed that warpage of lumber during drying can be prevented in whole or in part using special clamps and preset pressure forces. Elastic warping of pressed boards is insignificant compared to warping of dried boards without pressing. In addition, warpage can be reduced by final heat and moisture treatment, as well as the use of high temperatures at the end of drying.

However, it should be noted that in all the above studies, a rectangular cross-section of lumber was considered. There are practically no studies of lateral warping. Therefore, conducting research on the drying of bars of a corner profile is an urgent task.

The objective of this work is to study the possibility of drying wooden corner elements for the manufacture of I-beams of supporting building structures. To achieve the goal, it is necessary to solve the following tasks: determine the amount of transverse warping of corner elements and develop measures to reduce the amount of wood loss during further processing of these elements.

2. Methods

Samples cut from corner elements were selected as the object under study. The breed of wood is pine. Corner elements were made as follows. Initially, four-edged timber with a cross-sectional size of 160×160 mm was cut from round assortments with sound rot with a diameter of at least 190 mm. Then, by longitudinal cutting, four bars were obtained with the presence of rot. Overall dimensions of bars 75×75 mm. By milling, rot was removed from these bars. The length of the samples is 550 mm (Fig.3). The smallest diameter of round timber with sound rot, from which corner elements are obtained, is 200 mm. “Hydromette compact” electric moisture meter was used to measure the wood moisture content of the samples. Range of measurement of humidity is 5–20 %. To change the angles, a quadrant goniometer was used to measure internal and external angles from 0 to 180 °C. G type clamps of 125 mm were used to provide pressure.

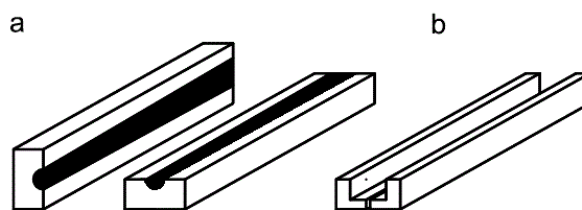


Figure 3. Corner profile elements production flow
a – bars with core rot; b – bars of the corner profile after removal of rot.

All bars are conditionally divided into three groups, each of which has its own quarter size: $b_1 = 20$ mm; $b_2 = 30$ mm; $b_3 = 37$ mm. The dimensions of the quarter corner elements are set depending on the diameter of the rot in round assortments. Determination of the moisture content of the wood samples before drying was carried out using an electric moisture meter. Measurements were taken every 15 cm of the sample length. Drying was carried out using clamps (clamps). Samples were fixed in pairs, or a bar was placed in a quarter (Fig. 4). One group of samples, also with a quarter size $b_4 = 37$ mm, was dried without the use of a clamp.

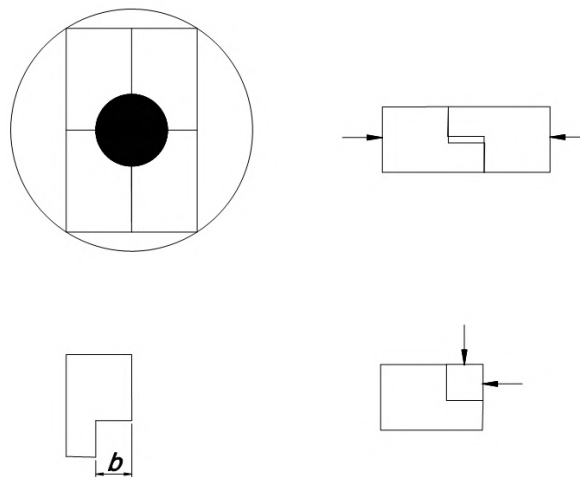


Figure 4. Schemes for fixing the bars during drying:
 b is the width of the selected quarter along which the corners are folded when pressing.

Samples were in the upper rows of lumber stacks. Forced drying mode. The temperature of the drying agent is 90 °C. This mode allows you to determine the maximum values of the angle and the size of the allowances.

Based on the conclusions given in the first section, we can assume that in the process of drying the shape of the bar will change as follows (Fig.5).

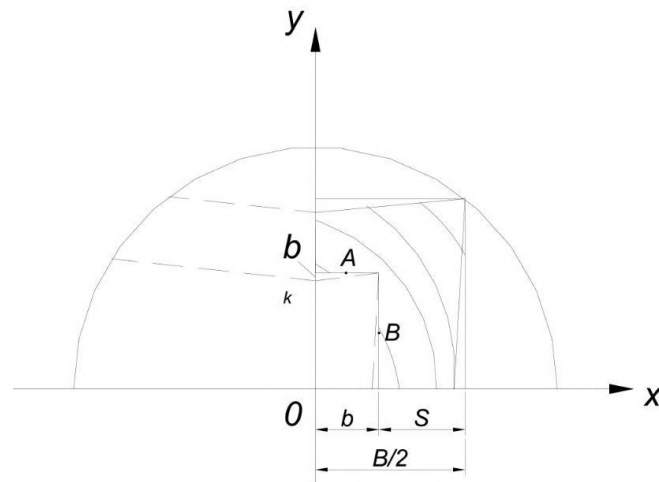


Figure 5. Changing the cross-sectional shape of the corner element during drying:
***A* is narrow surface of the selected quarter; *B* is wide surface of the selected quarter;**
***B/2* is the total width of the corner profile bar, mm;**
***S* is the width of the integral part of the angle bar, mm;**
***b* is width of the selected quarter, mm; *b_k* is bending value, mm.**

The section of the bar is divided into two rectangles, which are a continuation of the boards conditionally sawn from a round assortment. To calculate the magnitude of the transverse warpage, we use the formula (7). Consider the deformation of the cross section of the corner element as semi-radial boards. Therefore, the maximum strain may be at points A and B.

After drying was completed, exposure was carried out in the workshop at an air temperature of 18 °C for 30 minutes. Clamps were not removed. Measurement of wood moisture after drying was carried out similarly to measurements before drying.

Next, measurements were made of the angle of the quarter. Measurements were carried out with a goniometer-quadrant at five points.

During the study, the following tasks.

1. To establish the dependence of the deviation of the angle of the inner quarter of the element from its original position.
2. To determine the allowances for the processing of the corner element at different percentages of rot in round assortments.
3. To identify the difference in the values of the deviations of the angle of the inner quarter during drying with and without pressure.
4. To establish the validity of the assumption that during drying it will look as shown in Fig. 5.
5. The experimental plan is presented in Table. 1.

Table 1. The plan of the experiment.

| Experiment number | Drying method | Width <i>b</i> , mm |
|-------------------|------------------|---------------------|
| 1 | | 20 |
| 2 | With pressure | 30 |
| 3 | | 37 |
| 4 | Without pressure | 37 |

Based on the results of measurements of the deviations of the angle of the quarter of the sample, a statistical analysis of the deviations of the angle of the sides of the quarter from straightness was performed. According to the statistics obtained, we found the minimum number of measurements for the necessary security of the arithmetic mean of the deviations. Next, we found the regression equation for the change in the

deviation of the quarter angle depending on its width. The equation is obtained as a result of a multivariate experiment. The output parameter is the deviation of the quarter angle of the corner element. The output parameter is influenced by the wood species, the location of the element in the round assortment, the direction of the annual rings, the age of the tree, the presence of defects, the shape of the blanks, the conditions and place of growth, the anatomical structure of the wood, the percentage of moisture in the wood, the nature of the treatment, the mode and technology of drying, the condition inter-row gaskets and the location in the stack. Controllable factors: quarter size $b_1 = 20$ mm; $b_2 = 30$ mm; $b_3 = 37$ mm, drying method (with or without pressure). Factors with a constant value: drying mode and temperature of the drying agent, the direction of the annual rings, the shape of the blanks. Disturbing factors that are not controlled: presence of defects, age and anatomical features of wood, percentage of wood moisture. Checked the adequacy of the mathematical model.

3. Results and Discussion

Before drying, the moisture content of the wood samples was changed. The results of changes in wood moisture are given in Table. 2.

Table 2. Moisture values of wood samples before drying.

| Sample number | Quarter size, b , mm | Sample condition | Number of humidity measurements, W , % | | | | Average sample humidity, W , % |
|---------------|------------------------|------------------|--|------|------|------|----------------------------------|
| | | | 1 | 2 | 3 | 4 | |
| 1 | 20 | fixed | 17.2 | 17.3 | 18.4 | 19.2 | 18.02 |
| 2 | | | 16.4 | 18.3 | 15.6 | 17.1 | 16.85 |
| 3 | | | 17.3 | 18.6 | 17.8 | 16.2 | 17.47 |
| 4 | | | 15.8 | 16.5 | 18.7 | 18.4 | 17.35 |
| 5 | | | 18.4 | 17.3 | 16.3 | 17.7 | 17.42 |
| 6 | | | 19.3 | 18.6 | 18.2 | 17.3 | 18.35 |
| 7 | | | 16.5 | 17.3 | 18.7 | 15.6 | 17.02 |
| 8 | | | 16.8 | 16.3 | 17.1 | 16.3 | 16.62 |
| 9 | 30 | fixed | 16.7 | 17.1 | 17.0 | 16.8 | 16.90 |
| 10 | | | 14.5 | 14.8 | 16.3 | 15.2 | 15.20 |
| 11 | | | 15.2 | 17.5 | 16.4 | 15.8 | 16.22 |
| 12 | | | 14.8 | 15.3 | 17.1 | 16.6 | 15.95 |
| 13 | | | 16.7 | 17.1 | 17.0 | 16.8 | 16.90 |
| 14 | | | 14.5 | 15.7 | 17.4 | 15.2 | 15.70 |
| 15 | | | 15.2 | 17.5 | 17.5 | 15.8 | 16.50 |
| 16 | | | 16.3 | 15.3 | 17.1 | 16.7 | 16.30 |
| 17 | 37 | fixed | 19.3 | 22.5 | 21.4 | 20.2 | 20.85 |
| 18 | | | 19.1 | 20.4 | 21.3 | 21.6 | 20.60 |
| 19 | | | 19.3 | 21.3 | 20.3 | 19.7 | 20.15 |
| 20 | | | 18.3 | 21.8 | 22.2 | 19.8 | 20.52 |
| 21 | | | 19.3 | 23.4 | 21.4 | 20.7 | 21.20 |
| 22 | | | 20.6 | 20.4 | 21.3 | 21.6 | 20.97 |
| 23 | | | 18.8 | 22.5 | 22.6 | 20.2 | 21.02 |
| 24 | | | 21.3 | 20.4 | 23.6 | 21.6 | 21.72 |
| 25 | 37 | not fixed | 17.2 | 22.5 | 23.2 | 20.4 | 20.83 |
| 26 | | | 17.4 | 19.6 | 23.2 | 21.1 | 20.35 |
| 27 | | | 18.3 | 22.3 | 24.5 | 19.7 | 21.20 |
| 28 | | | 19.5 | 18.5 | 22.4 | 22.4 | 20.70 |
| 29 | | | 16.8 | 23.1 | 23.2 | 19.7 | 20.70 |
| 30 | | | 17.6 | 19.6 | 21.9 | 20.3 | 19.85 |
| 31 | | | 18.1 | 22.8 | 22.7 | 20.7 | 19.85 |
| 32 | | | 16.5 | 19.6 | 22.1 | 21.2 | 21.07 |

Analysis of the moisture content of the wood samples before drying shows that the moisture content of the wood is in the range from 15.2 to 21.7%. This humidity is pre-matured indoors wood.

Next, the samples of the angle profile were dried. The results of measurements of wood moisture after drying are given in table. 3. The moisture parameters of wood correspond to the results of studies in publications [26–33].

Table 3. Moisture values of wood samples after drying.

| Sample number | Quarter size, b , mm | Sample condition | Number of humidity measurements, W , % | | | | Average sample humidity, W , % |
|---------------|------------------------|------------------|--|-----|-----|-----|----------------------------------|
| | | | 1 | 2 | 3 | 4 | |
| 1 | 20 | fixed | 5.3 | 5.1 | 5.8 | 6.2 | 5.60 |
| 2 | | | 8.5 | 8.3 | 9.2 | 8.8 | 8.70 |
| 3 | | | 6.2 | 5.3 | 6.2 | 5.8 | 5.80 |
| 4 | | | 6.7 | 4.8 | 5.5 | 6.6 | 5.90 |
| 5 | | | 8.3 | 8.3 | 9.6 | 7.8 | 8.20 |
| 6 | | | 5.3 | 5.3 | 6.2 | 5.8 | 5.70 |
| 7 | | | 3.3 | 5.3 | 6.7 | 5.3 | 5.60 |
| 8 | | | 4.9 | 4.9 | 5.8 | 6.2 | 5.80 |
| 9 | 30 | fixed | 5.2 | 5.0 | 5.3 | 5.3 | 5.25 |
| 10 | | | 5.5 | 5.3 | 5.8 | 5.8 | 5.72 |
| 11 | | | 6.1 | 5.0 | 5.3 | 5.3 | 5.47 |
| 12 | | | 5.5 | 5.3 | 6.1 | 6.1 | 5.80 |
| 13 | | | 5.3 | 5.3 | 5.8 | 5.8 | 5.80 |
| 14 | | | 5.2 | 4.9 | 5.3 | 5.3 | 5.20 |
| 15 | | | 5.0 | 5.1 | 6.1 | 6.1 | 5.60 |
| 16 | | | 5.5 | 5.6 | 5.6 | 5.6 | 5.70 |
| 17 | 37 | fixed | 5.3 | 5.3 | 5.5 | 6.0 | 5.50 |
| 18 | | | 4.8 | 6.0 | 6.5 | 6.3 | 5.80 |
| 19 | | | 5.6 | 5.3 | 5.5 | 5.8 | 5.50 |
| 20 | | | 6.5 | 7.2 | 6.2 | 6.5 | 5.60 |
| 21 | | | 5.6 | 5.3 | 5.5 | 5.8 | 5.50 |
| 22 | | | 6.1 | 7.5 | 8.2 | 6.1 | 6.90 |
| 23 | | | 5.7 | 6.0 | 6.6 | 5.7 | 5.90 |
| 24 | | | 5.6 | 5.3 | 5.5 | 6.0 | 5.60 |
| 25 | 37 | not fixed | 4.9 | 5.2 | 5.1 | 5.0 | 5.05 |
| 26 | | | 5.5 | 5.7 | 5.6 | 5.5 | 5.60 |
| 27 | | | 6.0 | 5.5 | 5.2 | 5.8 | 5.60 |
| 28 | | | 5.5 | 7.5 | 5.3 | 6.3 | 6.10 |
| 29 | | | 7.2 | 5.3 | 5.0 | 5.3 | 5.70 |
| 30 | | | 6.3 | 6.3 | 5.6 | 7.1 | 6.20 |
| 31 | | | 5.7 | 8.3 | 5.1 | 6.5 | 6.20 |
| 32 | | | 6.1 | 4.6 | 5.2 | 5.2 | 6.40 |

The moisture content of the wood samples after drying is in the range of 6 ± 2 %. To determine the boundaries of the values of the deviations of the angle of the sides of the quarter for such a value of the final moisture content of the wood, we performed an estimated calculation of these values by the formula (5).

The final moisture content of the wood samples was taken equal to 6%. Wood density of the samples is 400 kg/m^3 . The coefficient of radial shrinkage was calculated by the formula: $K_r = 0.01\rho/W_s = 0.01 \cdot 400/30 = 0.13$. Tangential shrinkage coefficient: $K_t = 0.018\rho/W_s = 0.018 \cdot 400/30 = 0.24$.

We have obtained value $\alpha_2 - \alpha_1$ at $b = 20 \text{ mm}$:

$$\alpha_1 = \frac{20.11}{150} \left(75 \cdot \arctg \frac{150}{2.75} - 20 \cdot \arctg \frac{150}{2.20} \right) = 0.048,$$

then bending value will make:

$$b_k = \frac{b^2 \Delta W (\alpha_2 - \alpha_1)}{4S} = \frac{150^2 \cdot 0.24 \cdot 0.048}{455} = 1.18, \text{ mm}.$$

We have obtained value $\alpha_2 - \alpha_1$ at $b = 30$ mm:

$$\alpha_2 - \alpha_1 = \frac{20.11}{150} \left(75 \cdot \arctg \frac{150}{2.75} - 30 \cdot \arctg \frac{150}{2.30} \right) = 0.034,$$

then bending value will make:

$$b_k = \frac{b^2 \Delta W (\alpha_2 - \alpha_1)}{4S} = \frac{150^2 \cdot 0.240 \cdot 0.034}{455} = 1.02, \text{ mm.}$$

We have obtained value $\alpha_2 - \alpha_1$ at $b = 37$ mm:

$$\alpha_2 - \alpha_1 = \frac{20.11}{150} \left(75 \cdot \arctg \frac{150}{2.75} - 37 \cdot \arctg \frac{150}{2.37} \right) = 0.024,$$

then bending value will make:

$$b_k = \frac{b^2 \Delta W (\alpha_2 - \alpha_1)}{4S} = \frac{150^2 \cdot 0.240 \cdot 0.024}{455} = 0.87, \text{ mm.}$$

The calculations show that the magnitude of the transverse warpage will have a value of about one millimeter.

The required number of measurements was determined. In the calculation, the data of the fourth experiment were used, since the largest value of the mean square deviation is observed there. The formula for finding the minimum number of measurements:

$$n_{\min} = \left(\frac{t \cdot S}{\Delta} \right)^2, \quad (8)$$

where S is mean-square deviation; t is Student criterion; Δ is set confidence probability.

With a confidence probability of 0.95, the number of samples will be 7.35. We accept 8 samples for each experiment.

Further, for each sample, the angle of deviation of the sides of the quarter from the right angle was measured after drying. We performed a statistical analysis of the angle deviation for samples of each quarter size and the state of the sample during drying (with fixation and without fixation). In addition, the necessary allowance was calculated to straighten one side of a quarter of the sample after drying. Statistical indicators are given in Table. 4.

Table 4. Statistical indicators of the deviation of the angle of the sides of the quarter of the samples.

| Sample number | Quarter size, b , mm | Sample condition | Statistics | | | | | | |
|---------------|------------------------|------------------|---------------------|---------------|-----------|-----------------|---------|-------|----------|
| | | | \hat{Y} , degrees | S , degrees | ν , % | S_y , degrees | ζ | S_s | K , mm |
| 1 | 20 | fixed | 1.25 | 0.43 | 34.40 | 0.15 | 12.24 | 0.108 | 0.6 |
| 2 | 30 | | 2.37 | 0.48 | 20.25 | 0.17 | 7.20 | 0.120 | 1.0 |
| 3 | 37 | | 3.25 | 0.43 | 13.23 | 0.15 | 4.70 | 0.108 | 1.6 |
| 4 | 37 | not fixed | 4.87 | 0.59 | 12.29 | 0.21 | 4.34 | 0.140 | 2.5 |

Designation: \hat{Y} is arithmetic mean of the angle deviation; S is mean square deviation; ν is variation coefficient; S_y is arithmetic mean error; ζ is arithmetic mean accuracy indicator; S_s is standard deviation error; K is the amount of machining allowance on one side of the quarter.

The required prerequisites for statistical analysis are the normality of the distribution of the output value and the homogeneity of the variances of the experiments. The homogeneity of the dispersions of the experiments was checked with uniform duplication by G is Cochren criterion. For this, the calculated G_{calc} is ratio was calculated by the formula:

$$G_{calc} = \frac{s_{\max}^2}{s_1^2 + s_2^2 + \dots + s_N^2}, \quad (9)$$

Where $s_1^2, s_2^2, \dots, s_N^2$ are variance of experimental values 1, 2, N ; s_{\max}^2 is maximum dispersion value.

According to the selected level of significance, the number of degrees of freedom and the number of experiments, we obtain the value G_{tab} . If $G_{calc} < G_{tab}$, then the hypothesis of homogeneity of variances is accepted.

Check the adequacy of the regression model. Checking the adequacy of the mathematical model answers the question of whether the constructed model of the output quantity with sufficient accuracy.

Let N be the number of series of parallel experiments, n is the number of duplicated experiments in every series, p is the number of estimated regression coefficients of the mathematical model. We have determined the sum of the squares characterizing the adequacy of the model S_{ad} . With uniform duplication, we calculate it by the formula:

$$S_{ad} = n \sum_{j=1}^N (\hat{y}_i - y_j)^2, \quad (10)$$

where \hat{y}_j is average value of experimental results in the j -th series of duplicated experiments; $j = 1, 2, \dots, N$; \hat{y}_i value of the output value calculated by the regression equation for the i -th main experiment.

After the calculations, we obtained $S_{ad} = 0.42$. We calculated the value of F - Fisher criterion and compared it with the table value. Its value is 1.62. We compare the calculated F_{calc} and tabular F_{tab} of the value of Fisher criterion. The calculated value should not exceed the table value. $F_{calc} < F_{tab}$ 1.62 < 4.32. Thus, we proved that the chosen mathematical model is adequate to the experimentally obtained values.

Based on the data obtained, a point graph, a trend, and a model corresponding to the trend were constructed. A graph of the deviation of the angle of the sides of the quarter element for different sizes of the quarter is shown in Fig. 6. The dependence of the deviation of the angle of the inner quarter, depending on its width, is described by a regression equation of the form:

$$y = 0.043x^2 - 0.1013x + 1.57 \quad (11)$$

$$R^2 = 1$$

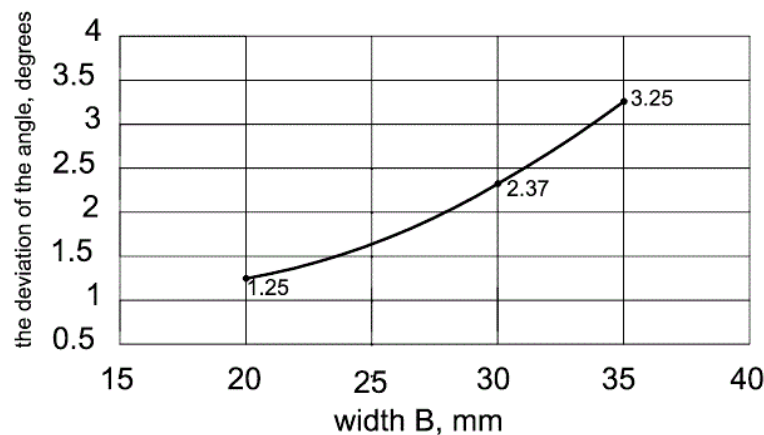


Figure 6. Diagram of the deviation of the angle of the side of the quarter from its width B is quarter width, mm.

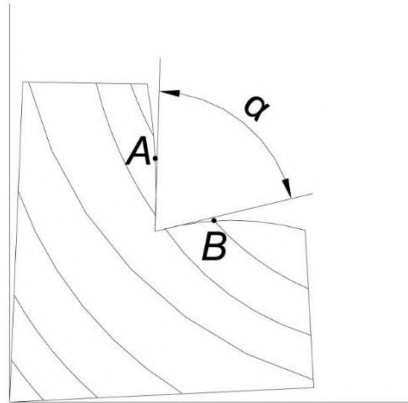
The values of the discrepancies in the calculation results of the deviation of the angle of the sides of the quarter of the element from straightness for different sizes of the quarters obtained theoretically and experimentally are given in Table 5.

Table 5. The values of the discrepancy in the results of calculations of the deviation of the angle of the sides of the quarter from straightness.

| Central rot content, % | Quarter side size, b , mm | S , mm | B , mm | b_k , mm | K , mm | Difference between K and b_k , % |
|------------------------|-----------------------------|----------|----------|------------|----------|--------------------------------------|
| 21 | 20 | 55 | 150 | 1.18 | 0.6 | 96.9 |
| 31 | 30 | 45 | 150 | 1.02 | 1.0 | 2.0 |
| 38 | 37 | 37 | 150 | 0.87 | 1.6 | 84.0 |
| 38 | 37 | 37 | 150 | 0.87 | 2.5 | 187.0 |

Designation: S is the size of the remainder of the bar after removing the quarter; B is width of the sides of a four-edged bar; b_k is bending value; K is machining allowance.

Analysis of the data given in Table 5 and the research results [34, 35] shows that the formula for calculating the magnitude of the transverse warpage (5) in the case of drying samples of elements of the angular cross section is not applicable. The experimental data indicate completely different trends in the magnitude of the deflection and the deviations of the sides of the corner bar from straightness. The cross-sectional shape of the bar after drying is shown in Fig. 7.



**Figure 7. Cross-sectional shape of the bar after drying:
A and B - sides of the selected quarter; α - the angle between the sides of the quarter, deg.**

The results of the studies show the absence of theoretical provisions for justifying the relationship between the deviation of the quarter side angle and various factors during drying, therefore, further studies are required for high-quality drying of the bars of the angular cross section.

4. Conclusion

Analyzing the results, we can draw the following conclusions:

1. The cross-sectional shape of the samples has changed as we expected.
2. It is impossible to consider a section of a bar of an angular cross section as two rectangles that are the continuation of the boards, conventionally cut from the round timber.
3. The calculation of the deviations of the angles of the side of the quarter bar of the corner cross-section by analogy with the calculation for calculating the amount of transverse warpage for boards will lead to incorrect results.
4. The amount of warping of the pressed samples is much smaller than that of the samples subjected to drying without pressing.
5. The allowances for the machining of dried non-pressed bars are significantly higher than for dried pressed bars.
6. The magnitude of the deviations of the angles of the side of the quarter of the bar of the angular cross section increases with increasing size of the quarter.
7. The angle of the quarter side after drying the bars with an angular cross-section deviates by 2–3° and is 92–93°.
8. The optimal size of the core (central) rot should be 30–35 % of the diameter of the round assortment at the top. Such rot sizes at the corresponding quarter sizes do not lead to significant machining allowances.
9. It is possible to dry wooden corner elements for the manufacture of beams of load-bearing building structures to operating humidity without significantly changing their shape.

References

1. Semenikova, I. G. Fitopatologiya. Derevorazrushayushchiye griby, gnili patologicheskiye okraski (opredelitelnyye tablitsy) [Plant pathology. Wood-destroying mushrooms rot and pathological stains (identification tables)]. 2nd ed Stereotyped. Moscow, 2002. 58 p. (rus)
2. Petrovskiy, V.S. Issledovaniya predelno-dopustimogo razmera gnili v pilovochnom syrye [Research on the maximum permissible size of rot in the saw log]. Lesnaya promyshlennost. Moscow. 1963. No. 11. Pp. 4–6. (rus)
3. Toropov, A.S., Toropov, S.A., Mikryukova, Ye.V. Sposob raskroya kruglykh lesomaterialov, porazhennykh serdtsevinnoy gnilyu [The method of cutting round timber, affected by heart rot]. Patent Russia no. 200813768103, 2010. (rus)
4. Toropov, S., Nikolayev, D. Proizvodstvo kleyenogo brusa iz sosny s serdtsevinnoy gnilyu [Production of glued laminated veneer lumber from pine with pith rot]. Sbornik materialov mezhvuzovskoy nauchno-prakticheskoy konferentsii adyunktov, kursantov,

- studentov i slushateley «Ugolovno-ispolnitelnaya sistema Rossii: istoriya i sovremennost (k 130-letiyu UIS» [Collection of materials of the interuniversity scientific-practical conference of adjuncts, cadets, students and listeners "The penal system of Russia: history and modernity (to the 130th anniversary of the UIS)". Vologda. 2009. Pp. 289–293. (rus)
5. Byzov, V.Ye., Toropov, A.S., Toropov, S.A. Sposob polucheniya konstruktsionnoy piloproductsii iz kruglykh lesomaterialov, imeyushchikh serdtsevinnyuyu gnul [The method of obtaining structural sawn timber from round timber with heart rot]. Patent Russia no. 2654720, 2018. (rus)
 6. Vorontsova, N.A., Filatov, N.V., Shestopalov, Ye.G. Ispolzovaniye kleyefanernykh elementov s perforirovannymi stenkami v konstruktsiyakh maloetazhnykh derevyannykh zdaniy [The use of glue-type elements with perforated walls in the structures of low-rise wooden buildings]. Vologdinskiye chteniya. 2012. No. 80. Pp. 74–76. (rus)
 7. Karelskiy, A.V., Zhuravleva, T.P., Labudin, B.V. Bending tests of wooden composite beams connected by metal toothed plates with breaking load. Magazine of Civil Engineering. 2015. 54(2). Pp. 77–85. DOI: 105862/MCE.54.9. (rus)
 8. Tusnin, A.R., Prokich, M. Experimental studies of the work of I-beam beams under the action of bending and torsion. Magazine of Civil Engineering. 2015. 53(1). Pp. 24–31. (rus) DOI: 10.5862/MCE.53.3
 9. Benjeddou, O., Limam, O., Oueddou, M. Experimental and theoretical study of a foldable composite beam. Engineering and Structures. 2012. No. 44. Pp. 312–321.
 10. Challamel, N., Girhammar, U. Lateral-torsional buckling of vertically layered composite beams with interlayer slip under uniform moment. Engineering and Structures. 2012. No. 34. Pp. 505–513.
 11. Khorsandnia, N., Valipour, H., Crews, K. Nonlinear finite element analysis of timber beams and joints using the layered approach and hypoelastic constitutive law. Engineering and Structures. 2013. No. 46. Pp. 606–614.
 12. Harte, A., Baylor, G. Structural evaluation of castellated timber I-joists. Engineering and Structures. 2011. 33(12). Pp. 3748–3754.
 13. Rassokhin, A.S., Ponomarev, A.N., Figovskiy, O.L. Ultra-light hybrid composite wood-polymer structural materials in construction. Magazine of Civil Engineering. 2018. 79(3). Pp. 132–139.
 14. O'Loinsigh, C., Oudjene, M., Shotton, E., Pizzi, A., Fanning, P. Mechanical behavior and 3D stress analysis of multi-layered wooden beams made with welded-through wood dowels. Composite Structures. 2012. 94(2). Pp. 313–321.
 15. Ugolev, B.N. Deformativnost drevesiny i napryazheniya pri sushke. Lesnaya promyshlennost [Timber industry]. Moscow. 1971. 176 p. (rus)
 16. Petrukhin, G.G. Issledovaniye korobleniya pilomaterialov i izdeliy iz drevesiny [Investigation of warpage of lumber and wood products]. Extended Abstract of Cand. Sci Dissertation. Moscow. MLTI Publ. 1971. 22 p. (rus)
 17. Ashkenazi, Ye.K. Anizotropiya drevesiny i drevesnykh materialov [Anisotropy of wood and wood materials]. Lesnaya promyshlennost. [Timber industry]. Moscow. 1978. 224 p. (rus)
 18. Leontyev, N.L. Uprugiyeh deformatsii drevesiny [Elastic deformation of wood]. M.-L. GLBI. 1952. 120 p. (rus)
 19. Glukhikh, V.N. Uprugaya deformativnost drevesiny poperek volokon [Elastic deformability of wood across the grain]. Lesnoy zhurnal. 2007. No. 5. Pp. 77–83. (rus)
 20. Glukhikh, V.N. Prognozirovaniye kachestva sushki pilomaterialov po kriteriyu deformativnosti pri sostavlenii skhemy raskroya brevna [Predicting the quality of drying sawn timber by the criterion of deformability when drawing up a cutting scheme for logs]. Izvestiya SPbGLTA [News SPbGLTA]. SPb. LTA. 2006. No. 178. (rus)
 21. Glukhikh, V.N., Zaripov, Sh.G. Poperechnoye korobleniye pilomaterialov pri sushke [Cross-warping of sawn timber during drying]. Izvestiya SPbGLTA [News SPbGLTA]. SPb. LTA. 2008. No. 181. (rus)
 22. Glukhikh, V.N., Chernykh, A.G. Anizotropiya drevesiny. Tekhnologicheskii aspekt [Anisotropy of wood. Technological aspect]. SPbGASU Publ.. SPb. 2013. 240 p.
 23. Petrukhin, G.G. K raschetu usilii prizhima pilomaterialov pri sushke [To the calculation of the pressing forces of sawn timber during drying]. Sbornik rabot MLTI. 1970. No. 35. Pp. 88–97. (rus)
 24. Sokolov, P.V. Opredeleniye neobkhodimykh usilii prizhima dlya predotvrashcheniya korobleniya pilomaterialov i zagotovok v protsesse sushki [Determination of the necessary pressing forces to prevent warping of lumber and workpieces during the drying process]. Nauchnyye trudy LTA. LTA. 1968. No. 68. Pp. 3–9. (rus)
 25. Kharitonov, G.N., Prelovskiy, V.G. Pruzhinnyye styazhki dlya szhatiya shtabelya pilomaterialov pri sushke [Spring ties for compressing a pile of sawn timber during drying]. Derevoobrabatvayushchaya promyshlennost. No. 5. 1963. Pp. 23–24. (rus)
 26. Almeida, G., Gagné, S., Hernández, R.E. A NMR Study of Water Distribution in Hardwoods at Several Equilibrium Moisture Contents. Wood Science and Technology, 2007, No. 41, Pp. 293–307. DOI: 10.1007/s00226-006-0116-3
 27. Alexiou, P.N., Wilkins, P., Hartley, J. Effect of Pre-Steam on Drying Rate, Wood Anatomy and Shrinkage of Regrowth Eucalyptus pilularis Sm. Wood Science Technology. 1990. No. 24. Pp. 103–110.
 28. Avramidis, S., Hatzikiriakos, S.G., Siau, J.F. An Irreversible Thermodynamics Model for Unsteady-State Nonisothermal Moisture Diffusion in Wood. Wood Science and Technology. 1994. No. 28. Pp. 349–358.
 29. Chen, P., Pei, D.C.T. A Mathematical Model of Drying Processes. International Journal of Heat and Mass Transfer. 1989. 32(2). Pp. 297–310.
 30. Comstock, G.L. Moisture Diffusion Coefficients in Wood as Calculated from Adsorption Desorption and Steady State Data. Forest Products Journal. 1963. 13(3). Pp. 97–103.
 31. Hagi, A.K. A Mathematical Model of the Drying Process. Acta Polytechnica. 2001. 41(3). Pp. 20–23.
 32. Bramhall, G. Mathematical Model for Lumber Drying. Journal Wood Science. 1979. No. 12. Pp. 14–31.
 33. Hutton, D.V. Fundamentals of Finite Element Analysis. McGraw-Hill, 2004. 494 p.
 34. Stamm, A. J., Nelson, R. M. Comparison between measured and theoretical drying diffusion coefficients for Southern pine. Forest Products Journal. 1961, No. 11, Pp. 536–543.
 35. Balantseva, N.B., Melekhov, V.I., Kalinicheva, O.A. Sovershenstvovaniye metoda rascheta protsessa konvektivnoy sushki pilomaterialov [Improvement of the method for calculating the process of convective drying of sawn timber]. Lesnoy zhurnal [Forest Journal]. 2018. 364(4). Pp.132–139.

Contacts:

Aleksandr Toropov, Toropov_A_S@mail.ru

Viktor Byzov, mapana@inbox.ru

Vladimir Melekhov, lti@narfu.ru

© Toropov, A.S., Byzov, V.E., Melekhov, V.I., 2020



ПОЛИТЕХ
Санкт-Петербургский
политехнический университет
Петра Великого

Инженерно-строительный институт
Центр дополнительных профессиональных программ

195251, г. Санкт-Петербург, Политехническая ул., 29,
тел/факс: 552-94-60, www.stroikursi.spbstu.ru,
stroikursi@mail.ru

Приглашает специалистов проектных и строительных организаций,
не имеющих базового профильного высшего образования
на курсы профессиональной переподготовки (от 500 часов)
по направлению «Строительство» по программам:

П-01 «Промышленное и гражданское строительство»

Программа включает учебные разделы:

- Основы строительного дела
- Инженерное оборудование зданий и сооружений
- Технология и контроль качества строительства
- Основы проектирования зданий и сооружений
- Автоматизация проектных работ с использованием AutoCAD
- Автоматизация сметного дела в строительстве
- Управление строительной организацией
- Управление инвестиционно-строительными проектами. Выполнение функций технического заказчика

П-02 «Экономика и управление в строительстве»

Программа включает учебные разделы:

- Основы строительного дела
- Инженерное оборудование зданий и сооружений
- Технология и контроль качества строительства
- Управление инвестиционно-строительными проектами. Выполнение функций технического заказчика и генерального подрядчика
- Управление строительной организацией
- Экономика и ценообразование в строительстве
- Управление строительной организацией
- Организация, управление и планирование в строительстве
- Автоматизация сметного дела в строительстве

П-03 «Инженерные системы зданий и сооружений»

Программа включает учебные разделы:

- Основы механики жидкости и газа
- Инженерное оборудование зданий и сооружений
- Проектирование, монтаж и эксплуатация систем вентиляции и кондиционирования
- Проектирование, монтаж и эксплуатация систем отопления и теплоснабжения
- Проектирование, монтаж и эксплуатация систем водоснабжения и водоотведения
- Автоматизация проектных работ с использованием AutoCAD
- Электроснабжение и электрооборудование объектов

П-04 «Проектирование и конструирование зданий и сооружений»

Программа включает учебные разделы:

- Основы сопротивления материалов и механики стержневых систем
- Проектирование и расчет оснований и фундаментов зданий и сооружений
- Проектирование и расчет железобетонных конструкций
- Проектирование и расчет металлических конструкций
- Проектирование зданий и сооружений с использованием AutoCAD
- Расчет строительных конструкций с использованием SCAD Office

П-05 «Контроль качества строительства»

Программа включает учебные разделы:

- Основы строительного дела
- Инженерное оборудование зданий и сооружений
- Технология и контроль качества строительства
- Проектирование и расчет железобетонных конструкций
- Проектирование и расчет металлических конструкций
- Обследование строительных конструкций зданий и сооружений
- Выполнение функций технического заказчика и генерального подрядчика

По окончании курса слушателю выдается диплом о профессиональной переподготовке
установленного образца, дающий право на ведение профессиональной деятельности

